

Advanced flamelet tabulation strategies for Large Eddy Simulations of single- and multi-phase turbulent jet flames

Erweiterte Flamelet-Tabellierungsstrategien für die Grobstruktursimulationen ein- und mehrphasiger turbulenter Freistrahlfammen

Zur Erlangung des akademischen Grades Doktor-Ingenieur (Dr.-Ing.)

genehmigte Dissertation von Sandro Gierth aus Räckelwitz

Tag der Einreichung: 17.08.2021, Tag der Prüfung: 27.09.2021

1. Gutachten: Prof. Dr.-Ing. Christian Hasse
 2. Gutachten: Prof. Dr.-Ing. Michael Wensing
- Darmstadt - D17



TECHNISCHE
UNIVERSITÄT
DARMSTADT



Simulation of reactive Thermo-Fluid Systems

Advanced flamelet tabulation strategies for Large Eddy Simulations of single- and multi-phase turbulent jet flames

Erweiterte Flamelet-Tabellierungsstrategien für die Grobstruktursimulationen ein- und mehrphasiger turbulenter Freistrahlfammen

genehmigte Dissertation von Sandro Gierth

1. Gutachten: Prof. Dr.-Ing. Christian Hasse
2. Gutachten: Prof. Dr.-Ing. Michael Wensing

Tag der Einreichung: 17.08.2021

Tag der Prüfung: 27.09.2021

Darmstadt - D17

URN: urn:nbn:de:tuda-tuprints-211223

Veröffentlicht unter CC-BY 4.0 International
<https://creativecommons.org/licenses>

Preface / Vorwort

Die vorliegende Dissertation entstand im Rahmen meiner Tätigkeit als wissenschaftlicher Mitarbeiter an der TU Bergakademie Freiberg und der TU Darmstadt. Teile dieser Arbeit wurden bereits in folgenden Publikationen veröffentlicht:

- [1] **S. Gierth**, F. Hunger, S. Popp, H. Wu, M. Ihme, C. Hasse, Assessment of differential diffusion effects in flamelet modeling of oxy-fuel flames, *Combustion and Flame* 197 (2018)
- [2] **S. Gierth**, P. Haspel, A. Scholtissek, Z. Sun, S. Popp, C. Hasse, Evaluation of the Unsteady Flamelet Progress Variable Approach in Large Eddy Simulations of the ECN Spray A, *Science and Technology for Energy Transition*, accepted for publication (2022)
- [3] Z. Sun, **S. Gierth**, M. Pollack, C. Hasse, A. Scholtissek, Ignition under strained conditions: Unsteady flamelet progress variable modeling for diesel engine conditions in the transient counterflow configuration, *Combustion and Flame* 240:111841 (2022)

An dieser Stelle möchte ich mich bei all denjenigen bedanken, die mich während dieser Zeit durch Höhen und Tiefen begleitet haben.

Mein besonderer Dank gilt an erster Stelle Prof. Dr.-Ing. Christian Hasse, meinem Doktorvater, der diese Arbeit ermöglicht hat. Vor allem danke ich ihm für die sehr gute Betreuung und Unterstützung im Laufe der letzten Jahre. Mit zahlreichen Anregungen hat er mir immer wieder neue Blickwinkel eröffnet und den Fortgang der Arbeit gefördert. Weiterhin bedanke ich mich bei Prof. Dr.-Ing. Michael Wensing für die Übernahme des Zweitgutachtens und die stets sehr gute Zusammenarbeit in den zahlreichen Projekten während der letzten Jahre.

An dieser Stelle gilt mein Dank auch den Mitarbeitern des LTT Dr.-Ing. Sebastian Rieß, Andreas Peter und Lukas Weiß für die zahlreichen Diskussionen in Bezug auf Sprayverbrennung und dessen Vermessung. Insbesondere Lukas Weiß gilt mein Dank für die Bereitstellung der experimentellen Daten des ECN Spray D Injektors, die in dem zweiten Teil dieser Dissertation gezeigt sind. I would also like to take the opportunity to thank Dr. Lyle Pickett for the approval of this data.

Mein Dank gilt weiterhin den Kollegen aus Freiberg (NTFD) und den Kollegen aus Darmstadt (STFS), die direkt oder indirekt zum Gelingen dieser Arbeit beigetragen haben. Dr.-Ing. Sebastian Popp sei hier als erster erwähnt, der mich als Masterand, Bürokollege und nun bis zum Ende der Promotion begleitet hat. Weiterhin möchte ich mich bei Philip Haspel und Dr.-Ing. Martin Pollack für die Zusammenarbeit und insbesondere für die Unterstützung in der letzten Phase dieser Arbeit bedanken. Frau Dr.-Ing. Franziska Hunger möchte ich für die Kooperation im Projekt "Sevault-Flamme" danken, dessen Ergebnisse den ersten Teil dieser Dissertation ausmachen. Dr.-Ing. Arne Scholtissek und Dr. Zhen Sun danke ich für die gemeinsame Arbeit an dem UFPV Modell. Molte grazie anche ai miei cari colleghi d'ufficio e collaboratori del progetto Dr.-Ing. Federica Ferraro, Andrea Pati e Magnus Kircher. Il loro atteggiamento sempre positivo e motivante è stato molto prezioso. Vorrei anche ringraziare Alessandro Stagni, Ph.D. per aver fornito i meccanismi cinetici per la simulazione dello spray e per la sua grande disponibilità.

Weiterhin gilt mein Dank den Kollegen, die bisher unerwähnt blieben, aber im Rahmen vieler Diskussionen zu dieser Arbeit beigetragen haben: Dr.-Ing. Sandra Hartl, Dr.-Ing. Danny Messig und Dr.-Ing. Steffen Salenbauch.

Frau Anne Koth gilt mein Dank für die Englischkorrektur von Auszügen der vorliegenden Arbeit.

Ein ganz besonderer Dank gilt meiner Familie, die mich während meines gesamten Studiums und der Promotion begleitet hat. Speziell bin ich für ihre Geduld, Rücksichtnahme und für die uneingeschränkte Unterstützung in aller Hinsicht dankbar.

An letzter, doch eigentlich an erster Stelle möchte ich mich bei meiner Frau bedanken für die zahlreichen liebevollen Worte und die uneingeschränkte Motivation während des gesamten Studiums und der Promotionszeit sowie für die kulinarischen Höhepunkte und für so vieles mehr.

Darmstadt, im August 2021

Abstract

The constantly increasing demands placed on modern combustion processes in terms of efficiency and pollutant reduction make it necessary to optimize existing combustion processes, develop new ones and use alternative fuels. Numerical simulations help to develop and understand these processes. One efficient combustion modeling methodology is the pre-tabulation of flame structures. For the simulation of non-premixed flames, the so-called Flamelet-Progress-Variable (FPV) approach has been established. This involves the flame structure, which is not resolved in 3D CFD, being modeled using one-dimensional diffusion flames with different strain rates. The progress variable is used as a reactive scalar to describe the reaction progress of these structures. This approach, in combination with the Large Eddy Simulation (LES) of the turbulent flow typically occurring in technical systems, provides very good results for many fields of application. However, the pre-assumption of flame structures implies modeling assumptions that have to be constantly verified for new applications.

For example, it is known how differential diffusion along the flame structure can be modeled. However, the damping of differential diffusion due to turbulent structures must be directly specified when modeling the diffusion within the flame structures. Thus, flames which are strongly influenced by differential diffusion and flames where that influence is not relevant can be modeled well. Experimental data from a non-premixed oxy-fuel jet flame with hydrogen admixture have shown, however, that the effect of differential diffusion can vary locally and for individual species. The first part of the present dissertation examines how suitable modern modeling approaches are for representing this effect. Existing diffusion modeling approaches describing the flame structure with different levels of complexity are systematically compared. The complexity of the resulting flame structure makes it necessary to develop a suitable table parameterization, which is presented in this dissertation. The different approaches are compared in a *prior* analysis of the flame structure and in coupled LES with experimental Raman/Rayleigh data. In this process, the potential of the individual modeling approaches is elaborated. The identified limitations indicate the need for further research in this area.

Another technical field in which the tabulation of flame structures has become established itself as a valid approach is high-pressure spray combustion, which is relevant for diesel engines. The challenge in this area is to map the multitude of processes occurring during the usually two-stage ignition process up to the formation of pollutants. The tabulation of igniting transient diffusion flames (Unsteady Flamelet Progress Variable Approach, UFPV) provides very good results in a large number of studies. The modeling approaches found in the literature employ a wide range of strain rates. However, the model quality is often very similar with respect to global combustion characteristics. The present dissertation contributes in this respect within the framework of a systematic discussion of the influence of different strain rates in spray simulation. The single-hole injector Spray A defined in the Engine Combustion Network is used as a reference case. This dissertation shows that the strain rate significantly delays the ignition upstream of the flame lift-off length. Moreover, local extinction during ignition is identified for this case. However, its probability is comparatively low.

In addition to ignition, the formation of pollutants in these spray flames is a problem of high technical relevance. The challenge here is to formulate the progress variables for the strongly differing time scales of ignition and the slow development of pollutant species such as nitrogen oxides and soot precursors. The present dissertation complements the approaches known in the literature by adding a new progress variable definition. This definition consists of two progress variables, which describe individual processes of ignition and pollutant formation. Their normalized value is added to obtain the progress variable used for the parameterization of the look-up table. The approach is therefore referred to as the Unsteady Flamelet Composed Progress Variable (UFCPV) approach in this dissertation. This approach is verified in a one-dimensional test case with respect to the representation of ignition, combustion and pollutant formation under conditions relevant to the diesel engines. Comparison with the original definition shows the improvement of the approach. The validation of the approach in the 3D simulation is again performed using ECN Spray A. For validation purpose, 355-nm PLIF data and recently published 355-nm high-speed PLIF data are used. These allow a detailed comparison of the spatially and temporally resolved structure of formaldehyde and soot precursors. Here, the simulation shows very good agreement with the experimental data. The validated model is also used to analyze experimentally obtained statements concerning the separation of the above-mentioned species and its dynamic detachment behavior for the first time in a numerical study and to relate them to periodic fluctuations of the mixture fraction field. Its application to the ECN Spray D also serves to investigate the suitability of the model when the nozzle hole diameter is varied. Here, an underestimation of the ignition delay time is found. However, it can be shown from comparison with so far unpublished 355-nm high-speed PLIF data that the resulting flame structure is well reproduced by the experimentally determined morphology when this time offset is included. This suggests that although chemical reactions are initiated too early, the resulting flame structure is valid. The validated model allows the development of a comprehensive overview of the structure of the spray flame, including all relevant variables along the cause-effect chain from injection to pollutant formation. This is presented for the ECN Spray A and the ECN Spray D.

Table of Contents

| | |
|---|------------|
| Preface / Vorwort | iii |
| Abstract | v |
| Table of Contents | vii |
| 1 Introduction | 1 |
| 1.1 Overview on turbulent combustion with application to differential diffusion and diesel spray flames | 2 |
| 1.1.1 Range of length and time scales in turbulent reacting flows | 2 |
| 1.1.2 Turbulent non-premixed combustion modeling approaches | 3 |
| 1.1.3 Differential diffusion and its modeling | 5 |
| 1.1.4 Diesel spray combustion and its modeling | 6 |
| 1.2 Scientific questions and structure of this thesis | 12 |
| 2 Modeling approach | 14 |
| 2.1 Gas phase | 14 |
| 2.1.1 Governing equations | 15 |
| 2.1.2 Closure models for the governing equations | 18 |
| 2.1.3 Description of the turbulent flow field | 21 |
| 2.2 Turbulent combustion model | 24 |
| 2.2.1 The concept of mixture fraction | 24 |
| 2.2.2 Flamelet equations | 26 |
| 2.2.3 Tabulation of flame structures | 28 |
| 2.2.4 Modifications introduced in this thesis | 32 |
| 2.2.5 Evaluation of filtered quantities | 37 |
| 2.2.6 Summary of applied tabulation strategies | 38 |
| 2.2.7 Flamelet-UFCPV coupling | 39 |
| 2.2.8 LES-FPV coupling | 39 |
| 2.2.9 LES-UFCPV coupling | 41 |
| 2.3 Liquid phase | 42 |
| 2.4 Numerical framework | 45 |
| 3 FPV modeling of differential diffusion in gaseous H₂/CH₄-Oxy-Fuel flame | 46 |
| 3.1 Experimental configuration | 46 |

| | | |
|----------|---|------------|
| 3.2 | Numerical setup | 46 |
| 3.3 | Evaluation procedure | 47 |
| 3.4 | Results and discussion | 49 |
| 3.4.1 | Results prior analysis | 49 |
| 3.4.2 | Coupled LES | 54 |
| 3.5 | Summary | 57 |
| 4 | UFPV and UFCPV modeling for ignition and pollutant formation in spray flames | 59 |
| 4.1 | Description of investigated test cases | 62 |
| 4.1.1 | ECN Spray A and D | 62 |
| 4.1.2 | Lagrangian flamelet model | 65 |
| 4.2 | Operating conditions and FLUT generation | 66 |
| 4.3 | Evaluation of the flamelet look-up table | 67 |
| 4.4 | Lagrangian flamelet model | 70 |
| 4.5 | ECN Spray A | 74 |
| 4.5.1 | Mixture formation under non-reacting conditions | 74 |
| 4.5.2 | Mixture formation under reacting conditions | 77 |
| 4.5.3 | Ignition characteristics | 77 |
| 4.5.4 | Influence of the scalar dissipation rate and S-curve model | 80 |
| 4.5.5 | Spray flame structure in physical space | 84 |
| 4.5.6 | Spray flame structure in mixture fraction space | 88 |
| 4.5.7 | Summary of the ECN Spray A flame structure | 90 |
| 4.6 | ECN Spray D | 92 |
| 4.6.1 | Mixture formation under reactive conditions | 92 |
| 4.6.2 | Ignition characteristics | 93 |
| 4.6.3 | Spray flame structure in physical space | 94 |
| 4.6.4 | Spray flame structure in mixture fraction space | 98 |
| 4.6.5 | Summary of the ECN Spray D flame structure | 100 |
| 4.7 | Summary | 101 |
| 5 | Summary and conclusion | 104 |
| | Appendix | ix |
| A | Comparison of chemical mechanism | ix |
| | Nomenclature | x |
| | List of Figures | xv |
| | List of Tables | xix |
| | Bibliography | xx |

1 Introduction

Although great efforts are being made today to deploy renewable energy systems on a large scale, the burning of fossil fuels such as coal, oil and gas still covers the majority of the primary energy consumption world wide according to the World Energy Outlook 2020 [4]. Even though the global primary energy demand dropped in 2020 due to the Covid-19 pandemic, a return back to the 2019's energy consumption level and beyond is forecast within the next years [4] making its coverage by renewable energy systems alone questionable in the near future. Hence, there is still a need to improve current combustion systems. Nowadays, the main focus of improvements is driven by environmental concerns. It is well accepted, that certain products of combustion processes have a negative influence on human health and contribute to climate change. For example, carbon-dioxide (CO_2) and nitrous oxide (N_2O) emissions act as greenhouse gases [5]. Furthermore, particulate matter leads to an increasing risk of respiratory diseases, cardiovascular dysfunctions, and cancers [6, 7]. They also contribute to global warming as the second most important human emission after CO_2 [8]. Furthermore, it is known that nitric oxides (NO_x) emissions lead to the formation of ozone in the atmosphere and acid rain [9].

The most obvious way to avoid the emissions is to remove the corresponding chemical elements from the combustion process. For example, the emission of nitrogen oxides is avoided by removing nitrogen from the combustion system. Within the oxy-fuel combustion process this is realized by removing nitrogen from the oxidizer prior to combustion. By doing so, the exhaust gas consists to large parts of H_2O and CO_2 . They can be easily separated by water condensation allowing the utilization of carbon capturing systems (CCS) to avoid CO_2 emissions [10]. Since the combustion of fuel with pure oxygen leads to high combustion temperatures, small amounts of nitrogen, usually present due to technical imperfections such as leakage or residual nitrogen content in the fuel or oxidizer stream [11–13], leading to a high amount of NO_x . Hence, it is favorable to reduce the combustion temperature in such systems. This can be realized for example by recirculation of CO_2 extracted from the exhaust gas [10]. One potential problem with using CO_2 is the reduced flame stability [10]. The stability of the flame can however be achieved by adding H_2 to the fuel [14, 15]. One major difference compared to conventional gaseous hydrocarbon fuel is the low molecular weight of H_2 , which makes the molecule highly diffusive compared to other species in the combustion system. As a result, the differential diffusion of single species becomes important.

Beside the potential of using hydrogen as a fuel also for internal combustion engines in the transportation sector [16], this application is currently not very wide-spread. Liquid hydrocarbon fuels are still common in internal combustion engines in the transportation sector due to their high power density and the well-established delivery infrastructure and system for storage and injection, see e.g., Reitz et al. [17]. Especially

in the heavy-duty transportation sector, the replacement of diesel engines by electric ones are facing difficulties, e.g., due to the energy storage system [17]. In the context of diesel engines, the direct-injection technology is the state of the art fuel delivery strategy. Here, fuel is injected into the compressed air in the cylinder, where self-ignition takes place at high pressures and temperatures. To improve modern combustion systems, numerical simulations have become established over the last few decades as a diagnostic technique in science and as a design tool in industry. However, as they involve multiple scales and species, modern approaches for simulating turbulent combustion still incorporate a variety of modeling assumptions. These have to be continuously assessed for new combustion techniques as the ones mentioned above.

1.1 Overview on turbulent combustion with application to differential diffusion and diesel spray flames

In the following section, the state of the art of turbulent combustion modeling and selected challenges are presented. For this purpose, the length and time scales of turbulent combustion are introduced in Section 1.1.1 and an overview of modeling strategies is given in Section 1.1.2. The specific challenges arising from differential diffusion are presented in Section 1.1.3. Diesel spray combustion and the state of the art concerning its modeling is addressed in Section 1.1.4. The test cases investigated in this thesis are presented in the following review. As non-premixed combustion models are known to be appropriate model approaches for their description, the review is restricted to non-premixed combustion.

1.1.1 Range of length and time scales in turbulent reacting flows

Turbulent flows usually occur when the Reynolds number $Re = l_{ch}u_{ch}/\nu$ with u_{ch} denoting the characteristic velocity and l_{ch} a characteristic length scale of the flow and ν the kinematic viscosity of the fluid reaches a critical value, which is depending on the configuration under investigation. A typical example of a turbulent non-reactive jet flow is shown on the left side of Figure 1.1. The characteristic velocity represents the inflow velocity while the characteristic length is defined as the nozzle diameter. A characteristic velocity scale for turbulent fluctuations u_t can be defined as the velocity fluctuation with respect to its mean value. This can be obtained by decomposing the magnitude of the flow field velocity u into a mean part $\langle u \rangle_t$, where $\langle \cdot \rangle_t$ denotes the average with respect to time and its fluctuation $u' = u - \langle u \rangle_t$. The corresponding size is denoted by l_t and characterizes the largest turbulence elements. This length is usually similar to the system size [18]. The Reynolds number of these elements is defined as $Re_t = l_t u_t / \nu$. Obviously, turbulent flows span a wide range of length and hence time scales ranging from the size of the system (e.g., the nozzle diameter) to very small turbulence elements, which smallest size is determined by the so-called Kolmogorov length η_k . They are derived for homogeneous isotropic turbulence to be determined by $\eta_k = (\nu/\varepsilon)^{1/4}$ [19]. In this expression, ε denotes the dissipation rate of the turbulent kinetic energy per unit mass $k = 0.5\langle u'u' \rangle_t$. It can

be shown, that the ratio of the largest turbulent motions to the Kolmogorov length is

$$\frac{l_t}{\eta_k} = \frac{u'^3/\varepsilon}{(\nu^3/\varepsilon)^{1/4}} = \text{Re}_t^{3/4}, \quad (1.1)$$

see, e.g., [18]. For technical applications, Re_t is in the order of 100 to 2000 [18] leading to a wide separation of possible scales within the turbulent flow field.

In addition to the different length and associated time scales of turbulent fluid motion, the time scales of chemical reactions vary over a wide range [20]. This is shown in the right part of Figure 1.1. The combustion process itself usually occurs on small time scales, while the time scales of gaseous pollutant formation are relatively large. In particular, the time scales of combustion can be orders of magnitudes smaller than the flow field ones. This separation in time scales is often used in turbulent combustion modeling approaches. An overview of these is given in the next section.

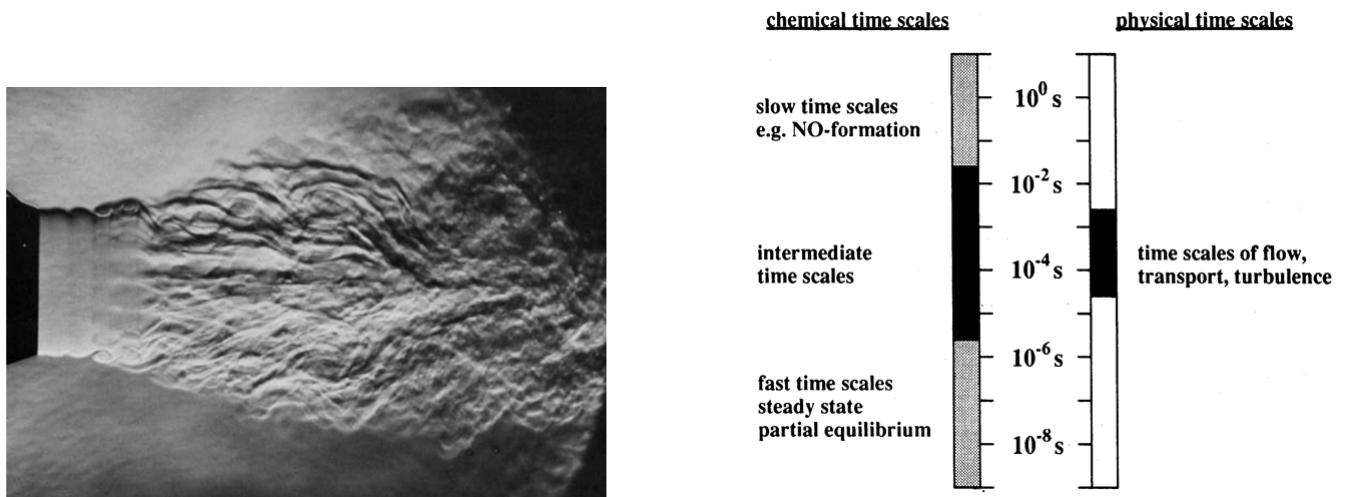


Figure 1.1: Left: Picture of a turbulent air jet (source: [21]), right: Time scales in chemical reacting flows (source: [20], Reprinted from Combustion and Flame, Volume 88, U.Maas, S.B.Pope, Simplifying chemical kinetics: Intrinsic low-dimensional manifolds in composition space, Pages 239-264, 1992, with permission from Elsevier.)

1.1.2 Turbulent non-premixed combustion modeling approaches

The most reliable and predictive approach for modeling turbulent combustion denotes the resolution of all relevant length and time scales in a so-called Direct Numerical Simulation (DNS). However, due to the large separation in scales, this is intractable for technical devices nowadays and in the next decades [18, 22]. Hence, different strategies have been developed: With regard to modeling the turbulent flow, the Reynolds averaged Navier Stokes (RANS) approach was mainly used in the last decades due to its relatively low resolution requirements and numerical cost, respectively. In this approach, the mean of the flow field vector $\langle \mathbf{u} \rangle_t$ is described by a set of governing equations. This approach, however, requires a model for the influence of all turbulent structures onto the mean field, which is a difficult task. Nowadays, the so-called Large Eddy

Simulation (LES) is getting more and more dominant in the scientific literature for gaseous flames as well as multi-phase combustion [23]. Within this approach, the largest scales of turbulent motion are resolved, while the smallest scales of turbulence¹ are modelled. This leads to less modelling effort with the drawback of increasing numerical cost. However, this approach is scalable in that the amount of turbulent structures resolved, and thus the reliability of the turbulence model, can be specified.

Even if the flow structures are resolved to a reasonable extent in LES, the smallest time and lengths of the turbulent non-premixed flames are hardly resolved, so that a combustion model has to be utilized. Another fact that makes combustion simulation a challenging task is that it involves many species for which a transport equation has to be solved. In general, the pressure, temperature and concentration of each species must be known in order to calculate the chemical source term. This leads to a high-dimensional problem with respect to the manifold spanned by the evolution of these variables. For LES of reactive flows, a statistical approach is needed for the smallest scales [24]. The main processes to be considered are the interaction of molecular diffusion and chemical reactions occurring at these scales [24]. Pope [24] divides combustion modeling approaches into PDF-like and flamelet-like methods. In the former model class, the sub-grid distribution is discretized by e.g., statistical particles. The evolution of the thermo-chemical state (defined as the combination of pressure, temperature and species mass fractions) is directly determined on each particle based on its actual state. Models of this class, do not introduce assumptions concerning the structure of the underlying flame, making the approach applicable to any flame type and combustion regime. However, they involve modeling assumptions concerning molecular diffusion and a relatively high computational cost compared to the models of the flamelet-like methods [24]. Models belonging to this class involve assumptions about the underlying flame structure, or in other words, they reduce the manifold dimension. A variety of models of this class were presented, e.g., the flamelet-generated manifolds (FGM) [25], flame prolongation of ILDM² (FPI) [26], and reaction-diffusion manifolds (REDIM) [27, 28] are mentioned by Pope [24].

In the context of modelling non-premixed combustion, the flamelet concept proposed by Peters [29] is often utilized. It is based on the assumption of a large Damköhler number $Da = \tau_f/\tau_c$ with τ_f denoting a characteristic flow time scale and τ_c the chemical time scale. In this case, combustion takes place in an asymptotically thin layer between fuel and oxidizer. These layers are small compared to the surrounding turbulent structures. A turbulent flame is then seen as an ensemble of this so-called flamelets, which are strained by the surrounding flow field, but not penetrated by them. A set of equations to describe species mass fraction and temperature along a flamelet were proposed by Peters [29]. By this means, an expression for the temperature and species mass fraction as function of the mixture fraction Z is obtained. The mixture fraction denotes a passive scalar, which equals one in the fuel stream and zero in the oxidizer stream and quantifies the mixing process. A further parameter is the scalar dissipation rate of the mixture fraction $\chi = 2D(\nabla Z \cdot \nabla Z)$ with D denoting the diffusion coefficient and ∇Z the gradient of the mixture fraction field. The approach was later extended to accounting for differential diffusion [30], pressure effects [31], multi-feed combustion [32, 33], flame curvature [34–36] and flame-tangential effects [37, 38]. The flamelet

¹The smaller the scales of turbulent motion, the more universal they become, and their physical influence becomes more and more limited to the dissipation of turbulent kinetic energy

²ILDM: Intrinsic Low dimensional manifold

assumption leads to a possible decoupling of the flame structure simulation and that of the flow field. The flame structure can be solved for either interactively during the flow field simulation or prior to it in conjunction with the tabulation of the results. An example for the interactive simulation is the representative interactive flamelet (RIF, [39]) model where one flamelet is solved interactively representative for the combustion system. With this, local variations in the scalar dissipation rate are not accounted for. To include this effect, the MRIF approach was proposed by Barths et al. [40, 41, 42], in which multiple flamelets representative for a certain domain are solved interactively. Beside its accuracy, this approach is connected with a high computational cost scaling non-linearly with the number of cells used for the flow simulation [43]. This can be overcome by pre-tabulating the flame structures as first done by Cook et al. [44]. Therein, Z and $\chi_{st} = \chi(Z_{st})$ is used to parameterize the look-up table. To improve this approach to account for extinction and re-ignition effects, the scalar dissipation rate is mapped to the so-called reaction progress variable Y_C , usually defined as a linear combination of species mass fraction in the flamelet progress variable approach proposed by Pierce [45], Pierce and Moin [46]. This model was shown to give well results in variety of combustion problems, see, e.g., [45, 47–52]. However, due to the incorporation of steady flamelets only, it is limited in the description of transient processes, e.g., sudden changes in the imposed strain rate [53], ignition phenomena [54, 55], or very slow processes, such as pollutant formation [56, 57] or radiation effects [57]. Hence, this approach was extended by the inclusion of unsteady igniting and extinguishing flame structures by Pitsch and Ihme [56], Ihme and See [55]. This approach is widely used nowadays in the context of diesel spray combustion with a specific review given in Section 1.1.4.

1.1.3 Differential diffusion and its modeling³

Differential diffusion in turbulent jet flames

“Differential diffusion” is a term that characterizes the separate evolution of initially perfectly correlated scalars in a turbulent or laminar flow caused by differences in the molecular diffusive properties between species. The first observation of differential diffusion in a methane diffusion flame was reported by Bilger [58]. Experimental and numerical investigations using reactive and also non-reactive flows followed; an overview can be found in [59]. It is well known that differential diffusion is significant in flames with substantial amounts of H_2 ($Le < 1$) or higher hydrocarbons ($Le \gg 1$). This is particularly true in laminar flames. In turbulent flames, differential diffusion is dampened by turbulent motion. Therefore, in many turbulent flames, unity Lewis number behavior for all species has been observed and confirmed, particularly for CH_4 /air flames [60], DME/air flames [50, 61] and recently also for a CH_4 /oxy-fuel flame [51, 52]. However, differential diffusion has been observed in other turbulent diffusion flame studies. In an experimental study of turbulent H_2 /air diffusion flames [62], differential diffusion was identified in the near-nozzle region and at low Reynolds numbers. A recent experimental study of turbulent CH_4 /oxy-fuel flames also confirmed the presence of differential diffusion [63]. Pitsch [64] indicated the following three phenomena

³This section is partly taken from the publication by Gierth et al. [1] which was created during the work on this thesis. In [1], my co-author Franziska Hunger and me equally contributed to this part.

relevant for turbulent flames: (i) laminar structures within the mixing layer in the near-nozzle field, (ii) large molecular diffusivities of single species and (iii) scale separation when the mixing layer width is small compared to the Kolmogorov scale. In addition, the position of the turbulent/non-turbulent interface relative to the reaction zone was recently identified as relevant for the existence of differential diffusion in shear flows [52]. Although these processes have clearly been associated with the occurrence of differential diffusion in turbulent flames, only few models are able to capture some or all of these effects, involving the competition between molecular diffusion and turbulence. The conditional moment closure (CMC) model was extended such that it explicitly contains a term in the species and enthalpy transport equation responsible for differential diffusion [65]. However, a similar approach is not yet available for tabulated chemistry as used in flamelet models.

Experimental reference data

In a CH₄/oxy-fuel flame investigated experimentally by Sevault et al. [63], differential diffusion was shown to dominate around stoichiometric conditions in all species profiles while approximate unity Lewis number behavior was found for many species such as H₂, CO₂ and CO in the fuel-rich part of the flame. This was confirmed by comparing experimental data and simulation results for opposed-flow diffusion flames using representative strain rates either accounting or not for differential diffusion.

Modeling attempts

Garmory and Mastorakos [66] confirmed the presence of differential diffusion in LES of this flame when applying a newly proposed unstructured CMC method. Since a unity Lewis number diffusion model was used, not all species could be predicted equally well. In a first attempt to model differential diffusion in this flame, Han et al. [67, 68] applied a modified flamelet model [69] in a Reynolds-averaged Navier-Stokes (RANS) framework. The model uses the mixture fraction and scalar dissipation rate as parameters and accounts for differential diffusion as well as its interaction with turbulent mixing. A significant improvement was achieved compared to unity Lewis number modeling, particularly for the profile of the CO and CO₂ mass fraction. Despite the improvements in CO, significant differences still persisted in this species and correspondingly in the profiles of the differential diffusion parameter. Thus, this flame denotes a challenging test case for the assessment of differential diffusion effects in combustion models in general and for tabulated chemistry approaches in particular.

1.1.4 Diesel spray combustion and its modeling

Diesel spray cause-effect chain

In contrast to gaseous jet flames, the fuel is delivered as liquid to the combustion chamber in the case of spray flames. After the fuel is injected to the combustion chamber, the liquid jet disintegrates due to aerodynamic

forces at its surface, turbulent motion inside the liquid core, relaxation of the velocity profile and cavitation [70]. This primary break-up is followed by the secondary break-up where the formed ligaments disintegrate even further. With decreasing ligament size, momentum, heat and mass transfer become more pronounced, leading to an acceleration of the gas phase, connected with an entrainment motion of the ambient gas towards the fuel jet. Due to the temperature and pressure conditions, auto-ignition of the vaporized fuel/oxidizer mixture takes place followed by the formation of slow chemical species like nitric oxides and the formation of soot. A schematic overview on these processes with focus on the combustion model is given in Figure 1.2.

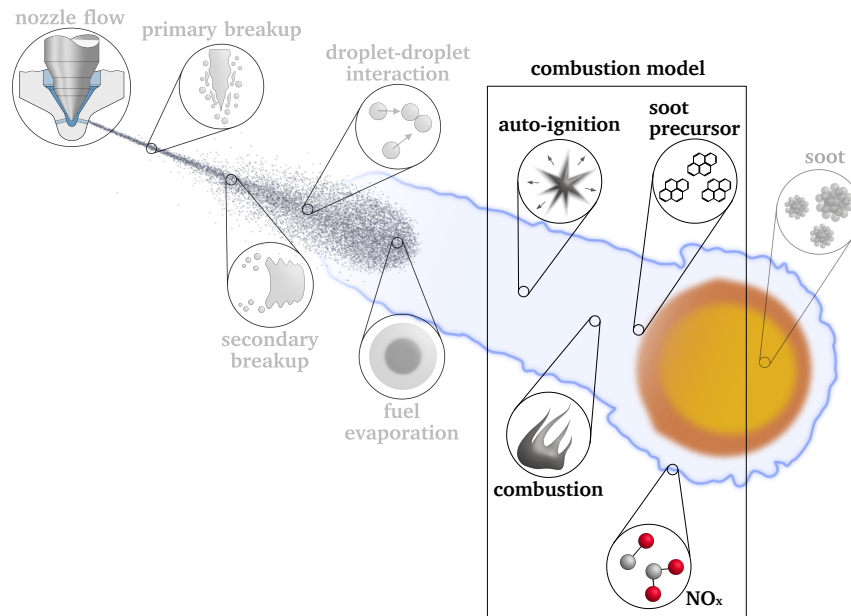


Figure 1.2: Cause-effect chain of diesel spray combustion with focus on the results of the combustion model

Experimental reference data

Various injector types were developed for different applications, e.g., fuel and engine types, see [70] for an overview. It is well known, that the design of the injector strongly influences the movement of the fuel and its thermodynamic behavior inside the nozzle and consequently the spray pattern. Especially, cavitation occurs when the fuel pressure falls below its vapor pressure leading to enhance disintegration of the liquid when entering the combustion chamber. Although the simulation of the entire injector flow and the near nozzle effects are feasible nowadays to a reasonable extend for application near injectors and diesel relevant boundary conditions the computation time is still unjustifiable for general application [71]. Hence, the injection process itself is usually modelled incorporating global quantities like mass flow rate and spray angle, which need to be known for the injector under investigation. Since the combustion model denotes the focus of this thesis, injectors are chosen for which knowledge about the injection parameters and other liquid phase model related parameters are established in the literature. In the frame of the Engine Combustion Network (ECN, [72]), several target injectors differing in their number of holes, size, fuels and

operating conditions are defined. Experiments are performed by several research institutions. In the context of diesel spray combustion, the so-called Spray H was investigated in former times. Therein, n-heptane is supplied utilizing a single hole injector into a high temperature / high pressure chamber. However, due to a more similar behavior compared to real diesel fuel, n-dodecane is nowadays used as surrogate fuel. The corresponding target case is denoted by Spray A. The corresponding single hole injector has a nominal nozzle diameter of $90\ \mu\text{m}$ representative for passenger car application. The nominal operating condition implies the injection of n-dodecane stored at 150 MPa into a constant volume combustion chamber at a pressure of 60 bar and 900 K in temperature with a O_2 content of 15 % by volume. More recently, the so-called Spray D injector is in the focus of the ECN. It is a single hole injector with a diameter of $186\ \mu\text{m}$ representative for heavy-duty applications. The operating conditions are the same as for the Spray A injector. After the presentation of the experimental configurations, the state of knowledge concerning diesel spray combustion is summarized in the following section.

Diesel spray flames

Based on the large amount of literature concerning the combustion of diesel sprays published within the last decades, a comprehensive view on the ignition process is established nowadays. Higher hydro-carbon fuels ignite in a two-stage process [73] at ambient temperatures typical for diesel engine combustion. In especial, the temperature rises in a first stage before the main ignition takes place. Kazakov et al. [73] found, that the slow down of reactions after the first stage is connected to the formation of HO_2 during the oxidation of formaldehyde (CH_2O) which is itself an exothermic process. The second stage ignition is afterwards initiated by the decomposition of H_2O_2 into OH atoms. In turbulent combustion, the mentioned process is accompanied by transport processes due to the evolving gradients in temperature and species concentration. The importance of this effect was investigated in detail by Dahms et al. [74]. During diesel spray injection, fuel at low temperature is mixing with the oxidizer at high temperature. Chemical reactions initiate at lean conditions marked by a slight temperature increase and the formation of CH_2O . Due to the establishing temperature and species gradients, the products of these reactions are transported towards the rich part of the flame. This shortens the time for the first stage ignition in this regions. This phenomena is denoted by cool flame wave propagation by Dahms et al. [74]. As a result, second stage ignition is taking place over a wide range of fuel rich mixtures. The same phenomena was also observed within the 2D DNS of a Dimethyl Ether (DME)/air mixing layer at 40 bar and 900 K by Minamoto and Chen [75]. These outcomes explain the experimental findings concerning the ignition behavior of the ECN Spray A [76]. Herein, ignition is observed mainly over wide parts of the spray head. This behavior was further confirmed in [77] where the experimental data obtained at the Spray A injector between different research institutions are compared. A different ignition behavior is observed for the ECN Spray D. For this injector, ignition is initiated at different positions at the spray flanks [78]. This is attributed to a different mixing behavior at this two injectors [79]. In particular, the fluid at the spray axis is too fuel-rich for the initiated ignition. This is also confirmed by [80, 81]. Concerning the difference in the scalar dissipation rate at the ignition delay time between Spray A and Spray D it was found that it increases with decreasing temperature [79]. The formation of

NO in diesel sprays is stemming from thermal, nitrous and prompt NO [82]. In this context, the thermal mechanism leads to most of the NO_x emissions [83]. This process is, however, rather slow compared to the main reactions of ignition and combustion [82]. The formation of soot is more complex and an overview of the known processes and their modeling is given in [84]. It is well known, that soot stems from soot precursor in the gas phase in fuel-rich conditions. Under these conditions, the formation of acetylene (C_2H_2) is triggered [85, 86]. Due to the lack of oxygen, the direct oxidation is hindered [86] and a conversion of C_2H_2 to aromatic compounds, so-called PAHs which are direct precursors for soot formation [85–88] takes place. The details of this conversion process and the transition to soot particles is rather complex. One point of importance is the fact, that, similar to the thermal NO, the PAH chemistry is relatively slow [89]. Hence, both processes need special treatment when utilized in the FPV and UFPV approach. Possible strategies known in literature are presented after the applied progress variable based tabulation approaches are presented in the next section.

Diesel spray flame modeling using progress variable based tabulation approaches

One of the earliest attempts to pre-tabulate flame structures utilizing a progress variable to capture the auto-ignition under diesel engine relevant conditions was preformed by Zhang et al. [90] utilizing unsteady flamelets. In contrast to the UFPV approach [23, 55], the progress variable is defined as the integral of species mass fractions along the reaction progress by the authors rather than a combination of single species mass fractions. The approach was used to examine auto-ignition of n-heptane in a numerical study. It was further utilized for spray combustion simulations by Chang et al. [91]. Therein, a good qualitative agreement with the experimental flame shapes was obtained, while the flame penetration was overestimated. Possible explanations are related to the spray model and the reduced four-step reaction mechanism utilized. Lehtiniemi et al. [92] applied the approach by using a sensible enthalpy based progress variable for the simulation of a heavy duty diesel engine using n-decane as fuel. Beside the demonstration of the applicability of the tabulation approach in diesel engine application, no validation with experimental data was shown. In the recent literature concerning diesel spray combustion, tabulated flame structures were mostly incorporated by means of the FGM and UFPV approaches. FGM was first utilized in diesel engine combustion by Bekdemir et al. [93] to perform RANS simulations with n-heptane as surrogate fuel. For this purpose, the FGM approach was extended towards autoignition and variable pressure conditions. The look-up table is generated by unsteady igniting counterflow simulations at different pressures. This FGM version is very similar to the UFPV approach due to the utilization of the flamelet concept along with the parameterization of the database by means a progress variable. However, the laminar diffusion flames are solved in physical space rather than mixture fraction space. Furthermore, only one igniting counterflow simulation is used to represent the ignition process. The application within the diesel engine simulation results in a qualitatively correct flame structure in terms of temperature and species distribution but a too short burn duration. This fact was attributed to the chemical mechanism utilized. This approach is furthermore utilized by Egüz et al. [94] to simulate the ECN Spray H under varying ambient O_2 content. A well agreement in terms of lift-off length and ignition delay time is obtained for 15 mol-% ambient O_2 content while an overprediction for

both quantities is obtained for 12 % and an underprediction for 21 % O₂ preserves. These results were improved by Egüz et al. [95] by an increase of the look-up table resolution in progress variable direction. The approach is further applied by Ayyapureddi et al. [96] within RANS simulations of the ECN Spray A nominal conditions showing an overprediction of around 13 % in terms of ignition delay time while a great sensitivity is observed with respect to the chemical mechanism. Moreover, the results depend on the utilized break-up model. The approach was later used by Wehrfritz et al. [97] for LES of the Spray A under varying oxygen concentration showing a slight underestimation of the ignition delay time which is most pronounced for the lowest investigated oxygen content of 13 %. Kahila et al. [98] further showed maximum deviations within the pressure variation at the Spray A in the range of 50, 100 and 150 MPa injection pressure of 14 % for the lift-off length and an underprediction of the ignition delay time of maximum 20 %. Based on this promising findings, the approach was utilized in further studies, e.g., dual fuel injection [99].

The first application of the UFPV approach [55, 56] to diesel spray combustion was performed by Bajaj et al. [100] within RANS simulations of the ECN Spray A and H under a wide range of operating conditions. Lift-off lengths and ignition delay times were predicted within an error of 25 %. In a subsequent study, Ameen [101] utilized the approach to investigate the ignition behavior of n-heptane jets under diesel relevant conditions. A further application of the UFPV approach is presented by Dhuchakallaya et al. [102] for RANS simulation of n-heptane injection from an injector of similar size as the ECN Spray D. A well qualitative agreement is obtained in terms of flame area and heat release rate while an overall overprediction of both quantities is obtained.

While the aforementioned approaches solve the flamelet equations either in the physical space (FGM) or in mixture fraction space (UFPV), an alternative approach is denoted by the so called approximated diffusion flamelets (ADF) [103]. Within this approach, the flamelet equations are solved for the progress variable only while its chemical source term is retrieved from a look-up table. This table itself stems from homogeneous reactor simulations. Thereby, this approach reduces the computation time at the expense of a decoupling of convection-diffusion and chemistry within the flame structure. This approach was first applied to diesel spray combustion by Winklinger [104] within RANS simulation of the ECN Spray A for different ambient temperatures and later by Desantes et al. [105] within the RANS simulation of the ECN Spray A for different ambient temperatures and oxygen content. Herein, the trend of increasing lift-off length with increasing ignition delay time was well captured, while quantitative differences preserve in acceptable range depending on the operating condition. The overall good agreement lead to further studies utilizing this approach for the investigation of the influence of the chemical mechanism within RANS simulation of the ECN Spray A injector [106], comparison of Spray A and Spray D injector based on RANS simulations [80] and validations within the LES of the Spray A [81, 107].

Furthermore, the application of perfectly stirred reactors (PSR) are found in the literature. Tap and Schapotschnikow [108] tabulate PSR for RANS simulation of the ECN Spray H and obtained a well agreement, beside a slight underestimation in the ignition delay time increasing with the ambient oxygen content. Comparative studies show, that the behavior is similar to the FGM approach within the Spray A conditions at different ambient oxygen levels [95] with a slide lower ignition delay time predicted by the PSR approach. A smaller ignition delay time within RANS simulations of Spray A was also obtained by [96].

In summary, all tabulation strategies used for diesel spray combustion are based on igniting diffusion flame-

lets. The approaches differ in details of the underlying flame-structures and their mathematical formulation. A further difference is related to the incorporated parameter range in terms of strained flamelet solutions. Beside the incorporation of the entire possible flamelet solutions in [101], only igniting flamelets are considered in [80, 81, 104–107]. Furthermore, only one igniting flamelet is incorporated within the FGM approach [93, 94, 96–98]. Beside the discrepancies obtained in the early literature, these recent studies show overall well agreement independent of the utilized flamelet model or incorporated number of scalar dissipation rates. Even one igniting flamelet within the FGM seems to be sufficient for the simulation of the ECN Sprays A and H in RANS as well as in LES. It should be noted, that this is attributed to the advances in spray modeling and reaction mechanisms. However, it also suggests that the ignition process depends only to a minor extend on the scalar dissipation rate. The reason for this is however not investigated under Spray A conditions in LES so far. In particular, no study was found investigating the influence of the unstable branch solutions within LES of the ECN Spray A and D.

Furthermore, the progress variable definition denotes a critical aspect for the performance of the approach. In particular to capture the onset of ignition is a challenging task. This is either done by incorporating HO_2 as early formed species within the progress variable definition [94, 96, 104] together with a sufficiently high FLUT resolution or by treating the source term in an integral manner, see e.g., [109, 110]. Hence, the proposed solutions can be directly adopted within this thesis.

Modeling pollutant formation using progress variable based tabulation approaches

In the context of diesel spray combustion, pollutants are either gas phase species or soot. While gaseous species are described by the combustion model, soot is described by a separate model, see e.g., [111] for an overview. The soot model however needs the information about the concentration of soot precursor in the gas phase and the local temperature for the description of the onset of soot formation as well as other species involved in surface growth or oxidation of soot particles. The combustion model hence directly determines the soot model prediction.

In the context of the tabulation approaches mentioned in the last section, the time-history of the thermochemical state is directly given by the unsteady flamelet solutions. With the definition of a proper progress variable, the formation of pollutants can directly be obtained from the look-up table. However, as stated by Kundu et al. [43], the definition of a progress variable for slow-forming species is a challenging task. As first attempt to capture the slow evolution of soot and NO_x under diesel engine relevant conditions, Yen and Abraham [112] extended the tabulation strategy of Bajaj et al. [100] by tabulating these species separately and replaced the progress variable by the time. Further attempts were made in the context of FGM for premixed combustion. Godel et al. [113] directly incorporated NO_x species directly within the progress variable definition. With this, the time range at which NO_x are formed can be accounted for. Note, that this approach can be utilized within the UFPV approach, too. However, the success of this approach depend on the weight of the NO_x species in the progress variable definition as noted by Van Oijen et al. [114], which was also confirmed by Zhao et al. [115] within the application in the FPV approach. A nowadays widely used approach in the frame of the FPV approach was proposed by Ihme and Pitsch [57]. In that approach,

the production and destruction rates of NO are tabulated separately, while the latter one is scaled by the mass fraction of NO itself. This is based on the fact, that the NO production rate does not depend on the NO concentration while the destruction rate scales linearly with it. A similar approach was suggested by Lucchini et al. [116] and applied to the ECN Spray A and diesel engine simulations. The authors solved a transport equation for the NO mass fraction with its chemical source term determined utilizing the Zeldovich mechanism [117] (thermal NO) based on the local values for temperature and species mass fraction to obtain the NO source term. With this, the approach differs from the one proposed by Ihme and Pitsch [57] by the step of the framework, where the NO mechanism is evaluated (during table generation or in the coupled simulation). A similar approach is chosen for the quantities needed for the utilized soot model in [116]. The approach was recently adopted by Zhou et al. [118]. More recently Zhou [119] proposed an approach, in which the NO_x source term is evaluated within a homogeneous reactor simulation and stored within the look-up table describing the ignition process. In the coupled simulation, NO is transported and its source term is retrieved from the look-up table. The parameterization of the table is then adapted by incorporating the normalized NO mass fraction as second progress variable. To account for the different time scales, the NO source term is either retrieved as function of the reaction progress variable or by the second progress variable. A free parameter is needed to switch between both.

In summary, recent approaches solve for a transport equation for each slow species within the CFD. The source term is tabulated in the look-up table for main reactions in a proper way or solved directly in the CFD [116]. The approach of Zhou [119] represents a promising approach in terms of discretization of the slow species' source terms. However, the need for parameter remains.

1.2 Scientific questions and structure of this thesis

Against the technical background given above, two aspects of modeling turbulent non-premixed combustion are addressed in this thesis in the context of flamelet tabulation approaches for turbulent jet flames: 1) differential diffusion effects under H₂ addition and 2) self-ignition and pollutant formation in diesel sprays. Concerning differential diffusion, the scientific question remains of whether flamelet tabulation approaches are able to capture different extents of differential diffusion along one flame structure. The present thesis aims to advance knowledge about differential diffusion by assessing a hierarchy of flamelet models to capture significant differential diffusion effects in a CH₄/oxy-fuel flame that was experimentally investigated by Sevault et al. [63]. These include flamelet models where the Lewis number is assumed to be unity [29] or differential diffusion is accounted for by variable Lewis numbers [30], and a recent model where the influence of local turbulence is considered by using effective Lewis numbers [69].

In the context of self-ignition in diesel sprays, flamelet-based tabulation techniques are applied with great success in the literature. However, these models vary in their complexity concerning e.g., the underlying flamelet structure and incorporation of strain effects. The question remains of why they work equally well and where potential limitations occur. This question is addressed within this thesis by utilizing the UFPV approach [23, 55] as the most comprehensive flamelet-based model concerning the incorporation of strain effects and a subsequent analysis of reduction of the tabulated information. This is performed on the ECN

Spray A. A further key aspect in the UFPV approach is the definition of a proper progress variable definition covering all physical time scales from first- and second-stage ignition up to pollutant formation. Several approaches are presented in the literature all having their benefits and drawbacks. This thesis aims to contribute with a new progress variable formulation, enabling the incorporation of processes acting on different time scales.

The remainder of this thesis is structured as follows: In Section 2 the modeling approach is described considering the gas and liquid phase involved. A description of the gas phase is given in Section 2.1. The different flamelet tabulation strategies utilized in this thesis are described in Section 2.2. Section 2.3 describes the liquid phase modeling approach. In Section 2.4, the numerical framework utilized is presented. The application of the FPV approach to model differential diffusion is addressed in Section 3 and the application of the UFPV approach to model ignition and pollutant formation is investigated in Section 4. Both of these sections contain the description of the verification and validation cases, their numerical representation as well as the presentation of the results. An intermediate summary closes the corresponding sections, while the summary and outlook of this thesis is given in Section 5.

2 Modeling approach

The flow configurations considered within this thesis are either single phase turbulent reacting flows (oxy-fuel jet flame) or two-phase flows (spray flames). Since the single phase flow can be considered as special case of the latter one in the absence of the liquid phase, the description within this section is given for the two-phase system. The following assumptions are applied for the model formulation: The continuous gaseous carrier phase is overlaid by the dispersed liquid phase (which is in particular true after primary break-up) whose volume fraction is considered to be negligible. It should be noted, that these assumptions are not fulfilled in all regions of the spray flame. In particular for the near injector region, they are questionable [120]. However, it was shown in former studies, that this modelling approach is working properly for the cases under investigation [97, 121, 122]. This is due to the fact, that the chosen approach relies on the prescription of model parameters, allowing for the compensation of neglected physical effects when appropriately chosen. This is further discussed in Section 2.3. Turbulent flows are considered, which's smallest scales are not resolved and have to be modelled. Chemical reactions are only taking place volumetrically and within the gas phase.

Under these assumptions, only the gas phase is modelled by a set of differential equations in an Eulerian frame of reference. The dispersed phases of liquid droplets is described in a statistical sense by the distribution functions with a characteristic set of internal coordinates. This is denoted by Eulerian–Lagrangian method [123] with further explanation given in [70, 124]. In the latter approach, Lagrangian particles representing a certain number of droplets with equal quantities are tracked. The exchange of mass, momentum and enthalpy between the liquid and the gas phase are described by models originating from individual droplets consideration. A sketch of the Eulerian–Lagrangian approach is shown in Figure 2.1. In the following, the model description is divided into gas phase (Section 2.1) and liquid phase (Section 2.3) with corresponding source terms described as coupling of both phases. The former one incorporates the models for combustion and pollutant formation which are described in the distinct Section 2.2 due to their weight within this thesis.

2.1 Gas phase

A multi-component gas with chemical reactions and source terms from other phases can be described in general by solving the conservation equations for mass of the phase and for every single species, momentum,

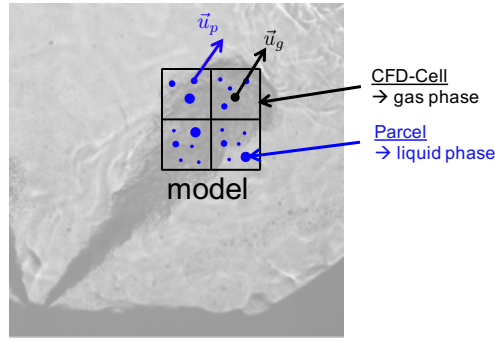


Figure 2.1: Schematic representation of the Eulerian–Lagrangian approach for spray simulation (Source Schlieren image: [125])

and energy. These equations are given in differential form applying the continuum assumption in Section 2.1.1. The models, needed to close the system of equations are given in Section 2.1.2. The descriptions within this section follows [18] with addition of source terms due to phase change, unless otherwise stated.

2.1.1 Governing equations

Mass conservation

The conservation of mass is given by⁴

$$\frac{\partial \rho}{\partial t} + \frac{\partial \rho u_j}{\partial x_j} = \dot{S}_m \quad (2.1)$$

where ρ denotes the density, u_j the velocity in direction j and \dot{S}_m the source term resulting from phase change (evaporation of liquid fuel).

Single species mass conservation

To describe the composition of a mixture, several quantities can be defined. The mole fraction X_k defines the ratio of the number of moles of species k to the the total number of moles in a given volume. Furthermore, the molar concentration $[X_k]$ is defined by the number of moles of species k per unit volume. In computational fluid dynamics, the single species mass fraction Y_k , defined as the mass of species k in a given mass, is commonly chosen as solution quantity. The mole fraction can be related to it by

$$X_k = \frac{M}{M_k} Y_k \quad (2.2)$$

with the mean molecular weight M defined by

⁴Note, that Einstein summation convention is used within this thesis, where a summation is taking place over all values of indices appearing twice in a term, e.g. $\partial u_j / \partial x_j = \sum_{j=1}^3 \partial u_j / \partial x_j$

$$M = \left(\sum_{k=1}^N \frac{Y_k}{M_k} \right)^{-1} \quad (2.3)$$

and M_k denoting the atomic weight of species k . The transport equation for a single species mass fraction is given by

$$\frac{\partial \rho Y_k}{\partial t} + \frac{\partial \rho Y_k (u_j + V_{k,j})}{\partial x_j} = \dot{\omega}_k + \dot{S}_{m,k} \quad (2.4)$$

where $\dot{\omega}_k$ represents the mass source term of species k per time and volume due to chemical reactions and $\dot{S}_{m,k}$ the corresponding mass source term due to phase change. The evaluation of the former one is described in Section 2.1.2 while the latter one is given in Section 2.3. Beside the flow velocity u_j , the diffusion velocity of the single species $V_{k,j}$ appears in the convection term on the left hand side, accounting for the differential diffusion of single species due to the difference in their molecular weights, as discussed in Section 1. The evaluation of this term is further addressed in Section 2.1.2.

Momentum conservation

The conservation of momentum is given by

$$\frac{\partial \rho u_i}{\partial t} + \frac{\partial \rho u_j u_i}{\partial x_j} = -\frac{\partial p}{\partial x_i} + \frac{\partial \tau_{ij}}{\partial x_j} + \rho g_i + \dot{S}_{u,i}. \quad (2.5)$$

Herein, p denotes the pressure, g_i the gravitational acceleration acting in direction i , $\dot{S}_{u,i}$ the momentum exchange term with the liquid phase and τ_{ij} the viscous stress tensor given by

$$\tau_{ij} = \mu \left(\frac{\partial u_i}{\partial x_j} + \frac{\partial u_j}{\partial x_i} - \frac{2}{3} \delta_{ij} \frac{\partial u_k}{\partial x_k} \right). \quad (2.6)$$

In the latter equation, δ_{ij} denotes the Kronecker delta⁵ and μ denotes the dynamic viscosity which has to be closed by a separate model which is described Section 2.1.2.

Energy conservation

The total energy of the gas phase per unit mass e_t is composed by its kinetic energy $0.5u_j u_j$ and the internal energy per unit mass, also denoted as specific internal energy, e . To account for chemical reactions within the energy balance, the latter one is decomposed into a sensible part e_s quantifying the change in temperature T and a part accounting for the energy needed to form the molecules of species k from their elements at

⁵Evaluates to 1, if $i = j$ and 0 otherwise

a defined reference temperature T_0 (usually 298.15 K [18]). The latter one is commonly measured and expressed in terms of the standard enthalpy of formation of $\Delta h_{f,k}^0$, where the specific enthalpy is related to the specific internal energy by $h = e + p/\rho$. Based on this definition, the specific enthalpy can be used itself to describe the thermodynamic state of a system and the decomposition introduced for the specific internal energy is defined accordingly by

$$h = \sum_{k=1}^n h_k Y_k = \sum_{k=1}^n \left(\int_{T_0}^T c_{p,k} dT + \Delta h_{f,k}^0 \right) Y_k. \quad (2.7)$$

Obviously, the information about the specific heat capacity at constant pressure for each species $c_{p,k}$ has to be known in addition to their standard enthalpy of formation. The methods for their evaluation are given in Section 2.1.2.

Based on the different energy definitions, corresponding conservation equations can be derived for them in differential form. Within this thesis, the specific total enthalpy $h_t = h + 0.5u_j u_j$ is used for the 3D Simulation of spray flames and the temperature T is used for the flamelet equations (see Section 2.2.2). Under the assumption, that no power is produced by volume force on specific species and including the source terms \dot{S}_{h_t} and \dot{S}_T due to phase change, these transport equations read

$$\frac{\partial \rho h_t}{\partial t} + \frac{\partial \rho u_j h_t}{\partial x_j} = \frac{\partial p}{\partial t} - \frac{\partial q_j}{\partial x_j} + \frac{\partial \tau_{ij} u_i}{\partial x_j} + \rho u_j g_j + \dot{S}_{h_t} \quad (2.8)$$

for the total enthalpy and

$$\frac{\partial \rho c_p T}{\partial t} + \frac{\partial \rho c_p u_j T}{\partial x_j} = \dot{\omega}_T + \frac{\partial p}{\partial t} + u_j \frac{\partial p}{\partial x_j} - \frac{\partial q_j}{\partial x_j} + \tau_{ij} \frac{\partial u_i}{\partial x_j} + \dot{S}_T \quad (2.9)$$

for the temperature. The energy flux q_j appearing in both equations is composed by a heat flux modelled by Fourier's law ($q_j \propto -\partial T / \partial x_j$) and a second term stemming from the diffusion of species with different enthalpies leading to

$$q_j = -\lambda \frac{\partial T}{\partial x_j} + \rho \sum_{k=1}^N c_{p,k} Y_k V_{k,j} T = -\frac{\lambda}{c_p} \frac{\partial h}{\partial x_j} + \rho \sum_{k=1}^N h_k Y_k V_{k,j} \quad (2.10)$$

where λ denotes the thermal conductivity. Furthermore, the term $\dot{\omega}_T$ in Eq. (2.10) denotes the source term arising from chemical reactions defined as

$$\dot{\omega}_T = - \sum_{k=1}^N h_k \dot{\omega}_k. \quad (2.11)$$

where $\dot{\omega}_k$ denotes the species mass source term introduced above in Eq. (2.4). The models needed to close the system of equations described above are given within the following section.

2.1.2 Closure models for the governing equations

The governing equations require further modeling of the coefficients within the transport equations as well as the diffusion velocities and chemical species source terms. Their evaluation is addressed within the following sections.

Diffusion velocity

To solve the transport equation for the single species mass fractions as well as one of the energy related equations, the diffusion velocities $V_{k,j}$ have to be determined. A complete multicomponent description results in a linear system of equations with size N^2 [18] whose solution is difficult and costly [126]. Therefore, the Hirschfelder and Curtiss approximation [127], also known as mixture averaged diffusion approach, is utilized within this thesis, which represents the best first-order approximation of the complete multicomponent system [126]. Herein, the diffusion velocity is given as

$$V_{k,j} = -D_k \frac{1}{X_k} \frac{\partial X_k}{\partial x_j} = -D_k \frac{1}{Y_k} \frac{\partial Y_k}{\partial x_j} - D_k \frac{1}{M} \frac{\partial M}{\partial x_j} \quad (2.12)$$

where D_k represents an equivalent diffusion coefficient of the species k into the mixture and is linked to the binary diffusion coefficients \mathcal{D}_{kl} of species k and l by

$$D_k = \frac{1 - Y_k}{\sum_{l \neq k} X_l / \mathcal{D}_{kl}}. \quad (2.13)$$

Within this approach, the Lewis number $Le_k = a/D_k$ can be used to link the diffusion coefficient to the thermal diffusivity $a = \lambda/(\rho c_p)$. The determination of the binary diffusion coefficients of each species pair is performed by the method given in [128] within this work. Since this approach does not fulfill the overall mass conservation, an additional correction velocity $V_{c,j}$ is added to the diffusion velocity which is obtained by summation over Eq. (2.4) with the definition of the diffusion velocity according to Eq. (2.12) and equalling the result to the mass continuity Eq. (2.1). This procedure leads to

$$V_{c,j} = \sum_{k=1}^N D_k \frac{M_k}{M} \frac{\partial X_k}{\partial x_j}. \quad (2.14)$$

In the case of binary diffusion or equal diffusivities for all species, the mixture averaged diffusion approach recovers Fick's law given by

$$V_k = -D \frac{1}{Y_k} \frac{\partial Y_k}{\partial x_j} \quad (2.15)$$

where D denotes the corresponding diffusion coefficient. This incorporates the equality of all species' Lewis numbers, usually set equal to unity: $Le_k = 1$. This case will be referred to as the unity Lewis number assumption within the remainder of this thesis.

Transport coefficients

The dynamic viscosity μ and the thermal conductivity λ of the mixture introduced by the models for the viscous stress tensor in Eq. (2.5) and the heat flux in Eq. (2.8) are modelled by combining the single species values μ_k and λ_k utilizing appropriate mixing rules. This can be either a linear weighting in the form

$$\mu = \sum_{k=1}^N Y_k \mu_k \quad (2.16)$$

$$\lambda = \sum_{k=1}^N Y_k \lambda_k \quad (2.17)$$

which are used for the 3D spray simulations within this thesis, or more complex (but even simplified) rules like

$$\mu = \sum_{k=1}^N \frac{\mu_k}{1 + 1/X_k \sum_{k=1, k \neq l}^N X_l \Phi_{k,l}} \quad (2.18)$$

proposed by Wilke [129], with

$$\Phi_{k,l} = \frac{1}{\sqrt{8}} \left(1 + \frac{M_k}{M_l}\right)^{-\frac{1}{2}} \left(1 + \left(\frac{\mu_l}{\mu_k}\right)^{\frac{1}{2}} \left(\frac{M_l}{M_k}\right)^{\frac{1}{4}}\right)^2 \quad (2.19)$$

or the semi-empirical expression

$$\lambda = \frac{1}{2} \left(\sum_{k=1}^N X_k \lambda_k + \left(\sum_{k=1}^N X_k / \lambda_k \right)^{-1} \right) \quad (2.20)$$

suggested in [130] for the thermal conductivity used for the flamelet calculations described in Section 2.2.2. The single species properties are evaluated based on binary diffusion coefficients and stored as function of temperature in polynomial form for the simulation.

Thermodynamic properties

As shown in equation (2.7), the information about c_{p_k} and h_k need to be known, to relate the enthalpy of the mixture to the temperature. Their molar based quantities are stored as well as the molar entropy in polynomial form, often denoted by NASA polynomials, as

$$\frac{c_p^m(T)}{R} = a_0 + a_1T + a_2T^2 + a_3T^3 + a_4T^4 \quad (2.21)$$

$$\frac{h^m(T)}{RT} = a_0 + \frac{a_1}{2}T + \frac{a_2}{3}T^2 + \frac{a_3}{4}T^3 + \frac{a_4}{5}T^4 + \frac{a_5}{T} \quad (2.22)$$

$$\frac{s^m(T)}{R} = a_0 \ln T + a_1T + \frac{a_2}{2}T^2 + \frac{a_3}{3}T^3 + \frac{a_4}{4}T^4 + a_6 \quad (2.23)$$

with $R = 8.314 \text{ J/K/mol}$ denoting the universal gas constant. The coefficients a_i are stored for a wide range of species [131]. The molar based quantities are related to the specific ones by the molar mass of the species, e.g. $c_{p,k} = c_{p,k}^m/M_k$. Furthermore, the ideal gas law

$$p = \rho \frac{R}{M} T \quad (2.24)$$

is utilized to close the system of equations.

Chemical reactions

Chemical reactions lead to the production and destruction of molecules of species k per unit mass and time denoted by $\dot{\omega}_k$ in Eq. (2.4) and Eq. (2.10). The computation of this term usually starts with the consideration of a system of N species connected via M reactions

$$\sum_{k=1}^N \nu'_{k,m} \mathcal{M}_k \rightleftharpoons \sum_{k=1}^N \nu''_{k,m} \mathcal{M}_k \text{ for } m \in [1, M] \quad (2.25)$$

where $\nu'_{k,m}$ and $\nu''_{k,m}$ represent the stoichiometric coefficients of species k in reaction m , M the number of reactions and \mathcal{M}_k represents species k symbolical. The source term $\dot{\omega}_k$ is then defined based on the reaction progress Q of reaction j as

$$\dot{\omega}_k = W_k \sum_{m=1}^M \nu_{k,m} Q_m \quad (2.26)$$

where the net stoichiometric coefficient $\nu_{k,m} = \nu''_{k,m} - \nu'_{k,m}$ gives the amount of species k build during the forward path of reaction m . The reaction progress of reaction m is further defined as

$$\mathcal{Q}_m = K_{f,m} \prod_{k=1}^N [X_k]^{\nu'_{k,m}} - K_{r,m} \prod_{k=1}^N [X_k]^{\nu''_{k,m}} \quad (2.27)$$

where $[X_k]$ denotes the molar concentration of species k . The terms $K_{f,m}$ and $K_{r,m}$ are the forward and reverse rates of reaction m . The forward rate is commonly modelled following the empirical Arrhenius law by

$$K_{f,m} = A_{f,m} T^{\beta_m} \exp\left(-\frac{E_m}{RT}\right) = A_{f,m} T^{\beta_m} \exp\left(-\frac{T_{a,m}}{T}\right) \quad (2.28)$$

while the reverse rate is obtained from the forward rate and the equilibrium constants

$$K_{r,m} = \frac{K_{f,m}}{\left(\frac{p_a}{RT}\right)^{\sum_{k=1}^N \nu_{k,m}} \exp\left(\frac{\Delta S_m^0}{R} - \frac{\Delta H_m^0}{RT}\right)}. \quad (2.29)$$

where $p_a = 1$ bar. ΔS_m^0 and ΔH_m^0 represent the entropy and enthalpy changes for reactions m which are tabulated. The pre-exponential constant $A_{f,m}$, the temperature exponent β_m and the activation temperature $T_{a,m}$ or the activation energy $E_m = RT_{a,m}$, respectively, have to be prescribed for each reaction m . These parameters are usually obtained from experiments and are summarized within so-called *reaction mechanisms* in a standardized format.

Hence, the choice of an appropriate reaction mechanism is of central importance for the simulation of an reactive flow system. Especially the applications considered in this thesis involve complex chemical pathways and will be discussed in more details within the corresponding sections concerning the numerical setups.

2.1.3 Description of the turbulent flow field

Large Eddy Simulation of turbulent flows

The basic idea in the context of Large Eddy Simulation (LES) denotes the resolution of large scale turbulent motions with an appropriate numerical grid resolution, while the influence of scales, which are not able to be resolved, is modelled. To formally separate these scales from each other, Leonard [132] introduced the idea of filtering the conservation equations. Therefore, the filter operator $\bar{\cdot}$ is introduced, which is defined for any quantity ϕ as

$$\bar{\phi}(x_i) = \int \phi(x_i, r_j) G(x_i, r_j) dr_j \quad (2.30)$$

where $G(x_i, r_j)$ represents a filter kernel which is centered around the point of interest x_i and evaluated as function of the distance r_j . Furthermore, the density weighted filter operator $\tilde{\cdot}$, also denoted as Favre-filter, is commonly used. In particular, Favre-filtered quantities are defined by

$$\tilde{\phi} = \frac{\overline{\rho\phi}}{\bar{\rho}}. \quad (2.31)$$

For the derivation of the filtered mass, momentum and energy conservation equations the filter operator is applied to both sides of the corresponding equation, in particular Eq. (2.1), Eq. (2.5), Eq. (2.8), where each term is filtered separately by making use of the linearity of the operator. Further, by accepting the so-called commutation error⁶, derivation and filtering is changed in the order of evaluation. Finally, to reduce the number of unclosed terms, all expressions of the form $\overline{\rho\phi}$ are replaced by $\bar{\rho}\tilde{\phi}$. With this, the following equations for the Favre-filtered mass, momentum and enthalpy read

$$\frac{\partial \bar{\rho}}{\partial t} + \frac{\partial \bar{\rho}\tilde{u}_j}{\partial x_j} = \bar{S}_m \quad (2.32)$$

$$\frac{\partial \bar{\rho}\tilde{u}_i}{\partial t} + \frac{\partial \bar{\rho}\tilde{u}_j\tilde{u}_i}{\partial x_j} = -\frac{\partial \bar{p}}{\partial x_i} + \frac{\partial \bar{\tau}_{ij}}{\partial x_j} - \frac{\partial \tau_{ij}^{\text{SGS}}}{\partial x_j} + \bar{\rho}g_i + \bar{S}_{u,i} \quad (2.33)$$

$$\frac{\partial \bar{\rho}\tilde{h}_t}{\partial t} + \frac{\partial \bar{\rho}\tilde{u}_j\tilde{h}_t}{\partial x_j} = \frac{\partial \bar{p}}{\partial t} - \frac{\partial \bar{q}_j}{\partial x_j} - \frac{\partial q_j^{\text{SGS}}}{\partial x_j} + \bar{\rho}\tilde{u}_j g_j + \bar{S}_{h_t} \quad (2.34)$$

with the filtered viscous stress tensor and heat flux given by

$$\bar{\tau}_{ij} = \bar{\mu} \left(\frac{\partial \tilde{u}_i}{\partial x_j} + \frac{\partial \tilde{u}_j}{\partial x_i} - \frac{2}{3} \delta_{ij} \frac{\partial \tilde{u}_k}{\partial x_k} \right) \quad (2.35)$$

$$\bar{q}_j = -\frac{\bar{\lambda}}{c_p} \frac{\partial \tilde{h}}{\partial x_j} + \bar{\rho} \sum_{k=1}^N \widetilde{h_k Y_k V_{k,j}} \quad (2.36)$$

where the second term in the \bar{q}_j definition as well as the mechanical source $\frac{\partial \tau_{ij} u_i}{\partial x_j}$ in equation (2.34) is neglected here following [97].

The terms $\tau_{ij}^{\text{SGS}} = \bar{\rho}(\widetilde{u_i u_j} - \tilde{u}_i \tilde{u}_j)$ and $\bar{q}_j^{\text{SGS}} = \bar{\rho}(\widetilde{u_j h_t} - \tilde{u}_j \tilde{h}_t)$ denote the unclosed terms due to the application of the filter operator. Applying the Boussinesq hypothesis [134], the anisotropic part of τ_{ij}^{SGS} is modelled in analogy to the viscous stress tensor as

$$\tau_{ij}^{\text{SGS}} - \frac{1}{3} \tau_{kk}^{\text{SGS}} \delta_{ij} = -\bar{\rho} \nu_{\text{SGS}} \left(\frac{\partial \tilde{u}_i}{\partial x_j} + \frac{\partial \tilde{u}_j}{\partial x_i} - \frac{2}{3} \delta_{ij} \frac{\partial \tilde{u}_k}{\partial x_k} \right). \quad (2.37)$$

The isotropic part $\frac{1}{3} \tau_{kk}^{\text{SGS}}$ equals twice the subgrid scale kinetic energy and is absorbed in the filtered pressure \bar{p} , as usually done within the limit of low Mach number flows [18]. The newly introduced quantity ν_{SGS}

⁶Which is zero when a homogeneous filter is applied to an infinite domain, see e.g. [133] for a compact description

denotes the subgrid scale viscosity and is modelled based on dimensional analysis in a unified manner by [135]

$$\nu_{\text{SGS}} = (C_m \Delta)^2 \mathcal{D}_m(u_i). \quad (2.38)$$

Herein, \mathcal{D}_m denotes a differential operator specific to the model utilized. In this thesis, the σ -model [135] is utilized, where the differential operator is based on the singular values of the velocity gradient tensor σ_i and is defined as

$$\mathcal{D}_\sigma = \frac{\sigma_3 (\sigma_1 - \sigma_2) (\sigma_2 - \sigma_3)}{\sigma_1^2} \quad (2.39)$$

The model constant usually takes values in the order of $C_\sigma = 1.5$ for well resolved LES [135, 136]. However, since the optimal value of this constant depends e.g., on the grid resolution [135], the application of a dynamic procedure can be beneficial. In this thesis, a dynamic procedure specifically derived for the σ -model is utilized [137] for the gaseous flame. Since this procedure is intended to be applied on the overall computational domain, it is expected to be inappropriate for the application within spray flames for the following reasons: 1) The evolution of the spray starts out from a quiescent gas-phase, which is accelerated by the liquid phase. Hence, shortly after the start of injection, there is a strong interaction between the liquid and gas phases influenced by the turbulence, either modeled or resolved, in the latter phase. The dynamic procedure in this period of injection is only evaluated based on the gas-phase information, neglecting the liquid phase acceleration leading to the potential wrong response of the turbulence model in the next time step. 2) The length scales of turbulent motion vary strongly within a spray simulation even if parts of it reach a quasi-steady state. Hence, different amounts of the energy spectrum are resolved in different parts of the computational domain, making the applicability of a dynamic procedure based on the overall domain questionable. Hence, the prescription of a model constant is preferred in this thesis for the spray simulations. It still remarks a compromise in the model adjustment following the given argumentation but is better controllable than the result of a dynamic procedure. In the numerical solution procedure, the filter width is modelled as a function of the cell volume V_{cell} as

$$\Delta = V_{\text{cell}}^{1/3}. \quad (2.40)$$

The unresolved enthalpy flux is modelled by means of a gradient-flux assumption leading to

$$q_j^{\text{SGS}} = -\bar{\rho} \frac{\nu_{\text{SGS}}}{\text{Pr}_{\text{SGS}}} \frac{\partial \tilde{h}_t}{\partial x_j} \quad (2.41)$$

where ν_{SGS} is obtained from the subgrid-scale model described above and Pr_{SGS} is a model constant set to 0.4 in this thesis [138, 139]. In addition to the equations given above, the filtered equation of state

$$\bar{p} = \bar{\rho} \frac{R}{M} \tilde{T} \quad (2.42)$$

is utilized.

The set of equations given above offer information about the filtered variables describing the flow field, but not about the chemical composition or related variables like the filtered transport properties. To evaluate these information, the turbulent combustion model described in the next section is utilized.

2.2 Turbulent combustion model

As described in the last section, a combustion model is needed, to close the filtered governing equations. Various models were developed within the last decades as summarized in Section 1.1.2, where the FPV and UFPV approach is applied in this work. They both combine the flamelet model for non-premixed combustion with pre-tabulation of the flame-structure. The description of the model is organized as follows: In Section 2.2.1, the concept of mixture fraction is introduced to quantify the local state of mixing between fuel and oxidizer as key variable of the modeling approach. Subsequently, the flamelet equations are briefly summarized in Section 2.2.2 including the discussion of model parameters as well as their evaluation. In Section 2.2.3, the strategies for the pre-tabulation within the FPV and UFPV approach are presented and comments concerning the progress variable definition are given. Thereupon, extensions of the tabulation strategies introduced in this thesis are described in Section 2.2.4. In Section 2.2.5, the evaluation of filtered quantities needed to close the filtered transport equations is described. A summary of the tabulation strategies utilized in this thesis is given in Section 2.2.6. The section closes with the description of the coupling of the UFPV and UFCPV approach to single flamelet simulations in Section 2.2.7, the FPV approach to single phase LES in Section 2.2.8 as well as the UFPV and UFCPV approach to spray LES in Section 2.2.9.

2.2.1 The concept of mixture fraction

For modeling non-premixed combustion, a variable quantifying the local fuel/oxidizer ratio has to be defined. For this purpose, the mixture fraction Z is commonly used. For a two feed system with one fuel stream (index 1) and one oxidizer stream (index 2), it quantifies the ratio of mass flux originating from the fuel stream to the overall mass flux as

$$Z = \frac{\dot{m}_1}{\dot{m}_1 + \dot{m}_2} \quad (2.43)$$

and is usually defined as normalized conserved scalar variable [30]. Early definitions of the mixture fraction are based on a one step reaction of fuel and oxidizer towards products [140] where the corresponding mass fractions are combined by an appropriate coupling function leading to cancellation of chemical source terms in the mixture fraction transport equation. Since this approach leads to problems when the fuel is first converted into intermediate species before the formation of products [30], Bilger [141] derived a definition based on a one-step reaction on elemental level



and by introducing the elemental mass fractions

$$Z_j = \sum_i^N \frac{a_{ij} M_j}{M_i} Y_i \quad (2.45)$$

where a_{ij} denotes the number of atoms of element j in species i , M_j the molecular weight of element j , N the number of species and Y_i the mass fraction of species i , the coupling function

$$\beta = \frac{Z_C}{\nu_C M_C} + \frac{Z_H}{\nu_H M_H} - 2 \frac{Z_O}{\nu_O M_O} \quad (2.46)$$

can be defined. The normalization of this coupling function by its values in the fuel and oxidizer stream leads to the definition according to Bilger [141]

$$Z_{\text{Bilger}} = \frac{\beta - \beta_2}{\beta_1 - \beta_2} \quad (2.47)$$

which reads

$$Z_{\text{Bilger}} = \frac{(Z_C - Z_{C,2})/(\nu_C M_C) + (Z_H - Z_{H,2})/(\nu_H M_H) + 2(Z_O - Z_{O,2})/(\nu_O M_O)}{(Z_{C,1} - Z_{C,2})/(\nu_C M_C) + (Z_{H,1} - Z_{H,2})/(\nu_H M_H) + 2(Z_{O,1} - Z_{O,2})/(\nu_O M_O)} \quad (2.48)$$

Note, that the mixture fraction value for a stoichiometric mixture $Z_{\text{Bilger},st}$ can be obtained from Eq. (2.47) by setting $\beta = 0$. This definition can be evaluated based on experimental data and is used for the comparison with simulation results within this thesis.

As noted by Pitsch and Peters [30], differential diffusion effects appear in a transport equation for the mixture fraction derived for the definition in Eq. (2.48). To circumvent this, Pitsch and Peters [30], defined the mixture fraction as conserved scalar described by the transport equation

$$\frac{\partial \rho Z}{\partial t} + \frac{\partial \rho Z u_j}{\partial x_j} = \frac{\partial}{\partial x_j} \left[\rho D_Z \left(\frac{\partial Z}{\partial x_j} \right) \right] \quad (2.49)$$

with $D_Z = a$ where a denotes the thermal conductivity and full-filling the boundary conditions $Z = 0$ in the oxidizer stream and $Z = 1$ in the fuel stream, which was used to derive flamelet equations incorporating differential diffusion effects in [30].

2.2.2 Flamelet equations

A widely used property of turbulent jet flames at high Damköhler number is the occurrence of thin flame sheets, so called flamelets, which are embedded in turbulent flows and strained by turbulent motions but not interpenetrated by them [29]. In an asymptotic analysis, Peters showed, that transport phenomena are occurring mainly in flame normal direction leading to a 1D-description of these flame structures [29]. By applying the transformation rules

$$\begin{aligned}\frac{\partial}{\partial t} &= \frac{\partial}{\partial \tau} + \frac{\partial Z}{\partial t} \frac{\partial}{\partial Z} \\ \frac{\partial}{\partial x_1} &= \frac{\partial Z}{\partial x_1} \frac{\partial}{\partial Z} \\ \frac{\partial}{\partial x_\beta} &= \frac{\partial}{\partial Z_\beta} + \frac{\partial Z}{\partial x_\beta} \frac{\partial}{\partial Z}, \quad \beta = 2, 3\end{aligned}\tag{2.50}$$

on the species mass fraction and temperature conservation equations Eq. (2.4), Eq. (2.10) and keeping only the leading order terms, the following equations for the description of the flamelet equations can be obtained [142]

$$\rho \frac{\partial Y_k}{\partial \tau} - \rho \frac{\chi}{2\text{Le}_k} \frac{\partial^2 Y_k}{\partial Z^2} = \dot{\omega}_k\tag{2.51}$$

$$\rho \frac{\partial T}{\partial \tau} - \rho \frac{\chi}{2} \frac{\partial^2 T}{\partial Z^2} - \rho \frac{\chi}{2c_p} \left[\sum_{k=1}^N \frac{c_{p_k}}{\text{Le}_k} \frac{\partial Y_k}{\partial Z} + \frac{\partial c_p}{\partial Z} \right] \frac{\partial T}{\partial Z} = \frac{1}{c_p} \left(\frac{\partial p}{\partial t} - \sum_{k=1}^N \dot{\omega}_k h_k \right).\tag{2.52}$$

The scalar dissipation rate of the mixture fraction field χ defined as

$$\chi = 2D \left(\frac{\partial Z}{\partial x_j} \right)^2\tag{2.53}$$

stems from the coordinate transformation. This parameter can be seen as the connection between the physical space and the mixture fraction space and acts as diffusion coefficient in the flamelet equations. Note, that enthalpy source due to phase change are neglected. This set of equations are simplified with respect to differential diffusion. The complete set of flamelet equations considering differential diffusion were derived by Pitsch and Peters [30] and are used additionally in this thesis. In particular for turbulent flames, further approaches were developed. In this context, Wang [69] proposed a model accounting for the penetration of turbulent eddies into the flame structure and hence damping the effect of differential diffusion between the single species. This is done by introducing a scaling factor θ to the single species Lewis numbers given as function of the turbulent diffusion coefficient D_t by

$$\theta = \frac{r}{1+r} \quad \text{with } r = \frac{D}{D_t},\tag{2.54}$$

$$\widehat{\text{Le}}_k = \frac{\text{Le}_k}{\text{Le}_k + \theta(1 - \text{Le}_k)}.\tag{2.55}$$

Following the notation used in [1], the flamelet models introduced above are denoted by ULNF for model Eqs. (2.51) - (2.52) (Unity Lewis number flamelet), VLNF for the flamelet equations considering differential diffusion (variable Lewis number flamelet) and NLVLNF (non-linear variable Lewis number flamelet) when the Lewis numbers are obtained from Eq. (2.55). Note, that the NLVLNF recovers the ULNF model for $\theta = 0$ and the VLNF in case of $\theta = 1$.

All the presented flamelet models incorporate the scalar dissipation rate. Hence, a closure for $\chi = \chi(Z)$ is needed. These profiles are usually derived from generic flame configurations, e.g., the steady laminar counterflow diffusion flame with constant density and diffusion coefficients as done by Peters [142] or the unsteady one-dimensional mixing layer with fuel in the center surrounded by pure oxidizer at both sides as done by Pitsch [143] in physical space, while a transport equation for this variable can be derived also in mixture fraction space [144]. The definition of Peters [142] is used in this thesis where the scalar dissipation rate is related to its value at stoichiometry $\chi_{st} := \chi(Z_{st})$ and the stoichiometric value of the mixture fraction Z_{st} by

$$\chi(Z) = \chi_{st} f(Z) / f(Z_{st}) = \chi_{st} \exp \left(2 \left([\operatorname{erfc}^{-1}(2Z_{st})]^2 - [\operatorname{erfc}^{-1}(2Z)]^2 \right) \right). \quad (2.56)$$

Since Z_{st} is defined by the fuel/oxidizer combination, the only free parameter is χ_{st} which has to be prescribed to solve the flamelet equations. As a consequence, the solution of the flamelet equations and hence the thermo-chemical state at given pressure $\phi = [T, Y_i]$ is a function of 3 variables: The mixture fraction Z , the Lagrangian-like time τ and the scalar dissipation rate at stoichiometric mixture fraction χ_{st} :

$$\phi = \phi(Z, \tau, \chi_{st}) \quad (2.57)$$

for the ULNF and VLNF model and

$$\phi = \phi(Z, \tau, \chi_{st}, \theta(Z)) \quad (2.58)$$

for the NLVLNF model. Since the flamelet equations are coupled to the flow field by the scalar dissipation rate only, they can be solved decoupled from it. This can be done interactively with actual values of the 3D simulation as done in the RIF [39] or the MRIF [40–42] approach. Due to the limited set of control variables, a pre-tabulation is feasible, too. This approach is utilized within this thesis and explained in more detail in the Section 2.2.3.

One fact, that should be discussed here, is the possible state space spanned by the flamelet solutions. For this, the distinction is made between unsteady and steady solutions of the flamelet equations. On the left hand side of Figure 2.2, the temperature is shown as a function of mixture fraction obtained by the ULNF model, Eq. (2.52), for the ECN Spray A nominal conditions, which are investigated in the second part of this thesis. The initial condition is denoted by an adiabatic mixing of n-Dodecane at 363 K with hot ambient gas at a temperature of 900 K containing 15 % O₂ by volume (mimicking exhaust gas recirculation, EGR)

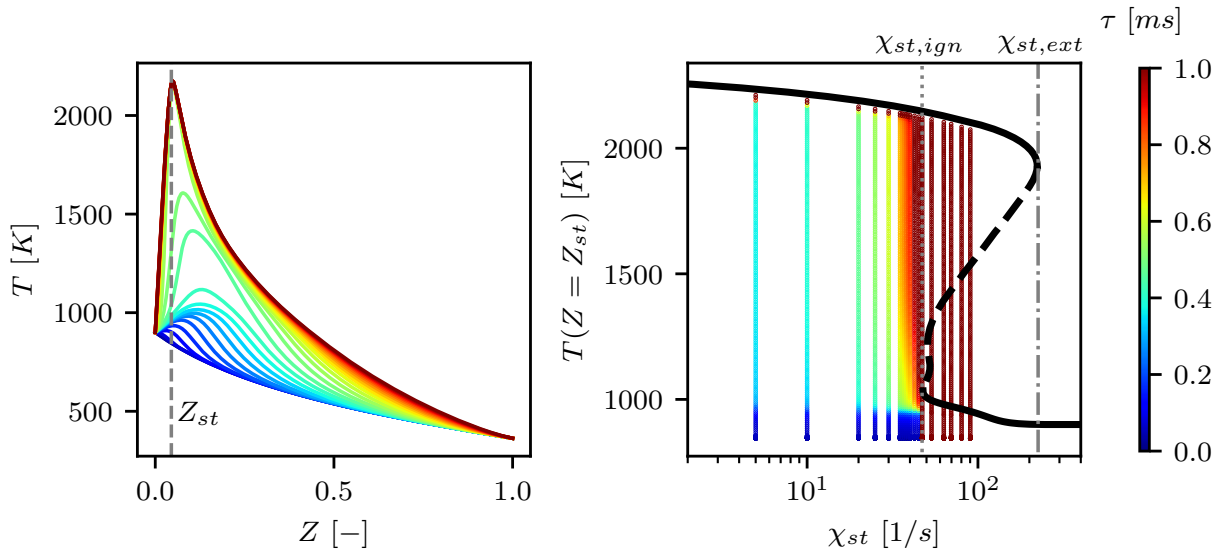


Figure 2.2: Transient evolution of an igniting flamelet with $\chi_{st} = 20/s$ under ECN Spray A nominal conditions [145] (n-Dodecane at 363K mixed adiabatically with hot oxidizer at 900 K containing 15 % O_2 by volume at 60 bar; left) and temperature at stoichiometric conditions $T(Z = Z_{st})$ as function of χ_{st} color coded by their corresponding time (for $\chi_{st} \leq \chi_{st,ign}$, arbitrary time scale for $\chi_{st} > \chi_{st,ign}$) for unsteady and steady solutions under the same operating conditions building the S-curve. Gray dashed line: Stoichiometric conditions, gray dotted line: $\chi_{st,ign}$, gray dash-dotted line: $\chi_{st,ext}$, black dashed line: Unstable steady solutions (unstable branch of the S-curve)

under a pressure of 60 bar. The color code identifies the time of the evolution. Starting from lean conditions ($Z < Z_{st}$) a rise in temperature is observed which propagates into the fuel-rich part where second stage ignition initiates. The maximum temperature propagates towards stoichiometry, where it remains at steady state. In this plot, stoichiometric conditions are denoted by the vertical dashed line. The evolution of the temperature at stoichiometric conditions as a function of χ_{st} is shown on the right hand side of Figure 2.2. The solutions can be divided into unsteady solutions (colored by their respective time) and steady solutions drawn in black. The steady solutions itself contain stable solutions building the upper part of the S-shaped curve (abbreviated by the term S-curve) and unstable solutions between the turning points $\chi_{st,ign}$ and $\chi_{st,ext}$. Starting from the adiabatic mixing line, high temperature ignition can only proceed if $\chi_{st} < \chi_{st,ign}$ while burning solution extinguish if $\chi_{st} > \chi_{st,ext}$. Initializing an unsteady simulation from the unstable branch will immediately lead to ignition if the scalar dissipation rate is slightly decreased and to extinction if the scalar dissipation rate is slightly increased, respectively [56].

2.2.3 Tabulation of flame structures

FPV approach

The FPV approach proposed by Pierce [45], Pierce and Moin [46] was developed with the aim, to describe a reactive multicomponent flow with only a minimum set of transported variables. As discussed in Section 2.2.1,

the mixture fraction as conserved scalar serves as transport variable to quantify the mixing of fuel and oxidizer. However, it does neither include any information about the progress of reaction nor about chemical variation perpendicular to its gradient [45]. To include these effects, a non-conserved scalar called *reaction progress variable*, abbreviated by progress variable Y_C in this thesis, is introduced governed by the transport equation

$$\frac{\partial \rho Y_C}{\partial t} + \frac{\partial \rho u_j Y_C}{\partial x_j} = \frac{\partial}{\partial x_j} \left[\rho D_{Y_C} \left(\frac{\partial Y_C}{\partial x_j} \right) \right] + \dot{\omega}_{Y_C}. \quad (2.59)$$

To use this definition, the thermo-chemical state must be completely determined by Z and Y_C , i.e., $\phi = \phi(Z, Y_C)$. This state relation is obtained from steady flamelet solutions in Pierce [45]⁷, see Section 2.2.2, by mapping the scalar dissipation rate as parameter distinguishing single flamelets (or short: flamelet parameter) λ to the progress variable. The progress variable is further defined as a linear combination of major reaction product mass fractions by Pierce [45] to determine the thermo-chemical state, even though other variables can be used. For example, the entropy was suggested by Pierce [45]. The benefits of this approach over the tabulation over the (Z, χ_{st}) tabulation are the following:

1. The mapping towards the progress variable enables the inclusion of all S-curve solutions into the look-up table [45–47], which is not possible with the (Z, χ_{st}) parameterization due to the ambiguity of the steady solutions with respect to χ_{st} , see Figure 2.2. With respect to this figure, the solution space is not mapped on the ordinate as done within the (Z, χ_{st}) parameterization but on the abscissa when using the temperature as progress variable or when it is replaced by any other progress variable definition for mapping.
2. The solution for the progress variable and request from steady flamelet solutions incorporates as such unsteady effects to a certain extend. Effectively, this approach does account for the fact, that χ_{st} does not change immediately in a turbulent flow field, but incorporates history effects [45, 46].
3. Recently, Han et al. [38] showed the incorporation of curvature effects (transport effects along iso- Z lines) by utilizing the FPV approach, even they are not included in the steady flamelet model.

UFPV approach

Beside the ability of the FPV approach to capture local extinction and re-ignition as well as partially premixed combustion, e.g., in lifted flames, shortcomings were observed e.g., in the prediction of CO [56]. Pitsch and Ihme [56] mention the missing unsteadiness within the FPV approach the main reason for this model shortcomings and proposed the unsteady flamelet progress variable (UFPV) approach as an extension of the FPV approach which was further validated and extended by means of turbulence-chemistry interaction by Ihme and See [55]. In contrast to the FPV approach, the thermo-chemical state space described by the unsteady flamelet solutions $\phi = \phi(Z, \tau, \chi_{st})$ is used to construct the database where the Lagrangian-like

⁷Where the the governing equation for a counter-flow diffusion flame are solved in physical space

time τ is mapped onto the flamelet parameter λ , defined following the FPV approach by $\lambda = Y_C(Z_{st})$. The resulting state space is parameterized by $\phi = \phi(Z, \lambda, \chi_{st})$. With this, the approach includes the thermochemical states of transient effects such as extinction and re-ignition, which are not incorporated by steady flamelet solutions. Beside the application investigated in Pitsch and Ihme [56] and Ihme and See [55], such processes are of main importance in the self-ignition of vaporized fuel in spray combustion, as investigated in the second part of this thesis. In contrast to the FPV approach, χ_{st} has to be determined as additional flamelet parameter to perform the table look-up.

Definition of the progress variable

In both approaches described above, the progress variable Y_C replaces one of the request parameters by

$$\phi(Z, \chi_{st}) \longrightarrow \phi(Z, Y_C) \quad (2.60)$$

in case of the FPV approach, and

$$\phi(Z, \tau, \chi_{st}) \longrightarrow \phi(Z, Y_C, \chi_{st}) \quad (2.61)$$

in case of the UFPV approach. Hence, a unique mapping $\chi_{st} \rightarrow Y_C$ and $\tau \rightarrow Y_C$ has to be ensured, respectively. Hence, the single species weights in the progress variable definition $Y_C = \sum_k \alpha_k Y_k$ with k denoting the species incorporated depend on the operating conditions. Beside the availability of advanced algorithm to define these weights in a automated manner [146–148], the Y_C -definitions utilized in this thesis are obtained from an inspection of the corresponding manifolds with values given for the operating conditions under investigation in Section 3.3 and Section 4.2, respectively.

Progress variable normalization

While the original FPV approach [45, 46] is based on the progress variable Y_C and the progress parameter λ to ensure a statistical independence with respect to Z , the normalized progress variable

$$C(Z, \chi_{st}) = \frac{Y_C(Z, \chi_{st}) - Y_{C,min}(Z)}{Y_{C,max}(Z) - Y_{C,min}(Z)} \quad (2.62)$$

is used to parameterize the flamelet look-up table (FLUT), which is independent of Z , too [149]. This property simplifies the evaluation of filtered quantities from the FLUT as described in Section 2.2.5. The suitability of this approach was demonstrated in former works considering turbulent jet flames [50, 51, 150]. Furthermore, the progress variable normalization leads to a cubically shaped look-up table, which allows an efficient table access [151, 152]. Note, that this normalization for the UFPV approach reads

$$C(Z, \tau, \chi_{st}) = \frac{Y_C(Z, \tau, \chi_{st}) - Y_{C,min}(Z, \chi_{st})}{Y_{C,max}(Z, \chi_{st}) - Y_{C,min}(Z, \chi_{st})}, \quad (2.63)$$

since, the progress variable is used to replace the Lagrangian-like time τ .

2.2.4 Modifications introduced in this thesis

After the description of the original FPV and UFPV approaches in the last sections, the modifications used and proposed in this thesis are presented in the following.

FPV modeling for differential diffusion⁸

One modification in contrast to the original FPV approach [45, 46] is related to the choice of the mixture fraction definition. Since the $Le_Z = 1$ mixture fraction definition does not enable the definition of a monotonically increasing progress variable definition for the oxy-fuel flame investigated in the first part of this thesis, see Figure 2.3, the FLUT is mapped onto Z_{Bilger} as defined in Eq. (2.48) as mixing variable. Hence, the flamelet equations are still solved for the ULNF, VLNF or NLVLNF equations and are mapped to Z_{Bilger} afterwards, resulting in $\phi = \phi(Z_{\text{Bilger}}, C)$ for the ULNF and VLNF equation and $\phi = \phi(Z_{\text{Bilger}}, C, \theta)$ for the NLVLNF model. Note, that the mapping towards Z_{Bilger} as mixing variable denotes a modification of the original FPV approach but is used within other tabulation strategies, like the FGM approach proposed by Bekdemir et al. [93] to simulate diesel spray combustion. To obtain the Bilger mixture fraction in the coupled simulation, the mass fraction of the species which are accessible from Raman measurements, are transported in this thesis, as described in Section 2.2.8.

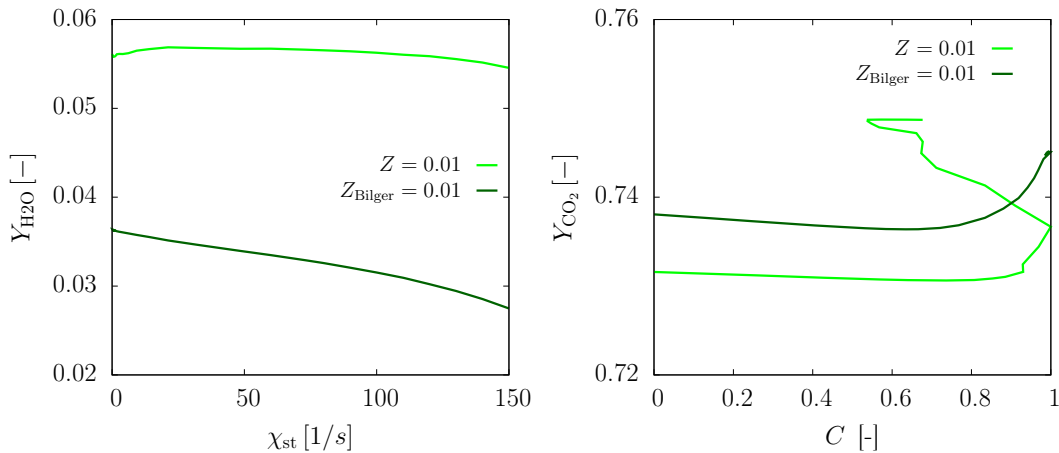


Figure 2.3: Comparison of VLNF-predicted H₂O mass fraction spanned by varying scalar dissipation rate (left) and resulting CO₂ mass fraction over normalized H₂O mass fraction C (right) at constant value for Z (light green) and Z_{Bilger} (dark green), respectively.

⁸This section is partly taken from the supplementary material of the publication by Gierth et al. [1] which was created during the work on this thesis. In [1], I was the main author of this part.

One challenge when describing the ignition process with the UFPV approach stems from the fact, that the source term of the progress variable might be zero if the normalized progress variable is zero, i.e., $\dot{\omega}_{Y_C}(Z, \chi_{st}, C = 0) = 0$. This could either be prevented by adding species to the progress variable definition with source term greater zero, as done e.g., in [94, 96, 104]. While this approach is obvious, it introduces a new constraint on the progress variable definition, which complicates its definition even further. Hence, an extension of the progress variable source term was introduced in a similar manner compared to [109, 110]. The source term of the progress variable is replaced by

$$\dot{\omega}_{init}^*(Z, \chi_{st}) = \frac{\int_0^{t(C=C_{init})} \dot{\omega}_{Y_C}(Z, \chi_{st}, t) dt}{\int_0^{t(C=C_{init})} dt} \quad \forall C \in [0, C_{init}], \quad (2.64)$$

where C_{init} is a small threshold value ($C_{init} = 10^{-5}$ in this thesis). This procedure is visualized in Figure 2.4. The patch further reduces the sensitivity of $\dot{\omega}_{Y_C}$ with respect to Y_C during the onset of initial reactions avoiding numerically rounding errors for very small Y_C and $\dot{\omega}_{Y_C}$ for all mixture fractions, while conserving the integral production of Y_C . Note, that it differs from the approach presented in [109, 110] by evaluating the integral in (2.64) over the progress variable source term, while the difference of Y_C was used within the mentioned works. Hence, only the chemical contribution is accounted for and transport processes establish consistently within the coupled simulation.

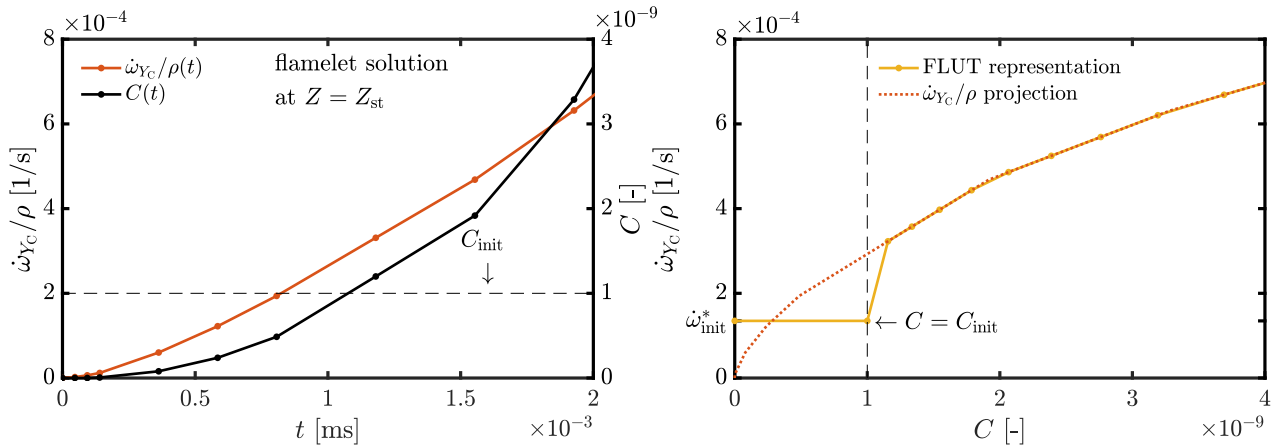


Figure 2.4: Normalized progress variable C (black line) and progress variable source term $\dot{\omega}_{Y_C}$ (red line) over time (left) for an unsteady flamelet solution ($Z = Z_{st}, \chi_{st} = 40/s$). The right graph shows the comparison of $\dot{\omega}_{Y_C}$ (red dashed line) and the patch introduced in the FLUT (orange line). Note, that the value of $C_{init} = 10^{-9}$ is used for visualization [3].

⁹This section is partially taken from the publication by Sun et al. [3], which was created during the work on this thesis. In [3], I equally contributed to this part with Zhen Sun and Martin Pollack.

Treatment of different time scales within the UFPV approach - UFCPV

As mentioned in Section 1.1.4, the formation of gaseous pollutants such as NO and soot precursors takes place at larger time scales than the main reaction process does. This effect cannot be accounted for in the FPV approach directly, since only steady flamelet solutions are used for tabulation. For this purpose, Ihme and Pitsch [57] introduced a correction to account for the transient effects describing NO in the coupled simulation. It is based on a decomposition of the NO source term into production and destruction rates, where the former one is independent of the NO concentration itself and the latter one shows a linear dependency. A transport equation is then solved for the NO mass fraction in the coupled simulation utilizing this decomposition. However, when the UFPV approach is followed, this transient behavior is incorporated into the unsteady flamelet solutions, shown in the left part of Figure 2.5 based on the example of an igniting flamelet under the ECN Spray A nominal conditions for temperature, as well as for the NO and pyrene (as a representative soot precursor) mass fraction. Beside the different time scales, the relatively low mass fraction values of NO and pyrene become obvious. Furthermore, their peak value is located in different regions in mixture fraction space. By defining a progress variable which enables a bijective mapping with respect to the flamelet time τ , these properties can directly be stored within the FLUT. The typical situation when considering a progress variable defined to capture the main ignition process is shown in the central and left-hand side parts of Figure 2.5: the progress variable shows a very similar behavior to the temperature, i.e., increases strongly over time during first- and second-stage ignition. Afterwards, it remains approximately constant. Hence, the time after which the second-stage ignition is completed cannot be distinguished by the progress variable. This is crucial when pollutant formation is of interest, since their evolution is improperly represented. The result of the representation in a look-up table based on such a progress variable is shown in the right-hand side of Figure 2.5. The temperature is described well as a function of the progress variable, while the mass fractions of NO and pyrene are zero over a wide range and then strongly increase over a short $Y_{C,1}$ interval. This problem can in principle be accounted for by including NO or other slow evolving species within the progress variable definition together with an appropriate scaling. However, since the time scale and quantitative value of gaseous pollutants also depend on the mixture fraction and its scalar dissipation rate, the definition of a suitable progress variable capturing species at different time scales and different orders of magnitude is a challenging task.

The idea proposed in this thesis is to simplify the problem by splitting it into two sub-problems: 1) define a progress variable that is able to capture the first and second stages of ignition $Y_{C,1}$ and 2) define a progress variable that is able to capture the evolution of slow species $Y_{C,2}$. Each of these requirements itself is potentially much easier to fulfill. The two progress variable definitions utilized in this thesis for the ECN Spray A nominal conditions are given by $Y_{C,1}$ as defined in the example above and $Y_{C,2} = Y_{\text{NO}} + Y_{\text{C}_{16}\text{H}_{10}} + Y_{\text{C}_{18}\text{H}_{10}}$. In the latter definition, $\text{C}_{16}\text{H}_{10}$ and $\text{C}_{18}\text{H}_{10}$ denote two representative poly-cyclic aromatic hydrocarbon (PAH) species serving as soot precursors. As shown in Figure 2.5, they span different time scales, as intended. However, their quantitative levels differ by three orders of magnitude. The summation of these progress variables to define the FLUT request parameter is misleading in this case, since the contribution of $Y_{C,2}$ does not span the time range in a balanced manner compared to $Y_{C,1}$. To circumvent this in a general way, both

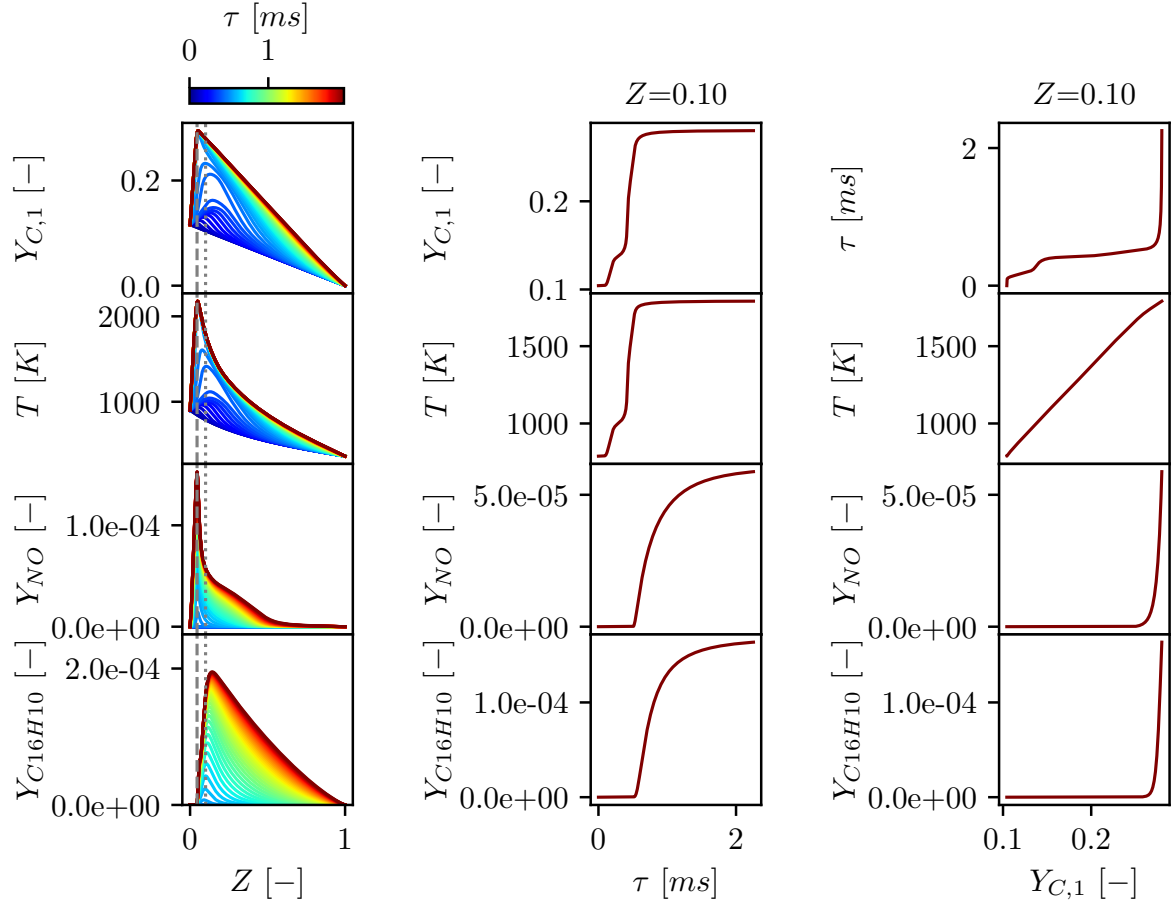


Figure 2.5: Evolution of progress variable $Y_{C,1} = 0.5Y_{\text{CO}} + 1.0Y_{\text{CO}_2} + 0.9Y_{\text{H}_2} + 1.0Y_{\text{H}_2\text{O}} + 0.8Y_{\text{CH}_2\text{O}}$ ([3], top row of first and second column), temperature (second row), NO mass fraction (third row) and $\text{C}_{16}\text{H}_{10}$ mass fraction (fourth row) as a function of mixture fraction at different times (left column), as function of time for rich conditions ($Z = 0.1$, central column, marked by dashed line in left column) and mapped as a function of $Y_{C,1}$ under the same conditions as in the middle row in an unsteady flamelet with $\chi_{st} = 20/s$ and ECN Spray A nominal conditions.

progress variables are normalized in line with Eq. (2.63) given by

$$C_i(Z, \tau, \chi_{st}) = \frac{Y_{C,i}(Z, \tau, \chi_{st}) - Y_{C,i,\min}(Z, \chi_{st})}{Y_{C,i,\max}(Z, \chi_{st}) - Y_{C,i,\min}(Z, \chi_{st})} \quad \text{with} \quad i \in [1, 2]. \quad (2.65)$$

With this definition, the progress variable of the look-up table is defined as

$$Y_C(Z, \tau, \chi_{st}) = C_1(Z, \tau, \chi_{st}) + C_2(Z, \tau, \chi_{st}) \quad (2.66)$$

which is normalized in a last step to enable an efficient table look-up [152] in line with to equation (2.63). Since the progress variable is composed of two single variables, the approach is described as the *unsteady*

flamelet composed progress variable (UFCPV) approach in this thesis. It is summarized in Figure 2.6. The approach has the following benefits:

- Progress variables for different time scales can be formulated separately.
- No limitation are present with respect to the order of magnitude of the single progress variables.
- No additional parameters are needed for blending between species with fast and slow time scale.
- Implementation in an existing UFPV code requires only the evaluation of the second progress variable and the calculation of the composed one.

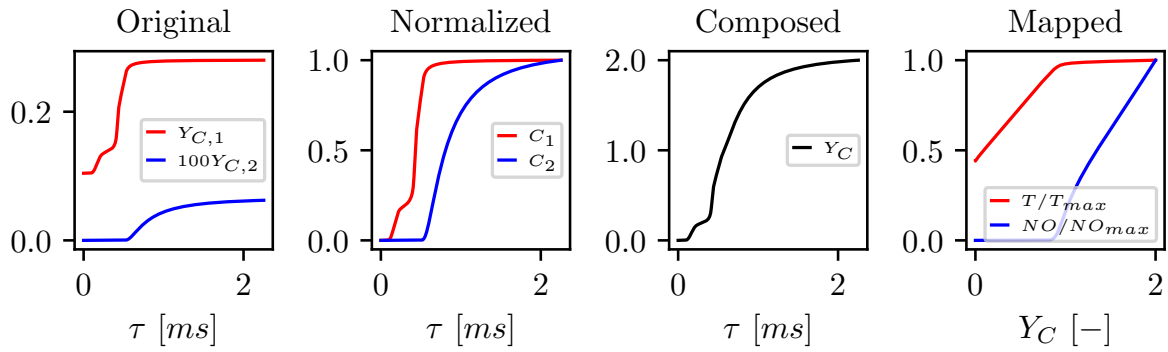


Figure 2.6: Visualization of the Y_C definition in the UFCPV approach: Temporal evolution of the progress variables $Y_{C,1} = 0.5Y_{CO} + 1.0Y_{CO_2} + 0.9Y_{H_2} + 1.0Y_{H_2O} + 0.8Y_{CH_2O}$ [3] and $Y_{C,2} = Y_{NO} + Y_{C_{16}H_{10}} + Y_{C_{18}H_{10}}$ as a function of time under rich conditions ($Z = 0.1$) extracted from the unsteady flamelet simulation shown in Figure 2.5 (left), their normalized values according to equation (2.65) (second plot), the composed progress variable according to Eq. (2.66) (third plot) and temperature and NO mass fraction mapped onto the composed progress variable (right)

2.2.5 Evaluation of filtered quantities

In the last section, the evaluation of single flamelet structures and their parameterization is described. However, based on the flamelet approximation for turbulent flows [153], an ensemble of flamelets represents the mean thermo-chemical state $\tilde{\phi}(x_i, t)$ when applying statistical approaches like RANS or LES¹⁰. In case of the UFPV approach, the Favre-filtered quantities can then be obtained by a convolution of the thermo-chemical state obtained from the flamelet equations $\phi(Z, C, \chi_{st})$ with the density weighted joint filtered density function (FDF) of the flamelet parameters Z, C, χ_{st} in case of LES $\tilde{P}(Z, C, \chi_{st})$ denoted by

$$\tilde{\phi}(x_i, t) = \int_0^1 \int_0^1 \int_{\chi_{st, min}}^{\chi_{st, max}} \phi(Z, C, \chi_{st}) \tilde{P}(Z, C, \chi_{st}) dZ dC d\chi_{st}. \quad (2.67)$$

where the density weighted FDF is defined following [55] as

$$\tilde{P}(Z, C, \chi_{st}) = \frac{\rho}{\bar{\rho}} P(Z, C, \chi_{st}). \quad (2.68)$$

the non-density weighted quantities are further obtained by

$$\bar{\phi}(x_i, t) = \int_0^1 \int_0^1 \int_{\chi_{st, min}}^{\chi_{st, max}} \phi(Z, C, \chi_{st}) P(Z, C, \chi_{st}) dZ dC d\chi_{st} \quad (2.69)$$

$$= \bar{\rho} \int_0^1 \int_0^1 \int_{\chi_{st, min}}^{\chi_{st, max}} \phi(Z, C, \chi_{st}) \frac{1}{\rho} \tilde{P}(Z, C, \chi_{st}) dZ dC d\chi_{st}. \quad (2.70)$$

which is applied e.g., to obtain the filtered species source terms and transport properties. From Eq. (2.70), the expression for the filtered density can be derived as

$$\bar{\rho}(x_i, t) = \left[\int_0^1 \int_0^1 \int_{\chi_{st, min}}^{\chi_{st, max}} \frac{1}{\rho} \tilde{P}(Z, C, \chi_{st}) dZ dC d\chi_{st} \right]^{-1}. \quad (2.71)$$

To obtain a model for the joint FDF $\tilde{P}(Z, C, \chi_{st})$, the argumentation given by Ihme and See [55] is followed: First, the joint FDF is decomposed into its marginal and conditioned FDFs given by

$$\tilde{P}(Z, C, \chi_{st}) = \tilde{P}(Z, \chi_{st}) P(C|Z, \chi_{st}). \quad (2.72)$$

As a result of the statistical independence of C with respect to Z and χ_{st} (following from its definition) reduces the conditional FDF in Eq. (2.72) to its marginal one. By further assuming statistical independence of Z and χ_{st} in Eq. (2.72) the joint FDF can be expressed as

¹⁰For LES in the sense, that a statistical distribution is present as result of the sub-grid scale fluctuations

$$\tilde{P}(Z, C, \chi_{st}) = \tilde{P}(Z)P(C)P(\chi_{st}). \quad (2.73)$$

Following [46], a β -PDF is used as model for $\tilde{P}(Z)$, which is given by

$$\tilde{P}(Z; \tilde{Z}, \widetilde{Z''^2}) = \frac{\Gamma(\beta_1 + \beta_2)}{\Gamma(\beta_1)\Gamma(\beta_2)} \quad (2.74)$$

for $Z \in [0, 1]$ where \tilde{Z} denotes the mixture fraction mean value, $\widetilde{Z''^2} = \widetilde{Z^2} - \tilde{Z}^2$ its sub-grid scale variance, Γ the gamma function and the parameters β_1 and β_2 are defined as

$$\beta_1 = \tilde{Z} \left[\frac{\tilde{Z}(1 - \tilde{Z})}{\widetilde{Z''^2}} \right] \quad \text{and} \quad \beta_2 = (1 - \tilde{Z}) \left[\frac{\tilde{Z}(1 - \tilde{Z})}{\widetilde{Z''^2}} \right] \quad (2.75)$$

where the normalized variance

$$\widetilde{Z''^2}^N = \left[\frac{\tilde{Z}(1 - \tilde{Z})}{\widetilde{Z''^2}} \right]^{-1} \quad (2.76)$$

is used as request parameter for the look-up table. For the FDFs of C and χ_{st} , a δ -function is utilized within this thesis.

The explanation given above is applied for the FPV approach as well under the assumption, that the statistical treatment of Z_{Bilger} is chosen in analogy to that of the mixture fraction Z and the composed progress variable is approximated by a δ -function, too. Furthermore, a delta function is also assumed as FDF for the parameter θ when the NLVLNF is used to construct the FPV FLUT.

2.2.6 Summary of applied tabulation strategies

In summary, two tabulation approaches are considered within this thesis. First, the FPV approach is used to simulate a statistically steady flame incorporating differential diffusion. In this approach, the flamelet models used to construct the FLUT are varied by adjusting how they treat differential diffusion, resulting in a different set of request parameters for the look-up table. Second, to simulate the spray flame, the UFPV approach and the newly introduced UFCPV approach are applied. In both approaches, unsteady igniting flamelets are used to build the FLUT considering a Lewis number of unity. Their main difference lies in the description of the progress variable. Furthermore, the look-up table incorporating the complete set of solutions also stemming from the unstable branch, see Figure 2.2, is compared with a FLUT, where only igniting solutions up to the stable solutions are incorporated into the UFPV approach. In Table 2.1, the tabulation strategies used are summarized based on the equation to be solved, the transport model

utilized, the resulting set of request parameters and the flame for which the model is applied for and the corresponding section.

Table 2.1: Overview of applied tabulation strategies

| Approach | Flamelet model | Solutions | Initial conditions | Request parameter | Application | Sec. |
|----------|----------------|--------------------|---------------------------------------|---|---------------------|------|
| FPV | ULNF | steady (stable) | - | $\tilde{Z}_{\text{Bilger}}, \widetilde{Z''^2}_{\text{Bilger}}^N, \tilde{C}$ | Jet flame [63] | 3 |
| | VLNF | | | $\tilde{Z}_{\text{Bilger}}, \widetilde{Z''^2}_{\text{Bilger}}^N, \tilde{C}$ | | |
| | NLVLNF | | | $\tilde{Z}_{\text{Bilger}}, \widetilde{Z''^2}_{\text{Bilger}}^N, \tilde{C}, \theta$ | | |
| UFPV | ULNF | unsteady | adiabatic mixing + unstable steady | $\tilde{Z}, \widetilde{Z''^2}^N, \tilde{C}, \tilde{\chi}_{st}$ | Spray flame [72] | 4 |
| UFPV | | unsteady | adiabatic mixing | $\tilde{Z}, \widetilde{Z''^2}^N, \tilde{C}, \tilde{\chi}_{st}$ | | |
| UFCPV | | unsteady | adiabatic mixing | $\tilde{Z}, \widetilde{Z''^2}^N, \tilde{C}, \tilde{\chi}_{st}$ | | |

2.2.7 Flamelet-UFCPV coupling

The solution of the flamelet equations for species and temperature involves a so-called full transport and chemistry (FTC) solution. However, the thermo-chemical state within a flamelet solution can also be retrieved from a FLUT based on their request parameters. Since Z denotes the coordinate in the flamelet equations and χ_{st} is a prescribed parameter to obtain $\chi(Z)$ by means of Eq. (2.56), only the progress variable Y_C has to be determined in the case of the UFPV approach, or the progress variables $Y_{C,1}$ and $Y_{C,2}$ in the case of the UFCPV approach have to be determined. For this purpose, the transformation rules given by Eq. (2.50) are applied to transform Eq. (2.59) written in terms of each $Y_{C,i}$ with $i \in [1, 2]$ leading to

$$\rho \frac{\partial Y_{C,i}}{\partial \tau} - \rho \frac{\chi}{2} \frac{\partial^2 Y_{C,i}}{\partial Z^2} = \dot{\omega}_{Y_{C,i}}, \quad (2.77)$$

where a Lewis number of unity is assumed for all species. The density and progress variable source terms are retrieved from the FLUT, to solve the Eq. (2.77). This approach is used in Section 4.4, to verify the UFPV and UFCPV FLUT prior to their application in the coupled 3D spray simulation.

2.2.8 LES-FPV coupling

To couple the FPV approach to the LES, the determination of the Favre-filtered request parameter $\tilde{Z}_{\text{Bilger}}$, its variance $\widetilde{Z''^2}_{\text{Bilger}}$ and the progress variable \tilde{Y}_C have to be evaluated. Therefore, transport equations are

solved for the filtered mass fraction of the species obtained by means of the Raman measurements [63]. This especially ensures a consistent comparison in the *prior* analysis described in Section 3.3. Their transport equations are derived in line with the filtered set of equations Eqs. (2.32)-(2.34) while also applying the mixture averaged diffusion approach for the diffusion velocity and closing the sub-grid scale flux by applying the gradient flux assumption, leading to

$$\frac{\partial \bar{\rho} \tilde{Y}_k}{\partial t} + \frac{\partial \bar{\rho} \tilde{u}_j \tilde{Y}_k}{\partial x_j} = \frac{\partial}{\partial x_j} \left[\bar{\rho} \left(\tilde{D}_{Y_k} + \frac{\nu_{\text{SGS}}}{\text{Sc}_{\text{SGS}}} \right) \left(\frac{\partial \tilde{Y}_k}{\partial x_j} \right) \right] + \bar{\omega}_{Y_k} \quad (2.78)$$

with $k \in [\text{CH}_4, \text{O}_2, \text{H}_2, \text{H}_2\text{O}, \text{CO}, \text{CO}_2]$. The diffusion coefficients D_{Y_k} are obtained from the thermal conductivity and single species Lewis numbers by $\tilde{D}_{Y_k} = \tilde{a} / \tilde{Le}_{Y_k}$ which are retrieved from the FLUT to consistently incorporate the effect of differential diffusion. Note that this approach is only used within the simulation of the gaseous jet flame, hence no source terms due to evaporation are incorporated. Sc_{SGS} denotes a model constant that is analogous to Pr_{SGS} in Eq. (2.41) and is set accordingly to 0.4 [138, 139]. From the solution of the species mass fractions, $\tilde{Z}_{\text{Bilger}}$ is evaluated in line with Eq. (2.48). The variance of the Bilger mixture fraction $\tilde{Z}''^2_{\text{Bilger}}$ is obtained by an algebraic expression following Pierce and Moin [46] based on the assumption of local homogeneity and equilibrium of the non-resolved scales given by

$$\tilde{Z}''^2_{\text{Bilger}} = C_{\tilde{Z}''^2_{\text{Bilger}}} \Delta^2 \left| \frac{\partial \tilde{Z}_{\text{Bilger}}}{\partial x_j} \right|^2 \quad (2.79)$$

where the model constant is set to $C_{\tilde{Z}''^2_{\text{Bilger}}} = 0.13$ following [50, 51]. Furthermore, the solution of the Favre-filtered mass fraction of H_2O obtained by means of Eq. (2.78), is directly used to calculate the progress variable, i.e. $\tilde{Y}_C = \tilde{Y}_{\text{H}_2\text{O}}$.

The utilization of the NLVLNF flamelet model furthermore requires the estimation of the parameter θ in equation Eq. (2.55) which depends on the turbulent diffusivity D_t . In the RANS simulation context, for which the model was originally developed, this parameter is directly obtainable from the turbulence model. It should be kept in mind that the flamelet concept requires turbulent eddies not to disturb the thin reaction zone. Hence, not all scales of turbulent motion affect species diffusion. Furthermore, using mean flow field information in accordance with RANS would require the sampling of instantaneous realizations and their statistical evaluation within the LES. Hence, the needed information needed is not available during the first phase of the simulation, introducing additional errors. To evaluate the potential of the NLVLNF model, the best possible fit of the parameter θ is thus evaluated based on the *prior* analysis with details given in Section 3.3. For each measurement height above the burner x , a value of θ is obtained which best fits the experimental data $\theta(Z_{\text{Bilger}}, x) = \theta^{\text{opt}}(Z_{\text{Bilger}}, x)$. This value is stored in a separate look-up table and then interpolated between different downstream locations within the coupled simulation.

In Figure 2.7, the coupling between the FPV-FLUT and the 3D-CFD for the gaseous jet flame is shown schematically.

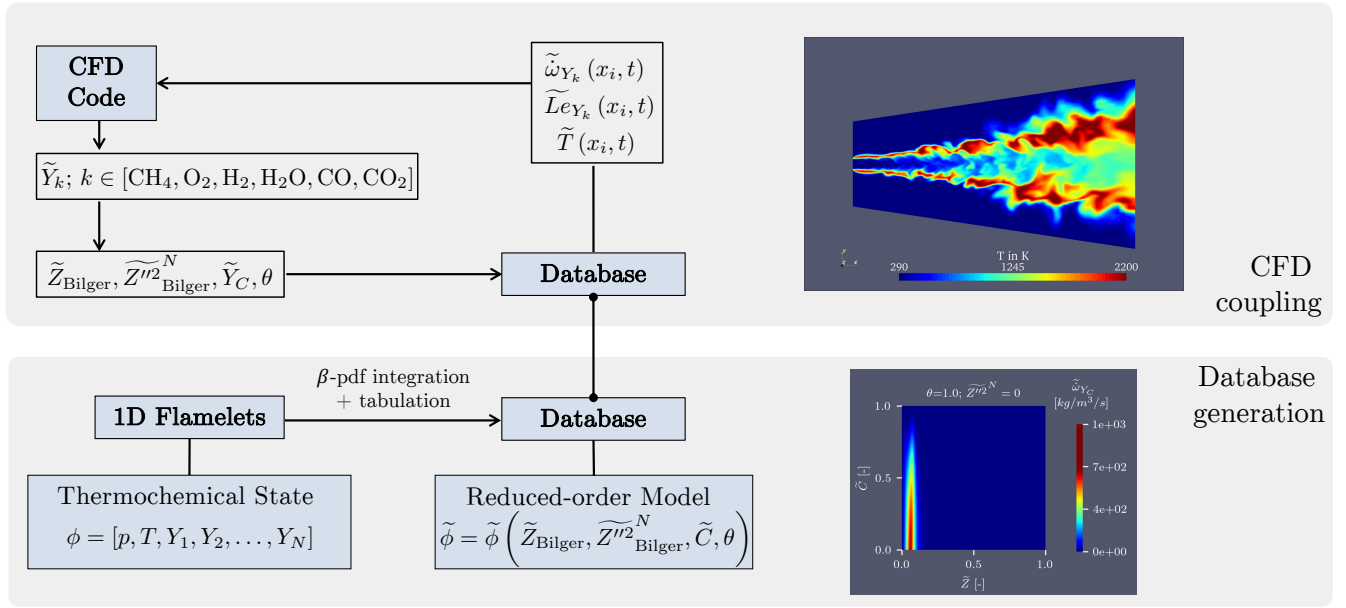


Figure 2.7: Coupling of the FPV approach to CFD for gaseous jet flame incorporating all the investigated flamelet models (ULNF, VLNF, NLVLNF). The different models are distinguished by the value of θ : ULNF: $\theta = 0$, VLNF: $\theta = 1$, NLVLNF: $\theta = \theta^{\text{opt}}$

2.2.9 LES-UFCPV coupling

As summarized in Section 2.2.6, the Favre-filtered unity Lewis number mixture fraction defined by Eq. (2.49), its variance \tilde{Z}''^2 and scalar dissipation rate at stoichiometry $\tilde{\chi}_{st}$ as well as the progress variable, are used as look-up parameters for the UFCPV approach. In addition, the two progress variables $\tilde{Y}_{C,1}$ and $\tilde{Y}_{C,2}$ have to be determined when utilizing the UFCPV approach. The transport equation for the mixture fraction and single progress variables follow from filtering the corresponding transport Eq. (2.49) under consideration of the evaporation source term \dot{S}_m and Eq. (2.59) while modeling the non-resolved fluxes again by applying the gradient flux assumption. They are given by

$$\frac{\partial \tilde{\rho} \tilde{Z}}{\partial t} + \frac{\partial \tilde{\rho} \tilde{u}_j \tilde{Z}}{\partial x_j} = \frac{\partial}{\partial x_j} \left[\tilde{\rho} \left(\tilde{D}_Z + \frac{\nu_{\text{SGS}}}{\text{Sc}_{\text{SGS}}} \right) \left(\frac{\partial \tilde{Z}}{\partial x_j} \right) \right] + \tilde{S}_m \quad (2.80)$$

$$\frac{\partial \tilde{\rho} \tilde{Y}_{C,i}}{\partial t} + \frac{\partial \tilde{\rho} \tilde{u}_j \tilde{Y}_{C,i}}{\partial x_j} = \frac{\partial}{\partial x_j} \left[\tilde{\rho} \left(\tilde{D}_{Y_{C,i}} + \frac{\nu_{\text{SGS}}}{\text{Sc}_{\text{SGS}}} \right) \left(\frac{\partial \tilde{Y}_{C,i}}{\partial x_j} \right) \right] + \tilde{\omega}_{Y_{C,i}}. \quad (2.81)$$

The variance of the mixture fraction is, in line with Eq. (2.79), obtained following [46] by

$$\tilde{Z}''^2 = C_{\tilde{Z}''^2} \Delta^2 \left| \frac{\partial \tilde{Z}}{\partial x_j} \right|^2 \quad (2.82)$$

with $C_{\widetilde{Z}''^2} = 0.13$ and $Sc_{SGS} = 0.4$ in accordance with the LES-FPV coupling. The Favre-filtered scalar dissipation rate is obtained by an algebraic relation given by [154]

$$\widetilde{\chi} = 2 \left(\widetilde{D}_Z + \frac{\nu_{SGS}}{Sc_{SGS}} \right) \left| \frac{\partial \widetilde{Z}}{\partial x_j} \right|^2 \quad (2.83)$$

From the local Favre-filtered scalar dissipation rate, the scalar dissipation rate at stoichiometric conditions used for the parameterization of the FLUT can be estimated following [155] by

$$\widetilde{\chi}_{st} = \frac{\widetilde{\chi}}{\int_{Z=0}^{Z=1} \frac{f(Z)}{f(Z_{st})} \widetilde{P}(Z) dZ}. \quad (2.84)$$

In Figure 2.8, the coupling of the UFCPV-FLUT and the 3D-CFD for spray flame simulation is shown schematically.

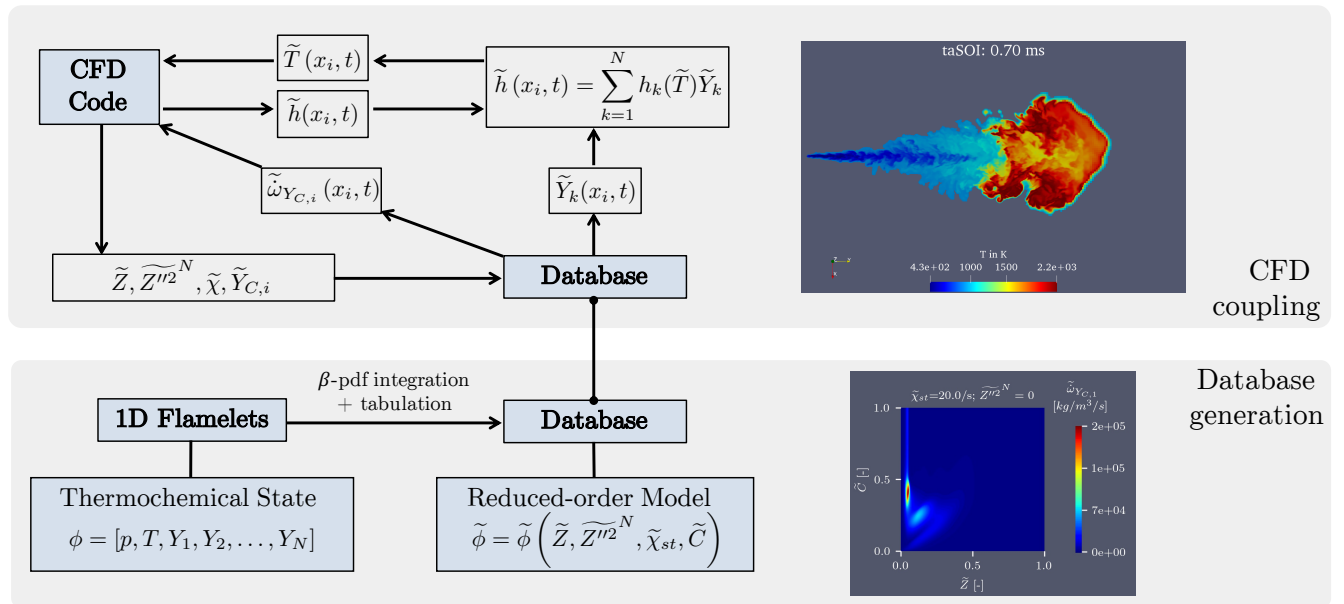


Figure 2.8: Coupling of the UFCPV approach to CFD for spray combustion. The UFCPV approach is retrieved for $Y_{C,i} = Y_C$, since only one progress variable is used in the standard approach.

2.3 Liquid phase

As mentioned in the introduction of this section, the liquid phase is modeled as a dispersed phase and approximated by an ensemble of droplets of different size, velocity and temperature among other quantities. The droplets can be expressed in terms of these quantities resulting in a number density function. This is discretized by stochastic particles. To make the simulation tractable, each of these particles represent a certain amount of droplets with the same properties. Therefore, they are denoted as parcel. To describe the

evolution of the droplets inside a parcel, single droplet models are utilized.

In line with the method described in [121, 156], the momentum for a single droplet (index, d) can be expressed as

$$\frac{du_{d,i}}{dt} = \frac{C_D \text{Re}_d}{\tau_d} \frac{1}{24} (u_{g,i} - u_{d,i}) \quad (2.85)$$

where τ_d denotes the droplet time scale given by

$$\tau_d = \frac{\rho_d d_d^2}{18\mu_g}. \quad (2.86)$$

and Re_d the droplet Reynolds Number evaluated as

$$\text{Re}_d = \frac{|\vec{u}_g - \vec{u}_d| d_d \rho_g}{\mu_g}. \quad (2.87)$$

The drag coefficient C_D is expressed as

$$C_D = \begin{cases} \frac{24}{\text{Re}_d} \left(1 + \frac{1}{6} \text{Re}_d^{2/3}\right) & \text{Re}_d < 1000 \\ 0.424 & \text{Re}_d \geq 1000 \end{cases} \quad (2.88)$$

The evolution of the droplet mass is evaluated from

$$\frac{dm_d}{dt} = -\dot{m}_d \quad (2.89)$$

where the mass flux from gas to liquid phase due to phase change \dot{m}_d is given by

$$\dot{m}_d = 2\pi r_d \frac{\lambda_g}{c_{p,g}} \text{Nu} \ln(1 + B_m). \quad (2.90)$$

The Spalding mass number B_m is defined for the fuel species f by

$$B_m = \frac{Y_f^s - Y_f^\infty}{1 - Y_f^s} \quad (2.91)$$

where the superscript s describes the surface of the droplet (but in the gas phase) and ∞ means the mass fraction of the fuel species f in large distance to the droplet. The Nusselt number Nu is obtained by the Ranz-Marshall [157] correlation as

$$\text{Nu} = 2 + 0.6\text{Re}^{1/2}\text{Pr}^{1/3}. \quad (2.92)$$

The material properties needed to close Eqs. (2.90) - (2.92), i.e. the Prandtl number $\text{Pr} = (\nu_g \rho_g c_{p,g}) / \lambda_g$, ν_g , ρ_g , and $c_{p,g}$ are evaluated as described in Section 2.1.2 based on an effective thermo-chemical reference state in the gas phase adjacent to the droplet. Here, the 1/3-rule [158] is utilized leading to

$$Y_i^{\text{ref}} = Y_i^s + \frac{1}{3} (Y_i^\infty - Y_i^s) \quad (2.93)$$

$$T^{\text{ref}} = T^s + \frac{1}{3} (T^\infty - T^s) \quad (2.94)$$

as the reference quantities for the property estimation. The temperature of the droplet surface is derived from an energy balance at the droplet incorporating the heat of vaporization as well as heat transfer processes at the droplet surface. Subsequent to the evaluation of the relations shown above during a time step of the gas phase Δt_g the source terms needed to solve the gas phase conservation equations Eqs. (2.32) - (2.34) are evaluated based on the old and new state of the $N_{d,q}$ droplets represented by the parcel q by

$$\bar{\dot{S}}_m = \sum_{q=0}^Q N_{d,q} \frac{m_{d,q}^{\text{new}} - m_{d,q}^{\text{old}}}{V_{\text{cell}} \Delta t_g} \quad (2.95)$$

$$\bar{\dot{S}}_{u,i} = \sum_{q=0}^Q N_{d,q} \frac{(u_{d,q,i} m_{d,q})^{\text{new}} - (u_{d,q,i} m_{d,q})^{\text{old}}}{V_{\text{cell}} \Delta t_g} \quad (2.96)$$

$$\bar{\dot{S}}_{h_t} = \sum_{q=0}^Q N_{d,q} \frac{\left((h_{d,q} + 0.5u_{d,q,i}^2) m_{d,q} \right)^{\text{new}} - \left((h_{d,q} + 0.5u_{d,q,i}^2) m_{d,q} \right)^{\text{old}}}{V_{\text{cell}} \Delta t_g} \quad (2.97)$$

where Q denotes the number of parcel in the corresponding gas phase cell.

During the injection of a parcel, the droplet size has to be described. This is set within this thesis in line with the so-called blob-method [159, 160] to the diameter of the nozzle. The primary and secondary break-up processes are modelled by means of the KH-RT break-up model [159]. This model relates the break-up of the droplets to Kelvin-Helmholtz (KH) and Rayleigh-Taylor (RT) instabilities in a competitive manner. It defines perturbation growth rates and wavelengths to estimate the time, at which break-up occurs and the new droplet size with details given in [70]. As it is common for most break-up models, a set of parameters has to be prescribed. These have to be adapted for the case under consideration. The values chosen for the sprays investigated in this thesis are given in Section 4.1.1 in the context of their numerical model description.

2.4 Numerical framework

The code infrastructure for numerical combustion modeling utilized within this thesis is developed in the group of Prof. Dr.-Ing. Christian Hasse and is presented in a similar manner previously in [161]. The solutions of the one-dimensional flamelet equations were conducted with the universal laminar flame solver (ULF) [162]. This object-oriented C++ code uses the finite difference method (FDM) for the spatial discretization of the flamelet equations presented in Section 2.2.2. For the solution of the steady flamelet equation within the FPV approach, a hybrid damped Newton method [163] is utilized. Details concerning its implementation in the ULF are given in [164, 165]. The solution of the unsteady flamelet equations are integrated with a differential algebraic equation (DAE) solver presented in [166]. For the evaluation of the thermodynamic and transport data, see Section 2.1.2, the software package `cantera` [167] is used which is available as third party library in the ULF. For the evaluation of transport properties, the software package `EGLib` [126, 168] is additionally available in the ULF. It is used for the solution of the steady flamelet equations incorporating differential diffusion. The collection of the flamelet solutions in the look-up table is performed with the in-house python framework `pyFLUT`. The retrieval of the data from the FLUT is performed with the corresponding ULF extension. They are used either in the one-dimensional flamelet simulation with the flamelet-UFCPV coupling (Section 2.2.7), in the 3D LES-FPV coupling (Section 2.2.8) or LES-UFCPV coupling (Section 2.2.9), respectively. For the 3D Large Eddy Simulations, the open-source C++ code `OpenFOAM` is utilized in this thesis. The implementation of the LES-FPV coupling was successfully applied in [1, 50–52, 169] previously. The LES-UFCPV coupling for spray combustion is based on this approach and validated in Section 4 of this thesis. Note, that the simulation results of the gaseous jet flame using the LES-FPV approach (see Section 3) were performed in version 2.1.x of `OpenFOAM`, while the spray simulation results, presented in Section 4, utilizing the LES-UFCPV coupling are performed in version v2012. The retrieval of the flame-structure from the FLUT are performed using the `flameletConfig` library [152]. It is written in C and uses a memory map (MMAP) technique for efficient memory management.

3 FPV modeling of differential diffusion in gaseous H₂/CH₄-Oxy-Fuel flame¹¹

3.1 Experimental configuration

The oxy-fuel flame investigated within this work is the flame B1 from the flame series experimentally investigated in [63]. The series used non-piloted, non-premixed turbulent oxy-fuel flames. The Damköhler number of all flames, evaluated with the mean jet time scale and the chemical time scale calculated following [153], was found to be greater than 1. The chosen flame is configuration B1 which was found to be fully burning and attached to the nozzle. The burner consists of two concentric tubes placed in a wind tunnel with a cross-section of 250 mm × 250 mm. The oxidizer flows through the outer tube with an inner diameter of 96.5 mm, and the fuel enters through the inner tube with a diameter of 5 mm and 0.5 mm wall thickness. The oxidizer is composed of 32 vol-% O₂ and 68 vol-% CO₂, whereas the fuel consists of 45 vol-% CH₄ and 55 vol-% H₂, which yields a stoichiometric mixture fraction of $Z_{st} = 0.0535$, evaluated from the composition in the oxidizer and fuel streams. All streams are conditioned to 294 K. The oxidizer inlet velocity is 0.622 m/s and the fuel has a fully developed turbulent inlet profile with a jet velocity of 78.6 m/s, corresponding to a Reynolds number of 12,000. The experimental data are stemming from Raman/Rayleigh measurements and include the temperature and mass fraction of O₂, CH₄, H₂, H₂O, CO₂ and CO.

3.2 Numerical setup

The numerical discretization of the flame is performed utilizing a stretched rectilinear mesh with a near-nozzle resolution of 0.025 mm and an overall mesh size of 2.3 million cells, see Figure 3.1. The length of the domain is 30 times the tube diameter to avoid an influence of the outlet boundary at the last measurement height of $x/d = 20$. The inflow boundary conditions are sampled from a pre-calculated fully developed turbulent pipe flow to ensure a proper jet spreading. An implicit second order scheme is utilized for time discretization. For spatial discretization a second order upwind stabilized CDS is used for the convective flux

¹¹This section is taken from the publication by Gierth et al. [1] which was created during the work on this thesis. In [1], I was the main author of the extracted parts beside the evaluation of the Wasserstein metric, which was performed by my Co-author Hao Wu

in the momentum equation and a TVD scheme utilizing the Sweby limiter [170] is used for the discretization of the convective scalar fluxes.

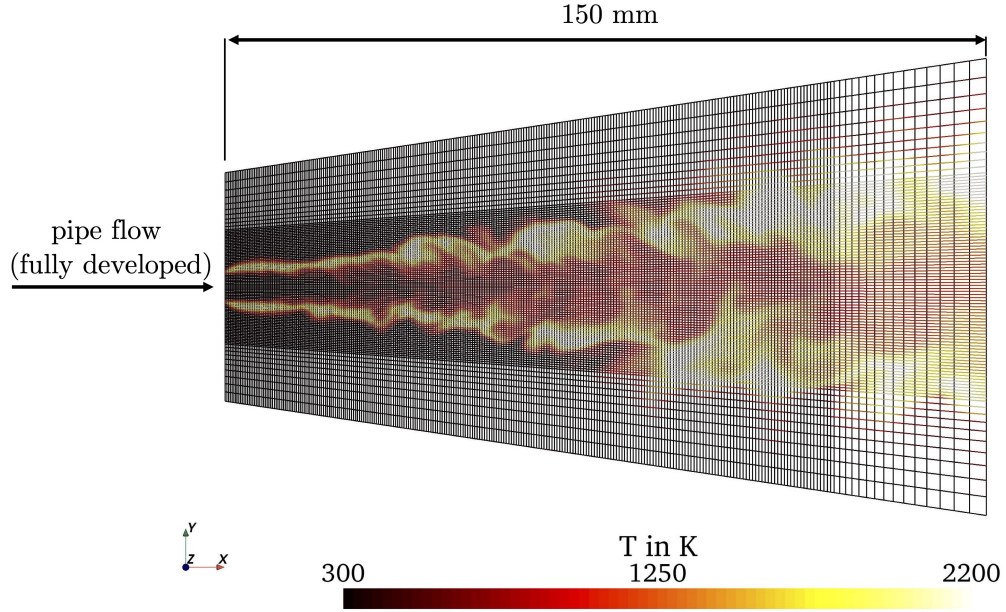


Figure 3.1: Mesh utilized for the simulation of the turbulent jet flame [63] colored by the temperature.

3.3 Evaluation procedure

Before evaluating the presented tabulation approaches within the coupled 3D-Simulation, it is beneficial to evaluate them in a pre-evaluation step. For this, the input data of the FLUTs are evaluated directly from the experimental or numerical reference data and the retrieved thermo-chemical state ϕ is compared to these data again. In terms of DNS data, these procedure is denoted by the term *a-priori* analysis. However, since experimental data contain uncertainties, the evaluation based on them is denoted by *prior* analysis within this thesis. The experimentally recorded thermo-chemical state ϕ^{Exp} is expressed as a function of the flamelet parameter vector ψ obtained by the experimental data. This is denoted by

$$\phi^{\text{Exp}}(\psi^{\text{Exp}}). \quad (3.1)$$

The numerical thermo-chemical state is retrieved from the flamelet look-up tables and are labeled with the diffusion model, e.g. ϕ^{ULNF} . The flamelet parameter vector is model-dependent. Due to the parameterization of the flamelet look-up tables by Z_{Bilger} , see Section 2.2.4, and $Y_C = Y_{\text{H}_2\text{O}}$ all of its entries can be obtained from the experimental Raman/Rayleigh data for the ULNF and VLNF model. With this,

$$\psi^{\text{ULNF}} = \psi^{\text{VLNF}} = \psi^{\text{Exp}} = (Z_{\text{Bilger}}^{\text{Exp}}, Y_C^{\text{Exp}}) \quad (3.2)$$

is used for the *prior* analysis. Hence, the thermo-chemical states

$$\phi^{\text{ULNF}}(\psi^{\text{Exp}}) \quad (3.3)$$

and

$$\phi^{\text{VLNF}}(\psi^{\text{Exp}}) \quad (3.4)$$

are compared with ϕ^{Exp} . For the NLVLNF model, the flamelet parameter vector also contains the parameter θ . Since this parameter cannot be determined from the experimental Raman/Rayleigh data directly, an optimization based on the error definition

$$E(\psi^{\text{Exp}}, \theta) = \frac{1}{N} \sum_{k=1}^N w_k \left| Y_k^{\text{Exp}}(\psi^{\text{Exp}}) - Y_k^{\text{NLVLNF}}(\psi^{\text{Exp}}, \theta) \right| \quad (3.5)$$

is performed for every experimental data point. Here, k denotes the species index and w_k the factor weighting the difference between experimentally and numerically obtained mass fraction of species k . The choice of w_k is arbitrary and the values used are reported in the corresponding chapters. The optimization is aimed at obtaining the value of θ where E shows a minimum. By denoting this value as θ^{opt} the problem can be expressed as

$$\theta^{\text{opt}} = \underset{\theta \in [0,1]}{\text{argmin}} E(\theta). \quad (3.6)$$

This problem is solved by means of a sequential search. By this means, the thermo-chemical state used for the evaluation of the NLVLNF in the *prior* analysis is defined as

$$\phi^{\text{NLVLNF}}(\psi^{\text{Exp}}, \theta^{\text{opt}}). \quad (3.7)$$

This complete flamelet parameter vector evaluated from experiments allows for the comparison of the measured and simulated quantities. To this end, each data point $(Z_{\text{Bilger}}^{\text{Exp}}, Y_C^{\text{Exp}})$ is used to perform a look-up from the flamelet manifold resulting in a scatter plot for each considered quantity. For convenience, the averages conditioned on Bilger mixture fraction are calculated for the experimental and numerical quantity and shown in the corresponding plots. Beside the comparisons of the temperature and the single species mass fractions, the differential diffusion parameter Z_{HC} based on the element mixture fractions of hydrogen and carbon as reported in [63] is incorporated in the comparison. It is defined as [171]

$$Z_{\text{HC}} = Z_{\text{H}} - Z_{\text{C}} = \frac{Y_{\text{H}} - Y_{\text{H},1}}{Y_{\text{H},2} - Y_{\text{H},1}} - \frac{Y_{\text{C}} - Y_{\text{C},1}}{Y_{\text{C},2} - Y_{\text{C},1}} \quad (3.8)$$

with indices 1 and 2 denoting the fuel and oxidizer stream, respectively. In case of unity Lewis number for all species, $Z_{\text{HC}} = 0$. Otherwise, its value quantifies the extent of differential diffusion.

The comparison between experimental and numerical results for the aforementioned models is further quantified by use of the Wasserstein metric [172]. The Wasserstein metric is a distance function defined

between probability distributions. It measures the dissimilarity between two distributions by considering the minimal effort required to transform one to the other, which is the solution to the optimal transport problem. The 2nd Wasserstein metric between discrete distributions $f(x)$ and $g(y)$ is defined as the p^{th} root of the optimal transport cost:

$$W_2(f, g) = \min_{\Gamma} \left(\sum_{i=1}^n \sum_{j=1}^{n'} \gamma_{ij} |x_i - y_j|^2 \right)^{1/2} \quad (3.9)$$

subject to $\sum_{j=1}^{n'} \gamma_{ij} = f_i$, $\sum_{i=1}^n \gamma_{ij} = g_j$, $\gamma_{ij} \geq 0$.

where $\Gamma = (\gamma_{ij})_{i=1\dots n; j=1\dots n'}$ represents the $n \times n'$ transport matrix, of which each entry γ_{ij} denotes the weight transported from x_i to y_j . Especially, the entries of the matrix Γ leading to the minimal overall distance between x_i and y_j in terms of the defined metric have to be found, additionally fulfilling the constraints given in Eq. (3.9). The distribution functions $f(x)$ and $g(y)$ are not known from the dataset itself, since only a distinct number (i.e. n and n') of samples are given. Therefore, empirical distributions from each given data set are constructed following the methodology presented in [173], where more details can be found.

This metric was first applied to the quantitative assessment of LES combustion models in [173]. By representing the experimental and numerical data of turbulent flames in the form of multivariate distributions, the effectiveness of the Wasserstein metric as a validation tool was demonstrated, providing an objective and quantitative evaluation of model deficiencies under consideration of boundary conditions and interscalar correlations on the simulation accuracy. In the present study, W_2 is applied to the joint distributions of H_2 , H_2O , CO_2 , CO , CH_4 , and O_2 , conditioned on the mixture fraction at different axial flow locations. The species considered are uniformly normalized by their corresponding standard deviations obtained from the experimental data. The contribution of each species to the overall Wasserstein metric is also identified. This is a direct result of interpreting each thermo-chemical scatter point as single sample x_i in the evaluation of Eq. (3.9).

3.4 Results and discussion

3.4.1 Results prior analysis

First, the experimental data are compared to all three flamelet models described in Section 2.2.2. The mean profiles of all quantities, conditioned on the Bilger mixture fraction, are presented at three different downstream locations: close to the nozzle ($x/d = 1$), at an intermediate position ($x/d = 5$) and at the farthest downstream position ($x/d = 20$). The prescribed model parameter θ , given in Eq. (2.55), is obtained using the procedure described in Section 3.3 setting $w_i = 1$ for all experimentally recorded species. The value θ^{opt} thus obtained is shown in the third column of Figure 3.2. In the reaction zone ($0 < Z < 2Z_{\text{st}}$),

high values for θ^{opt} are observed, peaking at Z_{st} . Hence, differential diffusion is accounted for in the NLVLNF model in this region. Lower values for θ^{opt} can be seen in the fuel-rich part of the flame. As the distance to the burner increases, the peak values in the reaction zone and the overall level of θ^{opt} decrease, indicating a reduced level of differential diffusion.

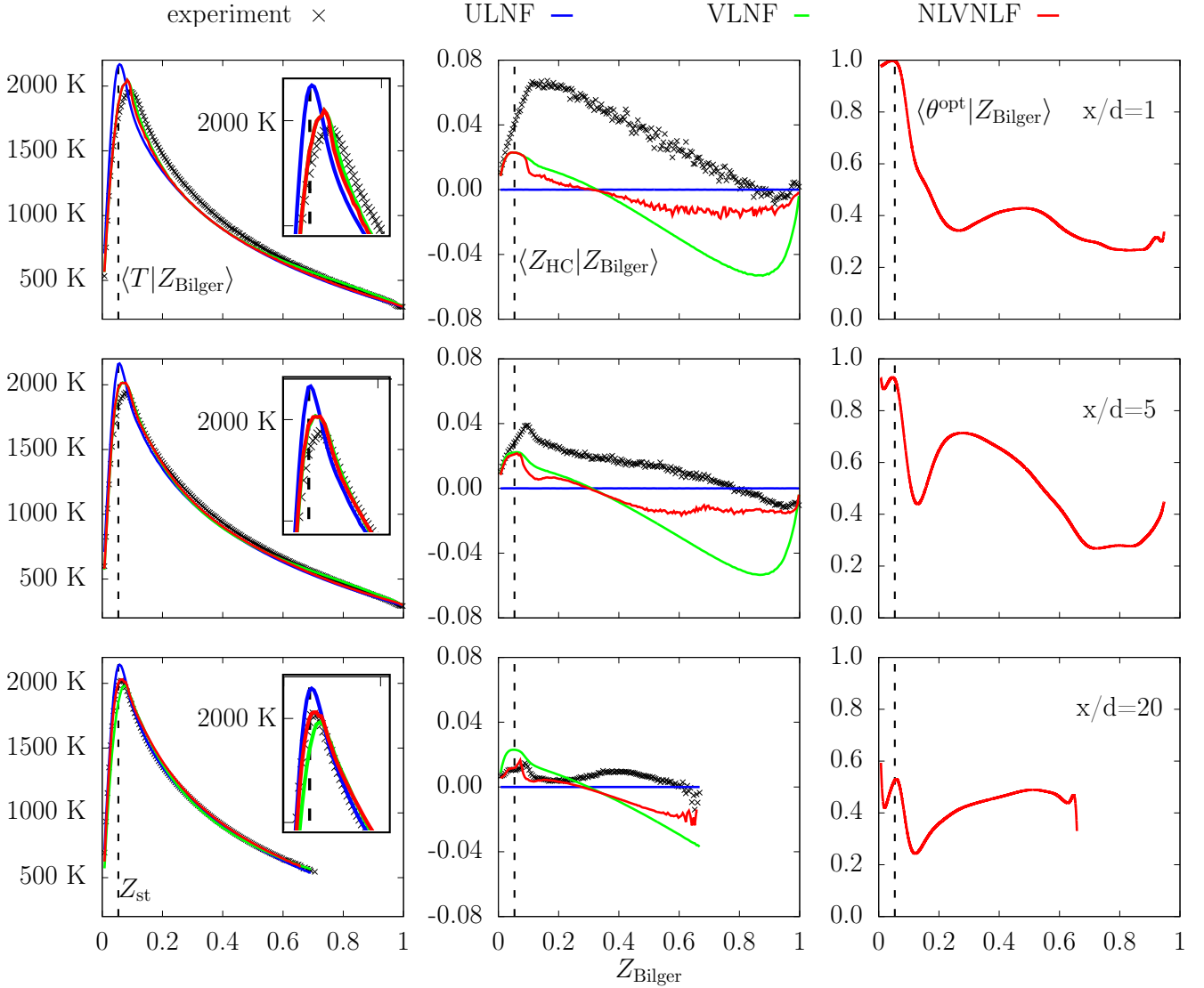


Figure 3.2: Comparison of experimental data and results of the prior analysis for the temperature T and differential diffusion parameter Z_{HC} (left and middle columns) at three experimentally recorded heights above the burner (top to bottom) using different diffusion modeling approaches. The most suitable value for the parameter θ in the NLVLNF model, optimized based on the measured Raman species, is shown in the right-hand column.

The temperature profile shown in the left part of Figure 3.2 is well reproduced in the fuel-rich part of the flame by all three models. However, pronounced differences are visible in the reaction zone. The ULNF model predicts the position of the temperature peak at Z_{st} , which is contrary to the experimental findings, and substantially overpredicts the peak value at all heights. The deviation between the ULNF

and the measured temperature data decreases further downstream, which is consistent with the reduced influence of differential diffusion. As values for θ^{opt} are close to unity in the reaction zone, the NLVLF and VLF model results are very similar and in good agreement with experimental data. Consequently, differential diffusion must be considered.

The importance of differential diffusion in the reaction zone is also supported by the experimental data for Z_{HC} shown in the middle of Figure 3.2. At $x/d = 1$, the peak in the reaction zone indicates large differential diffusion effects followed by a constant decrease in the rich part of the flame towards unity Lewis number behavior. By definition, the ULNF model predicts a value of $Z_{\text{HC}} = 0$ and therefore cannot reproduce the experimental Z_{HC} profile. In contrast, the VLF model is able to reproduce the behavior in the reaction zone, although the peak value is underestimated. Furthermore, the VLF model shows negative values for Z_{HC} in the fuel-rich part, which is not observed in the experimental data. The NLVLF model gives similar profiles to the VLF model, but with smaller deviations in the fuel-rich part. These findings are consistent with the results in [174, 175], where an overall improvement compared to the ULNF model was obtained by using the NLVLF model, but differences remain for the differential diffusion parameter. The decrease of Z_{HC} with increasing distance to the burner leads to reasonable agreement for the NLVLF model over a wide mixture fraction range at $x/d = 20$, showing the need of incorporating differential diffusion, but with a reduced amount as suggested by the VLF model, there.

The applicability of the models is further quantified through the use of the Wasserstein metric W_2 , which is shown in Figure 3.3. This metric considers the correlations among species by evaluating the deviation between their joint distributions calculated from experiments and simulations, respectively. Particularly, the contribution of each species to the overall deviation can be identified. This provides insights in the effect of differential diffusion on the single species profiles and quantifies the overall species deviation. The lowest overall error at Z_{st} is observed for the VLF model, whereas the ULNF model performs best in the fuel-rich part of the flame. In the intermediate range, a minimum and maximum in the profiles are obtained, followed by an increase in the error for the VLF model and a decrease for the ULNF model. This, again, confirms the reduced amount of differential diffusion in the fuel-rich part of the flame. The results also reveal that the main error contribution in the case of the ULNF and VLF models arises from discrepancies in the CO and H₂O mass fractions, which, dependent on the diffusive-transport model and axial location, occur at different mixture-compositions in the flame. Depending on the axial location, the NLVLF model minimizes this error by introducing an additional parameter enabling the transition from one transport model to the other. This is particularly evident for the axial locations of $x/d = 5$ and $x/d = 20$.

The species profiles of H₂, CO₂ and CO are shown in Figure 3.4, with overall good agreement for the NLVLF approach, which is consistent with the results in [174, 175]. However, the authors obtained larger differences in the CO₂ and CO profiles than those found in the present *prior* analysis. This is attributed to the zero deviation in the flamelet parameters used in the *prior* analysis, which is not ensured in the fully coupled RANS simulation in [174, 175]. However, not all species follow this trend. In particular, the H₂O profile also shown in Figure 3.4 is reproduced accurately by the VLF model throughout the entire mixture fraction range and at all downstream positions. For this model, the H₂ profile shows large deviations

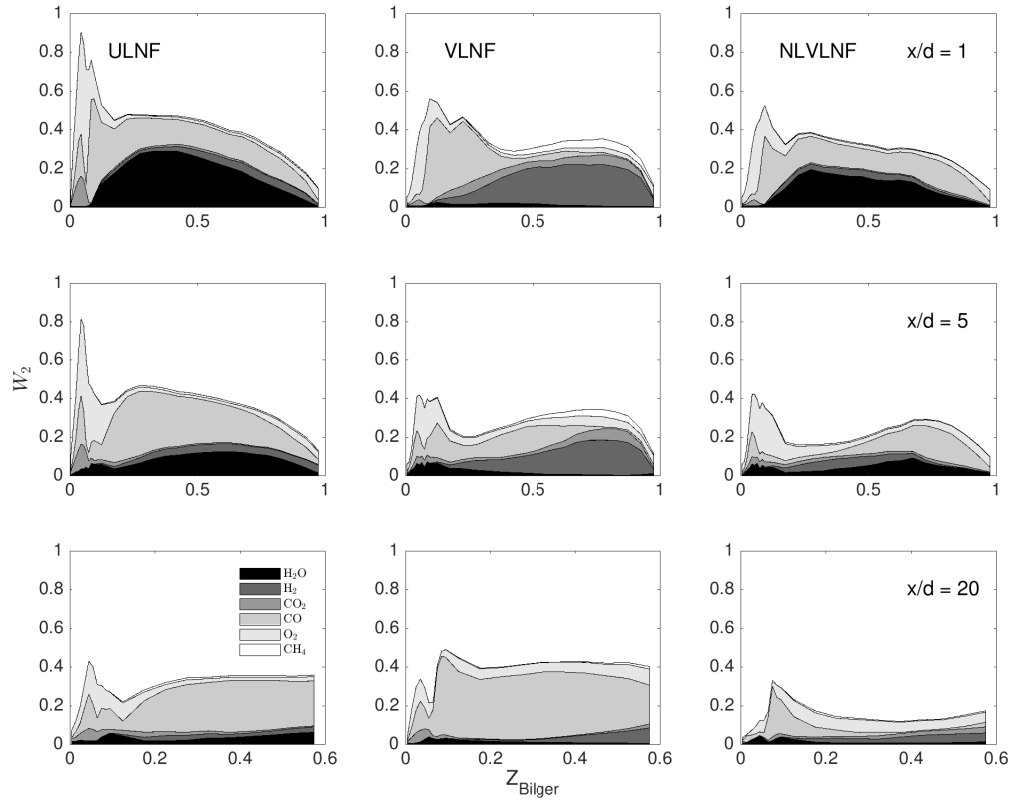


Figure 3.3: Comparison Wasserstein metric W_2 evaluated based on results of ULNF, VLNF and NLVLNF (left to right) for downstream locations of $x/d = 1$, $x/d = 5$ and $x/d = 20$ (top to bottom)

corresponding to large deviations in the CH_4 profile, which is not shown for brevity. However, H_2O is significantly underestimated when applying the ULNF approach. This was also noted, although not explicitly mentioned, by Sevault *et al.* [63] when comparing their experimental data with results from opposed-flow diffusion flame calculations with and without considering differential diffusion. Furthermore, Garmory and Mastorakos [176] underestimated H_2O when applying a unity Lewis number assumption within their CMC approach. The NLVLNF model also underpredicts the profile at $x/d = 1$, but slowly approaches the experimental data further downstream.

Since deficiencies exist when using a single parameter θ^{opt} optimized for all Raman species, the choice of θ is discussed next. Figure 3.5 shows the comparison of the parameter when optimized based on either H_2O or CO_2 , denoted by $\theta^{\text{opt},\text{H}_2\text{O}}$ and $\theta^{\text{opt},\text{CO}_2}$, together with the parameter optimized based on all measured Raman species ($\theta^{\text{opt},\text{all}}$). The $\theta^{\text{opt},\text{H}_2\text{O}}$ -profile approaches $\theta = 1$ very quickly, which confirms that H_2O can only be reproduced with mixture-averaged diffusion modeling throughout the entire mixture fraction range. In contrast, $\theta^{\text{opt},\text{CO}_2}$ exhibits similar behavior to $\theta^{\text{opt},\text{all}}$ but with a more significant decrease towards $\theta = 0$. It approaches unity in the reaction zone and quickly decreases in the fuel-rich zone. $\theta^{\text{opt},\text{all}}$ lies between the values of $\theta^{\text{opt},\text{H}_2\text{O}}$ and $\theta^{\text{opt},\text{CO}_2}$ in the fuel-rich part of the flame.

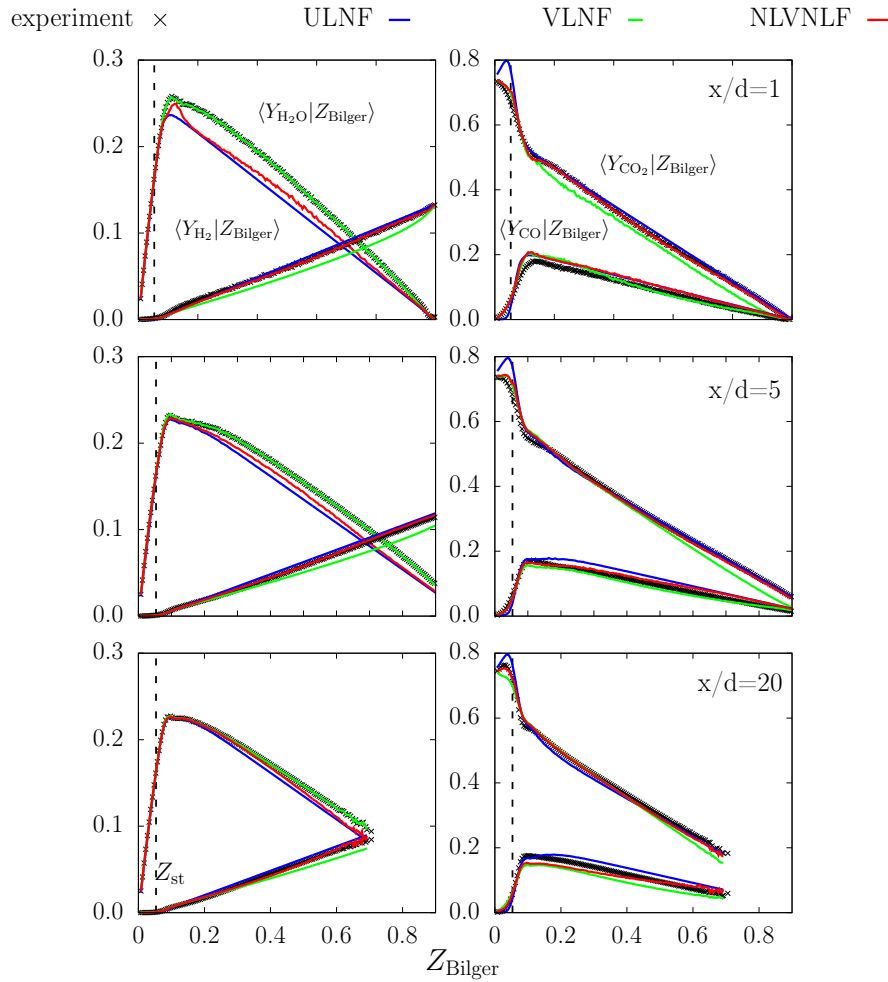


Figure 3.4: Comparison of experimental data and results of the prior analysis using three different diffusion modeling approaches for the species mass fractions of H_2O and H_2 (left column) as well as CO_2 and CO (right column) at three experimentally recorded heights above the burner.

In summary, the *prior* analysis is consistent with the findings in [63]. Differential diffusion is strong in the reaction zone, whereas unity Lewis number behavior can be observed in the fuel-rich region of the flame. Generally, differential diffusion decreases further downstream. Moreover, the analysis shows that the differential diffusion parameter is extremely sensitive with respect to measurement uncertainties, which makes an additional comparison with other parameters and single species profiles useful. As a general result, the VLNF model captures the H_2O profile and the reaction zone profiles of most species, whereas the ULNF model captures the development in the fuel-rich part. The NLVNLN model gives the best overall agreement and captures the downstream development. However, from the details shown in Figure 3.5, the NLVNLN is a compromise for all species considered, since they are affected by differential diffusion in different ways. A *prior* analysis as shown here can reveal such differences between the species, which might not be visible in a fully coupled simulation.

These results show that none of the tested flamelet models is able to capture the behavior related to diffusion

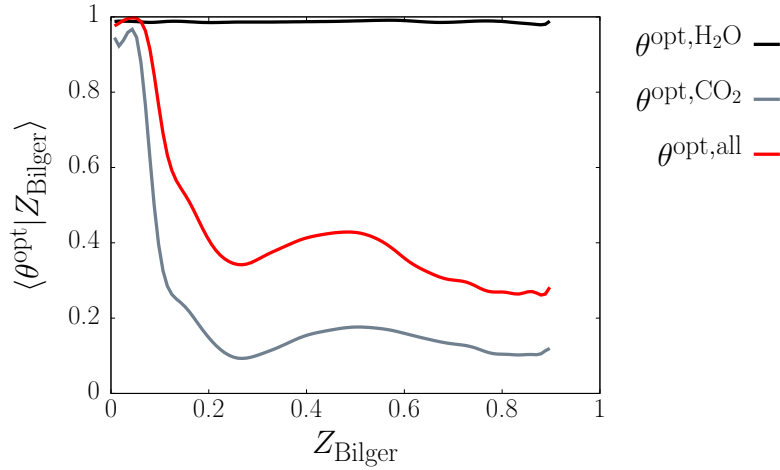


Figure 3.5: Comparison of profiles for θ^{opt} optimized based on H_2O ($\theta^{\text{opt}, \text{H}_2\text{O}}$) or CO_2 ($\theta^{\text{opt}, \text{CO}_2}$) with optimization based on all experimentally recorded Raman species ($\theta^{\text{opt}, \text{all}}$) at $x/d = 1$

in the flame considered. As a consequence, these discrepancies can be expected to influence the fully coupled LES. This is quantified in the following Section.

3.4.2 Coupled LES

In contrast to the *prior* analysis, the results obtained in the LES are additionally influenced by the pre-computed flame structures through the tabulated transport properties and source terms from the manifolds and all data are additionally FDF-integrated. This, in turn, changes the profiles of mixture fraction and progress variable which are used for the flamelet table request; hence, already these quantities differ between *prior* analysis and LES. Consequently, the applicability of the flamelet models in the LES will be investigated in the following in an *a posteriori* analysis. The influence of turbulent transport on the flame structure is further analyzed by performing a comparison between the tabulated major species and species resulting from the solution of transport equations, as discussed in Section 2.2.8. Since the evaluation of the parameter θ of the NLVNF model in LES would introduce more uncertainties as discussed in Section 2.2.8, $\theta = \theta^{\text{opt}}$ is used taken from the *prior* analysis in order to evaluate the model's capability. This also takes into account the downstream development of this parameter. Note that utilizing θ increases the manifold by considering the local turbulence level. However, it fails to incorporate history effects. To facilitate a direct comparison between the experiment, the *prior* analysis and the coupled simulation, mean values conditioned on the Bilger mixture fraction are compared. In the following, all results are shown at the downstream location $x/d = 5$, comparing experimental data with LES results.

Figure 3.6 shows the results for the tabulated temperature and the species mass fractions of H_2O , H_2 , CO_2 and CO ; note that H_2O corresponds to the progress variable. From the left column of this figure, reasonable agreement of H_2O in the reaction zone, *i.e.* $Z_{\text{Bilger}} < 0.1$, can be obtained for the VLNF model. This is in line with the *prior* analysis. However, an underestimation of H_2O is observed when the VLNF model is used in the fuel-rich part of the flame and when the ULNF or the NLVNF model are used throughout the entire mixture

fraction range. This is not as pronounced as in the *prior* analysis, see Figure 3.4. This underestimation of the progress variable has a minor effect on the H_2 mass fraction, also shown in the left column of Figure 3.6. For the latter, the VLNF model's inability to reproduce the unity Lewis number behavior in the fuel-rich part of the flame is also recovered in the LES. Other species are more affected by the underestimation of the progress variable. For CO_2 , which is shown in the middle column of Figure 3.6, a comparison of the flamelet models suggests that, in all cases, there is reasonable agreement with the experimental data in the reaction zone and, in the case of the VLNF model, also in the fuel-rich region. Hence, the underestimation of the progress variable leads to error compensation resulting in CO_2 agreeing reasonably well in the reaction zone when using the ULNF model and agreeing best when using the VLNF model. The comparison of the CO and temperature profile, see middle and right column of Figure 3.6, also shows similar agreement for all investigated models, with the VLNF model obtaining the best agreement with the experimental data and the NLVNF model performing slightly better than the ULNF model. These findings are consistent with the RANS simulation results from Han *et al.* [174, 175], confirming the improved description of the flame structure when using the NLVNF model compared to the ULNF model. In summary, the coupled LES-FPV simulations exhibit error compensation potentially leading to misinterpretation, which in turn accentuates the feasibility of the *prior* analysis to evaluate the suitability of manifold-based approaches.

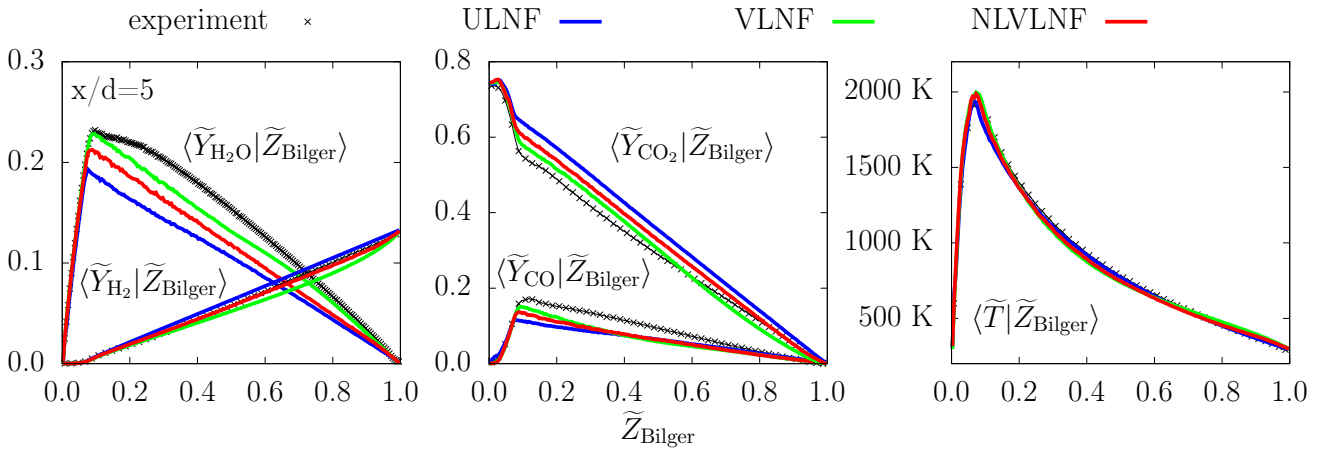


Figure 3.6: Comparison of measured on Bilger mixture fraction conditioned flame structure at downstream location $x/d = 5$ with LES results of tabulated quantities using different diffusion modeling approaches

To additionally compare tabulated and transported species mass fraction profiles, Figure 3.7 shows species profiles of CO_2 and H_2 and the differential diffusion parameter. In contrast to the tabulated species profiles, the transported species are affected only through tabulated source terms, Lewis numbers and the molecular viscosity influencing the velocity field by the manifolds. The interplay of the resolved and subfilter turbulence is directly accounted for. The comparison between the tabulated and transported species mass fractions is shown for CO_2 and H_2 using the VLNF and NLVNF models in the left column of Figure 3.7. The difference is negligible in the reaction zone. However, the transported species mass fractions exhibit a straight line in the fuel-rich part of the flame, indicating unity Lewis number behavior for both models. This leads to better agreement with the experimental data. Especially for H_2 , the transport behavior is correctly reproduced.

For CO_2 , the experimentally observed unity Lewis number transport in the fuel-rich part is also recovered. However, this does not lead to overall better agreement compared to the tabulated profiles due to the progress variable underestimation, which directly influences the species' source term. The comparison of the differential diffusion parameter Z_{HC} is shown in the right column of Figure 3.7. It is evident that the parameter calculated based on the transported species mass fractions shows much better agreement than the tabulated profiles. In particular, the unity Lewis number behavior in the fuel-rich part of the flame is recovered by all flamelet models. This is encouraging and can be considered a first step towards simulating flames with such complex diffusion phenomena. It is important to note that this approach requires the resolution of the major fraction of the turbulent structures. This can be ensured in the investigated laboratory flame with the current grid and numerical schemes due to its low Reynolds number. But it might not be guaranteed for cases with substantially higher Reynolds numbers as e.g. found in gas turbines. Further investigations are needed for these conditions.

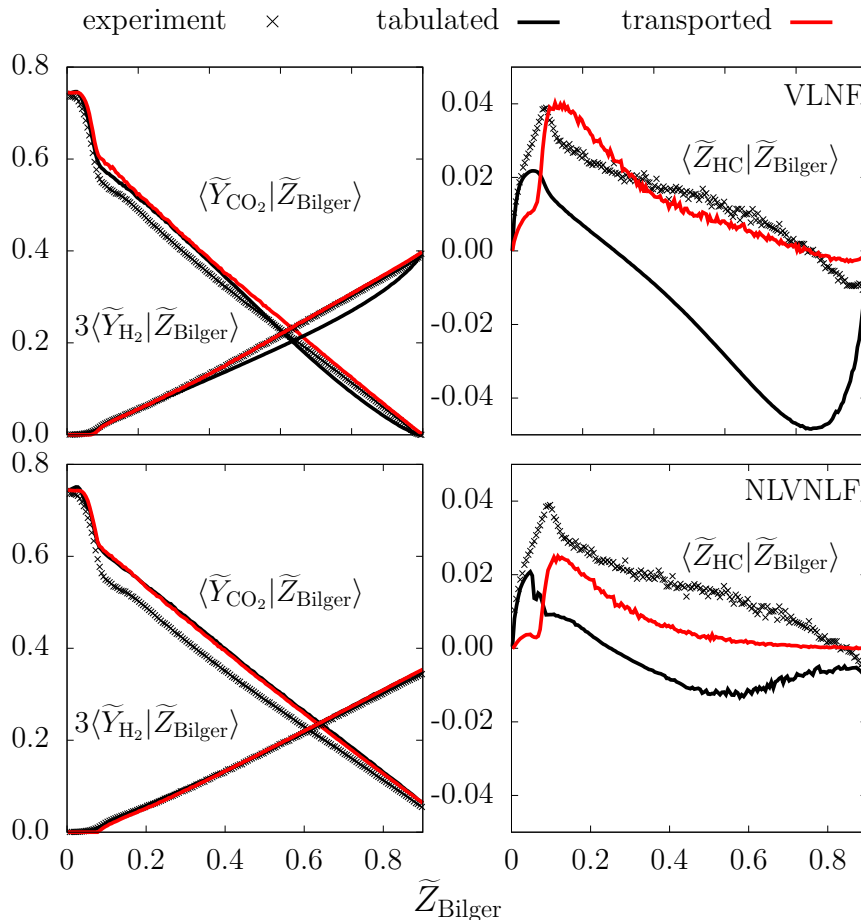


Figure 3.7: Mean values of the read-in tabulated and transported mass fractions of CO_2 and H_2 (multiplied by 3) (left) and the differential diffusion parameter Z_{HC} (right) at $x/d = 5$. All values are conditioned on the Bilger mixture fraction. The results for the VLNF model are shown in the top row and those for the NLVNLN model in the bottom row.

3.5 Summary

In this chapter, the modeling of differential diffusion effects in flamelet-based approaches is examined investigating a turbulent non-premixed oxy-fuel flame that was experimentally investigated by Sevault *et al.* [63]. The models considered are the unity Lewis number flamelet (ULNF) model, the variable Lewis number flamelet (VLNF) model and a model incorporating the influence of turbulence on variable Lewis numbers (NLVLNF). The analysis consists of two main steps: first a *prior* analysis based on experimental data is performed, and second, a fully coupled LES is carried out. In both analyses, the FPV model is applied using flamelet look-up tables that are parameterized by the Bilger mixture fraction and the progress variable. To enable a direct comparison with measured data, the Bilger mixture fraction is computed in the LES by solving transport equations for all Raman-accessible species. Comparisons are based on the experimentally recorded main species, the temperature and the differential diffusion parameter. In addition to the comparison of conditional results, discrepancies between experiments and simulations are quantified using the Wasserstein metric.

The results of the *prior* analysis can be summarized as follows:

- Differential diffusion is important in the reaction zone. This is accounted for in the VLNF model and the NLVLNF model.
- The unity Lewis number assumption is more appropriate in the fuel-rich part of the flame. This is accounted for in the ULNF model and the NLVLNF model.
- The influence of differential diffusion decreases downstream. This is only captured by the NLVLNF model.
- The NLVLNF model gives the best overall agreement, with improvements on the ULNF model and the VLNF model.
- Not all species are equally influenced by differential diffusion. This effect cannot be reproduced by any model.

The results of the LES-FPV approach can be summarized as follows:

- The best agreement for the tabulated flame structure is obtained by the VLNF model throughout the entire mixture fraction range. This is in contradiction to the findings of the *prior* analysis. Different levels of agreement are likely to be caused by error accumulation and error compensation and potentially also error amplification. Thus, the *prior* analysis is more reliable to estimate the quality of manifold-based flame structures.
- The results of the transported species and the derived parameters show an improvement with respect to tabulated profiles. Particularly, the unity Lewis number behavior in the rich part of the flame is reproduced even for the VLNF and NLVLNF models. This indicates the potential of transporting

species in fully coupled simulations to account for the interplay of differential diffusion and turbulent transport in reactive flows.

As shown in the study, the flamelet model in the applied formulation is not able to reproduce all details of the flame considered. This is mainly attributed to the competition between molecular and turbulent transport, and this balance is not captured in the considered flamelet models with sufficient accuracy.

4 UFPV and UFCPV modeling for ignition and pollutant formation in spray flames

The aim of this chapter denotes the re-examination of the UFPV approach in LES of spray flames and, based on this, the validation of the UFCPV approach used to predict ignition and pollutant formation for light- and heavy-duty applications under conditions relevant for diesel engines. The ECN Sprays A and D are chosen as reference cases in this chapter. These sprays share the same nominal operating conditions. The difference in their nozzle size, by a factor of two, makes it possible to investigate nozzle hole diameter variations.

The methodology used in this study is visualized in Figure 4.1. To gain an understanding of the ignition behavior and the retrievable thermo-chemical state under the ECN Spray A and D nominal conditions, an analysis of the underlying flamelet solutions used to generate the flamelet look-up table is performed first. In the following, an investigation based on the Lagrangian flamelet model (LFM) is performed. This model represents a single flamelet simulation with a time-varying scalar dissipation rate. Its change is chosen to include the feature of a decrease in the mean scalar dissipation rate when the vaporized fuel mixes with the surrounding gas phase. A reference solution is obtained transporting all the species mass fraction and temperature (full transport and chemistry, FTC). The results of this model stemming from the UFPV and UFCPV approaches are compared against this reference data to judge their ability to capture the ignition process and pollutant formation under a variable strain rate. Following the terminology of [177], this investigation can be classified in the context of the verification and validation procedure as follows: Since the LFM denotes a reduced order model in terms of dimensionality but still includes the processes relevant for diesel spray combustion, it is interpreted as a conceptual model of the diesel spray flame application here. The comparison of the UFPV and UFCPV solutions to the FTC reference solution of the conceptual model can hence be seen as the verification of the approaches.

The validation of the LES spray setup based on the ECN Spray A is performed subsequently, starting with the validation under non-reactive conditions to ensure that the mixture formation prior to ignition is predicted properly. This is followed by the validation of the LES-UFPV approach, incorporating the unstable steady solution of the S-curve as initial conditions in terms of mixture formation and global ignition characteristics such as the ignition delay time and lift-off length. Since this framework represents the most comprehensive approach utilized in this thesis concerning the incorporation of strain effects, it is used as a reference to investigate the influence of the $\tilde{\chi}_{st}$ distribution on the ignition behavior. In conjunction with this analysis, the need to incorporate the unstable solutions of the S-curve into the look-up table is questioned. The results of these investigations lead to the LES-UFCPV approach being used without considering the unstable

solutions of the S-curve to investigate the local flame structure of the Spray A and D from ignition to pollutant formation. This validation is based on recent 355-nm PLIF [76] and 355-nm high-speed PLIF data [178] for the Spray A. The validated model is further used to describe the spray flame evolution in mixture fraction space. Finally, the structure of the spray flame predicted by the LES-UFCPV approach is summarized including all relevant effects from injection to gaseous pollutant formation.

In line with the Spray A investigation, the validation based on the Spray D injector includes the comparison of global ignition characteristics as well as the local flame structure. For the latter so far unpublished experimental 355-nm high-speed data [179] are utilized. An investigation is also performed in mixture fraction space. The summary of the flame structure including gaseous pollutants closes this part.

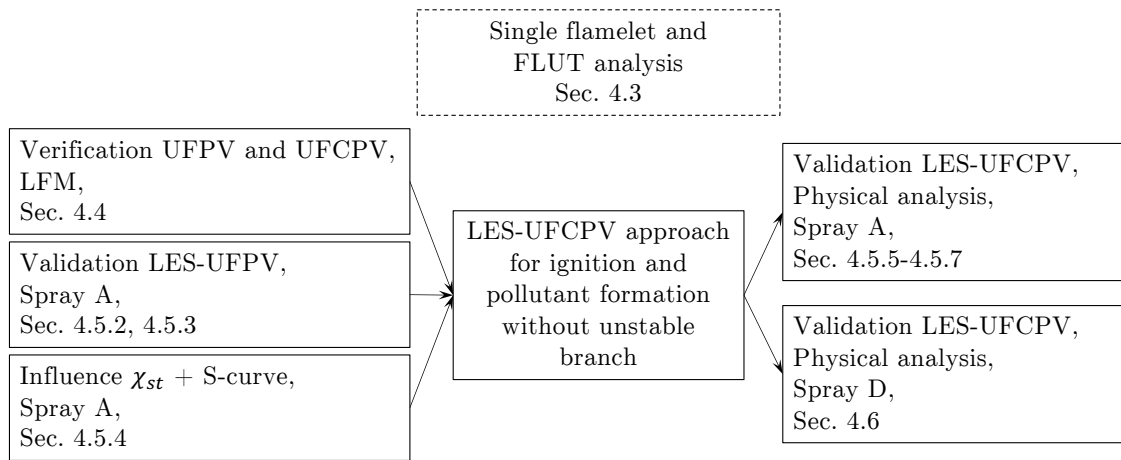


Figure 4.1: Connection between the investigations performed in Section 4.

All the investigations mentioned above are performed utilizing the detailed CRECK¹² reaction mechanism [180, 181] as it includes chemical pathways for NO and PAH species formation. However, the Spray A ignition behavior and the S-curve modeling are investigated with a reduced version as used in Sun et al. [3]. Its description is given in Section 4.2. In summary, two approaches are applied in this chapter to define the progress variable (UFPV and UFCPV approach) with and without including the transient flamelet solutions starting from the unstable branch of the S-curve and two reaction mechanisms (detailed and reduced CRECK mechanism). For the LFM, the UFPV approach is compared with the UFCPV approach based on the detailed CRECK mechanism. The overview of the ignition behavior of Spray A and the investigation of the influence of the scalar dissipation rate in the spray flame simulation is based on the UFPV approach in combination with the reduced mechanism. The results concerning the structural analysis of the spray flame to pollutant formation are based on the UFCPV approach, neglecting the unstable branch solutions and using the detailed CRECK mechanism. These combinations are summarized in Table 4.1. Furthermore, comparisons are made in terms of PAH species in the following sections. They are defined as the sum of $C_{16}H_{10}$ and $C_{18}H_{10}$ mass fractions in this thesis. The addition of $C_{18}H_{10}$ increases the extend of PAH species in mixture fraction space to more fuel-rich mixtures and is produced at larger time scales. With that, a wider range of the PAH species dynamics is incorporated compared to the inspection of $C_{16}H_{10}$ only.

¹²CRECK Modeling Lab, Department of Chemistry, Materials and Chemical Engineering “G.Natta”, Politecnico di Milano

Table 4.1: Overview of applied tabulation strategies and utilized mechanism for ignition and pollutant formation

| Approach | Initial conditions | Chem. Mechanism | Application | Section |
|---------------|---------------------------------------|-----------------|--------------------------------|--------------|
| UFPV UFCPV | adiabatic mixing | detailed CRECK | LFM | 4.4 |
| UFPV | adiabatic mixing + unstable steady | reduced CRECK | Spray A Validation LES-UFPV | 4.5.2, 4.5.3 |
| | adiabatic mixing + unstable steady | | Spray A S-curve test | 4.5.4 |
| | adiabatic mixing | | | |
| UFCPV | adiabatic mixing | detailed CRECK | Spray A flame structure | 4.5.5-4.5.7 |
| | | | Spray D | 4.6.1-4.6.5 |

The remainder of this chapter is organized as follows: In Section 4.1, a description of the test cases is given, with a numerical description of the ECN Sprays A and D being given in Section 4.1.1. The details concerning the Lagrangian flamelet model are given in Section 4.1.2. Section 4.2 describes the details of the operating conditions and the generation of the flamelet look-up table. The inspection of the FLUT is given in Section 4.3, followed by the LFM investigation in Section 4.4. Furthermore, the results for the ECN Spray A are presented in Section 4.5 and those related to the ECN Spray D in Section 4.6. In Section 4.7, a summary of this chapter is given.

4.1 Description of investigated test cases

In the following section, the test cases for the application of the UFPV and UFCPV approach are described. These include the description of the ECN Spray A and D in Section 4.1.1 as well as the Lagrangian flamelet model in Section 4.1.2.

4.1.1 ECN Spray A and D

The spray flames investigated in this thesis are the Engine Combustion Network (ECN) Spray A and D [145]. These cases are chosen because of their broad investigation in literature and during the course of the ECN workshop. Based on them, the modeling strategy for LES of diesel spray flames as well as ignition and pollutant formation is investigated and the general picture of the diesel spray structure is outlined. The same operating conditions are chosen for both injectors. They are presented in Section 4.2 along with the FLUT generation procedure. The only difference between the sprays is dedicate to the nozzle hole diameter which has a nominal value of 90 μm in case of the Spray A and 186 μm in case of Spray D. It should be noted however, that with increasing size of the injector effects like needle inertia during the opening and closing phase of the injector become more pronounced. For each injector, different samples are manufactured and hence, not all measurements within the ECN are conducted at the exactly same injector. For the investigations within this chapter, the ECN Spray A injector with serial number 210677 is simulated for the non-reactive conditions while more recent experimental data for the spray flame are available of the injector with serial number 210370. Both injectors differ slightly in the nozzle diameter but have otherwise similar characteristics. In case of ECN Spray D, the injector 209134 is investigated.

Numerical setup

The mesh, used for the discretization of the domain of interest for the ECN Spray A is based on the work of Wehrfritz et al. [121] and shown in Figure 4.2. The mesh has the shape of a cuboid with the dimension of (60 x 110 x 60) mm with a base cell size of 1 mm. Based on the recommendation given in [121], the near nozzle resolution is set to 64.5 μm , which is approximately 2/3 of the nozzle diameter, via an embedded grid refinement with 4 levels each halving the grid size in each direction resulting in an overall cell number of approximately 12.8 million. Hanging nodes are avoided due to the utilization of polyhedral cells between the refinement levels. The mesh used for the ECN Spray D shares the same properties but is adapted to the larger nozzle hole. The mesh dimensions are chosen as (80 x 150 x 80) mm with a base cell size of 2 mm and a near nozzle cell size of 125 μm resulting in an overall cell number of 5.8 million. An implicit second order scheme is utilized for time discretization with a maximum Courant number of 0.5 and a maximum allowed time step size of $\Delta t = 150$ ns set for all simulations resulting in a minimum time steps size of $\Delta t = 33$ ns for the Spray A flame while the maximum allowed time step size was established for the Spray D flame. For spatial discretization CDS is used for the convective flux in the momentum equation and a TVD

scheme utilizing the Sweby limiter [170] is used for the discretization of the convective scalar fluxes. The Lagrangian parcel discretizing the liquid phase are injected as a disc source inside the domain with the center at $y=1.5$ mm and a diameter equalling that of the nozzle. The half cone opening angle is set to 10.75° for all injectors. For the determination of the droplet size after primary and secondary break-up, the KH-RT model with parameters set to $B_0 = 0.61$, $B_1 = 5$, $C_\tau = 1$, $C_{RT} = 0.1$, $ms_{Limit} = 0.05$ and $We_{Limit} = 6$ is utilized close to the values suggested in literature for this spray and simulation strategy [121].

taSOI = 0.40 ms

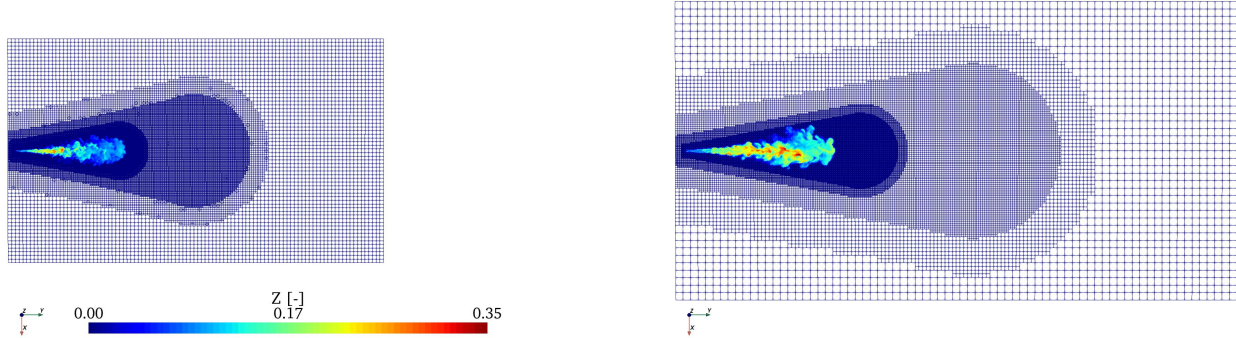
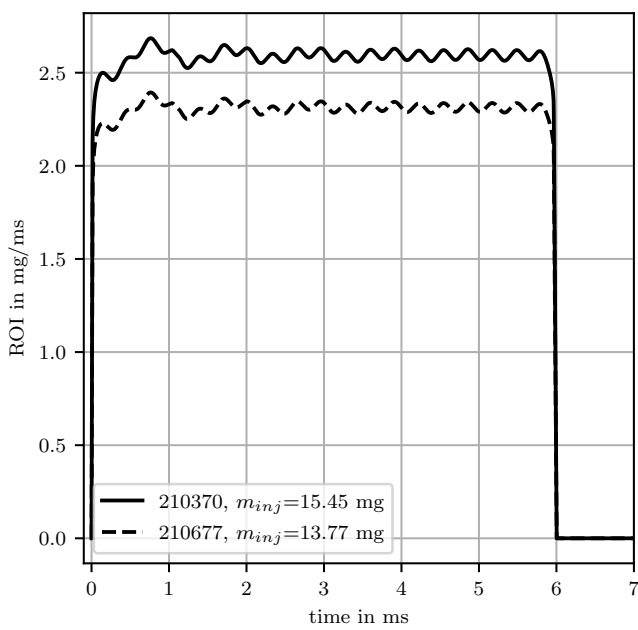
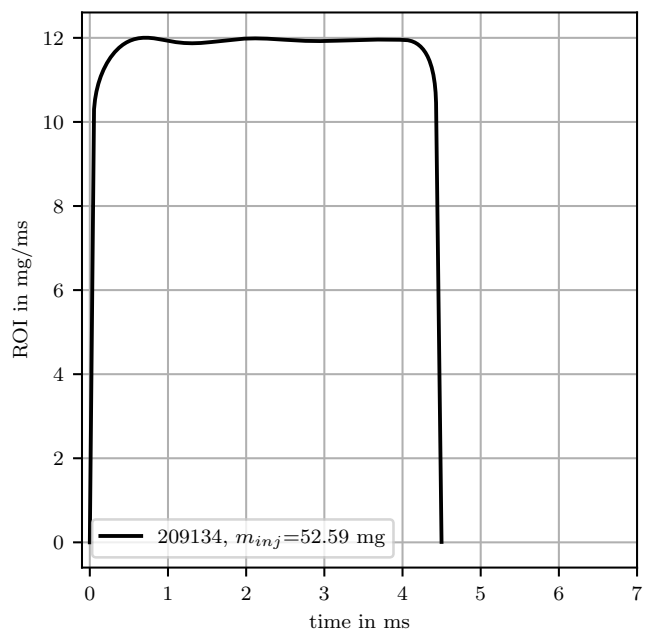


Figure 4.2: Computational mesh discretizing the gas phase color coded by the solution of the Favre-filtered mixture fraction field for the reactive Spray A (left) and Spray D case (right) at 0.4 ms after start of injection

The rate of injection (ROI) is obtained by utilizing the virtual injection rate generator [182] for Spray A while measured ROI are utilize for Spray D [183]. The corresponding profiles are shown in Figure 4.3. Note, that the ROI for the Spray A injector 210677 used for the non-reactive simulation is scaled to the given experimental overall mass of 13.77 mg for the overall injection time of 6 ms [184]. A number of 0.76 million parcel/ms are injected for the Spray A and 2.13 million parcel/ms for Spray D, resulting in an averaged parcel mass of $3.40e-6$ mg/parcel for Spray A (injector 210370) following the recommendation of [156, 185] and $5.44e-6$ mg/parcel for the ECN Spray D, respectively. Note, that the simulations were performed until 2 ms after start of injection unless otherwise stated.



(a) ECN Spray A



(b) ECN Spray D

Figure 4.3: Rate of Injection (ROI) profiles for the Spray A injectors (left) and Spray D injector (right). ROI shape for the ECN injectors are obtained from the virtual injection rate generator [182] with the overall injected mass as the integral of the given ROI profiles. Note, that the ROI for the injector 201677 is scaled to ensure the experimentally given value for the injected mass of 13.77 mg. ROI for ECN Spray D (209134) injector is taken from [183].

4.1.2 Lagrangian flamelet model

The Lagrangian flamelet model (LFM) with decaying χ_{st} is used as verification case. This is on the one hand motivated by the model's level of complexity being similar to that of the flamelet simulations used to generate the FLUT and on the other hand by the similarity to the flame characteristics observed in turbulent spray flames as noted by Dahms et al. [74]. For this model, a reference solution with full transport and chemistry (FTC) is generated, which is subsequently used for the evaluation of the UFPV and UFCPV approach applied in the LFM. The initial and boundary conditions for the LFM are the same as chosen for the flamelet simulations utilized for generating the FLUT, see Table 4.2. However, the parameter χ_{st} is not a constant anymore but varying with time as it is typical for sprays, which will be shown in Section 4.5.4. The profile chosen here follows the work of Dahms et al. [74]. However, the profile formulated here covers a larger time range to incorporate the formation of gaseous pollutant species. The temporal dependency follows the $1/t$ behavior typical for a decaying mixing layer [82]. The functional form utilized here is given by

$$\chi_{st}(\tau) = \begin{cases} \frac{\chi_{st,ref} \chi_{st,0}}{\chi_{st,ref} (1 - \tau/\tau_{ref}) + \chi_{st,0} (\tau/\tau_{ref})}, & 0 \leq \tau \leq \tau_{ref} \\ \chi_{st,ref}, & \text{else} \end{cases} \quad (4.1)$$

with $\chi_{st,0} = 50/s$, $\chi_{st,ref} = 1/s$, and $\tau_{ref} = 2.75 \text{ ms}$. The resulting profile is plotted together with the one used by Dahms et al. [74] in Figure 4.4.

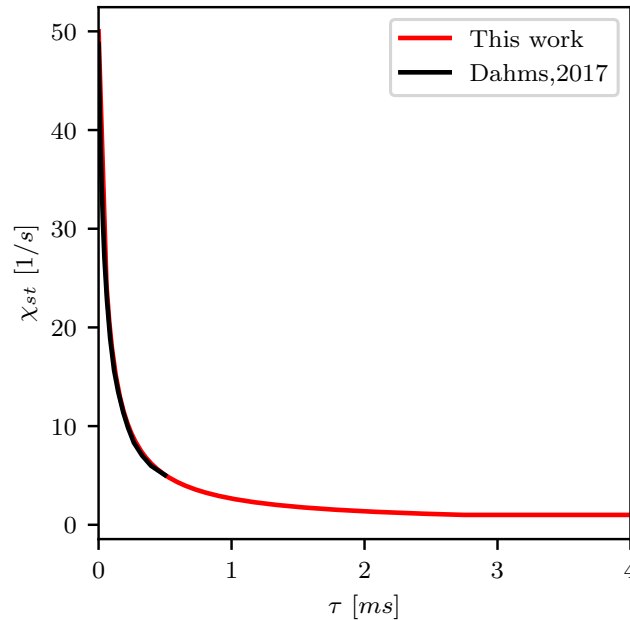


Figure 4.4: Comparison of the stoichiometric scalar dissipation rate's evolution used for the Lagrangian flamelet model between Dahms et al. [74] and the one described by equation (4.1) used in this thesis

4.2 Operating conditions and FLUT generation

The operating conditions investigated in this chapter are the ECN Spray A nominal conditions. Liquid n-dodecane is injected into a constant volume chamber at a pressure of 60 bar and an ambient temperature of 900 K from a rail at a pressure of 1500 bar and at a temperature of 363 K. In the chamber, the oxygen content is 15 % by volume. This composition together with the ambient temperature and pressure results from a premixed combustion of acetylene, hydrogen, oxygen and nitrogen prior to the liquid fuel injection. The corresponding set of boundary conditions applied in the flamelet calculations are given in Table 4.2. The stoichiometric mixture fraction derived from the fuel and oxidizer composition is given by $Z_{st} = 0.045$. Furthermore, the initial condition is retrieved from an adiabatic mixing between fuel and oxidizer.

Table 4.2: Boundary conditions for the flamelet model under the ECN Spray A nominal conditions

| Side | p [bar] | T [K] | $X_{nC_{12}H_{26}}$ | X_{O_2} | X_{N_2} | X_{CO_2} | X_{H_2O} |
|----------------|-----------|---------|---------------------|-----------|-----------|------------|------------|
| Z=0 (oxidizer) | 60 | 900 | 0 | 0.15 | 0.7515 | 0.0622 | 0.0362 |
| Z=1 (fuel) | 60 | 363 | 1 | 0 | 0 | 0 | 0 |

All flamelet calculations shown in this chapter are obtained on 150 points in Z-space with refinement in the range $Z \in [0, 0.4]$. Two chemical reaction mechanisms are utilized: For the investigation of the tabulation aspects in the ECN Spray A, a reduced version of the CRECK detailed mechanism [180, 181], is applied. This reduced mechanism is obtained using the DoctorSMOKE++ utility [181]. It combines a flux analysis technique [186] with sensitivity analysis [187, 188] to reach the optimal number of species. Reaction states were sampled by using OD, adiabatic, constant-pressure autoignition reactors, whose initial conditions were uniformly spread in the operating range $p \in [50, 80]$ bar, $T \in [600, 1700]$ K and $\phi \in [0.5, 4]$ ¹³. For the investigation of NO and PAH formation, the detailed CRECK mechanism¹⁴ is utilized. A comparison between both mechanism is shown in Appendix A based on the Lagrangian flamelet model.

The FLUT for the investigation of the influence of the scalar dissipation rate contains 19 values for the dissipation rate at stoichiometry χ_{st} ranging from $1/s$ to $90/s$ following Sun et al. [3], while 29 values ranging from $1/s$ to $140/s$ are utilized for the comparison of the UFPV and UFCPV approach. In particular the incorporation of the lower strain rates where important to capture the evolution of slow species within the LFM. The progress variable definition $Y_C = 0.5 Y_{H_2} + 1.0 Y_{H_2O} + 1.0 Y_{CO_2} + 0.9 Y_{CO} + 0.8 Y_{CH_2O}$ is utilized which ensures a unique mapping between time and Y_C , respectively [3]. For the UFCPV approach, the same definition is used for $Y_{C,1}$. $Y_{C,2}$ is defined as $Y_{C,2} = Y_{NO} + Y_{C_{16}H_{10}} + Y_{C_{18}H_{10}}$, as they are the species of interest either as gaseous pollutant (NO) or as soot precursor ($C_{16}H_{10}$, $C_{18}H_{10}$). A detailed investigation of this combination is shown in Figure 4.5 based on a representative χ_{st} value of $5/s$. In this figure, the iso-lines of the progress variables do not intersect, which would be the case for non-monotonicity. Furthermore,

¹³The reduction of the chemical mechanism was performed by Alessandro Stagni, CRECK Modeling Lab, in a collaboration during the work on this thesis in the frame of a research project covering a wide range of operating conditions. This explains the chosen limits in terms of pressure.

¹⁴Version 03.2020

the different time ranges spanned by the two progress variables are clearly visible. While the normalized first progress variable reaches its maximum for a wide range of mixture fractions before 1 ms at which the ignition process is completed, the second progress variable reaches its maximum value after several milliseconds covering the time for the formation of slow forming species. The resulting manifold spanned by the flamelet solutions will be investigated in Section 4.3. For the application in the spray simulation, a β -pdf integration with respect to the mixture fraction is performed, as described in Section 2.2.5.

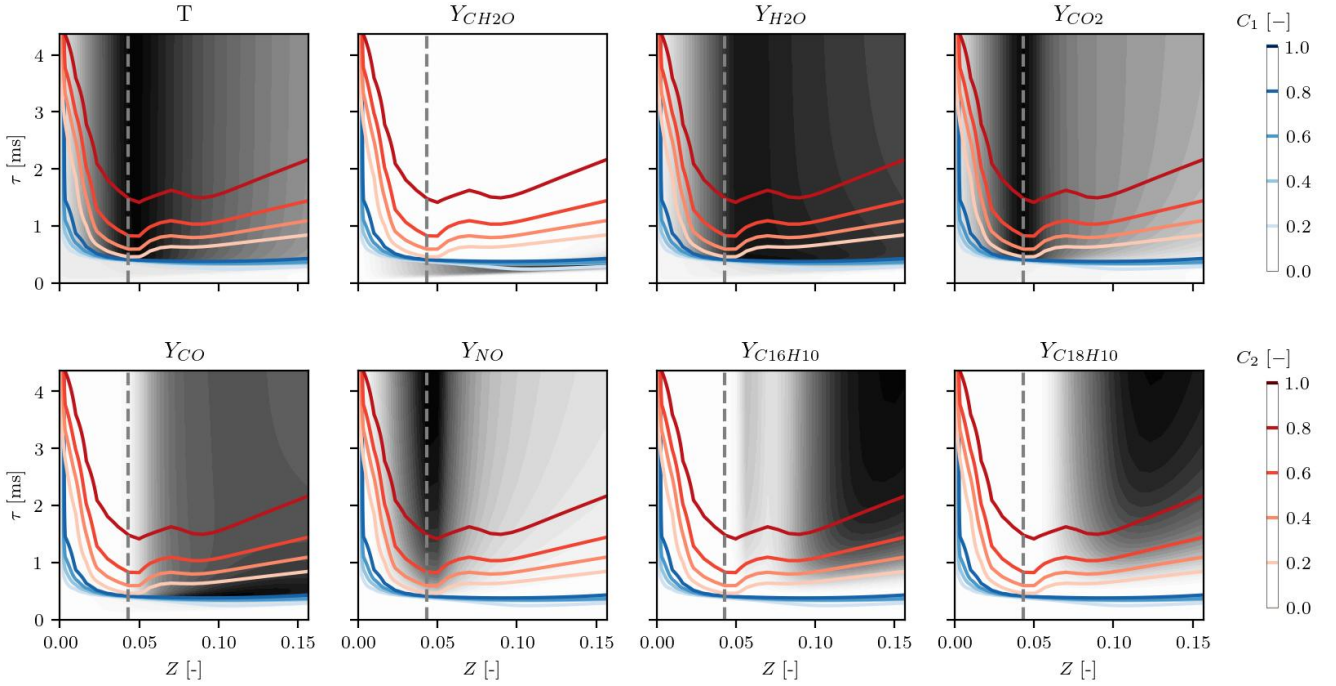


Figure 4.5: Iso-lines of the normalized progress variables C_1 and C_2 overlaying the single species evolution (heat map color-coded from white to black) for a flamelet calculation with $\chi_{st} = 5/s$.

4.3 Evaluation of the flamelet look-up table

The thermo-chemical state retrievable in the coupled simulation is directly determined by the utilized FLUT. Hence, an inspection of distinct characteristics of the look-up table manifold is important to understand the behavior in the Lagrangian flamelet model and the 3D spray simulation. This is performed in the following. In Figure 4.6, the ignition of a flamelet with constant scalar dissipation rate at stoichiometry of $\chi_{st} = 20/s$ is shown in terms of temperature, OH, and CH_2O mass fraction to illustrate the ignition process, and the mass fraction of NO and PAH species as gaseous pollutant and soot precursor, respectively. The left part of this figure shows the early stage of the ignition process where CH_2O is produced in the lean part of the flame ($Z < Z_{st} = 0.045$) connected with a slight increase in temperature. Due to heat and mass transfer it evolves towards stoichiometry and rich parts of the flame resulting in an enhancement of chemical activity in this regions. Its amount is thereby increasing reaching its peak value of $Y_{\text{CH}_2\text{O},max} = 0.017$ at approximately

$\tau=0.42$ ms for $Z = 0.21$. This process is denoted as *cool flame* propagation by Dahms et al. [74]. Note, that the production and transport of CH_2O does lead to an increase of the maximum temperature observed along the flamelet, which is denoted by black dots in Figure 4.6. However, this is only the case until a mixture fraction value of $Z = 0.12$ is reached. For more fuel rich mixtures, the elevation in temperature is visible, but does not reach that of the neighboring mixtures with lower Z values most likely due to the lower initial temperature. Furthermore, fast consumption of CH_2O is initiated at this point as shown in the center part of Figure 4.6, connected with a significant increase in temperature and OH mass fraction. This process denotes the second stage ignition. Hence, this point in mixture fraction space is denoted by Z_{ign} within this thesis, i.e., the most fuel rich mixture at which second stage ignition takes place. It is denoted by the most right black point and a vertical dotted line in Figure 4.6, respectively. The ignition process is subsequently evolving towards the stoichiometric mixture fraction, where the steady state flame temperature establishes. At the same time, CH_2O evolves into further rich parts of the flame, where a moderate temperature increase takes place. The establishment of high temperatures furthermore initiates the formation of NO and PAH species starting shortly after first stage ignition and proceeding over a large time range as shown in the right part of Figure 4.6. As expected, NO shows large amounts at stoichiometric conditions. However, due to the incorporated transport effects, NO is also transported in wide rich parts of the flame for this specific case. PAH species have their peak value at Z_{ign} .

Note, that the shown characteristics of the ignition behavior are similar for different values of χ_{st} but the details of the ignition process are different. As such, the ignition delay time τ_{ign} , the richest mixture at which second stage ignition occurs Z_{ign} as well as the location of the PAH mass fraction peak value $Z_{PAH,max}$ vary between the single flamelet solutions. Therefore, an overview of these global characteristics compared between different values of χ_{st} is given in Figure 4.7. In the left part, the evolution of the maximum temperature is shown for $\chi_{st} = 1/s$ and $\chi_{st} = 20/s$, respectively. Obviously, the onset and extend of the two ignition stages differ between the solutions. They are marked by the blue and red symbols denoting the corresponding first and second stage ignition delay times $\tau_{ign,1}$ and $\tau_{ign,2}$. Their comparison in the central plot shows the tendency, that both ignition delay times increase non-linearly with increasing χ_{st} . At a certain value, no ignition is taking place anymore. This value corresponds to $\chi_{st,ign}$ which was introduced within the discussion of the S-curve in Section 2.2.2. In the right part of Figure 4.7, Z_{ign} and $Z_{PAH,max}$ are shown. Obviously Z_{ign} is steadily increasing from a value slightly above $Z_{st} = 0.045$ up to a value of approximately $Z_{ign} = 0.15$. $Z_{PAH,max}$ on the other hand shows only a strong dependency on χ_{st} for low values of this parameter and takes values around $Z_{PAH,max} = 0.14$ for a wide range of χ_{st} . Especially the last two parameters are used in the discussion of the different spray flame structures in Section 4.5.6 and Section 4.6.4 and to explain the difference in the ignition process between Spray A and Spray D in Section 4.6.2. Note, that the NO peak value is always located at stoichiometry and does always propagate to a certain extend into fuel rich mixtures when transport effects are included ($\chi_{st} > 0$).

By incorporating flamelets with different scalar dissipation rates in the FLUT, the above shown characteristics are represented by the thermo-chemical state stored within the look-up table. Note, that the parameterization of the look-up table by means of Z , Y_C and χ_{st} involves the representation of the complex transient ignition process by the progress variable evolution. This affects in especial the source term in its transport equation

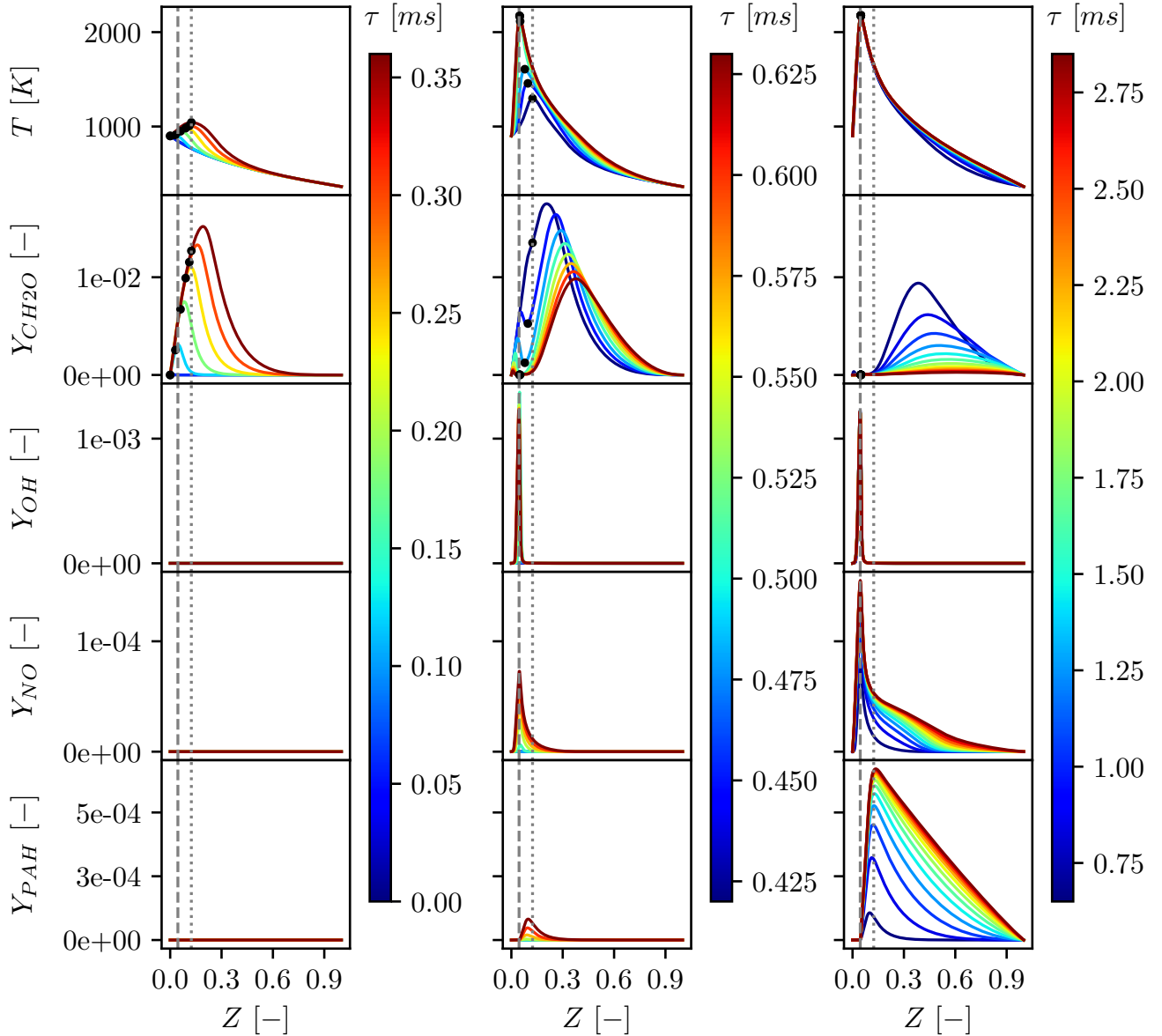


Figure 4.6: Evolution of temperature (top row), and mass fractions of CH_2O (second row), OH (third row), NO (fourth row) and PAH species (fifth row) for a single flamelet simulation with $\chi_{st} = 20/s$ used to generate the FLUT within three time intervals: Cool flame propagation [74] (left), main ignition (middle), slow chemistry (right). Black dots represent the (Z, T) and $(Z, \text{CH}_2\text{O})$ combination build from the instantaneous maximum temperature. Z_{st} is denoted by vertical dashed line while the maximum Z value, for which the maximum temperature is observed over time is marked by a dotted vertical line.

in case of the UFPV approach or in the transport equation of the two progress variables $Y_{C,1}$ and $Y_{C,2}$ in case of the UFCPV approach, respectively. These are shown in Figure 4.8 retrieved from the FLUT for different χ_{st} values. In correspondence with the cool flame propagation, the progress variable source term for describing the ignition and fast chemical reactions $\dot{\omega}_{Y_{C,1}}$ increases from lean to rich part of the flame for a early reaction

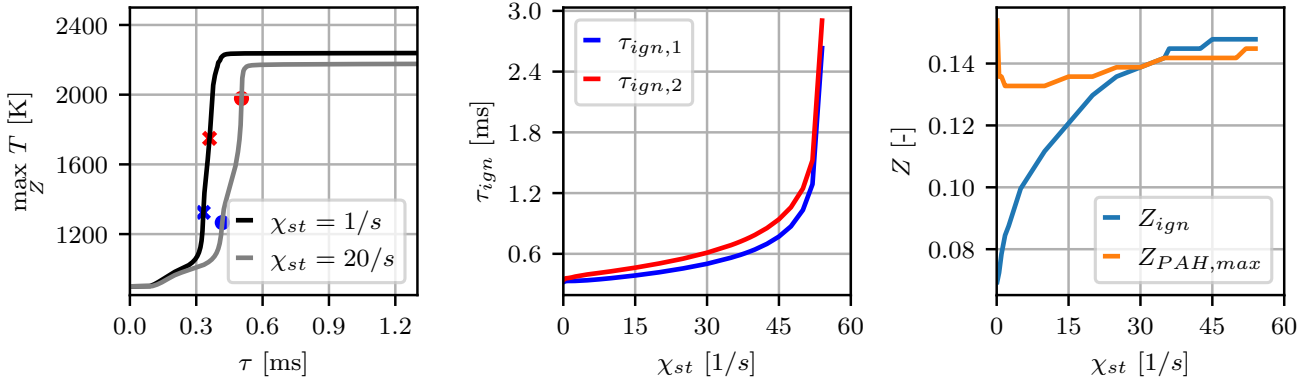


Figure 4.7: Global quantities defining the difference in the ignition process: Evolution of the maximum temperature over time for two χ_{st} values together with the corresponding first and second stage ignition delay times (left), the dependency of the ignition delay times on χ_{st} (middle) and the dependency of Z_{ign} and $Z(Y_{PAH,max})$ on χ_{st} (right)

progress (small values of normalized progress variable C). When the reaction proceeds, increasing values of the source term are observed in slight rich mixtures and their peak value is reached near stoichiometry. The extension of the source term into the rich part of the flame is varying with χ_{st} in line with the discussion of the single flamelet solutions. The source term of the progress variable representing the slow species evolution $\dot{\omega}_{Y_{C,2}}$ is shown in the lower part of Figure 4.8. Per definition, its contribution gets significant for $C > 0.5$, see (2.66). Its peak value is located in a region near $Z_{PAH,max}$ representing the strong formation of PAH species in this part of the flame. The results of utilizing this FLUT in the coupled LFM simulation is presented in the next section.

4.4 Lagrangian flamelet model

In Figure 4.9, the results for temperature and the mass fractions of CH_2O , NO and PAH species obtained in the Lagrangian flamelet model (LFM) are shown for the full transport and chemistry (FTC) reference solution as well as for the UFPV and the UFCPV approach. These results are shown for the different time ranges introduced in the last section, especially the cool flame propagation, main ignition and slow chemistry which are shown in the first to the third column in Figure 4.9. With regard to the first time span, a very good agreement is observed in terms of temperature and CH_2O evolution during the cool flame propagation. There is still a small delay establishing between the FTC solution and the UFPV as well the UFCPV approach which is a bit more pronounced for the latter one. This leads to a slight delay in the consumption of CH_2O at the start of the main ignition, shown in the second column in Figure 4.9. This effect is, however, not that obvious in the temperature profile, where the ignition behavior is nearly identical between the FTC solutions and the ones obtained by the tabulation approaches. After the end of the main ignition, the steady state temperature is reached as shown in the third column of Figure 4.9, which is exactly reproduced by the UFPV and the UFCPV approach. Hence, both tabulation strategies are able to capture the ignition behavior under

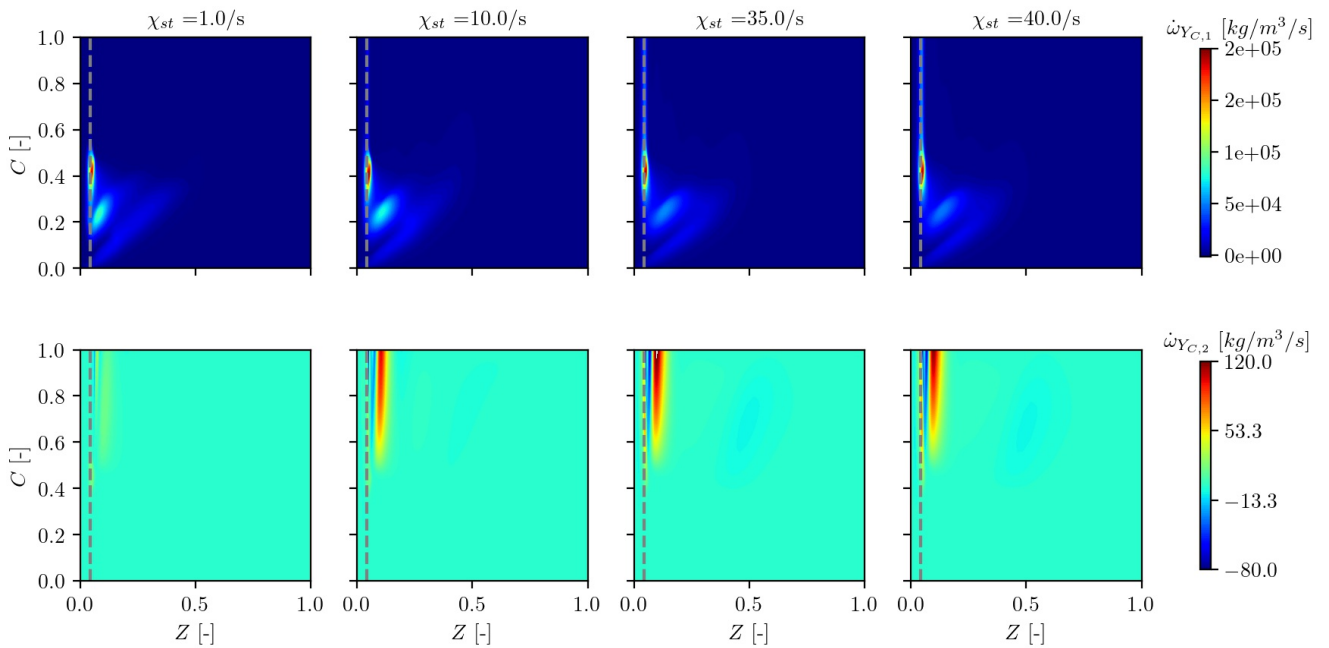


Figure 4.8: Distribution of the source terms of the two progress variables $Y_{C,1}$ and $Y_{C,2}$ in case of the UFCPV approach (with $Y_{C,1} = Y_C$ for the UFPV approach) $\dot{\omega}_{Y_{C,1}}$ (upper row) and $\dot{\omega}_{Y_{C,2}}$ (lower row) for different scalar dissipation rate values retrieved from the FLUT

time varying strain rate very well. The similarity between the behavior of the UFPV and the UFCPV approach is also expected, since the same progress variable definition is used for both to describe the ignition process. However, the same number of grid points were used by both approaches in Y_C direction. These are used in the UFCPV approach also to describe the slow evolving species leading to a reduced number of points to discretize the ignition process. This can indeed cause the slight deviation between the approaches in the transition from cool flame propagation to main ignition. The well description of the ignition process is visible in the fourth row of Figure 4.9 by inspecting the maximum temperature and CH_2O mass fraction over time. Beside a slight underprediction of the CH_2O peak value, the evolution of these quantities is predicted very well.

Obvious deviation arise between the approaches, when the slow evolving NO and PAH species start to build up. This is mainly the case when high temperatures are established and shown in the third column of Figure 4.9. As described in Section 2.2.4, the UFPV approach in combination with the chosen progress variable definition represents this time span at its best over a small range of progress variable values near its maximum value, i.e. $C = 1$. Hence, slight disturbance in the numerical solution lead to large errors in the NO and PAH species prediction. In the performed LFM simulations, this results in a strong overprediction of NO over the entire flame structure beside a strong undershoot between stoichiometry and $Z = 0.1$ for both time instances shown in the third row of Figure 4.9 followed by an overshoot in its vicinity towards the rich part of the flame. This is also visible in the right column, where the maximum value of NO is shown over time in the third row. Short after ignition, the NO mass fraction predicted by the UFPV approach increases to a high value and, after a short relaxation reaches its maximum value. Hence, the qualitative behavior does

not correspond to the reference solution, which suggests a continuously increase of the NO mass fraction over time. The UFCPV approach shows a much better agreement here. The spatial structure of the NO mass fraction is very well predicted for the instance of time shown and the maximum value over time is showing only a slight underestimation between approximately 2.75 ms and 7 ms. A similar conclusion can also be drawn for the PAH species, shown in the fourth column in Figure 4.9. Like NO they build up after the main ignition with the spatial structure shown in the third row. For the UFPV, this structure is not well reproduced. The UFCPV approach performs again much better here. However, the evolution is again slightly delayed. This leads to a slight underestimation of the maximum value, which is also visible in the fourth row.

In summary, the UFCPV approach shows the same quality in predicting the ignition behavior as the UFPV approach while significantly improving the prediction of the species evolution at large time scales. The remaining differences to the FTC reference solutions might be improved by an increase FLUT resolution in terms of both, Y_C and χ_{st} as well as the progress variable definition itself. However, due to the well overall agreement with the FTC reference solution, the UFCPV is judged as suitable extension of the UFPV approach to predict the evolution of species at large time scales. This will be investigated in the 3D Spray A simulation in Section 4.5.5. Beforehand, the spray simulation framework will be validated in terms of non-reacting and reacting conditions in Section 4.5.1 and Sections 4.5.2-4.5.3, respectively, together with the FLUT generation based on the reduced S-curve for predicting the ignition behavior properly in Section 4.5.4 to ensure a valid mixing and ignition of the spray before investigating the gaseous pollutant formation.

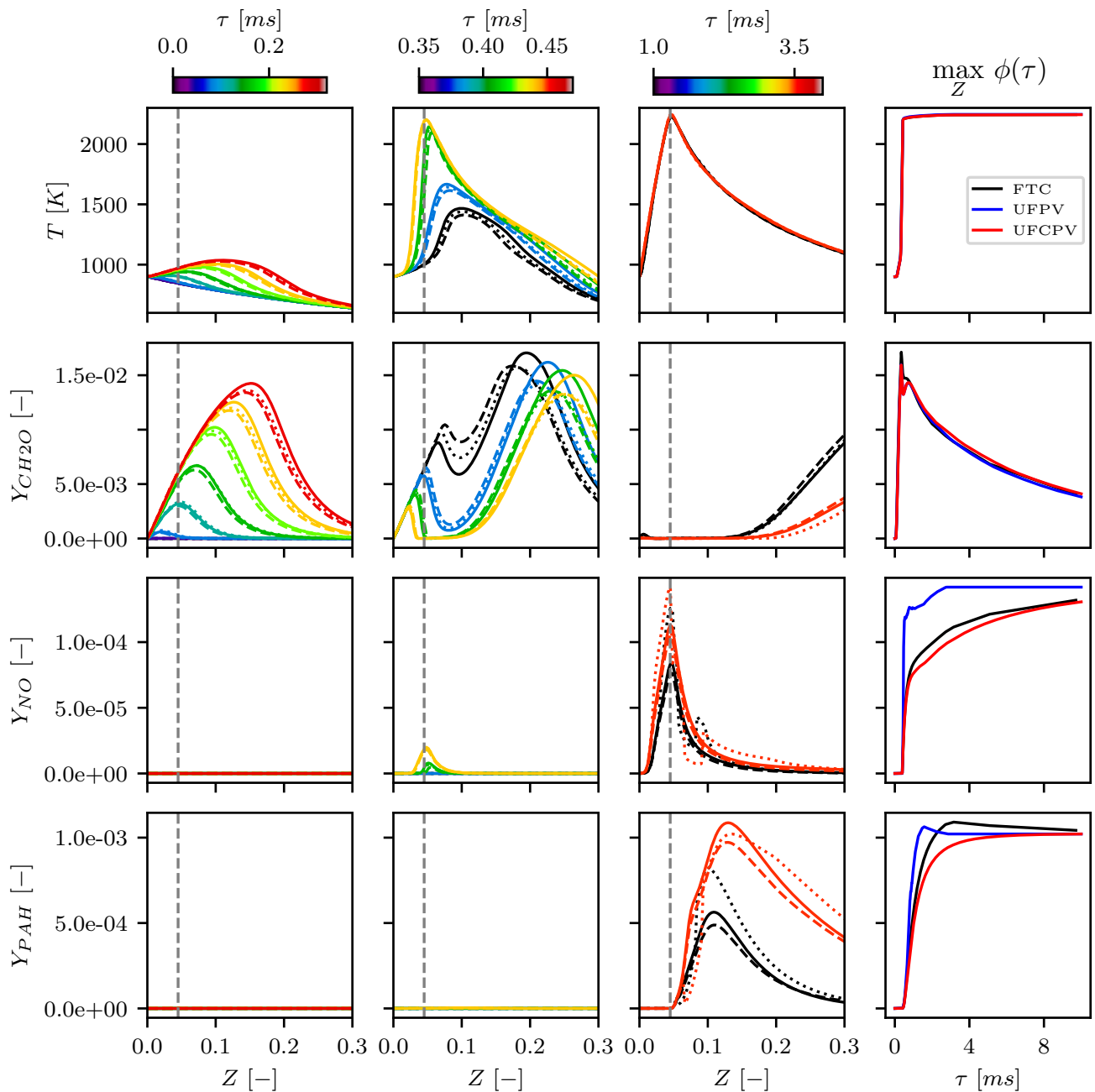


Figure 4.9: Comparison of temperature (top row) and species mass fraction of CH_2O (second row), NO (third row) and PAH species (bottom row), for the time of cool flame propagation (left column), main ignition (second column) and pollutant formation (third column) together with their maximum values over time (right column) for the LFM comparing the full transport and chemistry (FTC) reference solution (solid lines in first to third column, black line in right column) with the UFPV (dotted lines in first to third column, blue line in right column) and the UFCPV approach (dashed lines in first to third column, red line in right column).

4.5 ECN Spray A

4.5.1 Mixture formation under non-reacting conditions

As mentioned in Section 4.1.1, the non-reacting Spray A investigation is performed based on the injector with serial number 210677 due to the availability of Raman data quantifying the mixture fraction distribution along with Schlieren and Mie measurements [184] detecting the vapor and liquid penetration, respectively. The corresponding results for the penetration lengths are shown in Figure 4.10. The liquid and vapor penetration coincide for the first time interval after injection and separate at around 0.05 ms. At this point, the liquid penetration reaches its quasi-steady state while the fuel vapor continues to propagate into the chamber. For three instances of time, the liquid fuel distribution (parcel represented by black dots) along with mixture fraction distribution in the gas phase obtained from the simulation is shown in addition. Based on these data, the vapor penetration is evaluated as the maximum distance to the nozzle orifice, where the mixture fraction value falls below 0.1 %, and liquid penetration is evaluated as the axial location up to which 99 % of the liquid mass is contained. At this point, an overall very well agreement between the penetration lengths obtained by the measurement and the simulation is obtained.

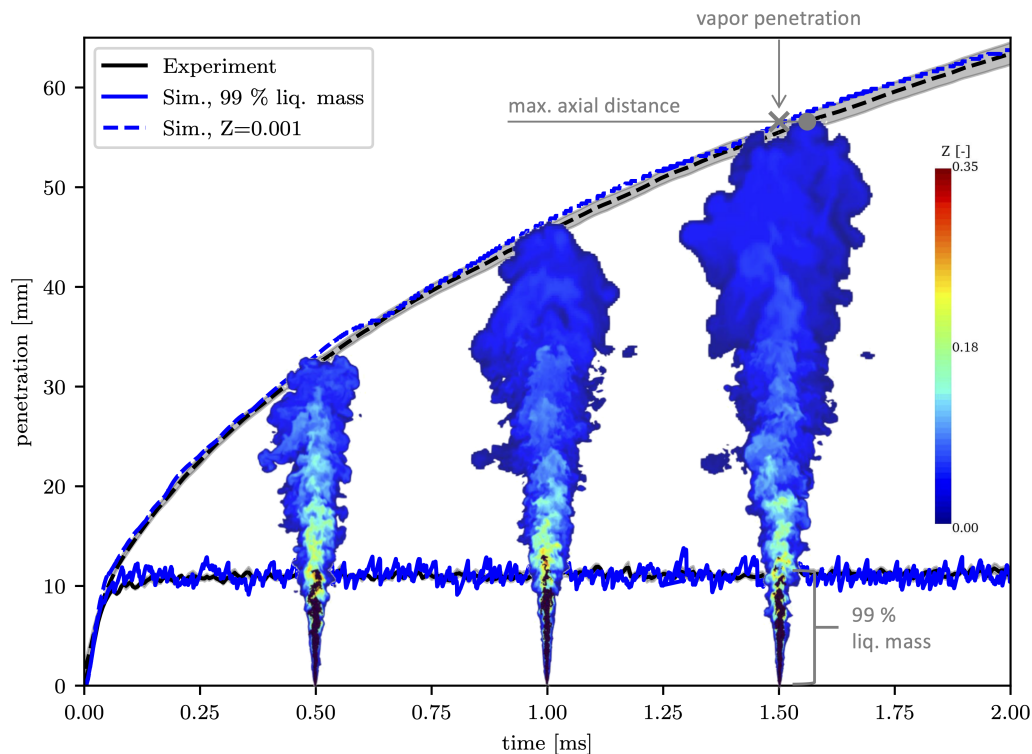


Figure 4.10: Comparison of the vapor (dashed lines) and liquid penetration (solid lines) lengths for ECN Spray A under non-reactive conditions between simulation with the turbulence model constant $C_\sigma = 2$ (blue curves) and experiments obtained by Schlieren measurements [184] and Mie scattering [184]. The evaluation of the liquid and vapor penetration lengths is visualized by gray symbols along with their corresponding description.

Since the σ -model is utilized in this thesis for the first time in the context of spray simulations, the value of the model constant C_σ has to be adapted to this spray modeling procedure. Therefore, a parametric study has been performed around the base value of $C_\sigma = 1.5$ which was proposed by Nicoud et al. [135] for isotropic decaying turbulence on fine grids. Furthermore, this value was also evaluated to show good agreement in turbulent channel flow. However, for coarser grid resolution, a higher value of the model constant was found to be more suitable. In isotropic decaying homogeneous turbulence, Nicoud et al. [135] found values in the range of 1.6 to 1.7 under that conditions. Due to the variation in the grid spacing in the current setup with a relatively large cell size compared to the length scale of turbulence structures near the nozzle, the range of model parameters tested within this thesis includes one value smaller than the recommended one and 2 larger ones resulting in the range $C_\sigma \in [1.3, 1.5, 1.7, 2.0]$. The results shown in Figure 4.11 suggest, that the liquid penetration is not notably affected by the value of the model constants. However, the differences are more pronounced for the vapor penetration length. For early times after start of injection, the simulations with a model constant of 1.3 and 1.5 show a relatively large temporal variation and overprediction of the penetration length. Compared to this, the penetration for the cases with model constants of 1.7 and 2.0 show much less fluctuations and are in much better agreement with the experimental data. Another aspect related to the vapor penetration is the behavior of the model when reaching the borders of the mesh refinement zone (see Figure 4.2), marked by dashed horizontal lines in the left part of Figure 4.11. For model constants $C_\sigma < 2.0$, the penetration length start to overestimate the experimental data at the end of the first refinement zone, even the prediction was appropriate before. For the model constant of 2.0, the slope of the penetration curve is not that obvious.

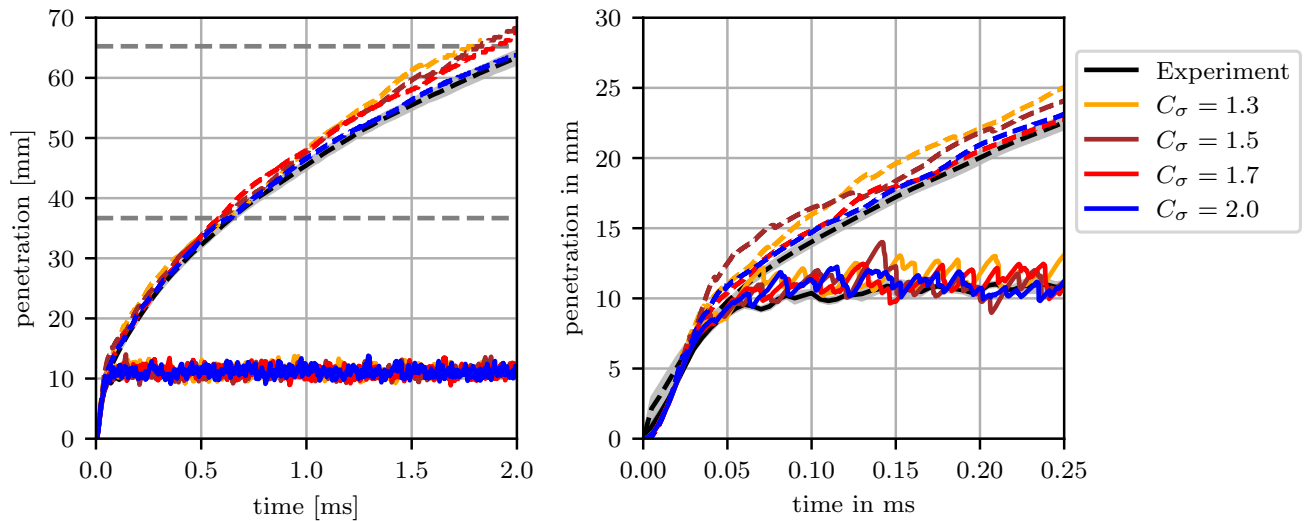


Figure 4.11: Comparison of the vapor (dashed lines) and liquid penetration (solid lines) lengths for ECN Spray A under non-reactive conditions between simulations under variation of the turbulence model constant C_σ (colored curves) and experiments obtained by Schlieren measurements [184] and Mie scattering [184]. The mesh coarsening regions are marked by grey dashed horizontal lines and the experimental standard deviation is marked by grey shadow.

Since the variation in the vapor penetration is not that high, the mixture fraction distribution obtained from

Raman measurements [184] are compared in the following. For this, the single-shot simulation are averaged over a period of 1.5 to 2.0 ms (where a quasi-steady state of the spray is reached in the regions of interest) in time and additionally in circumferential direction, see e.g., [97, 122]. The results are shown in Figure 4.12. Again, a very well agreement is obtained, underlying the suitability of the current LES modelling approach. In summary, a proper agreement between experimental and numerical data are obtained by the employed model strategy with the values of the constant C_σ tested. However, the influence of the refinement region is not neglectable in the non-reactive simulation. It is observed in a prior study, that the reduced spreading of the jet is connected with an qualitative under-resolution of the mixture fraction field. A model constant of 2.0 seems hence more applicable from point of view of resolved flow structures. The robustness of the penetration lengths as well as the relatively small under-prediction compared to lower values of the model constants in the radial mixture fraction distribution leads to the recommendation to use $C_\sigma = 2.0$ which is followed in the next sections.

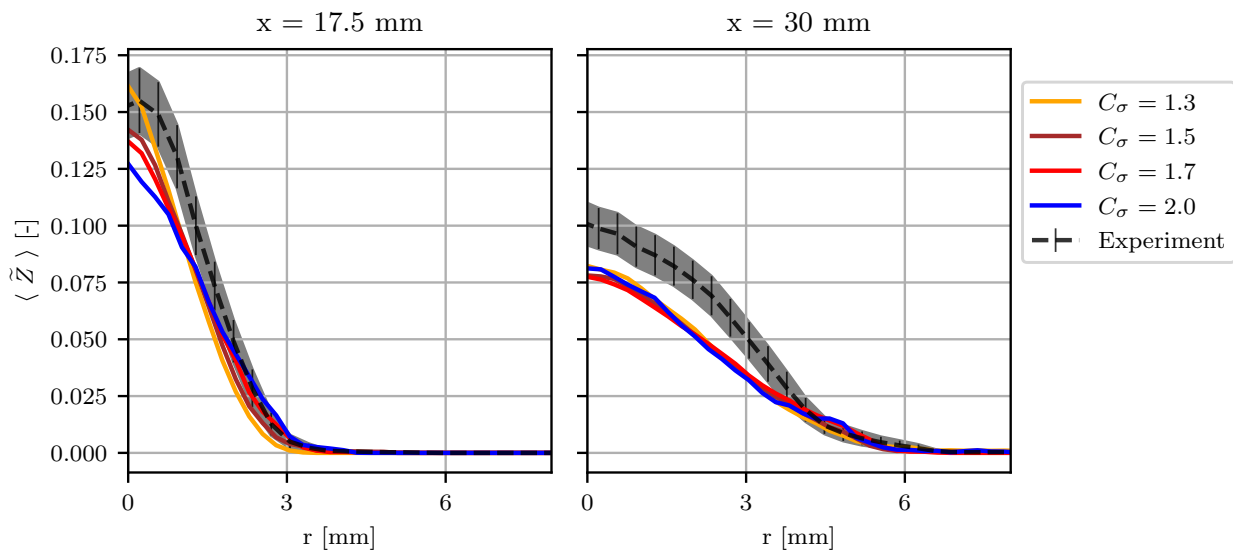


Figure 4.12: Averaged radial mixture fraction distribution obtained from Raman measurements [184] (black curve) and simulation with different values of the σ -model constant C_σ

4.5.2 Mixture formation under reacting conditions

After investigating the spray under non-reactive conditions, its simulation under reactive conditions is validated and analysed in the following. The reduced CRECK mechanism is incorporated for this investigation. As for the non-reacting case, the comparison of the liquid and vapor penetration is performed first to ensure the correct prediction of the fuel vaporization and the subsequent mixing in the gas phase. In Figure 4.13, the penetration lengths of the vapor phase obtained by means of Schlieren signals [189] and the liquid penetration obtained by means of Mie scattering [190] in comparison with the LES results are shown. The vapor penetration is evaluated based on the farthest downstream location, where the border of $Z = 0.001$ is reached and the liquid penetration as the distance to the nozzle, where 99 % liquid mass is included as used before in Section 4.5.1. The vapor penetration matches the experimental data very well. The liquid penetration is in overall well agreement with the experimental data, too. However, a slight overestimation is visible, which was not the case for the non-reactive conditions. The reason might be a combination of different aspects. For example, the measurements for the non-reactive and reactive cases are obtained on two different injectors (210677 for the non-reactive and 210370 for the reactive case). Since they have both a very similar diameter and injection system, the differences are not expected to be that obvious. Hence, the liquid penetration obtained by means of diffused back-illumination (DBI) [191] is shown additionally in Figure 4.13 for the non-reacting conditions on injector 201370. Note, that the inclusion of data obtained in a non-reactive environment is only meaningful for time ranges up to the experimentally determined ignition delay time of 0.41 ms [189], denoted by the dotted vertical line in Figure 4.13. Afterwards, the results might be influenced by the raise in temperature and corresponding heat transfer affecting the liquid penetration length. Up to this time, the liquid penetration obtained from DBI [191] is very similar to that obtained by the Mie scattering on the 210677 injector under non-reacting conditions shown in Figure 4.11 and is very well reproduced by the LES. This observation, together with the fact that the deviations with respect to the experimental Mie Scattering data on injector 210370 under reactive conditions are in an acceptable range leads to the conclusion that the utilized simulation framework is also able to capture the evaporation and mixing within the reactive environment.

4.5.3 Ignition characteristics

In Figure 4.14, a time sequence for a single injection event is shown in terms of mixture fraction, temperature, and OH mass fraction on the center plane of the spray flame for different times after start of injection. The complete UFPV approach utilizing the reduced CRECK mechanism is again used for this simulation. Herein, the left column shows a time instant approximately 0.10 ms prior to the main ignition, the middle column near the experimentally obtained ignition delay time of 0.41 ms [189] and the right column a time where parts of the flame are still in statistically steady state. Obviously, the high-temperature ignition mainly starts at the spray head and then proceeds towards the spray flanks. This is a well known behavior of this spray flame [77] and its reproduction serves as first qualitative validation of the UFPV approach. Two important quantities for quantitative comparison are the ignition delay time and the lift-off length.

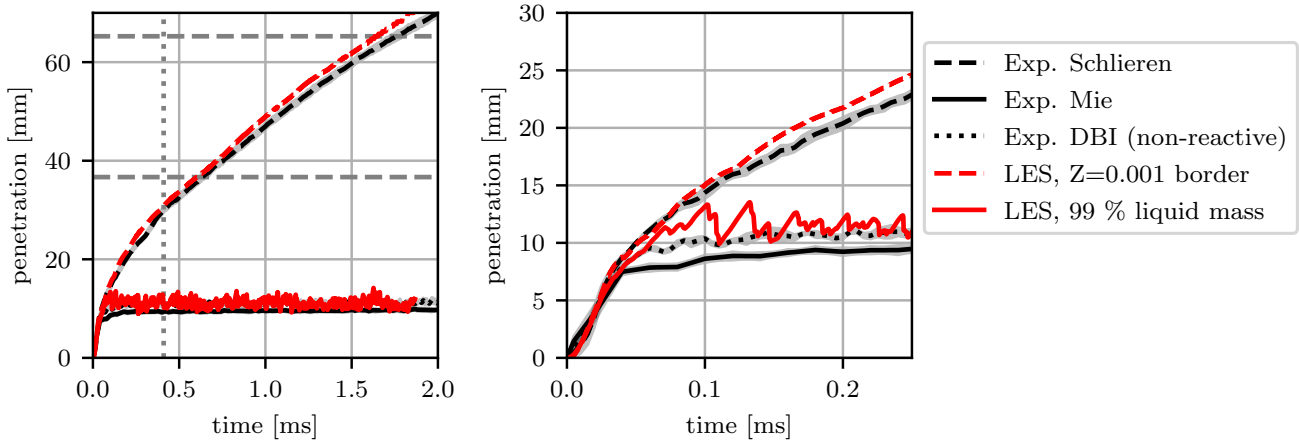


Figure 4.13: Comparison of the vapor (dashed lines) and liquid penetration (black solid lines) lengths for ECN Spray A under reactive conditions between simulation (red curves) and experiments obtained by Schlieren measurements [189] and Mie scattering [190]. In addition, experimentally recorded liquid lengths by means of diffused back-illumination (DBI) [191] for the non-reactive case are shown (black dotted line) as well as the mesh coarsening regions (grey dashed horizontal lines) and the experimentally determined ignition delay time of 0.41 ms ([189], gray dotted vertical line). The experimental standard deviation is marked by grey shadow.

Both are evaluated following the ECN recommendations based on 2 % of the maximum OH mass fraction obtained during the overall simulation time. To allow for a direct access to this criteria, the color range used for the OH mass fraction in Figure 4.14 is limited to this value. With this, a good agreement of the predicted steady lift-off length with the experimental data [189] including a slight overestimation is suggested. This is confirmed by the quantitative comparison in which the ignition delay time of the simulation shows with 0.368 ms an error of -8.0 % against the experimental determined value of 0.41 ms [189] and the steady lift-off length with 16.84 mm an error of 4.3 % against the experimental reference value of 16.10 mm [189]. With this, the validity of the approach for predicting the global ignition behavior is shown and can be used for the assessment of the tabulation parameters and the reduction of the look-up table within the next section. It should be noted, that the differences in the ignition delay time are directly linked to the chemical mechanism, as shown in the application of the UFCPV approach in conjunction with the detailed CRECK mechanism later on.

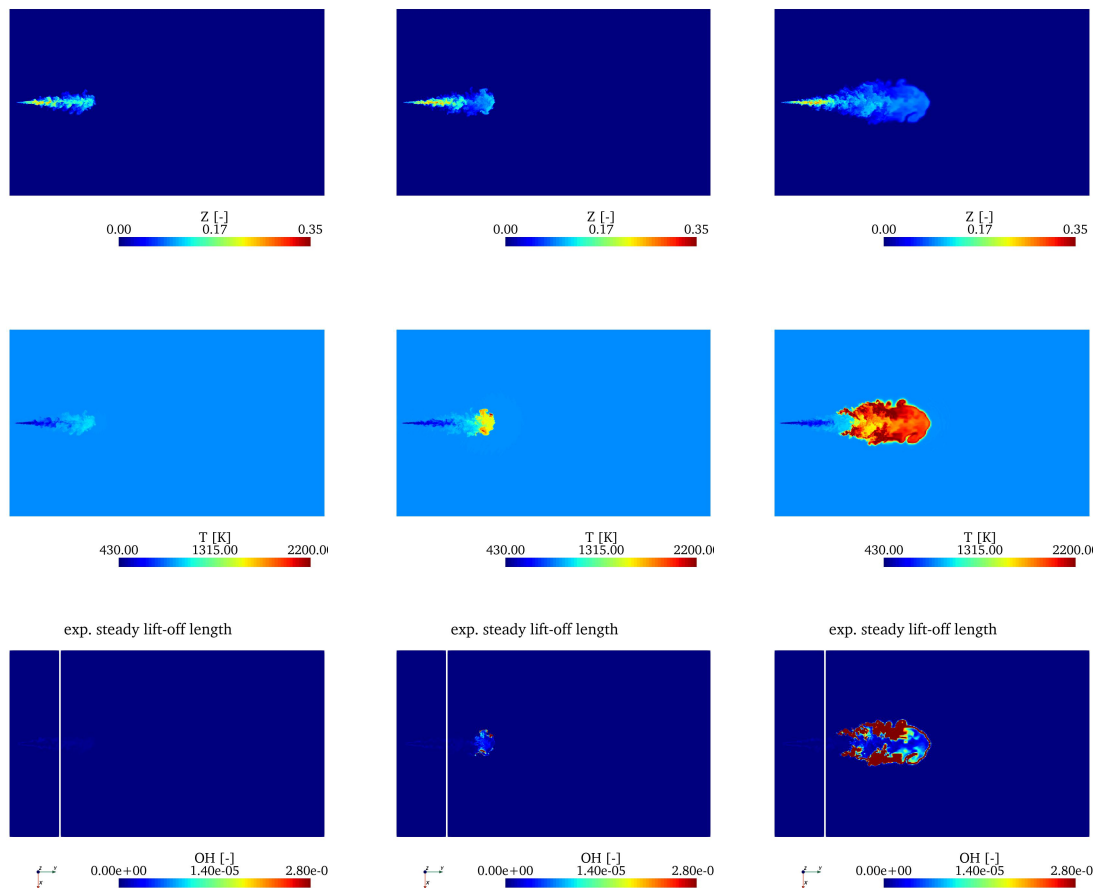


Figure 4.14: Series of Favre-filtered mixture fraction (top row), temperature (middle row), and OH mass fraction (bottom row, maximum color set to 2 % of the maximum value obtained during the simulation), on the centerplane during the injection of the ECN Spray A under reactive conditions for 0.30, 0.40 and 1.00 ms after start of injection including the experimentally obtained ignition delay time of approximately 0.41 ms [189]. The experimentally determined steady lift-off length [189] is indicated by a vertical white line in the bottom row.

4.5.4 Influence of the scalar dissipation rate and S-curve model¹⁵

In this section, the influence of the scalar dissipation rate on the ignition behavior is investigated. The outcomes motivate the assessment of the UFPV approach neglecting the region between the stable and unstable branches of the S-curve, see Section 2.2.2, which is performed subsequently. As in the last section, the utilized FLUTs are based on the reduced CRECK mechanism.

In Figure 4.15, a time sequence of the scalar dissipation rate $\tilde{\chi}_{st}$ is shown together with the corresponding temperature field. Obviously, high values of $\tilde{\chi}_{st}$ are present upstream of the liquid penetration length (left vertical line in Figure 4.15) which decreases downstream. Overall, small values are observed after the experimentally determined lift-off length is passed (right vertical line in Figure 4.15). Furthermore, upstream the lift-off length, large values of $\tilde{\chi}_{st}$ are found near the spray axis. With increasing distance to the nozzle, this is not the case and the scalar dissipation rate is larger at the border of the vaporized fuel jet than at the axis for all time instances shown. The temperature distribution presented in the lower row of Figure 4.15 shows the establishment of the flame downstream of the region with high $\tilde{\chi}_{st}$ values. Hence, $\tilde{\chi}_{st}$ is potentially acting as ignition inhibition upstream of the lift-off length. This phenomena is in line with the state of knowledge [100, 112]. It lead especially to the idea stated in Bajaj et al. [100], to connect the lift-off length to the ignition scalar dissipation rate $\chi_{st,ign}$ or the corresponding extinction scalar dissipation rate $\chi_{st,ext}$.

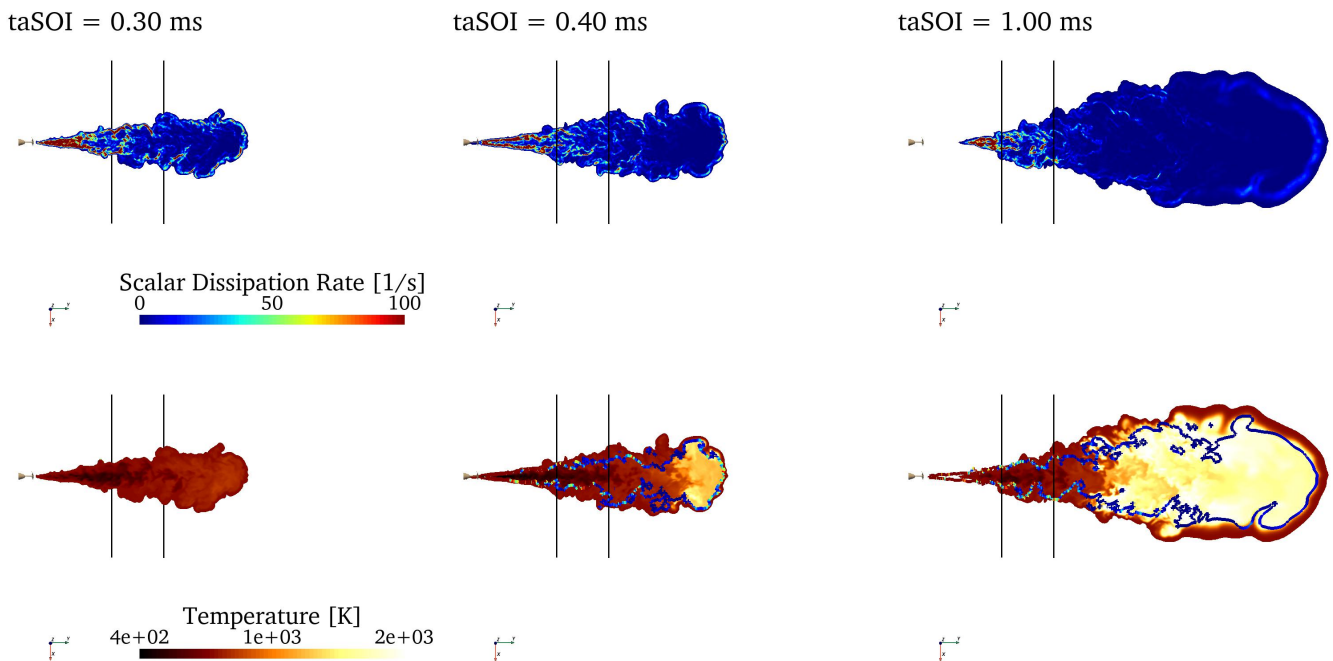


Figure 4.15: Series of scalar dissipation rate at stoichiometry used for table look-up (top row) together with temperature (bottom row) overlaid with isoline of $Z = Z_{st}$ colored by the scalar dissipation rate. The black vertical lines denote the experimentally obtained liquid penetration of 9.6 mm (left, [190]) and steady lift-off length of 16.1 mm (right, [189]), respectively.

¹⁵The results shown in this section are taken from the publication by Gierrth et al. [2] which was created during the work on this thesis. In [2], I was the main author of the extracted part.

In the following, the influence of the region between the stable and unstable branch of the S-curve is investigated. This is done based on stoichiometric conditions representative for the ignition process. In especial, the temperature at these conditions is analyzed in conjunction with the respective $\tilde{\chi}_{st}$ values. A cut through the incorporated data is visualized in the lower row of Figure 4.15 as iso-line of $\tilde{Z} = \tilde{Z}_{st}$. One fact, which is more obvious in this visualization than in the discussion above is the large values of $\tilde{\chi}_{st}$ at the spray head for 0.40 ms after start of injection, where second stage ignition is still proceeding. The question remains, if this $\tilde{T} - \tilde{\chi}_{st}$ combination only slows down the ignition process or lead to extinction. To answer this question, the temperature at stoichiometric conditions $\tilde{T}_{st} = \tilde{T}(\tilde{Z} = \tilde{Z}_{st})$ is plotted in $\tilde{\chi}_{st}$ -space in conjunction with the S-curve. Note, that fluid elements with even lower scalar dissipation rates are not shown for sake of proper visualization. As can be seen in the scatter plot in second column, there are indeed points with elevated temperatures below the unstable branch present. These fluid elements undergo extinction to a certain extend. This result suggests the necessity of considering this effect within the look-up table. However, these scatter are rather few. This is quantified in the lower row of Figure 4.15. The $\tilde{T}_{st} - \tilde{\chi}_{st}$ space is divided into bins and the mass of fuel and oxidizer represented by each computational cell (or scatter in the upper row, respectively) within each bin summed up with $\tilde{Z} = \tilde{Z}_{st}$. Obviously, the mass which undergoes extinction is relatively low. The same holds for fluid elements which undergoes a slowdown in ignition through passing $\tilde{\chi}_{st,ign}$ above the unstable branch at 1.00 ms after start of injection. Hence, the regions between the stable and unstable branch are retrieved from the look-up table, but only for small amount of mass. This leads to the suggestion, that the error connected to the neglect of this region within the FLUT generation will not alter the spray flame simulation.

In the following, a FLUT under neglect of the region between the stable and unstable branch of the S-curve is used for a coupled spray simulation and compared to the complete approach. The results for the temperature field is shown for the same time instances as above. Obviously, the onset of ignition is very similar for both setups. At 0.30 ms, only a slight increase in temperature is noticeable, while regions of elevated temperature are visible at the spray head at 0.40 ms. The similarity of the flame structure preserves also at 1.00 ms, where parts of the flame are in steady-state. At this time instance, a comparison of the steady lift-off length is reasonable, showing a close agreement between both simulations. The slight differences in the length of moderate temperature along the spray axis are potentially caused by a periodic detachment of the fuel-rich mixtures after the second stage ignition, as will be discussed later in Section 4.5.5.

To investigate the difference in the ignition behavior quantitatively, the evolution of the maximum temperature and OH mass fraction over time is shown in Figure 4.18. Obviously, only slight differences are present leading to approximately the same ignition delay time when evaluated based on these results. It can be concluded, that neglecting the unstable branch of the S-curve is a reasonable assumption for the ECN Spray A under nominal conditions. In front of this background, the reduced tabulation strategy will be applied in the further sections.

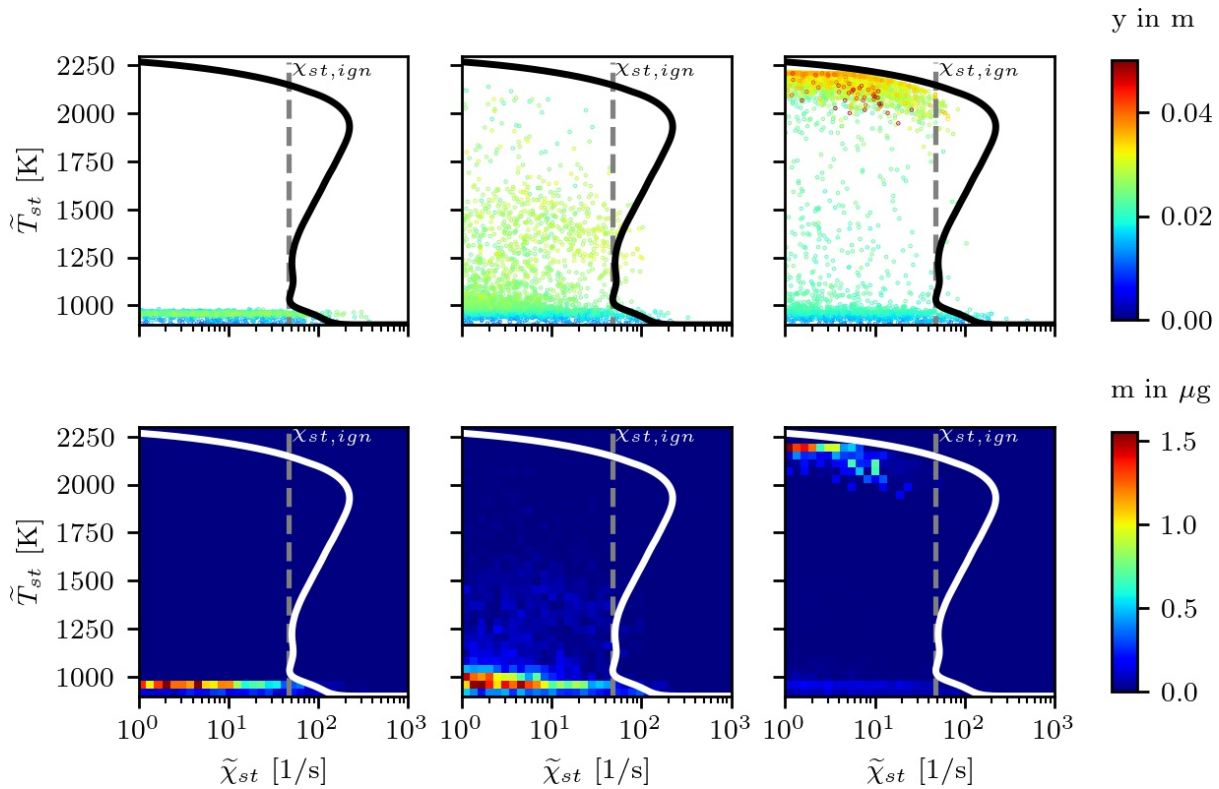


Figure 4.16: Distribution of the temperature at stoichiometric conditions $\tilde{T}_{st} = \tilde{T}(\tilde{Z}_{st})$ over the corresponding scalar dissipation rate $\tilde{\chi}_{st}$ in terms of scatter color-coded by the axial distance to the nozzle (top row) and mass distribution (fuel+oxidizer, represented by each scatter, bottom row) for 0.30 ms (left column), 0.40 ms (middle column) and 1.00 ms (right column) after start of injection.

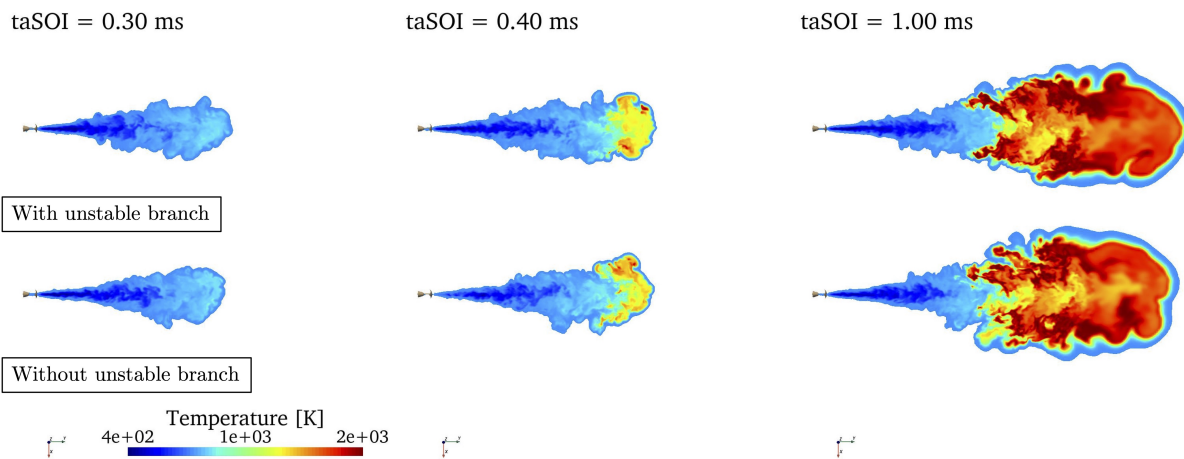


Figure 4.17: Contour plot of temperature obtained in the ECN Spray A simulation with (top) and without (bottom) incorporation of the unstable branch of the S-curve.

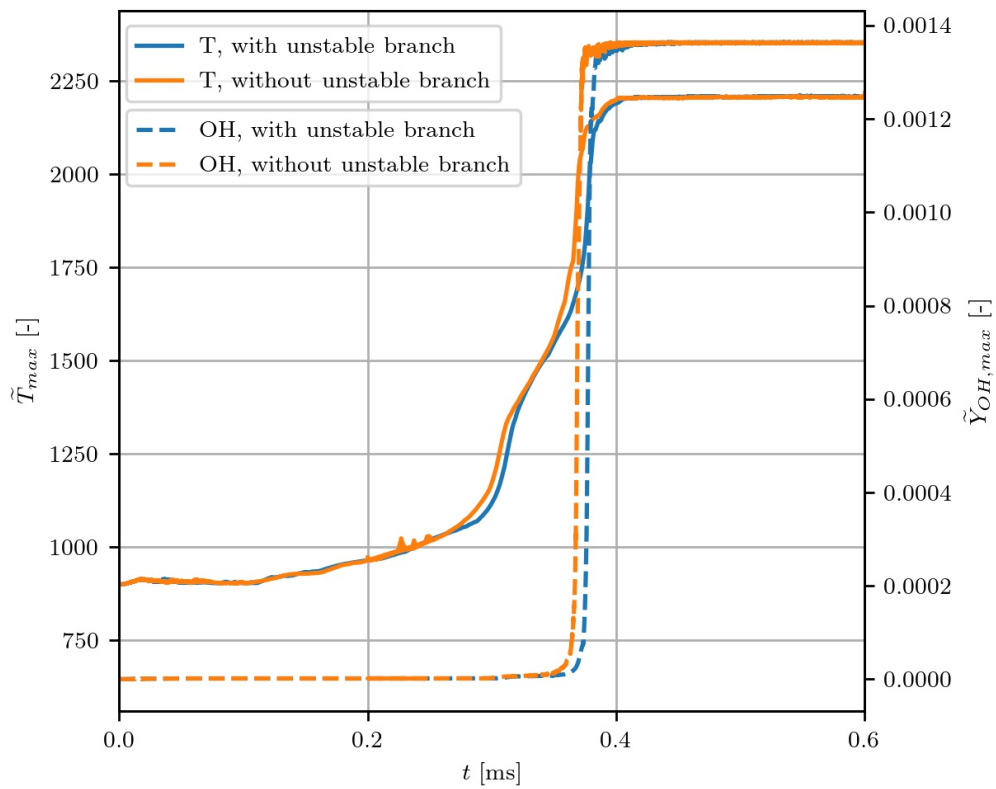


Figure 4.18: Evolution of the maximum temperature and OH mass fraction during the simulation for the ECN Spray A with (blue line) and without (orange line) considering the region between the stable and unstable branch of the S-curve.

4.5.5 Spray flame structure in physical space

After evaluating the UFCPV approach in the LFM and the reduced S-curve tabulation method based on the LES of the spray flame, the UFCPV approach with reduced S-curve tabulation is validated in the following and the results are used to investigate the spatial spray flame structure. Note, that the detailed CRECK mechanism is utilized for the simulation shown in this section. The simulation utilizing this mechanism shows a better agreement in the ignition delay time of 0.40 ms close to the measured value of 0.41 ms [189].

Detailed insights of the connection between the first stage ignition process and the transition to second stage ignition are given by the 355-nm PLIF measurements of Skeen et al. [76], from which the CH₂O distribution can be inferred. Their data are shown in Figure 4.19 together with the Favre-filtered CH₂O mass fraction obtained from the LES, the corresponding temperature distribution and the experimentally determined Schlieren images [76]. Note, that the PLIF image represents single shot measurement as well as the LES. Hence, the comparison shown in Figure 4.19 is affected by shot-to-shot variations. Keeping this fact in mind, the overall structure of the CH₂O profile looks very similar in both, spatial dimension as well as intensity distribution. In both cases, a noticeable amount of CH₂O builds up at 190 μ s after start of injection at the periphery of the jet. As discussed in Section 4.3 based on a single flamelet solution, an increase in CH₂O is connected to a slight increase in temperature. This increase is not that pronounced at this instance of time, but visible within the subsequent evolution. At 240 μ s, the influence of the CH₂O production and the increase in temperature becomes noticeable. At 290 μ s after start of injection, the CH₂O peak is developing towards the spray axis. The temperature rises above the chamber temperature in a region of remarkable size slightly upstream the measured steady lift-off length and downstream of it approximately until the spray head. At 340 μ s, the increase in CH₂O and the rise in temperature proceeds, with a resulting temperature slightly above the chamber temperature in larger regions up to the spray head. The temperature increase especially leads to a homogenisation of the density and hence refractive index distribution (not shown here), leading to a softening of Schlieren signal [76]. Note, that this softening in the Schlieren signal is not that pronounced in earlier time instances due the fact, that Schlieren measurements represent a line of sight methodology [76]. Hence, effects that are visible on a cutting plane of the spray might be compensated by the line of sight integration. Close to the experimentally obtained igniting delay time of 410 μ s [189], the CH₂O structure becomes disrupted at 390 μ s due to its consumption during second stage ignition connected with a strong temperatures raise locally. This happens mainly at the spray head, and latter proceeds towards the spray flank shown in the bottom row for 490 μ s after start of injection. In the region of high temperature, the Schlieren signal re-appears again due to the strong density gradients establishing.

During the subsequent evolution of the vaporized fuel jet, the fuel/air mixture proceeds further inside the combustion vessel leading to an increased residence time of fuel rich mixtures at the spray head. As shown in Figure 4.20, CH₂O is first consumed and PAH species shown on the example of the sum of C₁₆H₁₀ and C₁₈H₁₀ are produced with the highest values visible on the spray head. This is in line with the experimentally obtained PLIF signal. It shows high intensities in the regions, where CH₂O is predicted in large fractions by the simulation. Further downstream a reduction is observed in the signal intensity where the consumption

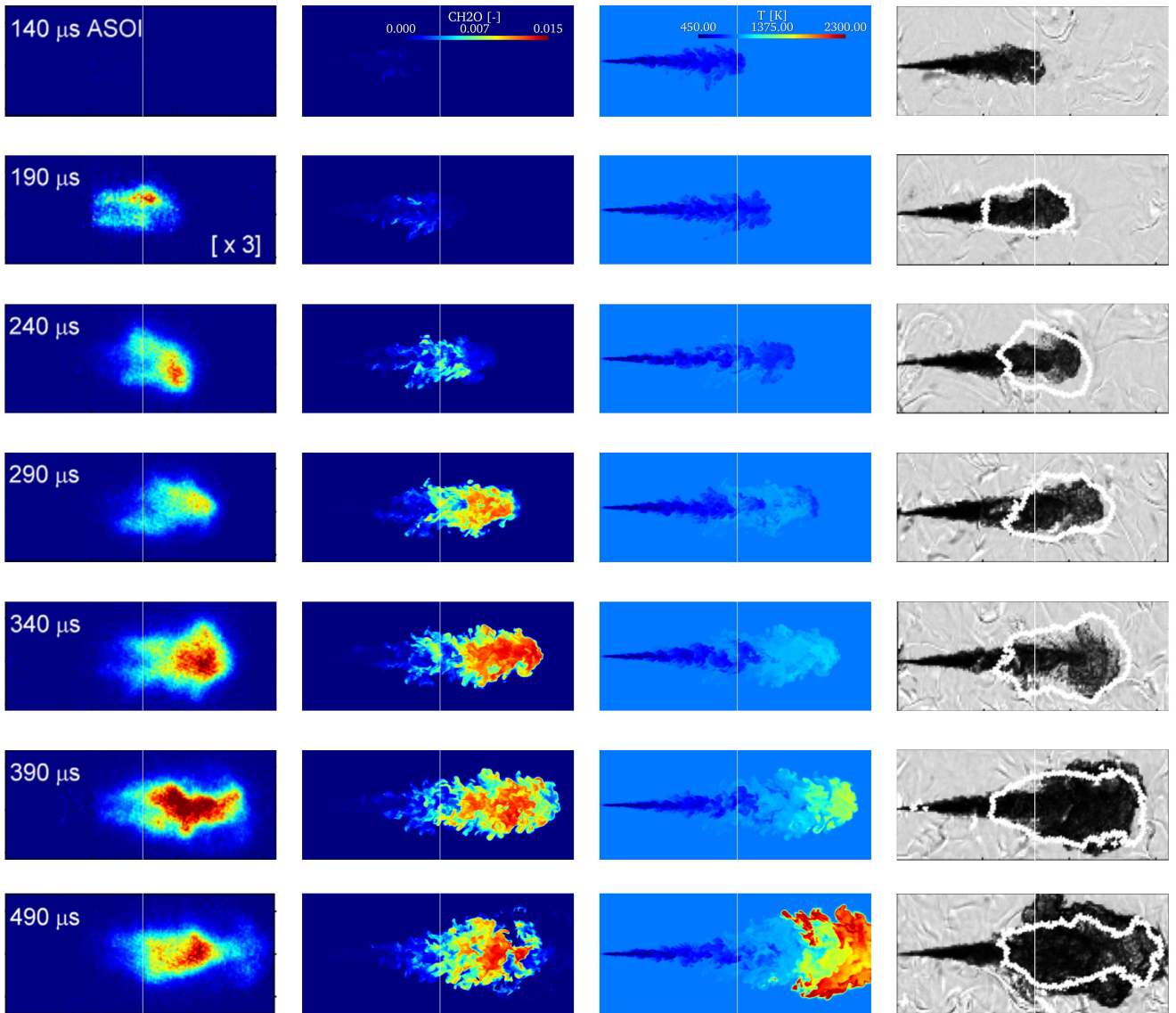


Figure 4.19: Experimentally obtained CH_2O PLIF data ([76], left column) in comparison with CH_2O mass fraction (second column from the left) and temperature distribution (third column from left) obtained from the simulation as well as the experimentally determined Schlieren signal with 10 % of the maximum PLIF signal obtained from the images in the left column represented by thick white border ([76], right column). Vertical white line denotes measured steady lift-off length [189]. Experimental data reprinted from Proceedings of the Combustion Institute Volume 35, Issue 3: Scott A. Skeen, Julien Manin, Lyle M. Pickett, Simultaneous formaldehyde PLIF and high-speed Schlieren imaging for ignition visualization in high-pressure spray flames, Pages 3167-3174, 2015, with permission from Elsevier.

of CH_2O is suggested by the LES but PAH species are not already build up. Downstream of this region, the PLIF signal shows high intensities, especially in the region where PAH species are predicted by the LES. With this, the simulation confirms the experimental assumption, that the spatial separation of the PLIF signal is caused by the spatial separation of CH_2O and PAH species [178].

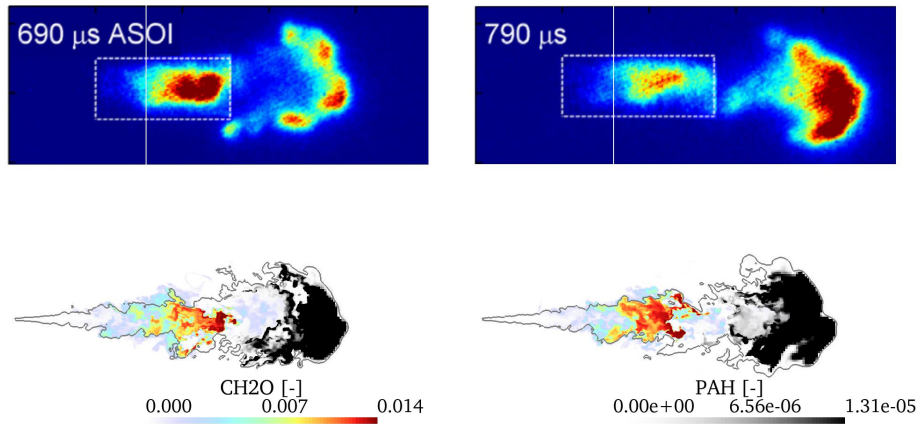


Figure 4.20: Experimentally obtained 355-nm PLIF data ([76], top row) in comparison with CH_2O and PAH mass fraction together with the iso-line of stoichiometric mixture obtained from the simulation (bottom row). Experimental data reprinted from Proceedings of the Combustion Institute Volume 35, Issue 3: Scott A. Skeen, Julien Manin, Lyle M. Pickett, Simultaneous formaldehyde PLIF and high-speed Schlieren imaging for ignition visualization in high-pressure spray flames, Pages 3167-3174, 2015, with permission from Elsevier.

A further characteristic obtained from high-speed 355-nm PLIF measurements [178] in this spray is the periodic behavior of CH_2O starting approximately at the instance of time, when it first reaches its maximum value initiating high temperature ignition. For earlier times, the CH_2O profile closely follows the mixture fraction boundary as previously shown in Figure 4.19. With this, it is produced and transported in mixture fraction space and afterwards consumed as discussed above. After reaching the point of high temperature ignition, the extend of CH_2O in axial direction follows a periodic behavior. This is shown in Figure 4.21 based on three instances of time chosen following Sim et al. [178]. In the top row, the detachment and consumption of CH_2O based on the PLIF data is shown. In the second row, the CH_2O and PAH species mass fraction is visualized. In the range of uncertainties of comparing single shot data against each other, similar structures are found. Especially the separation of CH_2O after it reaches its maximum is predicted in a similar spatial extend by the LES as seen in the PLIF signal. One explanation for this behavior found within the simulation results is the evolution of the mixture fraction field. In the shown instance of time, the distance between the lift-off length and the spray head became rather large. Inside the fuel vapor boundary, the detachment of fuel rich regions in a periodic manner is observed. These structure are very similar to that observed in the CH_2O profile. This leads to the conclusion, that the periodic structures detected within the PLIF signal is directly linked to the evolution of the mixture fraction field.

The similarity between the CH_2O and mixture fraction distribution can be explained by the underlying flame structure. In Figure 4.22, the predicted CH_2O mass fraction is shown as function of mixture fraction along the centerline starting from the measured lift-off length (marked by vertical line in Figure 4.21). When inspecting the evolution in this state space with regard to the distance to the nozzle, which is given by the color code of the data points, the following observations can be made: Near the lift-off length, rich mixtures with $Z > 0.15$ are present at moderate CH_2O mass fraction, depending on the time step. With

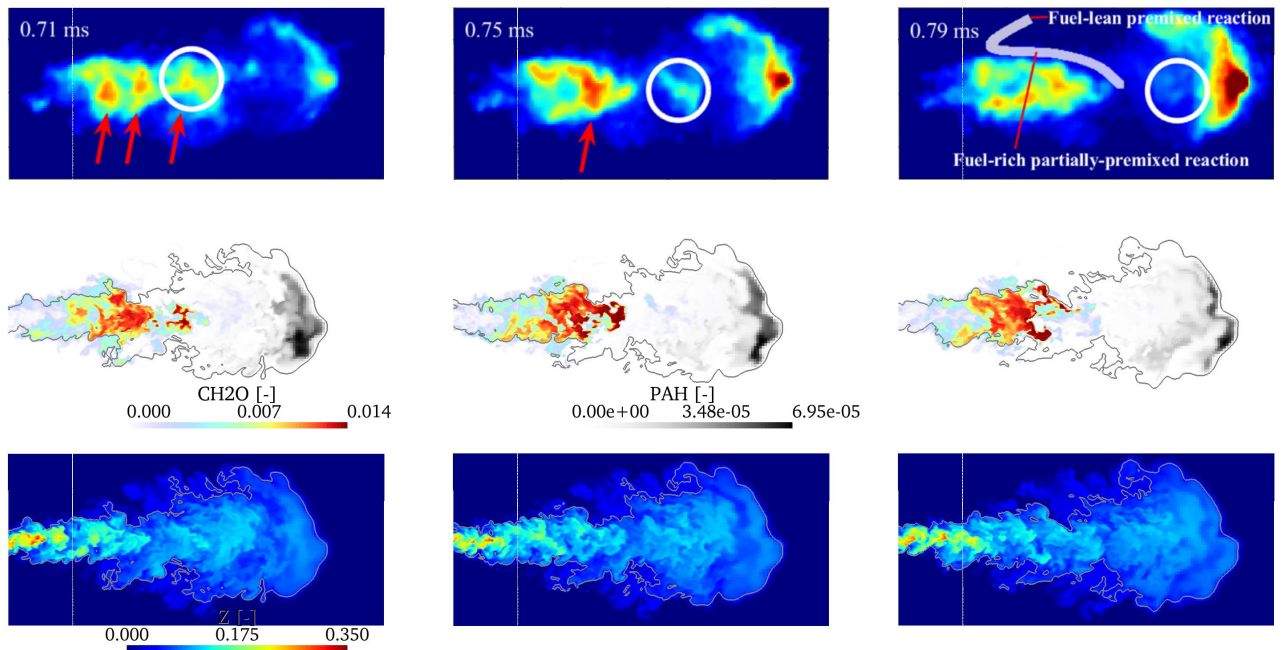


Figure 4.21: Instantaneous snapshots of experimental 355-nm high-speed PLIF data [178] (top row) and simulation data for the CH_2O and sum of $\text{C}_{16}\text{H}_{10}$ and $\text{C}_{18}\text{H}_{10}$ mass fractions (middle row) together with mixture fraction distribution obtained from the simulation (bottom row). The grey contour in the middle and bottom row represents stoichiometric conditions and the vertical white line denotes the measured steady lift-off length [189].

increasing distance to the lift-off length Δy_{lo} , the fuel/air mixture is getting leaner due to mixing processes and the CH_2O mass fraction increases. The latter fact can be attributed to the cool flame propagation from surrounding fluid elements. For a certain combination of CH_2O increase and equivalence ratio, a high reactivity is obtained leading to second stage ignition. This is shown based on the reaction progress variable source term $\dot{\omega}_{Y_{C,1}}$ which is given as contour in Figure 4.22 together with the maximum CH_2O mass fraction found within the ignition of a flamelet with $\chi_{st} = 1/s$. Obviously, the source term shows large values in the vicinity of the maximum CH_2O mass fraction. Both quantities depend furthermore on the mixture fraction. Most important here is the fact, that the maximum CH_2O mass fraction decreases with the mixture fraction and hence high CH_2O consumption rates are approached earlier. This explains the preservation of large CH_2O mass fraction, if fuel rich pockets detach from the jet core and furthermore the fast vanishing of CH_2O when these pockets are mixing with the surrounding gas leading to less rich mixtures.

This periodic behavior can be summarized in a condensed manner in a so-called I-y-t plot, defined as $I(y, t) = \int I(x, y, t) dx$, with $I(x, y, t)$ denoting the signal intensity, y the distance to the nozzle¹⁶ and x the lateral direction evaluated on the $x - y$ mid-plane (i.e. $z = 0$). The corresponding results are shown in Figure 4.23. On the left side, the experimental 355-nm PLIF signal is shown together with the first and

¹⁶In literature, x is usually used as distance to the nozzle and the corresponding plots are denoted by I-x-t plots. Due to the choice of the spray coordinate system in this thesis, y is used as distance to the nozzle to avoid confusion with the other plots shown in this chapter

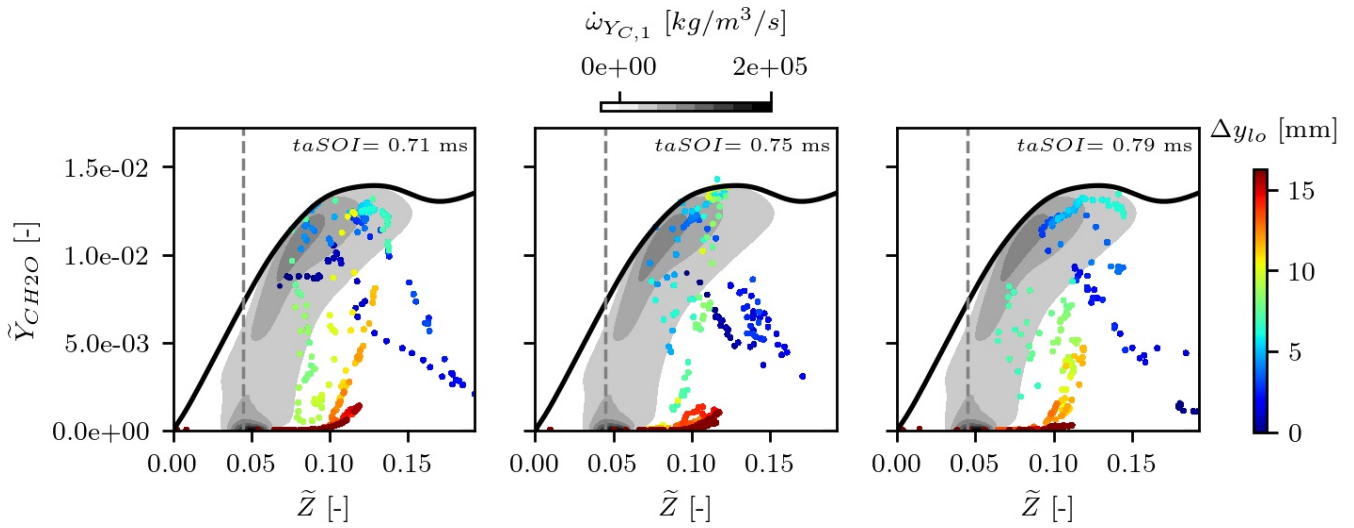


Figure 4.22: Scatter plot of the Favre-filtered CH_2O mass fraction as function of mixture fraction obtained from the LES color coded by the distance to the measured lift-off length Δy_{lo} for the three time instances shown in Figure 4.21. The black solid line denotes the maximum CH_2O mass fraction obtained in a flamelet calculation with $\chi_{st} = 1/s$ and the gray scale contourplot the corresponding reaction progress variable source term. Z_{st} is denoted by a dashed vertical line.

second stage ignition delay times and the time, at which maximum CH_2O was observed, together with the onset of the signal on the injector side and the discrimination line between CH_2O and PAH species suggested from the signal intensity and its spatial distribution. On the right hand side, the integrated mass fraction of CH_2O and PAH species is plotted together with the vapor penetration length obtained by the LES. Obviously, very similar structures are obtained, for the part of the experimental signal below the discrimination line. The periodic detachment of CH_2O is well replicated. Also the presence of PAH species predicted by the LES shows strong similarities. This lead to the conclusion, that the UFCPV approach is able to reproduce the experimental data very well for the ignition and pollutant formation over a the overall range of simulation time.

After this analysis of the flame structure in physical space, their projection into mixture fraction space is discussed in the next section.

4.5.6 Spray flame structure in mixture fraction space

Since the underlying flame structure is directly connecting the thermo-chemical state among the progress variable and scalar dissipation rate to the mixture fraction, the inspection of the spray flame in mixture fraction space gives further insides into the ignition and pollutant formation process. It answers the question, which parts of the flamelet manifold is effectively addressed within the spray flame simulation and which consequences this have. Since the ignition of the spray flames is taking place in an evolving mixture fraction field, this analysis is performed for four representative times after start of injection selected from Figure 4.19 and in addition for 1.00 ms after start of injection where parts of the flame are in statistically steady state. For

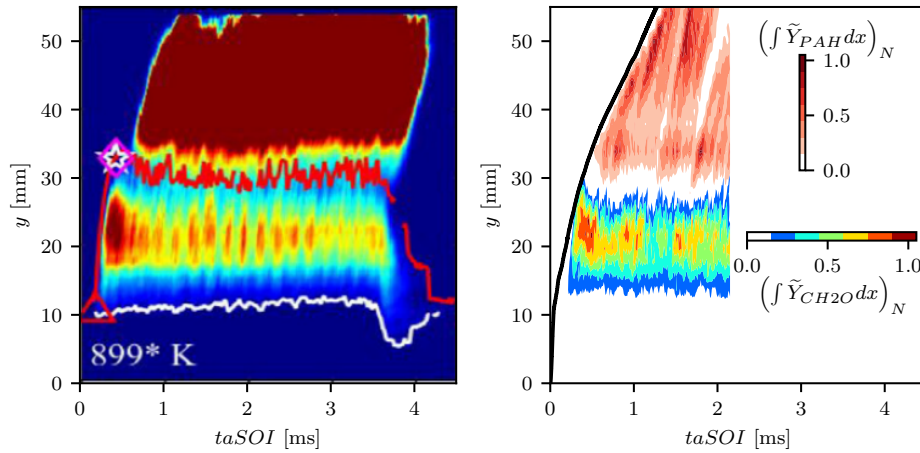


Figure 4.23: I-y-t plot of the measured 355-nm high-speed PLIF signal ([178], left) for the ECN Spray A together with simulation data for the CH_2O (lower part of the right diagram) and PAH as sum of $\text{C}_{16}\text{H}_{10}$ and $\text{C}_{18}\text{H}_{10}$ mass fraction (upper part of the right diagram) integrated in lateral direction along the mid-plane of the spray and normalized by its maximum value (right). The vapor penetration obtained from the simulation is indicated by a black line in the right plot.

all time instances shown, a decrease in temperature below the adiabatic mixing line due to the evaporation of the liquid fuel is observed with the lowest temperature present at approximately $\tilde{Z} = 0.1$. This effect is observed for nozzle distances up to around 10 mm (dark blue scatter), which corresponds approximately to the liquid penetration length. With increasing nozzle distances, CH_2O is produced in the lean part of the flame and transported in mixture fraction space leading to a moderate temperature increase. The possible residence time for this evolution is limited by the fuel vapor propagation in the early stages of its evolution, which is well noted when comparing the plots for 0.24 ms and 0.34 ms after start of injection. During the further evolution of the spray, CH_2O is consumed at $\tilde{Z} \approx 0.1$ where second stage ignition is initiated. First fluid elements reach this state for 0.39 ms after start of injection, shortly prior to the experimental observed ignition delay time of 0.41 ms [189]. As previously shown in the inspection of single flamelet solutions and within the Lagrangian flamelet model, the ignition for larger residence times is then determined by a consumption of CH_2O and high temperature ignition proceeding towards stoichiometric conditions, where the steady flame structure shows its maximum temperature. At the same time CH_2O is further produced and transported towards further fuel rich regions. These are, however, limited by a value of around $\tilde{Z} = 0.1$ with most of the fluid elements at mixture fraction values below 0.2. It should also be noted, that only fluid elements with $\tilde{Z} < 0.15$ are present at large distance to the nozzle, which is due to the mixing of the vaporized fuel jet with the surrounding oxidizer. This together with the fact that the CH_2O production, transport and consumption for this very rich mixtures takes place at large time scales leads to the absence of elevated temperature states for $\tilde{Z} > 0.15$, even at 1.00 ms after start of injection. This finally affects the distribution of NO and PAH species. NO is produced within a range of a around $\Delta Z = 0.05$ around stoichiometry with a peak value at $Z = Z_{st}$ which is well within the ignited region in mixture fraction space. The absence of ignited fluid elements in very rich regions on the other hand limits the PAH peak value directly and with this the potential soot formation. In the following section, the resulting spatial distribution

of NO and PAH species is used draw a comprehensive overview of the ECN Spray A structure.

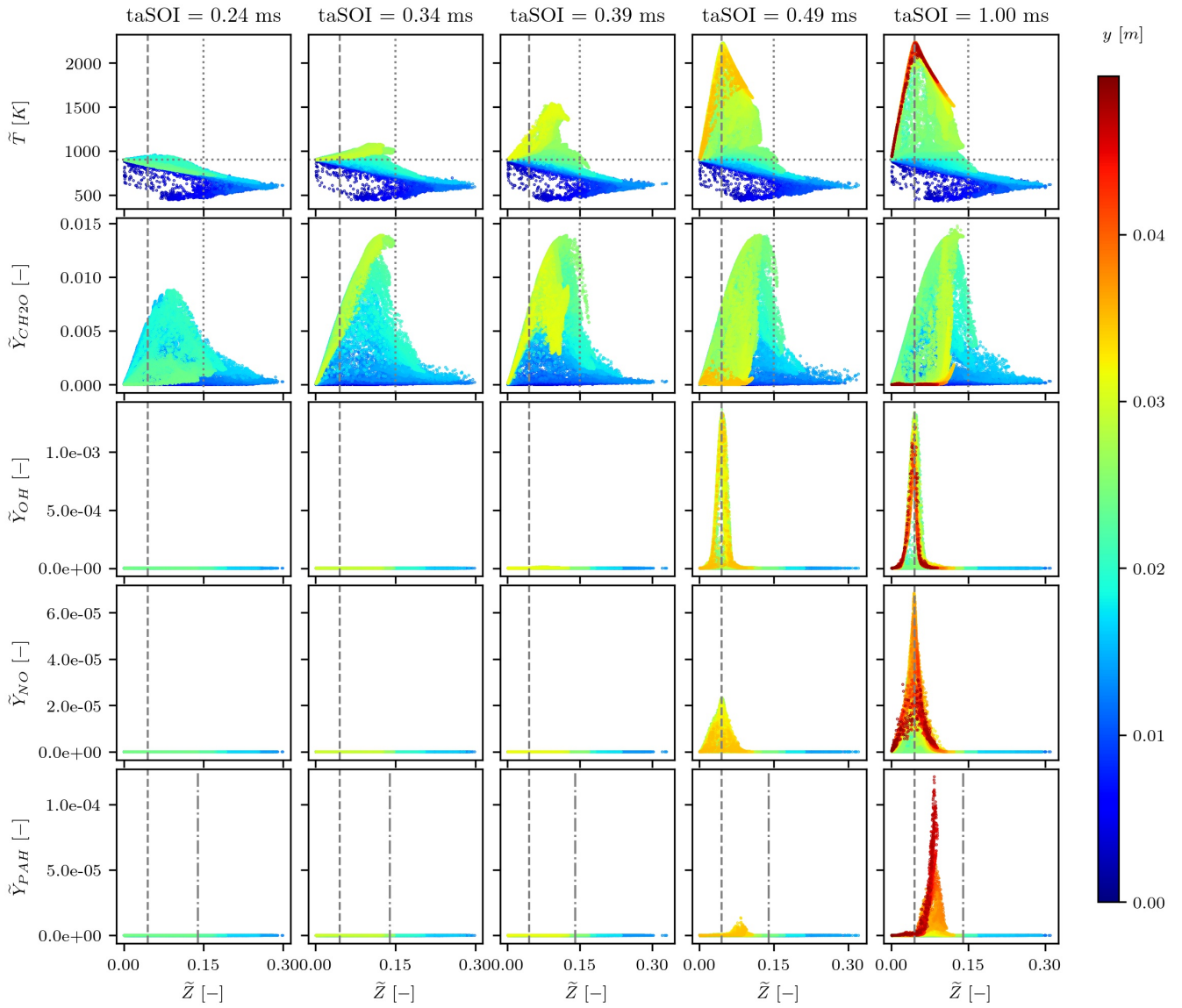


Figure 4.24: Scatter plot of Favre-filtered temperature and CH_2O , OH, NO, and PAH mass fraction (top to bottom, respectively) in mixture fraction space for the ECN Spray A color coded by the distance from the nozzle for distinct times after start of injection together with the location of stoichiometric mixture $Z_{st} = 0.045$ (vertical dashed line), the chamber temperature (horizontal dotted line in the first row), $Z_{ign} = 0.15$ (vertical dotted line in first and second row) and $Z_{PAH,max} = 0.14$ (vertical dashed-dotted line in bottom row).

4.5.7 Summary of the ECN Spray A flame structure

Based on the validated model and the investigation of the spray evolution from first to second stage ignition up to the formation of soot precursor, a comprehensive summary of the ECN Spray A spray flame structure at distinct times after start of injection is presented in the following. For this purpose, the structure of

the spray is shown by means of Favre-filtered temperature and CH_2O , OH, NO and PAH species mass fraction in Figure 4.25 for three instances of time after start of injection. Within this figure, the parcel denoting the liquid phase are shown together with the injector they are originating from. Furthermore, the contour of stoichiometric mixture is colored by the temperature. The discussion of this picture follows the cause-effect-chain of the diesel fuel injection: The liquid fuel is originating from the injector and disintegrates into ligaments and subsequently smaller droplets which undergoes phase change driven by the heat transfer from the high temperature gas in the surrounding until most the fuel is present in the vapor phase downstream of the liquid length (left vertical black line in Figure 4.25). The vaporized fuel then mixes with the surrounding gas phase, leading to a spreading of the turbulent fuel jet. With increasing distance to the nozzle and hence increasing residence times, the auto-ignition process evolves. After first intermediate species are formed, CH_2O is produced close upstream of the experimental steady lift-off length in lean mixtures and subsequently evolves towards rich mixtures. Its subsequent consumption leads to a strong increase in temperature, denoting the second stage ignition. This is especially obvious in the right plot of Figure 4.25 where parts of the flame are in statistically steady state. Having a look on the further evolution of the spray flame at 1.00 ms after start of injection, the appearance of OH is visible near stoichiometric and slightly lean conditions as soon as temperature has increased. The production of NO takes place further downstream due to its larger time scale compared to the OH formation but also in near stoichiometric and slightly rich conditions. The PAH species on the other hand are produced more downstream than NO and in more rich conditions. Note, that the findings concerning the initiation of second stage ignition via CH_2O and the subsequent production of OH are in line with several studies found in literature. However, the discussion concerning NO and PAH species are only little investigated in spray LES in such detail.

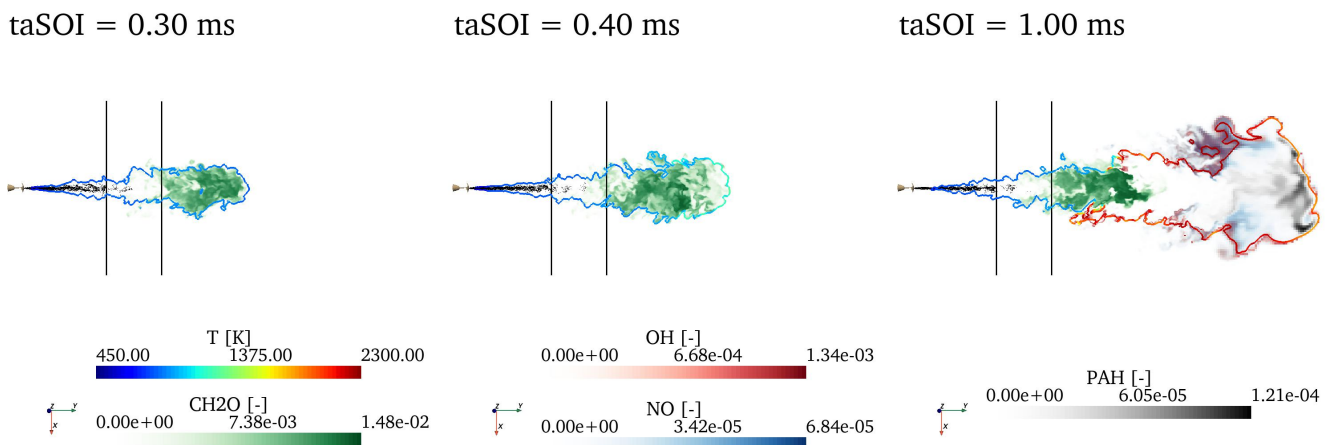


Figure 4.25: The structure of the ECN Spray A from injection to gaseous pollutant formation. Black dots denote parcel representing the liquid phase. The contour denotes stoichiometric conditions color-coded by the temperature. The left vertical line denotes the measured liquid penetration and the right vertical line the measured lift-off length, respectively.

4.6 ECN Spray D

After the UFCPV approach without incorporating the unstable solutions of the S-curve was validated based on the ECN Spray A injector and used to explain the evolution of the spray flame from ignition to gaseous pollutant formation, its applicability for the simulation of the ECN Spray D is assessed in the following section. This starts with the investigation of the mixture formation which is directly compared to the Spray A results. The resulting ignition behavior is investigated subsequently. This is followed by the validation of the local flame structure proposed by the UFCPV approach against the so far unpublished 355-nm high-speed PLIF signals obtained by Weiß et al. [179] on single shot basis as well as on the derived I-y-t plot. The section closes with an overview of the Spray D flame as done for Spray A in the last section.

4.6.1 Mixture formation under reactive conditions

In the following section the mixture formation within the Spray D is investigated and compared to that of the Spray A. In Figure 4.26, a comparison of the penetration lengths obtained from the experiments and simulations are shown. Due to the higher rate of injection, see Figure 4.3, the steady liquid penetration length of the ECN Spray D is approximately twice the penetration length of the ECN Spray A. This trend is correctly predicted by the simulation. The slight overshoot in the liquid penetration visible for Spray D starting from 0.10 ms shows the challenge of predicting correctly the transition from the ballistic operation of the injector during the opening phase and the steady penetration length establishing at full-lift of the injector needle. This also affects the vapor penetration, which overestimates the experimentally determined vapor penetration in a short time interval from 0.10 ms until 0.25 ms. Note, that same trends were observed in the simulation of this spray by Ong et al. [79] obtained by a similar simulation strategy. After this first time period, the quasi steady liquid penetration establishes within the simulation showing a well agreement with the experimental data. Due to the higher momentum flux in case of Spray D, the vapor penetration evolves also much faster compared to the Spray A injector. Again, the simulation framework is able to predict the experimental data in reasonable agreement with a slight overestimation after approximately 1.00 ms which are attributed to the mesh coarsening shown in Figure 4.2 reached by the vaporized fuel at this time. A comparison of the mixture fraction field is given in the right part of Figure 4.26 for a time of 0.35 ms after start of injection. Note, that this time is prior to the main ignition of both sprays. Obviously, the fuel rich core is much longer in case of Spray D than within the Spray A. It can be found, that the mixtures along the spray axis are much richer compared to the Spray A. In especial, fuel rich mixtures with values greater than $Z > Z_{ign} = 0.15$ dominate along the spray axis in case of Spray D. Furthermore, higher gradients of the mixture fraction are observed at the tip of the Spray D. This influences the ignition behavior significantly as shown in the next section.

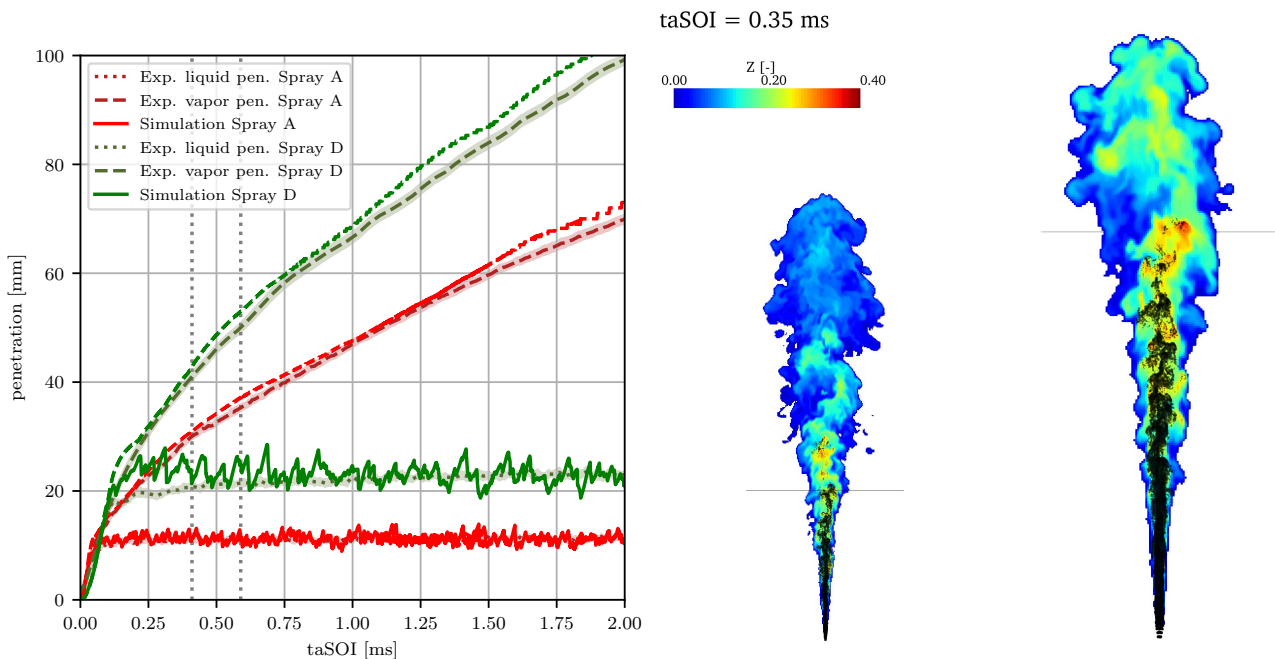


Figure 4.26: Left: Comparison of the vapor (dashed lines) and liquid penetration (solid lines) lengths for ECN Spray A (red colored) and ECN Spray D (green colored) under reactive conditions between simulation (light colored) and experiments (dark colored) obtained by Schlieren measurements ([189] for Spray A, [192] for Spray D), Mie scattering for Spray D [193] and diffused back-illumination (DBI) [191] for the non-reactive Spray A case (see Figure 4.13) and experimentally determined ignition delay time of 0.41 ms ([189] for Spray A, left gray dotted vertical line) and 0.59 ms ([193] for Spray D, right gray dotted vertical line). The experimental standard deviation is marked shadows in corresponding color. Right picture: Mixture fraction for Spray A (left) and Spray D at $taSOI=0.35$ ms together with the steady liquid penetration lengths from Mie measurements (see left figure, black lines) and numerical parcel representing the liquid phase (black dots).

4.6.2 Ignition characteristics

The influence of the mixture formation on the ignition behavior is illustrated in Figure 4.27 based on the spatial distribution of the mixture fraction and OH mass fraction. The chosen time instances correspond to a time short after the experimentally obtained ignition delay time for Spray A (0.41 ms [189]), at the ignition delay time for ECN Spray D obtained from the simulation (0.48 ms, see Figure 4.28) and obtained from the experiments (0.59 ms [193]) as well as an instance of time where parts of the spray flames are in quasi steady state. The OH mass fraction color code is limited in a narrow range above 2 % of the maximum OH mass fraction for visualization purpose. At the first time shown, the Spray A still ignited and the occurrence of OH can be observed over a part of the spray head and of the spray flank. During the subsequent development of the spray, OH appears in further upstream regions at the spray flank until the steady lift-off length is reached. Furthermore, OH is observed in regions near the spray axis, depending on the local mixture fraction distribution. In statistically steady state, OH is found over a wide part of the spray flank having a relatively large radial extend. In contrast, no OH is visible for the Spray D at 0.45 ms above

the chosen threshold. At 0.55 ms, OH is observed at the different positions at the spray flank. Furthermore, there is no clear evolution of the OH mass fraction visible like in the Spray A but a rather distributed ignition across the entire spray flank. This behavior is well known from experimental [78] and numerical [79] studies in literature and its replication serves as qualitative validation of the current modeling approach. At latter times after start of injection, OH is visible along the entire spray flank and in very narrow region around the entire jet. This is also the case for Spray A. Compared to the overall spray volume, the regions in which OH occur are more narrow for Spray D in comparison to Spray A.

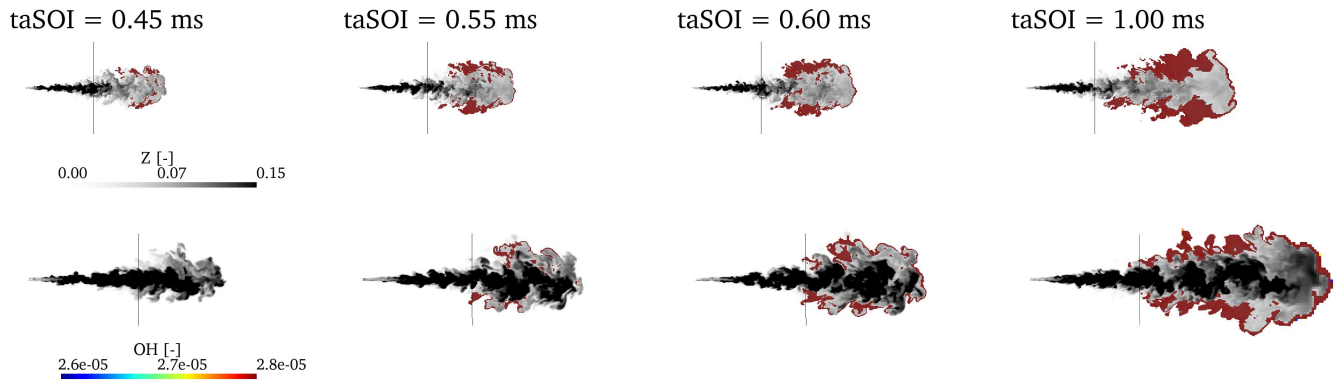


Figure 4.27: Time sequence of mixture formation and OH distribution during the injection from ECN Spray A injector (top row) and ECN Spray D injector (bottom row) together with the steady lift-off lengths obtained from the experimental data ([189] for Spray A and [193] for Spray D). The maximum color for mixture fraction correspond to $Z = Z_{ign} = 0.15$ while the limits for OH are set to 2 % of the maximum OH mass fraction value obtained during the simulation and slightly above.

To evaluate the ignition delay time, the evolution of the maximum temperature and OH mass fraction over time is given in Figure 4.28. From the experimental data, a delayed ignition for the ECN Spray D in comparison to the ECN Spray A of approximately 0.18 ms is observed. The simulations, evaluated based on 50 %¹⁷ of the maximum OH mass fraction obtained during the simulation show very good agreement for the ECN Spray A as shown in the last section and an underprediction of approximately 20 % compared to the experimental data for the Spray D. It can be stated, that the delay in the ignition for the increased nozzle hole injector is reproduced by the simulation while a deviation in its absolute value preserves. One possible reason might be the neglect of the enthalpy source term due to phase change of the liquid fuel onto the flame structure. Its influence might be more pronounced than in the Spray A due to the higher mass flow rate. To investigate, if the spatial structure of the spray is reproduced correctly, a validation based on 355-nm PLIF data [179] is performed within the next section.

4.6.3 Spray flame structure in physical space

In Figure 4.29, the spatial distribution of the 355 nm-PLIF signal [179] is compared to the simulation data of CH_2O mass fraction, temperature and OH mass fraction for four selected times after start of injection. For

¹⁷Threshold value chosen to avoid distortion arising from small numerical perturbations

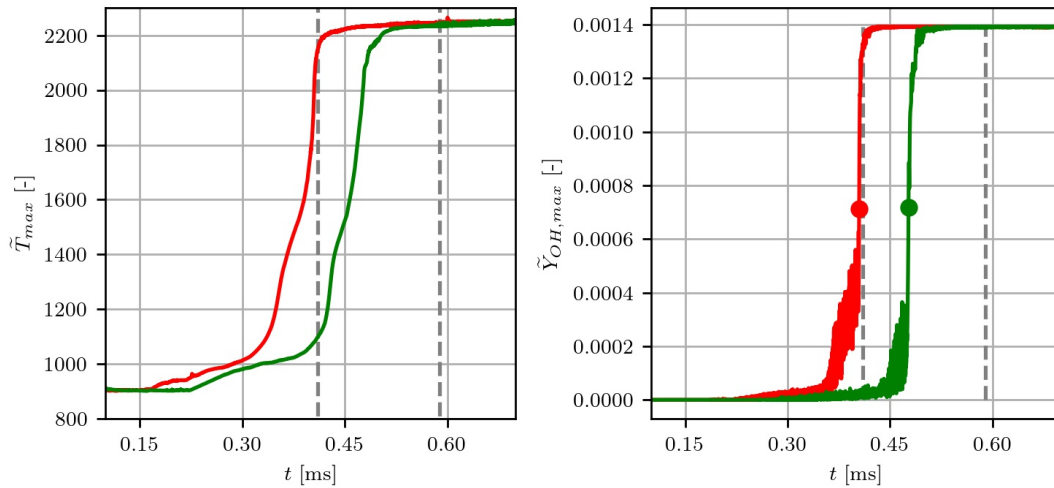


Figure 4.28: Evolution of the maximum temperature and OH mass fraction during the simulation for the ECN Spray A (red line) and ECN Spray D (green line) together with the experimentally determined ignition delay time of 0.41 ms (left vertical gray dashed line, [189]) for Spray A and 0.59 ms for Spray D (right vertical gray dashed line, [193]). The ignition delay times obtained from the LES based on 50 % of the maximum OH mass fraction are marked by filled circles and given by 0.40 ms for Spray A and 0.48 ms for Spray D.

the first time step (0.4 ms), the experimental data are within the phase of CH_2O production and transport which proceed during the second and third time step (0.48 and 0.58 ms) after which the consumption takes place denoted by a decrease of the PLIF signal at 0.60 ms near the experimentally determined steady lift-off length and at the spray flanks. Since the ignition delay time is underpredicted by the simulations by 0.11 ms only the first time shown corresponds to the production phase of CH_2O with moderate temperature increase and neglectable OH mass fraction. The second time step shown corresponds to the ignition delay time estimated from the simulation. At this time, CH_2O is consumed at various locations around the spray flank ranging in axial direction from the experimentally obtained steady lift-off length up the spray head. At the spray head, the CH_2O consumption takes place in certain locations close to the spray axis, too. After the second stage ignition, high values of the CH_2O mass fraction are predicted near the spray axis and small values at the spray flanks are connected to high temperatures and OH mass fractions denoting its consumption in these regions. The spatial extend of the PLIF signal and the simulation results agree very well after ignition (last row in Figure 4.29). Especially, as shown in Figure 4.29 based on the OH mass fraction and temperature distribution, the steady lift-off length is met very well. This also holds for the comparison of the experimental data with that of the simulation shifted by 0.11 ms, i.e. the underestimation in the ignition delay time. Hence, the spatial structure is reproduced properly by the simulation framework and the deviations are limited to a prediction of too early activation of chemical reactions. To investigate this hypothesis, further time instances of the PLIF signal are compared with the CH_2O mass fraction obtained from the simulation during the onset of PAH species formation in the following.

In Figure 4.30 a time series of the PLIF signal and the simulation results for the CH_2O and the PAH mass fraction starting from 0.70 ms after start of injection and ending at 0.88 ms with 0.06 ms between each

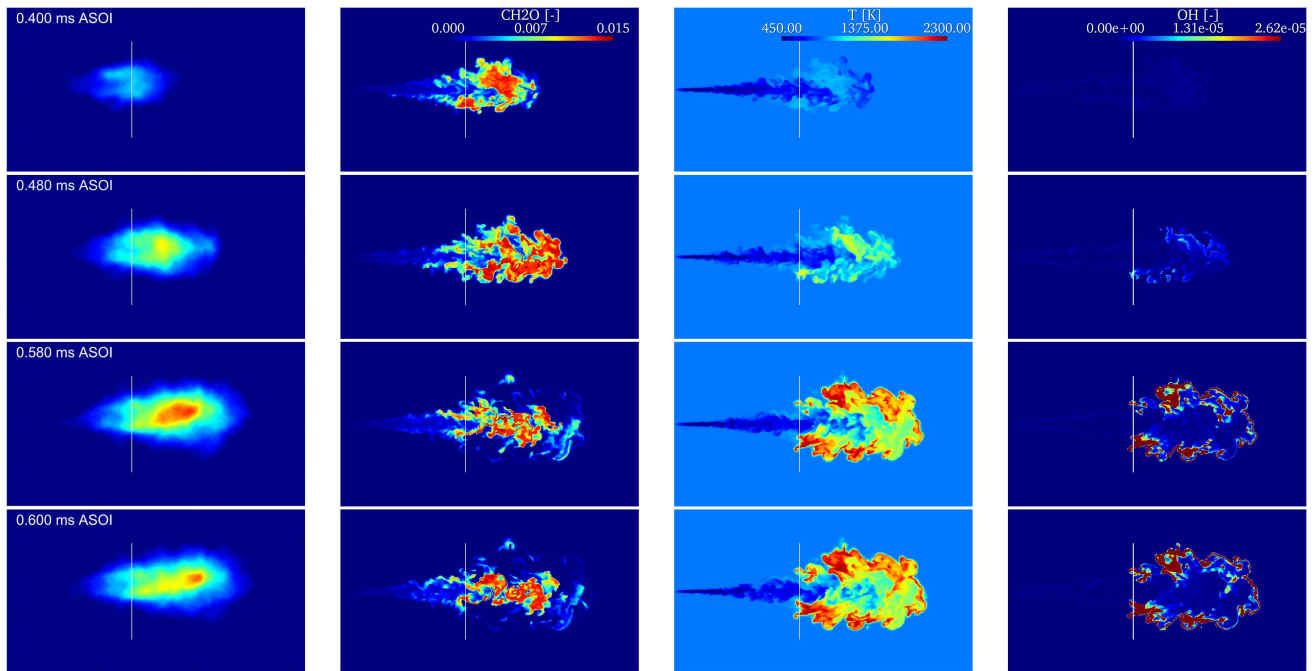


Figure 4.29: Experimentally obtained 355 nm-PLIF data ([179], left column) in comparison with CH_2O mass fraction obtained from the simulation (second column from the left), temperature distribution (third column from left) and OH mass fraction (right column, color code limit to 2% of its maximum value) obtained from the LES. Vertical white line denotes measured steady lift-off length [193].

frame is shown. Based on the findings above, the simulation data are shifted by 0.11 ms to account for the underprediction in the ignition delay time. Thus, the experiments and the simulations are shown for the same times after their corresponding ignition occurred. Obviously, the left border of the PLIF signal coincides approximately with the CH_2O mass fraction, even though a small amount of CH_2O is visible in the near nozzle region. However, since the shown comparison is biased by the difference between the PLIF signal and CH_2O mass fraction as well as chosen colorbar scale, these results can be seen as a reasonable validation of the CH_2O evolution in the vicinity of the lift-off length. Also the spatial extend of high signal intensity regions coincides with the location of high CH_2O mass fractions. Furthermore, the surrounding region of low PLIF intensity can be found in the region, where CH_2O consumption is predicted by the simulation. As discussed previously for the late evolution of the Spray A, the PLIF signal also stems from PAH species with increasing time after start of injection. This is again confirmed by the PAH mass fraction obtained from the simulation. It is of low quantitative amount at 0.71 ms and subsequently build up to large amount in lateral parts near the spray head. At the corresponding time within the PLIF signal of 0.82 ms after start for injection, an increase in the signal is observed at two branches within the spray head. These structures can be found in the simulation as the detachment of two CH_2O pockets and the subsequent formation of PAH species. This structure then evolves in terms of increasing intensity at the branches, while an increase in PAH mass fraction is predicted by the simulation in similar regions. However, the connection of these branches is not that obvious within the simulation. This can on the one hand be attributed to the comparison of single uncorrelated injection events between simulation and experiment and on the other hand might again be an

artefact the direct comparison of the PLIF signal to species mass fractions and hence does not necessarily indicate a mismatch of the predicted spray flame structure. In summary, the overall agreement between the structures found in the PLIF signal and the simulation results when shifted to equal times after ignition confirms again, that the underestimation of the ignition delay is however connected to a reasonable flame structure with chemical reactions still establishing too fast.

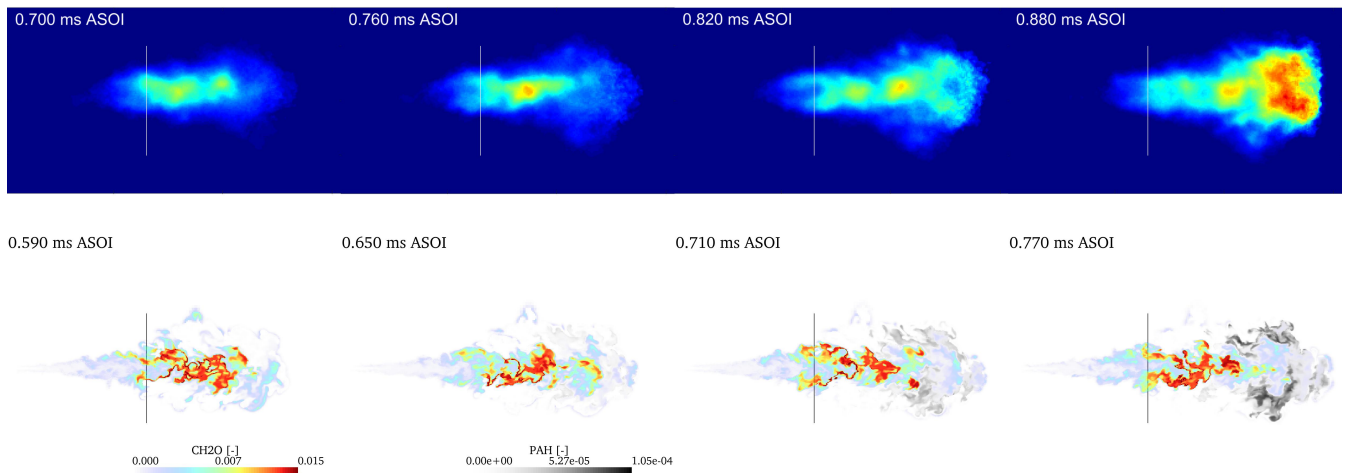


Figure 4.30: Time sequence of high-speed 355-nm PLIF data [179] for the ECN Spray D injector (top row) together with simulation results for CH_2O and PAH species mass fractions (bottom row)

One characteristic in the CH_2O and PAH distribution within the Spray D is that both are located at same axial location on different radial distance to the spray axis. Note, that this is not the case for the Spray A, see Figure 4.20. This leads to an overlap when the overall set of high-speed PLIF images are collected into the I-y-t plot, as described above for the Spray A in Section 4.5.5. This plot is shown in Figure 4.31 together with the one obtained from the mass fractions of CH_2O and PAH species predicted by the simulation. In the experimentally obtained plot, a clear overlap of the lower moderate signal and intense upper part of the signal is visible. The corresponding plot, obtained from the simulation results shows a similar structure. In especial, the region of low intensities of the PLIF data corresponds well with the area in which CH_2O is found in the simulation. The high intensity region on the other hand corresponds to the regions, where PAH is predicted by the simulation. However, the extension of this high intensity regions are wider and show a larger overlap with the low intensity region than the CH_2O and PAH mass fraction predicted by the simulation. This is again attributed to the uncertainties in the comparison of PLIF signal and mass fractions. However, together with the single frame data comparison shown above, the spatial flame structure looks very close to the experimental data.

The validation of the mixture formation within the Spray D as well as the spatial flame structure indicates a proper flame assumption made during the look-up table generation. This allows a meaningful inspection of the flame evolution in mixture fraction space. As shown previously for the Spray A, a better understanding of the influence of the mixture formation on the ignition and pollutant formation characteristics can be established by this means, which is presented in the next section.

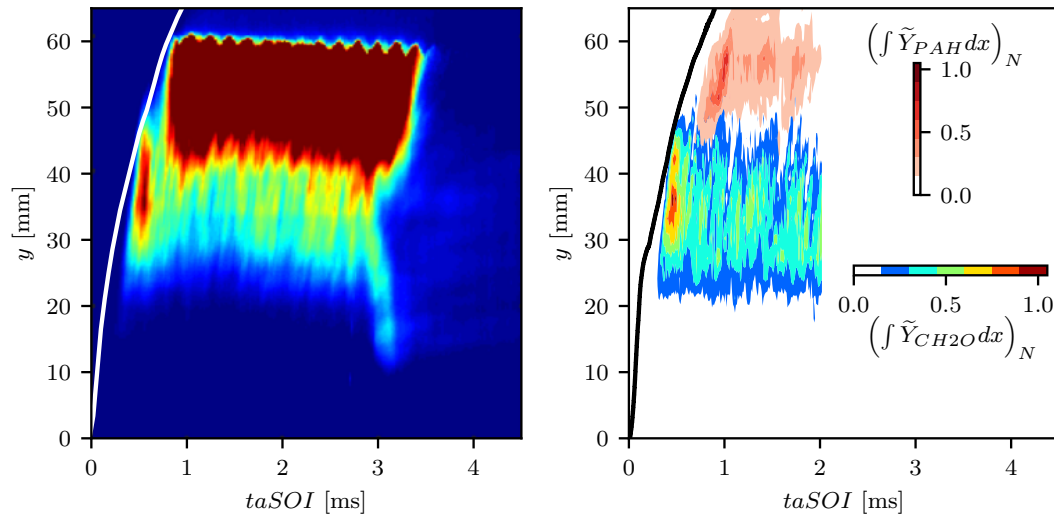


Figure 4.31: I-y-t plot of the measured 355-nm high-speed PLIF signal ([179], left) for the ECN Spray D together with simulation data for the CH_2O (lower part of the right diagram) and PAH as sum of $\text{C}_{16}\text{H}_{10}$ and $\text{C}_{18}\text{H}_{10}$ mass fraction (upper part of the right diagram) integrated in lateral direction along the mid-plane of the spray and normalized by its maximum value (right). The solid lines represent the measured (white line in left plot, [192]) vapor penetration and the one obtained from the simulation (black line in right plot)

4.6.4 Spray flame structure in mixture fraction space

After investigating the spatial structure of the Spray D flame, its evolution in mixture fraction space is performed within the following section. For five different instances of time after start of injection the temperature as well as the mass fraction of CH_2O , OH , NO as well as PAH is shown in Figure 4.32. For all times shown, fuel-rich mixtures are observable over a wider range of axial distance to the nozzle as it was previously observed for the Spray A. Hence, also the CH_2O propagation in mixture fraction space can proceed to more fuel-rich mixtures leading second stage ignition there. At 0.24 ms, small amounts of CH_2O are build up at the lean part of the spray and evolve towards the fuel-rich part. The peak value of CH_2O is subsequently reached for many fuel-rich fluid elements at 0.39 ms. These points are, however not located at the spray tip, but at intermediate axial nozzle distances, shown by the mostly yellow colored scatter with highest CH_2O mass fraction in the second row of Figure 4.32. This behavior also persists for subsequent times, at which the fluid elements at the spray tip reach the maximum CH_2O values, while the CH_2O consumption and second stage ignition is still initiated for fluid elements at intermediate heights. After 0.59 ms, there are fluid elements for each axial position that have experienced second stage ignition. However, ignition is limited to fuel/air mixtures with $Z < Z_{ign} = 0.15$. This underlines in particular the argumentation in the physical space that no ignition takes place at the fuel-rich parts along the axis of the spray. As shown within the spatial analysis of the spray, very rich fluid elements still persists until high distance to the nozzle. For them, CH_2O increases but is not consumed even for distances to the nozzle of 60 mm as shown for 1.00 ms. It can be stated, that the existence of fuel rich mixtures, i.e. with $Z > Z_{ign}$ lead to high CH_2O mass fraction increasing with the residence time. NO is observed at the similar peak values as

compared to the Spray A, since near stoichiometric fluid elements are present at large axial distances and high temperatures. Moreover, the presence of rich mixtures at large axial distance from the nozzle leads to the presence of PAH species with high mass fraction. The location of the peak to the left of $Z_{PAH,max}$ for all time points shown also indicates that the evolution of PAHs extends into more rich parts of the flame. This was not the case for Spray A, where the maximum PAH mass fraction in mixture fraction space is limited due to the faster mixing process. The spatial distribution and absolute effect on quantitative pollutant formation will be discussed in the next section.

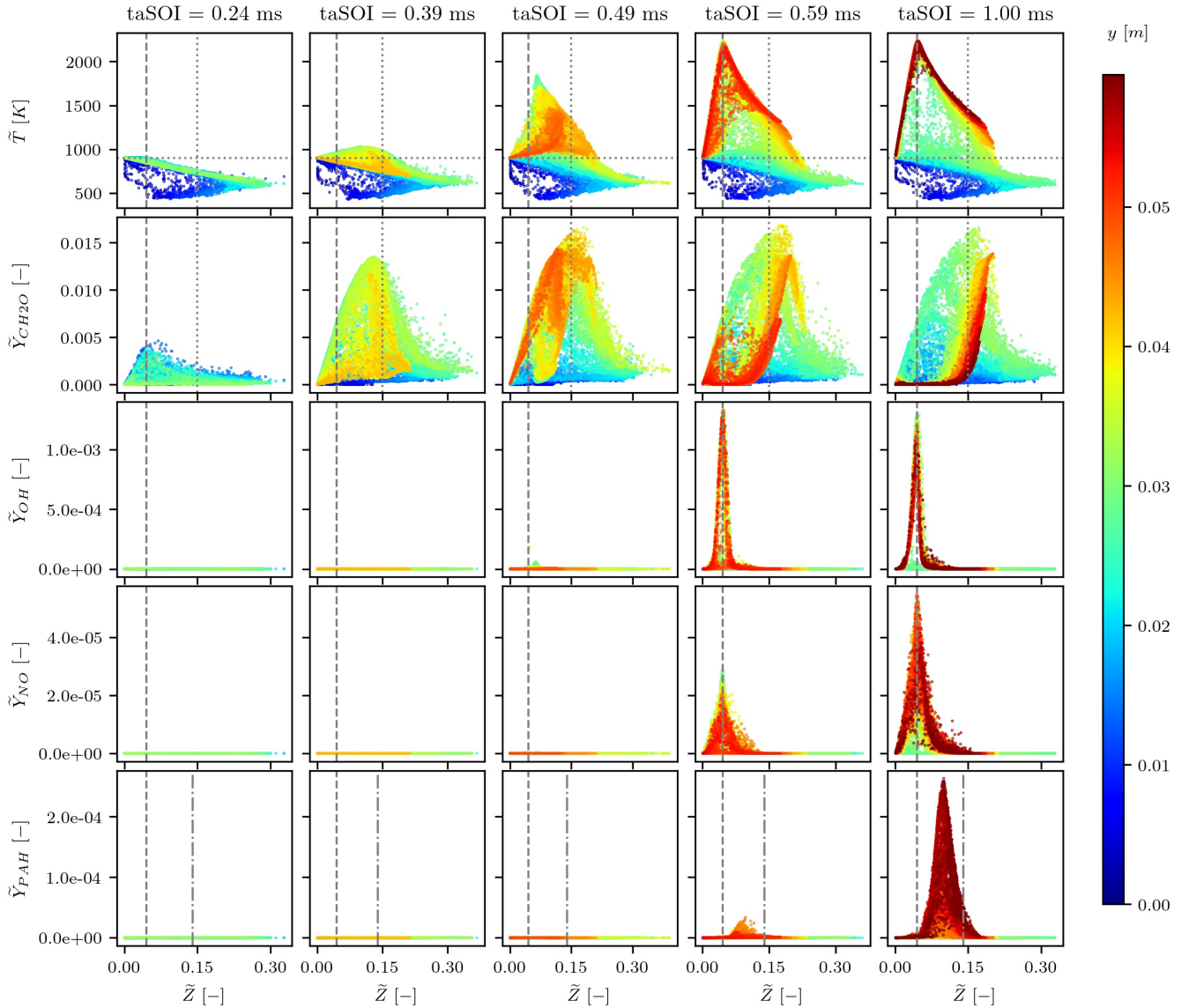


Figure 4.32: Scatter plot of Favre-filtered temperature and CH_2O , OH, NO, and PAH mass fraction (top to bottom, respectively) in mixture fraction space for the ECN Spray D color coded by the distance from the nozzle for distinct times after start of injection together with the location of stoichiometric mixture $Z_{st} = 0.045$ (vertical dashed line), the chamber temperature (horizontal dotted line in the first row), $Z_{ign} = 0.15$ (vertical dotted line in first and second row) and $Z_{PAH,max} = 0.14$ (vertical dashed-dotted line in bottom row).

4.6.5 Summary of the ECN Spray D flame structure

Based on the findings concerning the spatial structure during the ignition process and the corresponding evolution in mixture fraction space, the structure of the ECN Spray D during ignition is summarized in Figure 4.33. As in the Spray A, the penetration of the liquid phase proceeds until the liquid penetration length is reached. Slight upstream of the liquid penetration length, CH_2O begins to build up and evolves towards the axis of the spray. Along the axis, CH_2O persists over a large distance downstream the lift-off length until it is consumed followed by the formation of PAH at the spray head. The ignition itself takes place at the spray flanks where large values of OH and NO can be found. Herein, OH is directly present at large fractions, while the NO mass fraction is increasing with the distance to the nozzle. NO itself is also present in slight rich parts of the flame partially overlapping with the PAH species. Hence, going from the spray axis outwards in radial direction one finds CH_2O at the axis followed by soot precursor if the distance to the nozzle is large enough. Further out, NO is found together with an inherited OH structure under approximately stoichiometric conditions. This holds until the intact CH_2O core persists. Downstream of it at the spray head, PAH species are mainly found with largest fractions at the periphery which are connected to upstream fluid elements from the peripheries of the fuel-rich core region.

taSOI = 0.30 ms

taSOI = 0.55 ms

taSOI = 1.00 ms

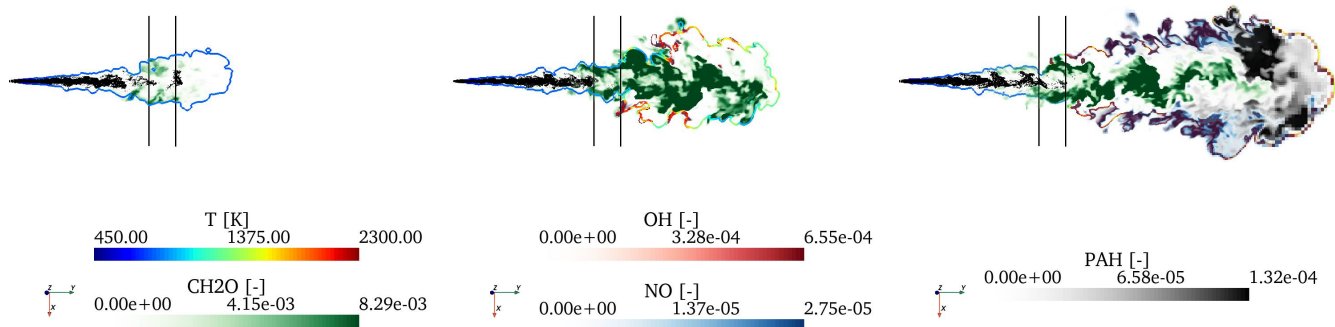


Figure 4.33: The structure of the ECN Spray D from injection to gaseous pollutant formation. Black dots denote parcel representing the liquid phase. The contour denotes stoichiometric conditions color-coded by the temperature. The vertical lines denote the measured liquid penetration and lift-off length, respectively.

4.7 Summary

In this section, the LES-UFCPV approach is examined within the ECN Spray A and Spray D injector and corresponding nominal conditions. This includes first an inspection of the flamelet solutions used to build look-up table and subsequently the verification of the model in the LFM. Before the application to the spray flames, the LES-UFPV was validated in advance for the Spray A as a reference. This includes a discussion of the influence of the scalar dissipation rate influence on ignition and the validity of leaving out the unstable branch of the S-curve. The LES-UFCPV approach was further utilized to simulate of the ECN Spray A. The spatial flame structure was investigated in detail based on 355-nm PLIF signals [76, 178]. A flame structure analysis is performed followed by an overview of the Spray A flame including the relevant effects from injection to pollutant formation. The application to the Spray D injector was performed subsequently utilizing the so far unpublished 355-nm PLIF data [179] for validation purposes. Following the Spray A investigation, the ignition process is analyzed in mixture fraction space and a subsequent overview of the Spray D structure is given.

The inspection of the look-up table revealed thereby the following findings:

- The ignition delay times of first- and second-stage ignition both increase with χ_{st}
- The ignition process within a single flamelet confirms the findings in the literature [74] that a cool-flame propagates from lean to rich parts of the flame prior to second-stage ignition.
- The location of the onset of second stage ignition in mixture fraction space depend on χ_{st} . A maximum value up to which second stage ignition takes place is found to be $Z_{ign} = 0.15$. However, this value decreases with a decrease in χ_{st} and is hence a limiting value.
- NO is produced in large amounts near stoichiometry but is also present in the rich part of the flame. The mass fraction in the rich parts increases with χ_{st}
- PAH species start to be produced in slightly rich conditions. The location of their peak value depends only slightly on χ_{st} , except for very small values of this parameter. It was found to be $Z_{PAH,max} \approx 0.14$.

Furthermore, the Lagrangian flamelet simulation showed that:

- The ignition process is reproduced overall well by both, the UFPV and the UFCPV approach for temperature and CH_2O , with only a slight delay observed.
- The prediction of the NO mass fraction shows large deviations from the reference solution while the UFCPV predicts its evolution very well.
- The prediction of PAH species also features large discrepancies when using the UFPV approach. The UFCPV approach shows a proper agreement with the reference solution.

In the Spray A simulation, the following findings were obtained:

- The prediction of the mixing field is in overall good agreement with the experimental data. However, the results depend on the chosen parameter of the turbulence model. A value of $C_\sigma = 2.0$ is recommended to avoid the diffusion being insufficient for the meshes utilized while maintaining good agreement with the experimental data.
- The LES-UFPV with incorporating the unstable solutions of the S-curve is able to predict the mixture formation under reacting conditions. The remaining underestimation of the ignition delay time by 8 % and the overprediction of the lift-off length by 4.3 % are attributed to the chemical mechanism utilized in the investigation.
- The influence of $\tilde{\chi}_{st}$ is mainly indicated by an ignition inhibition at the spray base. The steady lift-off length is located just downstream of the axial location, where $\tilde{\chi}_{st}$ decreases.
- Local quenching of igniting fluid elements due to large $\tilde{\chi}_{st}$ is observed. However, the affected mass remains small. The inclusion of the unstable branch of the S-curve is hence not necessary for this case. This is confirmed by a coupled simulation comparing the two approaches.
- The application of the LES-UFCPV approach utilizing the detailed CRECK mechanism gives better agreement in the global ignition characterizations than the LES-UFPV approach. This is attributed to the mechanism utilized.
- The comparison of the 355-nm PLIF signal and the CH_2O mass fraction obtained by the LES-UFCPV shows a remarkable similarity in terms of both the spatial extension and peak values during the phase of cool-flame propagation and second-stage ignition. The same holds when comparing the time after start of injection for the formation of PAH species.
- The periodic behavior of detachment of high-intensity regions of the PLIF signal [178] is also reproduced by the CH_2O mass fraction within the LES-UFCPV approach and was able to be explained in fluctuations in the mixture fraction field.
- The experimentally observed separation between low- and high-intensity regions in the PLIF signal can be explained by the simulation to be attributed to the separation of CH_2O and PAH species in the axial direction which confirms the experimental suggestion [178].
- The analysis of the flame structure in mixture fraction space revealed that second-stage ignition mainly takes place for $Z < Z_{ign}$. This is related to the fast mixing with respect to the distance to the nozzle within this spray. The fast mixing also leads to $Z < Z_{PAH,max}$ in the distance to the nozzle where the residence time would be large enough to form PAH species. Hence, their fraction is limited within this flame. NO, on the other hand, reaches large fractions.
- Spray structure analysis: at a sufficient time after start of injection, NO is observed in parts of the spray flank, increasing with distance to the nozzle. The region, where PAH species are observed, is limited to the spray axis at a sufficient distance to the nozzle and the central part of the spray head where fuel-rich mixtures appear.

The Spray D simulation revealed that:

- The application of the LES-UFCPV agrees well in terms of the vapor and liquid formation with a slight overshoot in the first phase of injection
- Ignition occurs rather distributed at the spray flank rather than in the vicinity of the spray head, as it is the case for Spray A, which confirms previous findings in the literature [78, 79]. This is due to mixture with $Z > Z_{ign}$ over a wide range along the spray axis.
- In contrast to the Spray A simulation, the ignition delay time is underestimated by approximately 20 %, while the steady lift-off length is predicted well.
- However, the CH₂O and PAH species mass fractions that are obtained agree very well with the measured 355-nm PLIF signal [179] when the difference in the ignition delay is accounted for. Notably, the characteristic finding of an overlap of CH₂O and PAH species in axial direction suggested by the PLIF data is reproduced by the simulation. This leads to the conclusion that the underlying flame structure is appropriate but the ignition process is initiated too fast.
- The inspection in mixture fraction space reveals, that slight rich mixtures at intermediate heights initiate second stage ignition. Furthermore, NO and PAH species both exists at large fractions due to the extension of possible mixture fraction values far above $Z = Z_{PAH,max}$ for a wide range of axial distances.
- Between the lift-off length and the end of fuel-rich core region with $Z > Z_{ign}$, there is a radial structure visible, constituting of CH₂O at the spray axis, followed by PAH species and NO, where the latter containing a OH structure near stoichiometry. Downstream of the fuel-rich core, mainly PAH species are found, with the largest fraction at the periphery. The evolution of this structure depends on the time after start of injection.

5 Summary and conclusion

In this thesis, selected combustion applications of current technical interest are investigated by means of Large Eddy Simulation in combination with advanced flamelet tabulation approaches. In particular, this includes the modeling of differential diffusion in turbulent jet flames and the ignition and pollutant formation in spray flames under conditions relevant for diesel engine.

In the context of differential diffusion modeling, the turbulent non-premixed oxy-fuel jet flame investigated experimentally by Sevault et al. [63] is chosen as a reference case. For this flame, the experimental data suggests varying extents of differential diffusion depending on the location in the flame and the species under consideration. This makes it a challenging test-case for modelling differential diffusion in turbulent jet flames. The FPV approach parameterized by the Bilger mixture fraction and progress variable is utilized in this thesis. The flamelet models are systematically varied with respect to the diffusion modeling approach. The models considered are the unity Lewis number flamelet (ULNF) model, the variable Lewis number flamelet (VLNF) model and a model incorporating the influence of turbulence on variable Lewis numbers (NLVLNF). The analysis was performed by means of *prior* analysis, which involves the table look-up parameters being directly obtained from the experimental data, and by means of coupled Large Eddy Simulation where the Raman-accessible species are transported to retrieve the Bilger mixture fraction and the progress variable. The comparisons are performed in terms of temperature, experimentally recorded species mass fraction and a derived differential diffusion parameter, where the latter quantifies the separation of chemical elements due to differential diffusion. The *prior* analysis revealed, that differential diffusion effects are pronounced in the reaction zone and in the near-nozzle region. In these regions, the VLNF and NLVLNF models perform well. However, in the fuel-rich part of the flame, a unity Lewis number assumption is more appropriate. This is taken into account by the ULNF and NLVLNF models. The decrease in the differential diffusion with increasing nozzle distance is only accounted for by the NLVLNF model. This means that the NLVLNF model offers the best overall agreement compared to the ULNF and VLNF. However, the different degree of differential diffusion for individual species is not captured by any of these models. The results of the coupled LES lead to contradictory findings. The VLNF model is supposed to give the best overall agreement with the experimental data. This is attributed to error accumulation and compensation within the coupled simulation. Thus, the *prior* analysis is more reliable to estimate the quality of manifold-based flame structures. Furthermore, the transported Raman species and derived variables were compared with the experimental data. Better agreement is observed in this context. Notably, the unity Lewis number behavior in the rich part of the flame is reproduced, even the underlying flamelet structure incorporates differential diffusion effects,

as it is the case for the VLNF and the NLVLNF model. The transport of single species is hence promising to account for the interplay of differential diffusion and turbulent transport in reactive flows. However, the flamelet model in the applied formulation is not able to reproduce all the details of the flame considered.

In the context of ignition and pollutant formation in spray flames relevant for diesel engine, the ECN Sprays A and D are chosen as reference cases due to their broad scientific database. In particular, the availability of recent experimental 355-nm PLIF data with high spatial resolution [76, 178, 179] and temporal resolution [178, 179] enables a detailed validation of CH₂O and PAH species prediction.

The UFPV approach is first applied in its original formulation including both the stable and the unstable steady flamelet solutions along the S-curve. The ignition process in the ECN Spray A is well captured by this approach. The remaining underestimation of the ignition delay time by 8 % and the overprediction of the lift-off length by 4.3 % are attributed to the reduced reaction mechanism used. An inspection of the results reveals that the scalar dissipation rate takes high values near the nozzle until the lift-off length is reached. Hence, it inhibits ignition in this region, which confirms earlier findings in the literature [100, 112]. The examination of the temperature/scalar dissipation rate dependency in stoichiometric conditions reveals, that igniting fluid elements are present below the unstable branch of the S-curve and therefore undergo extinction. However, the amount of mass affected by these conditions is found to be small, suggesting that there is a negligible influence on the overall combustion process. This is confirmed in a coupled simulation neglecting the unstable branch. No noteworthy difference in terms of the ignition delay time, lift-off length and spatial flame structure is found compared to the utilization of the complete UFPV approach. It is concluded that the UFPV approach only including igniting flamelets is a valid choice for the LES of ECN Spray A. This detailed explanation has not been available in the literature so far.

Beside the investigation concerning ignition and combustion, the tabulation strategy for covering processes on different time scales is addressed. For this purpose, a new progress variable definition is proposed in this thesis. It is evaluated as the sum of two normalized progress variables. Hence, the resulting approach is described as the unsteady flamelet composed progress variable (UFCPV) approach. Each of these progress variables is defined separately. By that means, a suitable definition for each sub-process to be covered can be derived independently. In particular, a progress variable previously used to describe the ignition process can be directly combined with a second one covering the formation of slow species, as done in this thesis. The verification of this approach is performed in the Lagrangian flamelet model (LFM) and with both ECN sprays. To incorporate NO and PAH species, the detailed CRECK mechanism is utilized in conjunction with this approach. Compared to the LFM reference solution, very good agreement of the UFPV and the UFCPV is obtained in capturing the ignition process. The formation of pollutant species at large time scales is, however, inaccurately predicted by the UFPV approach. The UFCPV approach shows much better agreement here. The newly proposed UFCPV approach is thus shown to perform better than the original formulation and to give accurate results in terms of pollutant prediction.

Its application in the LES of ECN Spray A confirms these findings. The ignition behavior is met very well in terms of ignition delay time and lift-off length. An in-depth comparison of the predicted spatial CH₂O and PAH species distribution with experimental 355-nm PLIF data validates the approach for capturing details of the first- and second-stage ignition as well as the formation of PAH species. The experimentally observed

periodic detachment of high-intensity regions in terms of the PLIF signal after the second-stage ignition is also reproduced by the LES-UFCPV approach, predicting similar structures for the CH₂O distribution. Based on the validated model, an explanation of this effect is found in terms of a periodic detachment of the mixture fraction field. Furthermore, the experimentally suggested contribution made by low- and high-intensity regions of the PLIF signal to CH₂O and PAH species is confirmed by the simulation results. The analysis of the ignition process in the mixture fraction space shows the influence of the relatively fast mixing in this spray with the surrounding gas. For distances to the nozzle with a residence time high enough for ignition and PAH species formation, respectively, only slightly fuel-rich mixtures are observed, i.e. $Z < Z_{PAH,max} = 0.14$ with $Z_{PAH,max}$ obtained as a mixture fraction with the maximum PAH mass fraction in single flamelet calculations. Hence, ignition takes place at slightly fuel-rich conditions while the PAH production is limited. However, the maximum NO mass fraction is large for this reason. This is also shown in the summarizing cause-effect chain analysis. At a sufficiently large time after the start of injection, NO is observed in parts of the spray flank, with its mass fraction increasing with the distance to the nozzle. The regions where PAH species are observed are limited to the spray axis at sufficient distance to the nozzle and the central part of the spray head where fuel-rich mixtures persist.

The application of the LES-UFCPV to the ECN Spray D injector shows an underestimation in the ignition delay time of approximately 20 %. To evaluate the influence on the flame structure, the predicted CH₂O and PAH species and the 355-nm high-speed PLIF data [179] are compared. When the simulation data are shifted by the observed difference in the ignition delay time, a very similar spatial extent and structures are observed. This leads to the conclusion, that the observed deviation in the ignition delay is attributed to the onset of chemical reactions being too early, but within a proper underlying flame structure and mixture distribution. In particular, spatial features of this flame, such as the well-known ignition at the spray flanks [78, 79], are retrieved when following the LES-UFCPV approach. This effect is shown to be connected to fuel-rich mixtures over a wide part of the spray axis with $Z > Z_{ign} = 0.15$. The aforementioned value is retrieved from the analysis of single flamelets incorporated into the look-up table generation. It is thus determined to be the most fuel-rich mixture, for which second stage ignition occurs. The comparison with the measured 355-nm PLIF for times after start of injection where PAH species are formed again confirmed that high-intensity PLIF signal regions corresponded to the presence of PAH species. In particular, the occurrence of CH₂O and PAH species at the same axial location suggested by the experimental data was confirmed by the LES-UFCPV approach. The evolution of the axial length over which this effect occurs is, however, not fully reproduced by the simulation for all time instances. This is partially attributed to the comparison for PLIF signals against species mass fractions. The analysis of the flame evolution in mixture fraction space explains the ignition behavior observed in physical space by the occurrence of slightly rich mixtures at intermediate heights, which initiate second-stage ignition. Furthermore, both NO and PAH species exist at large fractions due the presence of fluid elements with $Z > Z_{PAH,max}$ over a wide range along the spray axis. The summarizing cause-effect chain analysis shows that the preservation of a fuel-rich core for larger times after start of injection compared to the Spray A leads to the following radial structure downstream of the lift-off length: At the spray axis, CH₂O is found. In the adjacent fuel-rich mixtures, PAH species are present. These are followed by NO in slightly fuel-rich until lean conditions with peak value at stoichiometry. In a narrow range around stoichiometry, OH is present. Downstream of the fuel-rich core

($Z < Z_{ign}$), PAH species are mainly found for a sufficient time after start of injection, the largest amount being in the lateral periphery.

In summary, the UFCPV approach not incorporating the unstable branch of the S-curve is able to capture the ignition and combustion characteristics just as well as the original UFPV approach, and is further able to capture the evolution of slowly evolving species. This makes it an appropriate approach to investigate ignition and pollutant formation under diesel-relevant conditions. The generic formulation makes it also applicable to other application cases where different time scales have to be incorporated.

Beside the potentials of the flamelet-based approaches for modeling differential diffusion and pollutant formation, several limitations were also shown. In the context of modeling of differential diffusion, the flamelet model in the applied formulation is not able to reproduce all details of the flame considered. In particular, the interplay between molecular and turbulent transport is not captured in the flame considered with sufficient accuracy. Flamelet model extensions to turbulent regimes [194, 195] show potential in addressing this issue.

In the context of spray combustion, the underestimation of the ignition delay time in Spray D should be investigated further. One explanation might be an influence of the evaporation source term on the flame structure. Due to the higher mass flow rate in case of Spray D connected with less mixing, this effect might be more pronounced than in case of Spray A. The incorporation of enthalpy losses in the look-up table would be an attempt to incorporate this effect. Good agreement was obtained for the 355-nm PLIF signal when comparing the CH_2O mass fraction. However, the comparison of PAH species with this signal is altered in some aspects. The comparison of the single species mass fraction to the signal should be improved in future by recalculating an equivalent signal as, for example, in [50]. However, modeling of this signal for CH_2O is still based on model assumptions, due high spectral density of transitions and the lack of available quenching cross sections at flame temperatures [196]. Hence, a procedure of this kind, also incorporating PAH species, might be a difficult task. Furthermore, coupling the approach to a soot model, e.g. the ESQMOM model [197], denotes the next steps to complete the emission simulation. Further points, that should be addressed are related to the spray modeling itself. For the sprays under investigation, the injection strategy and the break-up model parameters are known in the literature [121]. However, when dealing with heavy-duty multi-hole injectors or marine injectors, for example, these parameters and strategy might not be applicable [198, 199]. The utilization of more advanced near-nozzle modeling [200] might be beneficial. Another point is related to the description of the mixing process in the gas phase. The results show a sensitivity to the turbulence model constant. The use of a Lagrangian dynamic procedure [201] adapted for the σ model [135] might be beneficial.

Appendix

A Comparison of chemical mechanism

As mentioned in Section 4.2, two mechanisms were used within this work, i.e. the detailed CRECK mechanism utilized for pollutant formation and a reduced version (based on an older version of the detailed one) only optimized regarding the ignition delay time. In Figure A.1 the ignition delay times obtained based on 2 % of the maximum OH mass fraction differs by 0.03 ms (0.35 ms for the reduced mechanism vs. 0.38 ms for the complete mechanism), which has to be kept in mind when performing the coupled simulations.

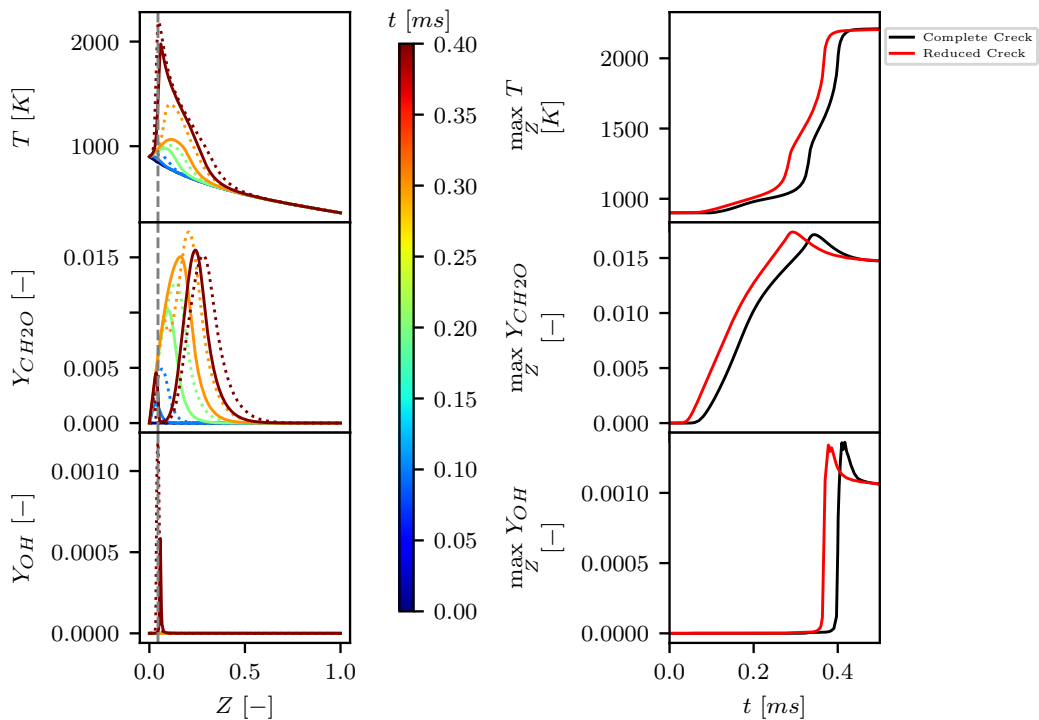


Figure A.1: Lagrangian flamelet model solution obtained by utilizing the detailed CRECK mechanism and a reduced version optimised to match the ignition delay time. Note, that the reduced mechanism is based on an older version of the complete mechanism.

Nomenclature

Abbreviations

| | |
|--------|---|
| CFD | Computational Fluid Dynamics |
| DNS | Direct Numerical Simulation |
| ECN | Engine Combustion Network |
| FDF | Filtered density function |
| FLUT | Flamelet look-up table |
| FPV | Flamelet Progress Variable Approach |
| LES | Large Eddy Simulation |
| NLVLNF | Non-Linear Variable Lewis Number Flamelet |
| SGS | Sub-grid scale |
| UFPCPV | Unsteady Flamelet Composed Progress Variable Approach |
| UFPV | Unsteady Flamelet Progress Variable Approach |
| ULNF | Unity Lewis Number Flamelet |
| VLNF | Variable Lewis Number Flamelet |

Greek Symbols

| | |
|------------------|---|
| β_m | Temperature exponent of reaction m |
| χ | Scalar dissipation rate of the mixture fraction |
| Δ | Filter width |
| δ_{ij} | Kronecker delta |
| $\dot{\omega}_k$ | Mass source term of species k per time and volume due to chemical reactions |
| $\dot{\omega}_T$ | Source term in gas phase enthalpy conservation equation in temperature form due to chemical reactions |
| λ | Thermal conductivity |
| λ_k | Thermal conductivity of species k |
| μ | Dynamic viscosity |
| μ_k | Dynamic viscosity of species k |

| | |
|--------------------|--|
| ν | Kinematic viscosity |
| ν_{SGS} | Turbulent (sub-grid scale) viscosity |
| $\nu_{k,j}$ | Net stoichiometric coefficient of species k in forward and backward path of reaction j |
| $\nu''_{k,j}$ | Stoichiometric coefficient of species k in backward path of reaction j |
| $\nu'_{k,j}$ | Stoichiometric coefficient of species k in forward path of reaction j |
| ρ | Density |
| τ | Lagrangian-like time in the flamelet equations |
| τ_c | characteristic chemical time scale |
| τ_d | Droplet time scale |
| τ_f | characteristic flow time scale |
| τ_{ij} | Viscous stress tensor |
| θ | Scaling factor in NLVNF flamelet model |

Latin Symbols

| | |
|----------------------|---|
| $[X_k]$ | Molar concentration of species k |
| $\Delta h_{f,k}^0$ | Standard enthalpy of formation of species k per unit mass |
| ΔH_m^0 | Change of enthalpy for reaction m |
| ΔS_m^0 | Change of entropy for reaction m |
| \dot{S}_{h_t} | Source term in gas phase total enthalpy conservation equation due to liquid-gas enthalpy transfer |
| \dot{S}_m | Mass source term of species k per time and volume due to liquid-gas phase change |
| \dot{S}_T | Source term in gas phase enthalpy conservation equation in temperature form due to liquid-gas enthalpy transfer |
| \dot{S}_u | Source term in gas phase momentum conservation equation due to liquid-gas momentum transfer |
| η_k | Kolmogorov length scale |
| \mathcal{D}_σ | Differential operator in the σ model |
| \mathcal{D}_{kl} | Binary diffusion coefficient of species k into species l |
| \mathcal{M}_k | Symbol for species k |
| Q_j | Progress of reaction m |
| ε | Dissipation rate of turbulent kinetic energy |
| a | Thermal diffusivity |
| $A_{f,m}$ | Pre-exponential factor of reaction m |
| C | Normalized progress variable |

| | |
|-------------|--|
| $c_{p,k}^m$ | Molar heat capacity at constant pressure for species k |
| C_1 | Normalized first progress variable in the UFCPV approach |
| C_2 | Normalized second progress variable in the UFCPV approach |
| C_σ | Model constant in the σ model |
| $c_{p,k}$ | Specific heat capacity at constant pressure for species k |
| D | Diffusion coefficient when using Fick's law |
| D_k | Diffusion coefficient of species k into the mixture |
| e | Specific internal energy |
| E_m | Activation energy of reaction m |
| e_t | Specific total energy (total energy per unit mass) |
| G | Filter kernel |
| g | Gravitational acceleration |
| h | Specific enthalpy (enthalpy per unit mass) |
| h_k^m | Molar enthalpy of species k |
| h_t | Specific total enthalpy (total enthalpy per unit mass) |
| I | Signal intensity |
| k | Turbulent kinetic energy |
| $K_{f,m}$ | Forward rate of reaction m |
| $K_{r,m}$ | Reverse rate of reaction m |
| l_t | Size of largest turbulent eddies |
| M | Mean molecular weight of a mixture |
| M_k | Atomic weight of species k |
| N | Number of species |
| p | Pressure |
| p_a | Pressure in equilibrium constant for evaluation of $K_{r,m}$ |
| q_i | Energy flux in direction i |
| R | Universal gas constant |
| r_j | Distance in direction j |
| s_k^m | Molar entropy of species k |
| T | Temperature |
| t | Time |
| $T_{a,m}$ | Activation temperature of reaction m |

| | |
|---------------------|---|
| u_i | Velocity in direction i |
| V | Volume |
| V_{cell} | Volume of a CFD cell |
| $V_{c,i}$ | Correction velocity in direction i within the mixture averaged diffusion approach |
| $V_{k,i}$ | Diffusion velocity of species k in direction i |
| X_k | Mole fraction of species k |
| Y_C | Progress variable |
| Y_k | Mass fraction of species k |
| $Y_{C,1}$ | First progress variable in the UFCPV approach |
| $Y_{C,2}$ | Second progress variable in the UFCPV approach |
| Z | Mixture fraction |
| Z_{Bilger} | Bilger mixture fraction |

Subscripts

| | |
|-------|---------------------------------------|
| d | Droplet |
| g | Gas phase |
| i,j | Direction indices |
| k | Species index |
| l | Liquid phase |
| m | Reaction index |
| q | Parcel index |
| 0 | Standard conditions |
| ext | Condition for extinction |
| ign | Condition for ignition |
| max | Maximum value |
| min | Minimum value |
| new | State at the end of a time step |
| old | State at the beginning of a time step |
| SGS | Sub-grid scale |
| st | Stoichiometric conditions |

Superscripts

| | |
|---|----------------------|
| 0 | Standard conditions |
| m | Molar based quantity |

N Normalized quantity

SGS Sub-grid scale

Characteristic number

B_m Spalding mass number

Da Damköhler number

Le Lewis number

Nu Nusselt number

Pr Prandtl number

Re Reynolds number

Sc Schmidt number

Operators

$\tilde{\cdot}$ Density weighted filter / Favre filter

$\langle \cdot \rangle_t$ Average with respect to time

∇ Gradient

$\bar{\cdot}$ Spatial filter

List of Figures

| | | |
|-----|--|----|
| 1.1 | Left: Picture of a turbulent air jet (source: [21]), right: Time scales in chemical reacting flows (source: [20], Reprinted from Combustion and Flame, Volume 88, U.Maas, S.B.Pope, Simplifying chemical kinetics: Intrinsic low-dimensional manifolds in composition space, Pages 239-264, 1992, with permission from Elsevier.) | 3 |
| 1.2 | Cause-effect chain of diesel spray combustion with focus on the results of the combustion model | 7 |
| 2.1 | Euler-Lagrange-Approach | 15 |
| 2.2 | S-curve Spray A | 28 |
| 2.3 | Comparison of VLNF-predicted H ₂ O mass fraction spanned by varying scalar dissipation rate (left) and resulting CO ₂ mass fraction over normalized H ₂ O mass fraction C (right) at constant value for Z (light green) and Z_{Bilger} (dark green), respectively. | 32 |
| 2.4 | Normalized progress variable C (black line) and progress variable source term $\dot{\omega}_{Y_C}$ (red line) over time (left) for an unsteady flamelet solution ($Z = Z_{\text{st}}, \chi_{\text{st}} = 40/s$). The right graph shows the comparison of $\dot{\omega}_{Y_C}$ (red dashed line) and the patch introduced in the FLUT (orange line). Note, that the value of $C_{\text{init}} = 10^{-9}$ is used for visualization [3]. | 33 |
| 2.5 | Evolution of progress variable $Y_{C,1} = 0.5Y_{\text{CO}} + 1.0Y_{\text{CO}_2} + 0.9Y_{\text{H}_2} + 1.0Y_{\text{H}_2\text{O}} + 0.8Y_{\text{CH}_2\text{O}}$ ([3], top row of first and second column), temperature (second row), NO mass fraction (third row) and C ₁₆ H ₁₀ mass fraction (fourth row) as a function of mixture fraction at different times (left column), as function of time for rich conditions ($Z = 0.1$, central column, marked by dashed line in left column) and mapped as a function of $Y_{C,1}$ under the same conditions as in the middle row in an unsteady flamelet with $\chi_{\text{st}} = 20/s$ and ECN Spray A nominal conditions. | 35 |
| 2.6 | Visualization of the Y_C definition in the UFCPV approach: Temporal evolution of the progress variables $Y_{C,1} = 0.5Y_{\text{CO}} + 1.0Y_{\text{CO}_2} + 0.9Y_{\text{H}_2} + 1.0Y_{\text{H}_2\text{O}} + 0.8Y_{\text{CH}_2\text{O}}$ [3] and $Y_{C,2} = Y_{\text{NO}} + Y_{\text{C}_{16}\text{H}_{10}} + Y_{\text{C}_{18}\text{H}_{10}}$ as a function of time under rich conditions ($Z = 0.1$) extracted from the unsteady flamelet simulation shown in Figure 2.5 (left), their normalized values according to equation (2.65) (second plot), the composed progress variable according to Eq. (2.66) (third plot) and temperature and NO mass fraction mapped onto the composed progress variable (right) | 36 |
| 2.7 | FPV CFD coupling gaseous jet flame | 41 |
| 2.8 | UFCPV CFD coupling spray combustion | 42 |
| 3.1 | Mesh utilized for the simulation of the turbulent jet flame [63] colored by the temperature. | 47 |
| 3.2 | Comparison of experimental data and results of the <i>prior</i> analysis for the temperature T and differential diffusion parameter Z_{HC} (left and middle columns) at three experimentally recorded heights above the burner (top to bottom) using different diffusion modeling approaches. The most suitable value for the parameter θ in the NLVLNF model, optimized based on the measured Raman species, is shown in the right-hand column. | 50 |
| 3.3 | Comparison Wasserstein metric W_2 evaluated based on results of ULNF, VLNF and NLVLNF (left to right) for downstream locations of $x/d = 1$, $x/d = 5$ and $x/d = 20$ (top to bottom) | 52 |

| | | |
|------|--|----|
| 3.4 | Comparison of experimental data and results of the <i>prior</i> analysis using three different diffusion modeling approaches for the species mass fractions of H ₂ O and H ₂ (left column) as well as CO ₂ and CO (right column) at three experimentally recorded heights above the burner. | 53 |
| 3.5 | Comparison of profiles for θ^{opt} optimized based on H ₂ O ($\theta^{\text{opt,H}_2\text{O}}$) or CO ₂ ($\theta^{\text{opt,CO}_2}$) with optimization based on all experimentally recorded Raman species ($\theta^{\text{opt,all}}$) at $x/d = 1$. . . | 54 |
| 3.6 | Comparison of measured on Bilger mixture fraction conditioned flame structure at downstream location $x/d = 5$ with LES results of tabulated quantities using different diffusion modeling approaches | 55 |
| 3.7 | Mean values of the read-in tabulated and transported mass fractions of CO ₂ and H ₂ (multiplied by 3) (left) and the differential diffusion parameter Z_{HC} (right) at $x/d = 5$. All values are conditioned on the Bilger mixture fraction. The results for the VLNF model are shown in the top row and those for the NLVLNF model in the bottom row. | 56 |
| 4.1 | Connection between the investigations performed in Section 4. | 60 |
| 4.2 | Computational mesh discretizing the gas phase color coded by the solution of the Favre-filtered mixture fraction field for the reactive Spray A (left) and Spray D case (right) at 0.4 ms after start of injection | 63 |
| 4.3 | Rate of injection for ECN Spray A and D | 64 |
| 4.4 | $\chi_{st}(t)$ Lagrangian flamelet model (LFM) | 65 |
| 4.5 | Iso-lines of the normalized progress variables C_1 and C_2 overlaying the single species evolution (heat map color-coded from white to black) for a flamelet calculation with $\chi_{st} = 5/s$ | 67 |
| 4.6 | Evolution of temperature (top row), and mass fractions of CH ₂ O (second row), OH (third row), NO (fourth row) and PAH species (fifth row) for a single flamelet simulation with $\chi_{st} = 20/s$ used to generate the FLUT within three time intervals: Cool flame propagation [74] (left), main ignition (middle), slow chemistry (right). Black dots represent the (Z, T) and ($Z, \text{CH}_2\text{O}$) combination build from the instantaneous maximum temperature. Z_{st} is denoted by vertical dashed line while the maximum Z value, for which the maximum temperature is observed over time is marked by a dotted vertical line. | 69 |
| 4.7 | Global quantities defining the difference in the ignition process: Evolution of the maximum temperature over time for two χ_{st} values together with the corresponding first and second stage ignition delay times (left), the dependency of the ignition delay times on χ_{st} (middle) and the dependency of Z_{ign} and $Z(Y_{\text{PAH,max}})$ on χ_{st} (right) | 70 |
| 4.8 | Distribution of the source terms of the two progress variables $Y_{C,1}$ and $Y_{C,2}$ in case of the UFCPV approach (with $Y_{C,1} = Y_C$ for the UFPV approach) $\dot{\omega}_{Y_{C,1}}$ (upper row) and $\dot{\omega}_{Y_{C,2}}$ (lower row) for different scalar dissipation rate values retrieved from the FLUT | 71 |
| 4.9 | Validation UFCPV approach in Lagrangian flamelet model | 73 |
| 4.10 | Evaluation of penetration lengths in non-reactive Spray A | 74 |
| 4.11 | Penetration lengths Spray A non-reactive | 75 |
| 4.12 | Averaged radial mixture fraction distribution obtained from Raman measurements [184] (black curve) and simulation with different values of the σ -model constant C_σ | 76 |
| 4.13 | Penetration lengths Spray A reactive | 78 |
| 4.14 | Ignition sequence ECN Spray A | 79 |
| 4.15 | Series of scalar dissipation rate at stoichiometry used for table look-up (top row) together with temperature (bottom row) overlayed with isoline of $Z = Z_{st}$ colored by the scalar dissipation rate. The black vertical lines denote the experimentally obtained liquid penetration of 9.6 mm (left, [190]) and steady lift-off length of 16.1 mm (right, [189]), respectively. | 80 |

| | | |
|------|---|----|
| 4.16 | Distribution of the temperature at stoichiometric conditions $\tilde{T}_{st} = \tilde{T}(\tilde{Z}_{st})$ over the corresponding scalar dissipation rate $\tilde{\chi}_{st}$ in terms of scatter color-coded by the axial distance to the nozzle (top row) and mass distribution (fuel+oxidizer, represented by each scatter, bottom row) for 0.30 ms (left column), 0.40 ms (middle column) and 1.00 ms (right column) after start of injection. | 82 |
| 4.17 | Contour plot of temperature obtained in the ECN Spray A simulation with (top) and without (bottom) incorporation of the unstable branch of the S-curve. | 82 |
| 4.18 | Evolution of the maximum temperature and OH mass fraction during the simulation for the ECN Spray A with (blue line) and without (orange line) considering the region between the stable and unstable branch of the S-curve. | 83 |
| 4.19 | Experimentally obtained CH ₂ O PLIF data ([76], left column) in comparison with CH ₂ O mass fraction (second column from the left) and temperature distribution (third column from left) obtained from the simulation as well as the experimentally determined Schlieren signal with 10 % of the maximum PLIF signal obtained from the images in the left column represented by thick white border ([76], right column). Vertical white line denotes measured steady lift-off length [189]. Experimental data reprinted from Proceedings of the Combustion Institute Volume 35, Issue 3: Scott A. Skeen, Julien Manin, Lyle M. Pickett, Simultaneous formaldehyde PLIF and high-speed Schlieren imaging for ignition visualization in high-pressure spray flames, Pages 3167-3174, 2015, with permission from Elsevier. | 85 |
| 4.20 | Experimentally obtained 355-nm PLIF data ([76], top row) in comparison with CH ₂ O and PAH mass fraction together with the iso-line of stoichiometric mixture obtained from the simulation (bottom row). Experimental data reprinted from Proceedings of the Combustion Institute Volume 35, Issue 3: Scott A. Skeen, Julien Manin, Lyle M. Pickett, Simultaneous formaldehyde PLIF and high-speed Schlieren imaging for ignition visualization in high-pressure spray flames, Pages 3167-3174, 2015, with permission from Elsevier. | 86 |
| 4.21 | Instantaneous snapshots of experimental 355-nm high-speed PLIF data [178] (top row) and simulation data for the CH ₂ O and sum of C ₁₆ H ₁₀ and C ₁₈ H ₁₀ mass fractions (middle row) together with mixture fraction distribution obtained from the simulation (bottom row). The grey contour in the middle and bottom row represents stoichiometric conditions and the vertical white line denotes the measured steady lift-off length [189]. | 87 |
| 4.22 | Scatter plot of the Favre-filtered CH ₂ O mass fraction as function of mixture fraction obtained from the LES color coded by the distance to the measured lift-off length Δy_{lo} for the three time instances shown in Figure 4.21. The black solid line denotes the maximum CH ₂ O mass fraction obtained in a flamelet calculation with $\chi_{st} = 1/s$ and the gray scale contourplot the corresponding reaction progress variable source term. Z_{st} is denoted by a dashed vertical line. | 88 |
| 4.23 | I-y-t plot of the measured 355-nm high-speed PLIF signal ([178], left) for the ECN Spray A together with simulation data for the CH ₂ O (lower part of the right diagram) and PAH as sum of C ₁₆ H ₁₀ and C ₁₈ H ₁₀ mass fraction (upper part of the right diagram) integrated in lateral direction along the mid-plane of the spray and normalized by its maximum value (right). The vapor penetration obtained from the simulation is indicated by a black line in the right plot. | 89 |
| 4.24 | Scatter plot of Favre-filtered temperature and CH ₂ O, OH, NO, and PAH mass fraction (top to bottom, respectively) in mixture fraction space for the ECN Spray A color coded by the distance from the nozzle for distinct times after start of injection together with the location of stoichiometric mixture $Z_{st} = 0.045$ (vertical dashed line), the chamber temperature (horizontal dotted line in the first row), $Z_{ign} = 0.15$ (vertical dotted line in first and second row) and $Z_{PAH,max} = 0.14$ (vertical dashed-dotted line in bottom row). | 90 |

| | | |
|------|--|-----|
| 4.25 | The structure of the ECN Spray A from injection to gaseous pollutant formation. Black dots denote parcel representing the liquid phase. The contour denotes stoichiometric conditions color-coded by the temperature. The left vertical line denotes the measured liquid penetration and the right vertical line the measured lift-off length, respectively. | 91 |
| 4.26 | Penetration and mixture formation for Spray A and Spray D under reactive conditions . . . | 93 |
| 4.27 | Time sequence of mixture formation and OH distribution during the injection from ECN Spray A injector (top row) and ECN Spray D injector (bottom row) together with the steady lift-off lengths obtained from the experimental data ([189] for Spray A and [193] for Spray D). The maximum color for mixture fraction correspond to $Z = Z_{ign} = 0.15$ while the limits for OH are set to 2 % of the maximum OH mass fraction value obtained during the simulation and slightly above. | 94 |
| 4.28 | Evolution of the maximum temperature and OH mass fraction during the simulation for the ECN Spray A (red line) and ECN Spray D (green line) together with the experimentally determined ignition delay time of 0.41 ms (left vertical gray dashed line, [189]) for Spray A and 0.59 ms for Spray D (right vertical gray dashed line, [193]). The ignition delay times obtained from the LES based on 50 % of the maximum OH mass fraction are marked by filled circles and given by 0.40 ms for Spray A and 0.48 ms for Spray D. | 95 |
| 4.29 | Experimentally obtained 355 nm-PLIF data ([179], left column) in comparison with CH ₂ O mass fraction obtained from the simulation (second column from the left), temperature distribution (third column from left) and OH mass fraction (right column, color code limit to 2% of its maximum value) obtained from the LES. Vertical white line denotes measured steady lift-off length [193]. | 96 |
| 4.30 | Time sequence of high-speed 355-nm PLIF data [179] for the ECN Spray D injector (top row) together with simulation results for CH ₂ O and PAH species mass fractions (bottom row) . . | 97 |
| 4.31 | I-y-t plot of the measured 355-nm high-speed PLIF signal ([179], left) for the ECN Spray D together with simulation data for the CH ₂ O (lower part of the right diagram) and PAH as sum of C ₁₆ H ₁₀ and C ₁₈ H ₁₀ mass fraction (upper part of the right diagram) integrated in lateral direction along the mid-plane of the spray and normalized by its maximum value (right). The solid lines represent the measured (white line in left plot, [192]) vapor penetration and the one obtained from the simulation (black line in right plot) | 98 |
| 4.32 | Scatter plot of Favre-filtered temperature and CH ₂ O, OH, NO, and PAH mass fraction (top to bottom, respectively) in mixture fraction space for the ECN Spray D color coded by the distance from the nozzle for distinct times after start of injection together with the location of stoichiometric mixture $Z_{st} = 0.045$ (vertical dashed line), the chamber temperature (horizontal dotted line in the first row), $Z_{ign} = 0.15$ (vertical dotted line in first and second row) and $Z_{PAH,max} = 0.14$ (vertical dashed-dotted line in bottom row). | 99 |
| 4.33 | The structure of the ECN Spray D from injection to gaseous pollutant formation. Black dots denote parcel representing the liquid phase. The contour denotes stoichiometric conditions color-coded by the temperature. The vertical lines denote the measured liquid penetration and lift-off length, respectively. | 100 |
| A.1 | Mechanism comparison in Lagrangian flamelet model | ix |

List of Tables

| | | |
|-----|---|----|
| 2.1 | Overview of applied tabulation strategies | 39 |
| 4.1 | Overview of applied tabulation strategies and utilized mechanism for ignition and pollutant formation | 61 |
| 4.2 | Boundary conditions for the flamelet model under the ECN Spray A nominal conditions . . | 66 |

Bibliography

- [1] S. Gierth, F. Hunger, S. Popp, H. Wu, M. Ihme, C. Hasse, Assessment of differential diffusion effects in flamelet modeling of oxy-fuel flames, *Combustion and Flame* 197 (2018) 134–144.
- [2] S. Gierth, P. Haspel, A. Scholtissek, Z. Sun, S. Popp, C. Hasse, Evaluation of the Unsteady Flamelet Progress Variable Approach in Large Eddy Simulations of the ECN Spray A, *Science and Technology for Energy Transition*, accepted for publication (2022).
- [3] Z. Sun, S. Gierth, M. Pollack, C. Hasse, A. Scholtissek, Ignition under strained conditions: Unsteady flamelet progress variable modeling for diesel engine conditions in the transient counterflow configuration, *Combustion and Flame* 240 (2022) 111841.
- [4] International Energy Agency, *World Energy Outlook 2020*, 2020.
- [5] M. Audi, A. Ali, M. Kassem, Greenhouse gases: A review of losses and benefits, *International Journal of Energy Economics and Policy* 10 (2020) 403–418.
- [6] G. De Falco, C. Colarusso, M. Terlizzi, A. Popolo, M. Pecoraro, M. Commodo, P. Minutolo, M. Sirignano, A. D’Anna, R. P. Aquino, A. Pinto, A. Molino, R. Sorrentino, Chronic Obstructive Pulmonary Disease-Derived Circulating Cells Release IL-18 and IL-33 under Ultrafine Particulate Matter Exposure in a Caspase-1/8-Independent Manner, *Frontiers in immunology* 8 (2017) 1415.
- [7] R. Niranjana, A. K. Thakur, The toxicological mechanisms of environmental soot (black carbon) and carbon black: Focus on Oxidative stress and inflammatory pathways, *Frontiers in Immunology* 8 (2017) 1–20.
- [8] T. C. Bond, S. J. Doherty, D. W. Fahey, P. M. Forster, T. Berntsen, B. J. Deangelo, M. G. Flanner, S. Ghan, B. Kärcher, D. Koch, S. Kinne, Y. Kondo, P. K. Quinn, M. C. Sarofim, M. G. Schultz, M. Schulz, C. Venkataraman, H. Zhang, S. Zhang, N. Bellouin, S. K. Guttikunda, P. K. Hopke, M. Z. Jacobson, J. W. Kaiser, Z. Klimont, U. Lohmann, J. P. Schwarz, D. Shindell, T. Storelvmo, S. G. Warren, C. S. Zender, Bounding the role of black carbon in the climate system: A scientific assessment, *Journal of Geophysical Research Atmospheres* 118 (2013) 5380–5552.
- [9] Environmental Protection Agency (EPA), *Nitrogen oxides (NOx), why and how they are controlled*, Epa-456/F-99-006R (1999) 48.
- [10] M. A. Nemitallah, M. A. Habib, H. M. Badr, S. A. Said, A. Jamal, R. Ben-Mansour, E. M. A. Mokheimer, K. Mezghani, Oxy-fuel combustion technology: current status, applications, and trends, *International Journal of Energy Research* 41 (2017) 1670–1708.
- [11] M. Ditaranto, J. C. Sautet, J. M. Samaniego, Structural aspects of coaxial oxy-fuel flames, *Experiments in Fluids* 30 (2001) 253–261.
- [12] J. Sautet, M. Ditaranto, J. Samaniego, O. Charon, Properties of turbulence in natural gas-oxygen diffusion flames, *International Communications in Heat and Mass Transfer* 26 (1999) 647–656.

-
- [13] J. C. Sautet, L. Salentey, M. DiTaranto, Large-scale turbulent structures in non-premixed, oxygen enriched flames, *International Communications in Heat and Mass Transfer* 28 (2001) 277–287.
- [14] P. Kutne, B. K. Kapadia, W. Meier, M. Aigner, Experimental analysis of the combustion behaviour of oxyfuel flames in a gas turbine model combustor, *Proceedings of the Combustion Institute* 33 (2011) 3383–3390.
- [15] M. A. Nemitallah, M. A. Habib, Experimental and numerical investigations of an atmospheric diffusion oxy-combustion flame in a gas turbine model combustor, *Applied Energy* 111 (2013) 401–415.
- [16] H. L. Yip, A. Srna, A. C. Y. Yuen, S. Kook, R. A. Taylor, G. H. Yeoh, P. R. Medwell, Q. N. Chan, A review of hydrogen direct injection for internal combustion engines: Towards carbon-free combustion, *Applied Sciences (Switzerland)* 9 (2019) 1–30.
- [17] R. D. Reitz, H. Ogawa, R. Payri, T. Fansler, S. Kokjohn, Y. Moriyoshi, A. K. Agarwal, D. Arcoumanis, D. Assanis, C. Bae, K. Boulouchos, M. Canakci, S. Curran, I. Denbratt, M. Gavaises, M. Guenther, C. Hasse, Z. Huang, T. Ishiyama, B. Johansson, T. V. Johnson, G. Kalghatgi, M. Koike, S. C. Kong, A. Leipertz, P. Miles, R. Novella, A. Onorati, M. Richter, S. Shuai, D. Siebers, W. Su, M. Trujillo, N. Uchida, B. M. Vaglieco, R. M. Wagner, H. Zhao, *IJER editorial: The future of the internal combustion engine*, *International Journal of Engine Research* 21 (2020) 3–10.
- [18] T. Poinso, D. Veynante, *Theoretical and numerical combustion*, 3rd ed., 2012.
- [19] A. N. Kolmogorov, The local structure of turbulence in an incompressible viscous fluid at very high reynolds numbers, *Proceedings of the USSR Academy of Sciences* 30 (1941) 299–303.
- [20] U. Maas, S. Pope, Simplifying chemical kinetics: Intrinsic low-dimensional manifolds in composition space, *Combustion and Flame* 88 (1992) 239–264.
- [21] M. van Dyke, *An Album of Fluid Motion*, The Parabolic Press, 1982.
- [22] S. B. Pope, *Turbulent Flows*, Cambridge University Press, 2000.
- [23] H. Pitsch, O. Desjardins, G. Balarac, M. Ihme, Large-eddy simulation of turbulent reacting flows, *Progress in Aerospace Sciences* 44 (2008) 466–478.
- [24] S. B. Pope, Small scales, many species and the manifold challenges of turbulent combustion, *Proceedings of the Combustion Institute* 34 (2013) 1–31.
- [25] J. A. van Oijen, L. P. de Goey, Modelling of premixed laminar flames using flamelet-generated manifolds, *Combustion Science and Technology* 161 (2000) 113–137.
- [26] O. Gicquel, N. Darabiha, D. Thévenin, Laminar premixed hydrogen/air counterflow flame simulations using flame prolongation of ILDM with differential diffusion, *Proceedings of the Combustion Institute* 28 (2000) 1901–1908.
- [27] V. Bykov, U. Maas, The extension of the ILDM concept to reaction-diffusion manifolds, *Combustion Theory and Modelling* 11 (2007) 839–862.
- [28] V. Bykov, U. Maas, Problem adapted reduced models based on reaction-diffusion manifolds (REDIMs), *Proceedings of the Combustion Institute* 32 I (2009) 561–568.
- [29] N. Peters, Laminar flamelet concepts in turbulent combustion, *Symposium (International) on Combustion* 21 (1988) 1231–1250.
- [30] H. Pitsch, N. Peters, A consistent flamelet formulation for non-premixed combustion considering differential diffusion effects, *Combustion and Flame* (1998).

-
- [31] V. Mittal, H. Pitsch, A flamelet model for premixed combustion under variable pressure conditions, *Proceedings of the Combustion Institute* 34 (2013) 2995–3003.
- [32] C. Hasse, N. Peters, A two mixture fraction flamelet model applied to split injections in a di Diesel engine, *Proceedings of the Combustion Institute* 30 II (2005) 2755–2762.
- [33] E. M. Doran, H. Pitsch, D. J. Cook, A priori testing of a two-dimensional unsteady flamelet model for three-feed combustion systems, *Proceedings of the Combustion Institute* 34 (2013) 1317–1324.
- [34] C. Kortschik, S. Honnet, N. Peters, Influence of curvature on the onset of autoignition in a corrugated counterflow mixing field, *Combustion and Flame* 142 (2005) 140–152.
- [35] Y. Xuan, G. Blanquart, M. E. Mueller, Modeling curvature effects in diffusion flames using a laminar flamelet model, *Combustion and Flame* 161 (2014) 1294–1309.
- [36] A. Scholtissek, R. W. Pitz, C. Hasse, Flamelet budget and regime analysis for non-premixed tubular flames, *Proceedings of the Combustion Institute* 36 (2017) 1349–1356.
- [37] A. Scholtissek, W. L. Chan, H. Xu, F. Hunger, H. Kolla, J. H. Chen, M. Ihme, C. Hasse, A multi-scale asymptotic scaling and regime analysis of flamelet equations including tangential diffusion effects for laminar and turbulent flames, *Combustion and Flame* 162 (2015) 1507–1529.
- [38] W. Han, A. Scholtissek, C. Hasse, The role of tangential diffusion in evaluating the performance of flamelet models, *Proceedings of the Combustion Institute* 37 (2019) 1767–1774.
- [39] H. Pitsch, Y. P. Wan, N. Peters, Numerical investigation of soot formation and oxidation under diesel engine conditions, *SAE Technical Papers* (1995).
- [40] H. Barths, C. Antoni, N. Peters, Three-dimensional simulation of pollutant formation in a di diesel engine using multiple interactive flamelets, in: *International Fall Fuels and Lubricants Meeting and Exposition*, SAE International, 1998.
- [41] H. Barths, C. Hasse, G. Bikas, N. Peters, Simulation of combustion in direct injection diesel engines using a eulerian particle flamelet model, *Proceedings of the Combustion Institute* 28 (2000) 1161–1168.
- [42] H. Barths, C. Hasse, N. Peters, Computational fluid dynamics modelling of non-premixed combustion in direct injection diesel engines, *International Journal of Engine Research* 1 (2000) 249–267.
- [43] P. Kundu, J. Scroggins, M. M. Ameen, A Novel In Situ Flamelet Tabulation Methodology for the Representative Interactive Flamelet Model, *Combustion Science and Technology* 192 (2020) 1–25.
- [44] A. W. Cook, J. J. Riley, G. Kosály, A laminar flamelet approach to subgrid-scale chemistry in turbulent flows, *Combustion and Flame* 109 (1997) 332–341.
- [45] C. D. Pierce, *Progress-Variable Approach for Large Eddy Simulation of Turbulent Combustion*, Ph.D. thesis, Stanford University, 2001.
- [46] C. D. Pierce, P. Moin, Progress-variable approach for large-eddy simulation of non-premixed turbulent combustion, *Journal of Fluid Mechanics* 504 (2004) 73–97.
- [47] M. Ihme, C. M. Cha, H. Pitsch, Prediction of local extinction and re-ignition effects in non-premixed turbulent combustion using a flamelet/progress variable approach, *Proceedings of the Combustion Institute* 30 (2005) 793–800.

-
- [48] M. Ihme, H. Pitsch, Prediction of extinction and reignition in nonpremixed turbulent flames using a flamelet/progress variable model: 1. A priori study and presumed PDF closure, *Combustion and Flame* 155 (2008) 70–89.
- [49] M. Ihme, H. Pitsch, Prediction of extinction and reignition in nonpremixed turbulent flames using a flamelet/progress variable model: 2. Application in LES of Sandia flames D and E, *Combustion and Flame* 155 (2008) 90–107.
- [50] S. Popp, F. Hunger, S. Hartl, D. Messig, B. Coriton, J. Frank, F. Fuest, C. Hasse, LES flamelet-progress variable modeling and measurements of a turbulent partially-premixed dimethyl ether jet flame, *Combust. Flame* 162 (2015) 3016 – 3029.
- [51] F. Hunger, M. Zulkifli, B. Williams, F. Beyrau, C. Hasse, A combined experimental and numerical study of laminar and turbulent non-piloted oxy-fuel jet flames using a direct comparison of the Rayleigh signal, *Flow, Turbulence and Combustion* 97 (2016) 231–262.
- [52] F. Hunger, M. Zulkifli, B. Williams, F. Beyrau, C. Hasse, Comparative flame structure investigation of normal and inverse turbulent non-premixed oxy-fuel flames using experimentally recorded and numerically predicted Rayleigh and OH-PLIF signals, *Proceedings of the Combustion Institute* 36 (2017) 1713 – 1720.
- [53] F. Mauß, D. Keller, N. Peters, A lagrangian simulation of flamelet extinction and re-ignition in turbulent jet diffusion flames, *Symposium (International) on Combustion* 23 (1991) 693–698.
- [54] H. Pitsch, C. Cha, S. Fedotov, Flamelet modelling of non-premixed turbulent combustion with local extinction and re-ignition, *Combust. Theor. Model.* 7 (2003) 317–332.
- [55] M. Ihme, Y. C. See, Prediction of autoignition in a lifted methane/air flame using an unsteady flamelet/progress variable model, *Combustion and Flame* 157 (2010) 1850–1862.
- [56] H. Pitsch, M. Ihme, An unsteady/flamelet progress variable method for les of nonpremixed turbulent combustion, *43rd AIAA Aerospace Sciences Meeting and Exhibit - Meeting Papers* (2005) 2593–2606.
- [57] M. Ihme, H. Pitsch, Modeling of radiation and nitric oxide formation in turbulent nonpremixed flames using a flamelet/progress variable formulation, *Physics of Fluids* 20 (2008).
- [58] R. Bilger, Reaction rates in diffusion flames, *Combustion and Flame* 30 (1977) 277 – 284.
- [59] T. Lavertu, L. Mydlarski, S. Gaskin, Differential diffusion of high-Schmidt-number passive scalars in a turbulent jet, *Journal of Fluid Mechanics* 612 (2008) 439–475.
- [60] International workshop on measurement and computation of turbulent flames, <https://tnfworkshop.org>, 2021.
- [61] J. You, Y. Yang, S. Pope, Effects of molecular transport in LES/PDF of piloted turbulent dimethyl ether/air jet flames, *Combustion and Flame* 176 (2017) 451 – 461.
- [62] M. Drake, M. Lapp, C. Penney, S. Warshaw, B. Gerhold, Measurements of temperature and concentration fluctuations in turbulent diffusion flames using pulsed Raman spectroscopy, *Symposium (International) on Combustion* 18 (1981) 1521 – 1531.
- [63] A. Sevault, M. Dunn, R. S. Barlow, M. Ditaranto, On the structure of the near field of oxy-fuel jet flames using Raman/Rayleigh laser diagnostics, *Combustion and Flame* 159 (2012) 3342–3352.
- [64] H. Pitsch, Unsteady flamelet modeling of differential diffusion in turbulent jet diffusion flames, *Combustion and Flame* 123 (2000) 358 – 374.

-
- [65] A. Kronenburg, R. Bilger, Modelling differential diffusion in nonpremixed reacting turbulent flow: Model development, *Combustion Science and Technology* 166 (2001) 195–227.
- [66] A. Garmory, E. Mastorakos, Numerical simulation of oxy-fuel jet flames using unstructured LES–CMC, *Proceedings of the Combustion Institute* 35 (2015) 1207 – 1214.
- [67] C. Han, R. Barlow, H. Wang, Flamelet modeling of differential molecular diffusion in oxy-fuel turbulent jet flames, in: *Thirteenth International Workshop on measurement and Computation of Turbulent Flames*, 2016.
- [68] C. Han, R. Barlow, H. Wang, Examination of flamelet differential molecular diffusion models in oxy-fuel turbulent jet flames, in: *DFD16 Meeting of The American Physical Society*, 2016.
- [69] H. Wang, Consistent flamelet modeling of differential molecular diffusion for turbulent non-premixed flames, *Physics of Fluids* 28 (2016).
- [70] C. Baumgarten, *Mixture Formation in Internal Combustion Engine*, Heat, Mass Transfer, Springer-Verlag, Berlin/Heidelberg, 2006.
- [71] M. Blume, P. Schwarz, H. Rusche, L. Weiß, M. Wensing, R. Skoda, 3d simulation of turbulent and cavitating flow for the analysis of primary breakup mechanisms in realistic diesel injection processes, *Atomization and Sprays* (2020) 861–893.
- [72] L. Pickett, *Engine Combustion Network*, Sandia National Laboratory, 2013.
- [73] A. Kazakov, M. Chaos, Z. Zhao, F. L. Dryer, Computational singular perturbation analysis of n-heptane two-stage ignition, *Chemical and Physical Processes of Combustion - 2005 Technical Meeting of the Eastern States Section of the Combustion Institute* (2005) 46–49.
- [74] R. N. Dahms, G. A. Paczko, S. A. Skeen, L. M. Pickett, Understanding the ignition mechanism of high-pressure spray flames, *Proceedings of the Combustion Institute* 36 (2017) 2615–2623.
- [75] Y. Minamoto, J. H. Chen, DNS of a turbulent lifted DME jet flame, *Combustion and Flame* 169 (2016) 38–50.
- [76] S. A. Skeen, J. Manin, L. M. Pickett, Simultaneous formaldehyde PLIF and high-speed schlieren imaging for ignition visualization in high-pressure spray flames, *Proceedings of the Combustion Institute* 35 (2015) 3167–3174.
- [77] N. Maes, M. Meijer, N. Dam, B. Somers, H. Baya Toda, G. Bruneaux, S. A. Skeen, L. M. Pickett, J. Manin, Characterization of Spray A flame structure for parametric variations in ECN constant-volume vessels using chemiluminescence and laser-induced fluorescence, *Combustion and Flame* 174 (2016) 138–151.
- [78] J. V. Pastor, J. M. Garcia-Oliver, A. Garcia, A. Morales López, *An Experimental Investigation on Spray Mixing and Combustion Characteristics for Spray C/D Nozzles in a Constant Pressure Vessel*, 2018.
- [79] J. C. Ong, K. M. Pang, X. S. Bai, M. Jangi, J. H. Walther, Large-eddy simulation of n-dodecane spray flame: Effects of nozzle diameters on autoignition at varying ambient temperatures, *Proceedings of the Combustion Institute* 000 (2020) 1–8.
- [80] J. García-Oliver, R. Novella, J. M. Pastor, L. Pachano, Computational study of ECN Spray A and Spray D combustion at different ambient temperature conditions, *Transportation Engineering* 2 (2020).

-
- [81] J. M. Desantes, J. M. García-Oliver, R. Novella, E. J. Pérez-Sánchez, Application of a flamelet-based CFD combustion model to the LES simulation of a diesel-like reacting spray, *Computers Fluids* 200 (2020) 104419.
- [82] N. Peters, *Turbulent Combustion*, volume 53, Cambridge University Press, 2000.
- [83] T. Yoshikawa, R. D. Reitz, Development of an improved nox reaction mechanism for low temperature diesel combustion modeling, *SAE International Journal of Engines* 1 (2008) 1105–1117.
- [84] S. Salenbauch, Modeling of soot formation and oxidation in reacting flows, Ph.D. thesis, TU Darmstadt, München, 2019.
- [85] H. Wang, Formation of nascent soot and other condensed-phase materials in flames, *Proceedings of the Combustion Institute* 33 (2011) 41–67.
- [86] C. K. Law, *Combustion Physics*, Cambridge University Press, Cambridge, 2006.
- [87] H. Bockhorn (Ed.), *Soot Formation in Combustion*, volume 59 of *Springer Series in Chemical Physics*, Springer Berlin Heidelberg, Berlin, Heidelberg, 1994.
- [88] H. Bockhorn, A. D’Anna, A. Sarofim, H. Wang, *Combustion Generated Fine Carbonaceous Particles*, KIT Scientific Publishing, 2009.
- [89] F. Bisetti, G. Blanquart, M. E. Mueller, H. Pitsch, On the formation and early evolution of soot in turbulent nonpremixed flames, *Combustion and Flame* 159 (2012) 317–335.
- [90] Y. Zhang, B. Rogg, K. N. Bray, 2-D Simulation of Turbulent Autoignition with Transient Laminar Flamelet Source Term Closure, *Combustion Science and Technology* 105 (1995) 211–227.
- [91] C. S. Chang, Y. Zhang, K. N. Bray, B. Rogg, Modelling and simulation of autoignition under simulated diesel-engine conditions, *Combustion Science and Technology* 113-114 (1996) 205–219.
- [92] H. Lehtiniemi, F. Mauss, M. Balthasar, I. Magnusson, Modeling diesel engine combustion with detailed chemistry using a progress variable approach, *SAE Technical Papers* (2005).
- [93] C. Bekdemir, L. M. Somers, L. P. De Goey, Modeling diesel engine combustion using pressure dependent Flamelet Generated Manifolds, *Proceedings of the Combustion Institute* 33 (2011) 2887–2894.
- [94] U. Egüz, S. Ayyapureddi, C. Bekdemir, B. Somers, P. De Goey, Modeling fuel spray auto-ignition using the FGM approach: Effect of tabulation method, *SAE Technical Papers* (2012).
- [95] U. Egüz, S. Ayyapureddi, C. Bekdemir, B. Somers, P. De Goey, Manifold resolution study of the FGM method for an igniting diesel spray, *Fuel* 113 (2013) 228–238.
- [96] S. Ayyapureddi, U. Egüz, C. Bekdemir, L. M. T. Somers, L. P. H. D. Goey, Application of the FGM Method to Spray A Conditions of the ECN database Eindhoven University of Technology, the Netherlands, *Iclass 2012 12th* (2012) 1–8.
- [97] A. Wehrfritz, O. Kaario, V. Vuorinen, B. Somers, Large Eddy Simulation of n-dodecane spray flames using Flamelet Generated Manifolds, *Combustion and Flame* 167 (2016) 113–131.
- [98] H. Kahila, A. Wehrfritz, O. Kaario, M. Ghaderi Masouleh, N. Maes, B. Somers, V. Vuorinen, Large-eddy simulation on the influence of injection pressure in reacting Spray A, *Combustion and Flame* 191 (2018) 142–159.

-
- [99] H. Kahila, A. Wehrfritz, O. Kaario, V. Vuorinen, Large-eddy simulation of dual-fuel ignition: Diesel spray injection into a lean methane-air mixture, *Combustion and Flame* 199 (2019) 131–151.
- [100] C. Bajaj, M. Ameen, J. Abraham, Evaluation of an unsteady flamelet progress variable model for autoignition and flame lift-off in diesel jets, *Combustion Science and Technology* 185 (2013) 454–472.
- [101] M. M. Ameen, Unsteady flamelet progress variable modeling of reacting diesel jets, Dissertation, Purdue University, 2014.
- [102] I. Dhuchakallaya, P. Rattanadecho, P. Watkins, Auto-ignition and combustion of diesel spray using unsteady laminar flamelet model, *Applied Thermal Engineering* 52 (2013) 420–427.
- [103] J. B. Michel, O. Colin, D. Veynante, Comparison of differing formulations of the PCM model by their application to the simulation of an auto-igniting H₂/air Jet, *Flow, Turbulence and Combustion* 83 (2009) 33–60.
- [104] J. F. Winklinger, Implementation of a Combustion Model based on the Flamelet Concept and its Application to turbulent reactive Sprays, Ph.D. thesis, Universitat Politècnica de València, 2014.
- [105] J. M. Desantes, J. M. García-Oliver, R. Novella, E. J. Pérez-Sánchez, Application of an unsteady flamelet model in a RANS framework for spray A simulation, *Applied Thermal Engineering* 117 (2017) 50–64.
- [106] F. Payri, J. M. García-Oliver, R. Novella, E. J. Pérez-Sánchez, Influence of the n-dodecane chemical mechanism on the CFD modelling of the diesel-like ECN Spray A flame structure at different ambient conditions, *Combustion and Flame* 208 (2019) 198–218.
- [107] E. J. Pérez-Sánchez, J. M. Garcia-Oliver, R. Novella, J. M. Pastor, Understanding the diesel-like spray characteristics applying a flamelet-based combustion model and detailed large eddy simulations, *International Journal of Engine Research* 21 (2020) 134–150.
- [108] F. Tap, P. Schapotschnikow, Efficient combustion modeling based on Tabkin® CFD look-up tables: A case study of a lifted diesel spray flame, *SAE Technical Papers* (2012).
- [109] M. Embouazza, Etude de l'Auto-Allumage par Reduction des Schemas Cinétiques Chimiques. Application a la Combustion Homogene diesel, Ph.D. thesis, Ecole Centrale Paris, 2005.
- [110] J. Galpin, C. Angelberger, A. Naudin, L. Vervisch, Large-eddy simulation of H₂-air auto-ignition using tabulated detailed chemistry, *Journal of Turbulence* 9 (2008) 1–21.
- [111] F. Zhao, W. Yang, W. Yu, A progress review of practical soot modelling development in diesel engine combustion, *Journal of Traffic and Transportation Engineering (English Edition)* 7 (2020) 269–281.
- [112] M. Yen, J. Abraham, Modeling lifted diesel jets: Insights into the correlation between flame lift-off height and soot formation, *8th US National Combustion Meeting 2013 1* (2013) 579–591.
- [113] G. Godel, P. Domingo, L. Vervisch, Tabulation of NO_x chemistry for Large-Eddy Simulation of non-premixed turbulent flames, *Proceedings of the Combustion Institute* 32 I (2009) 1555–1561.
- [114] J. A. Van Oijen, P. H. De Goey, L. P. H. De Goey, Predicting NO formation with flamelet generated manifolds, *Proc. European Comb. Meeting* (2009) 810248.
- [115] C. Zhao, K. Luo, R. Cai, J. Xing, Z. Gao, J. Fan, Hybrid Flamelet/Progress Variable Approach for NO Prediction in Pulverized Coal Flames, *Energy and Fuels* 34 (2020) 10000–10009.

-
- [116] T. Lucchini, G. D'errico, A. Onorati, A. Frassoldati, A. Stagni, G. Hardy, Modeling non-premixed combustion using tabulated kinetics and different fame structure assumptions, *SAE International Journal of Engines* 10 (2017) 593–607.
- [117] Y. B. Zeldovich, The Oxidation of Nitrogen in Combustion and Explosions, *Acta Physicochimica U.S.S.R.* 21 (1946) 577–628.
- [118] Q. Zhou, T. Lucchini, G. D'Errico, N. Maes, B. Somers, X. C. Lu, Computational Modeling of Diesel Spray Combustion with Multiple Injections, *SAE Technical Papers 2020-April* (2020).
- [119] Q. Zhou, Multi-Dimensional numerical modeling of Combustion in Compression - Ignition Engines using tabulated kinetics and Turbulence-Chemistry Interaction, Ph.D. thesis, Politecnico DI Milano, 2021.
- [120] P. Pakseresht, S. V. Apte, Volumetric displacement effects in Euler-Lagrange LES of particle-laden jet flows, *International Journal of Multiphase Flow* (2019) 16–32.
- [121] A. Wehrfritz, V. Vuorinen, O. Kaario, M. Larimi, Large eddy simulation of high-velocity fuel sprays: Studying mesh resolution and breakup model effects for spray A, *Atomization and Sprays* 23 (2013) 419–442.
- [122] M. Davidovic, T. Falkenstein, M. Bode, L. Cai, S. Kang, J. Hinrichs, H. Pitsch, LES of n -Dodecane Spray Combustion Using a Multiple Representative Interactive Flamelets Model, *Oil and Gas Science and Technology* 72 (2017).
- [123] J. K. Dukowicz, A particle-fluid numerical model for liquid sprays, *Journal of Computational Physics* 35 (1980) 229–253.
- [124] G. Stiesch, *Modeling Engine Spray and Combustion Processes, Heat and Mass Transfer*, Springer Berlin Heidelberg, Berlin, Heidelberg, 2003.
- [125] L. Weiß, A. Peter, M. Wensing, Diesel Spray characterization with Schlieren-Mie Technique, in: *18th Laser Lisbon Int. Symposium on Application of Laser Imaging Techniques to Fluid Mechanics*, 2016.
- [126] A. Ern, V. Giovangigli, Multicomponent Transport Algorithms, volume 24 of *Lecture Notes in Physics Monographs*, Springer Berlin Heidelberg, Berlin, Heidelberg, 1994.
- [127] J. O. Hirschfelder, C. F. Curtiss, R. B. Bird, *Molecular Theory of Gases and Liquids*, John Wiley Sons, New York, 1969.
- [128] R. Kee, M. Coltrin, P. Glarborg, *Chemically reacting flow: theory and practice*, John Wiley & Sons, New Jersey, 2003.
- [129] C. R. Wilke, A Viscosity Equation for Gas Mixtures, *The Journal of Chemical Physics* 18 (1950) 517–519.
- [130] S. Mathur, S. C. Saxena, Viscosity of polar gas mixtures: Wilke's method, *Applied Scientific Research* 15 (1965) 404–410.
- [131] A. B. Ruscic, Branko, Extended Third Millenium Ideal Gas and Condensed Phase Thermochemical Database for Combustion with Updates from Active Thermochemical Tables, Technical Report, Technical Report ANL-05/20 TAE 960, Argonne National Laboratory, 2005.
- [132] A. Leonard, Energy Cascade in Large-Eddy Simulations of Turbulent Fluid Flows, 1975, pp. 237–248.
- [133] M. Klein, M. Germano, Analysis and modelling of the commutation error, *Fluids* 6 (2021) 1–15.

-
- [134] J. Boussinesq, Théorie de l'écoulement tourbillant, Mémoires présentés par divers savants à l'Académie des Sciences 23 (1877) 46–50.
- [135] F. Nicoud, H. B. Toda, O. Cabrit, S. Bose, J. Lee, Using singular values to build a subgrid-scale model for large eddy simulations, *Physics of Fluids* 23 (2011).
- [136] M. Rieth, F. Proch, O. T. Stein, M. W. A. Pettit, A. M. Kempf, Comparison of the Sigma and Smagorinsky LES models for grid generated turbulence and a channel flow, *Computers and Fluids* 99 (2014) 172–181.
- [137] B. T. Hubert, O. Cabrit, K. Truffin, B. Gilles, F. Nicoud, A dynamic procedure for advanced subgrid-scale models and wall-bounded flows, *International Symposium on Turbulence and Shear Flow Phenomena* (2011) 1–6.
- [138] H. Pitsch, H. Steiner, Large-eddy simulation of a turbulent piloted methane/air diffusion flame (Sandia flame D), *Physics of Fluids* 12 (2000) 2541–2554.
- [139] A. Kempf, F. Flemming, J. Janicka, Investigation of lengthscales, scalar dissipation, and flame orientation in a piloted diffusion flame by les, *Proceedings of the Combustion Institute* 30 (2005) 557–565.
- [140] S. P. Burke, T. E. W. Schumann, Diffusion Flames, *Industrial & Engineering Chemistry* 20 (1928) 998–1004.
- [141] R. W. Bilger, The Structure of Diffusion Flames, *Combustion Science and Technology* 13 (1976) 155–170.
- [142] N. Peters, Laminar diffusion flamelet models in non-premixed turbulent combustion, *Progress in Energy and Combustion Science* 10 (1984) 319–339.
- [143] H. G. Pitsch, Modellierung der Zündung und Schadstoffbildung bei der dieselmotorischen Verbrennung mit Hilfe eines interaktiven Flamelet-Modells 82 (1998) VI, 148 S. : Ill., graph. Darst.
- [144] C. Hasse, A Two-Dimensional Flamelet Model for Multiple Injections in Diesel Engines 82 (2004) 134.
- [145] Engine Combustion Network, ECN Spray A webpage, 2010. URL: <https://ecn.sandia.gov/diesel-spray-combustion/target-condition/spray-ab/>.
- [146] M. Ihme, L. Shunn, J. Zhang, Regularization of reaction progress variable for application to flamelet-based combustion models, *Journal of Computational Physics* 231 (2012) 7715–7721.
- [147] Y.-S. Niu, L. Vervisch, P. D. Tao, An optimization-based approach to detailed chemistry tabulation: Automated progress variable definition, *Combust. Flame* 160 (2013) 776 – 785.
- [148] U. Prüfert, S. Hartl, F. Hunger, D. Messig, M. Eiermann, C. Hasse, A constrained control approach for the automated choice of an optimal progress variable for chemistry tabulation, *Flow, Turbulence and Combustion* 94 (2015) 593–617.
- [149] P. Domingo, L. Vervisch, D. Veynante, Large-eddy simulation of a lifted methane jet flame in a vitiated coflow, *Combustion and Flame* 152 (2008) 415–432.
- [150] F. Hunger, B. Stelzner, D. Trimis, C. Hasse, Flamelet-modeling of inverse diffusion flames, *Flow and Turbulence and Combustion* 90 (2013) 833–857.
- [151] S. Weise, D. Messig, B. Meyer, C. Hasse, An abstraction layer for efficient memory management of tabulated chemistry and flamelet solutions, *Combust. Theor. Model.* 17 (2013) 411–430.

-
- [152] S. Weise, C. Hasse, Reducing the memory footprint in large eddy simulations of reactive flows, *Parallel Comput.* 49 (2015) 50–65.
- [153] N. Peters, Length Scales in Laminar and Turbulent Flames, *Numerical Approaches to Combustion Modeling* (1991) 155–182.
- [154] H. Steiner, H. Pitsch, Scalar Mixing and Dissipation Rate in Large-Eddy Simulations of Non-Premixed Turbulent Combustion, *Proceedings of the Combustion Institute* 28 (2000) 1–9.
- [155] T. Hellström., RIF Implementation and Testing, Technical Report, 1997.
- [156] A. Wehrfritz, Large Eddy Simulation of Fuel Spray Combustion, Ph.D. thesis, Aalto University, 2016.
- [157] W. Ranz, W. R. Marshall, Evaporation from drops—I–II, *Chemical Engineering Progress* 48 (1952) 141–146.
- [158] G. L. Hubbard, V. E. Denny, A. F. Mills, Droplet evaporation: Effects of transients and variable properties, *International Journal of Heat and Mass Transfer* 18 (1975) 1003–1008.
- [159] R. D. Reitz, Modeling atomization processes in high-pressure vaporizing sprays, *Atomization and Spray Technology* 3 (1987) 309–337.
- [160] R. D. Reitz, R. Diwakar, *Structure of High-Pressure Fuel Sprays*, 1987.
- [161] S. Popp, Large Eddy Simulation of Turbulent Multi-Regime Combustion: Potentials and Limitations of Flamelet-Based Chemistry Modeling, Ph.D. thesis, TU Darmstadt, 2020.
- [162] A. Zschutschke, D. Messig, A. Scholtissek, C. Hasse, Universal Laminar Flame Solver (ULF), 2017. doi:<https://doi.org/10.6084/m9.figshare.5119855.v2>.
- [163] J. F. Grcar, R. J. Kee, M. D. Smooke, J. A. Miller, A hybrid newton/time-integration procedure for the solution of steady, laminar, one-dimensional, premixed flames, *Symposium (International) on Combustion* 21 (1988) 1773–1782. Twenty-First Symposium (International on Combustion).
- [164] D. Messig, Numerical Simulation of Pulverized Coal Combustion, Ph.D. thesis, Technische Universität Bergakademie Freiberg, 2017.
- [165] A. Scholtissek, Flamelet Modeling in Composition Space for Premixed and Non-Premixed Combustion, Ph.D. thesis, TU Darmstadt, 2019.
- [166] G. Buzzi-Ferraris, F. Manenti, *Differential and Differential-Algebraic Systems for the Chemical Engineer*, 1 ed., Wiley-VCH, Weinheim, 2014.
- [167] D. G. Goodwin, R. L. Speth, H. K. Moffat, B. W. Weber, Cantera: An object-oriented software toolkit for chemical kinetics, thermodynamics, and transport processes, <https://www.cantera.org>, 2021. Version 2.5.1.
- [168] A. Ern, C. Yale Univ., New Haven, V. Giovangigli, Fast and accurate multicomponent transport property evaluation 120 (1995).
- [169] F. Hunger, M. Gauding, C. Hasse, On the impact of the turbulent/non-turbulent interface on differential diffusion in a turbulent jet flow, *Journal of Fluid Mechanics* 802 (2016) R5.
- [170] P. K. Sweby, High Resolution Schemes Using Flux Limiters for Hyperbolic Conservation Laws, *SIAM Journal on Numerical Analysis* 21 (1984) 995–1011.
- [171] R. S. Barlow, G. J. Fiechtner, C. D. Carter, J. Y. Chen, Experiments on the scalar structure of turbulent CO/H₂/N₂ jet flames, *Combustion and Flame* 120 (2000) 549–569.

-
- [172] C. Villani, *Optimal transport: old and new*, volume 338, Springer Science & Business Media, 2008.
- [173] R. Johnson, H. Wu, M. Ihme, A general probabilistic approach for the quantitative assessment of les combustion models, *Combustion and Flame* 183 (2017) 88–101.
- [174] C. Han, R. Barlow, H. Wang, Flamelet modeling of differential molecular diffusion in oxy-fuel turbulent jet flames, in: *Thirteenth International Workshop on measurement and Computation of Turbulent Flames*, 2016.
- [175] C. Han, R. Barlow, H. Wang, Examination of flamelet differential molecular diffusion models in oxy-fuel turbulent jet flames, in: *DFD16 Meeting of The American Physical Society*, 2016.
- [176] A. Garmory, E. Mastorakos, Numerical simulation of oxy-fuel jet flames using unstructured LES–CMC, *Proceedings of the Combustion Institute* 35 (2015) 1207 – 1214.
- [177] W. L. Oberkampf, T. G. Trucano, Verification and validation in computational fluid dynamics, *Progress in Aerospace Sciences* 38 (2002) 209–272.
- [178] H. S. Sim, N. Maes, L. Weiß, L. M. Pickett, S. A. Skeen, Detailed measurements of transient two-stage ignition and combustion processes in high-pressure spray flames using simultaneous high-speed formaldehyde PLIF and schlieren imaging, *Proceedings of the Combustion Institute* 38 (2020) 5713–5721.
- [179] L. Weiß, H. S. Sim, N. Maes, L. M. Pickett, S. A. Skeen, High-speed formaldehyde PLIF measurements on the ECN Spray D, unpublished work ECN/Sandia, contact: lukas.weiss@fau.de, 2021.
- [180] E. Ranzi, A. Frassoldati, R. Grana, A. Cuoci, T. Faravelli, A. P. Kelley, C. K. Law, Hierarchical and comparative kinetic modeling of laminar flame speeds of hydrocarbon and oxygenated fuels, *Progress in Energy and Combustion Science* 38 (2012) 468–501.
- [181] G. Bagheri, E. Ranzi, M. Pelucchi, A. Parente, A. Frassoldati, T. Faravelli, Comprehensive kinetic study of combustion technologies for low environmental impact: MILD and OXY-fuel combustion of methane, *Combustion and Flame* 212 (2020) 142–155.
- [182] R. Payri, F. Salvador, J. Gimeno, G. Bracho, Virtual Injection Rate Generator, 2013. URL: <https://www.cmt.upv.es/#/ecn>.
- [183] R. Payri, J. Gimeno, J. Cuisano, J. Arco, Hydraulic characterization of diesel engine single-hole injectors, *Fuel* 180 (2016) 357–366.
- [184] L. M. Pickett, J. P. Abraham, C. Bajaj, ECN Diesel Database, SprayA nominal conditions (non-reactive), dataset bkldaAL4 (2009).
- [185] M. Gadalla, J. Kannan, B. Tekgül, S. Karimkashi, O. Kaario, V. Vuorinen, Large-Eddy Simulation of ECN Spray A: Sensitivity Study on Modeling Assumptions, *Energies* 2020, Vol. 13, Page 3360 13 (2020) 3360.
- [186] P. Pepiot-Desjardins, H. Pitsch, An efficient error-propagation-based reduction method for large chemical kinetic mechanisms, *Combustion and Flame* 154 (2008) 67–81.
- [187] X. L. Zheng, T. F. Lu, C. K. Law, Experimental counterflow ignition temperatures and reaction mechanisms of 1,3-butadiene, *Proceedings of the Combustion Institute* 31 I (2007) 367–375.
- [188] K. E. Niemeyer, C. J. Sung, M. P. Raju, Skeletal mechanism generation for surrogate fuels using directed relation graph with error propagation and sensitivity analysis, *Combust. Flame* 157 (2010) 1760–1770.

-
- [189] L. M. Pickett, S. A. Skeen, ECN Diesel Database, Spray A nominal conditions, dataset jkldnAL4, 2012.
- [190] L. M. Pickett, ECN Diesel Database, Spray A nominal conditions, dataset AJKLDNLRFA, 2017.
- [191] L. M. Pickett, ECN Diesel Database, Spray A nominal conditions, dataset ABKLDNLRFA, 2015.
- [192] J. M. García-Oliver, ENERXICO Database, 2020. URL: <https://www.cmt.upv.es/#/ecn>.
- [193] L. M. Pickett, ECN Diesel Database, Spray D nominal conditions, dataset AJKLDDLRSREK, 2016.
- [194] L. Wang, Analysis of the filtered non-premixed turbulent flame, *Combustion and Flame* 175 (2017) 259–269.
- [195] W. Chan, M. Ihme, Flamelet regime characterization for non-premixed turbulent combustion simulations, *Combustion and Flame* 186 (2017) 220 – 235.
- [196] B. Coriton, M. Zendejdel, S. Ukai, A. Kronenburg, O. T. Stein, S. K. Im, M. Gamba, J. H. Frank, Imaging measurements and LES-CMC modeling of a partially-premixed turbulent dimethyl ether/air jet flame, *Proceedings of the Combustion Institute* 35 (2015) 1251–1258.
- [197] S. Salenbauch, C. Hasse, M. Vanni, D. L. Marchisio, A numerically robust method of moments with number density function reconstruction and its application to soot formation, growth and oxidation, *Journal of Aerosol Science* 128 (2019) 34–49.
- [198] L. Bravo, C.-b. Kweon, A Review on Liquid Spray Models for Diesel Engine Computational Analysis (DROPLET BREAKUP), Army Research Laboratory (2014) 54.
- [199] H. Li, R. Verschaeren, G. Decan, T. Beji, S. Verhelst, Evaluation of breakup models for marine diesel spray simulations (2019) 2–4.
- [200] F. Fischer, Primary breakup model considering the spray core development, Ph.D. thesis, TU Darmstadt, Aachen, 2011.
- [201] C. Meneveau, T. S. Lund, W. H. Cabot, A Lagrangian dynamic subgrid-scale model of turbulence, *Journal of Fluid Mechanics* 319 (1996) 353–385.